.

Novel NDE Techniques in the Power Generation Industry

Chris Ward

Thesis submitted to the University of Nottingham
for the degree of Doctor of Engineering

March 2010

Abstract

The thesis presented here comprisises the work undertaken for research into novel NDE techniques in the power generation industry. This has been undertaken as part of the Engineering Doctorate Scheme run by the Research Centre for Non-Destructive Evaluation (RCNDE), which aims to bridge the technological gap between university research and industrial application. In this case, the scheme consisted of two projects completed in conjunction with RWE npower looking at current NDE problems in steam turbine and steam-raising plant. The first project was concerned with detecting microstructural transformation in steam turbine blades, which can act as a precursor to failure by environmentally assisted cracking. This project, and indeed, this entire thesis is principally based on electromagnetic testing methods. An eddy current technique for mapping the microstructural phases was produced and validated as far as was acheivable; this offered a significant time-saving advantage over the previous method, by reducing inspection time from 5 man days to just 1.5. The technique has novelty in producing a 2-dimensional map of the blade surface which highlights areas where microstructural phases differ. The second project focuses on the detection of microstructural damage associated with material creep life expiry. This forms a review of the current state of technology and highlights potentially useful paths for future research in both established and emerging NDE technologies, including Magnetic Barkhausen Noise testing and laser-gereated ultrasound. Both projects have provided tangible benefit to the sponsoring company and have pushed forward research in a number of technological applications.

Acknowledgements

The author would like to thank the following people for all their help and support during this project:

Prof. Richard Challis, Mr. Paul Crowther, Prof. Chris Scruby, Mr Roger Lyon, Dr. Steve Dixon, Prof. Gui Tian, Dr Marion Unwin, Dr Steve Sharples, Mr John Wilson, Prof. Peter Nagy, Prof. Mike Somekh, Dr Theodoros Theodoulidis, Dr. Maxim Morozov, Dr V Moorthy Vaidhianathasamy, Mr Giuseppe Sposito, Prof. Bruce Drinkwater, Dr. Mark Potter, Mr Robert Spencer, Mr Richard Day, Mr Kevin Stamps, Mr Antony Farrar, Mr Chris Charlesworth, Dr David Oates, Dr Steve Brett, Dr Juan Sanchez-Hanton, Dr Neville Shaw, Dr Ken Mitchell, Mr Jeff Hulance, Mr Geoff Spink, Mr Chris Johnston, Mr Mike Goodbun, Mr Andrew Tweedie, Mr Adam Lea, Mr Robert Quimby, Mr David Edgar, Miss Katie Milne, Mr John Russell, Mr Murad El-Bakry, Mr Sean Winwood, Mr Ben Weekes, Mr David Crowle, Ms Colombe Dalpe, Mr Michael Sirois, Mr Joe Renaud, Mr Jean-Francois Bureau. With special thanks to Steph for all your love and support.

Table of Contents

Preface

Authors Profile

Chris Ward is a graduate in Mechanical Engineering from the University of Warwick. He has worked in the electricity generation industry for over 8 years occupying various roles in the plant integrity section of engineering. He joined the RWE npower Inspection Management (NDE) group 5 years ago, working on the development of new techniques. The author is currently the Development Technical Officer for the Inspection Management group, responsible for management of all NDE related research and development activities. This includes representing RWE npower in RCNDE led initiatives, and the author also actively participates in industry/university collaborations led by ESR (Electricity Supply Research) Network, EPRI, SuperGen and TWI.

Chapter 1 Introduction, Background, Aims and Objectives

1.1. Introduction general

This thesis investigates the use of principally electromagnetic non-destructive evaluation methods for specific applications within the power generation industry. It covers two individual projects which form the research element of the Engineering Doctorate Scheme. The research in these projects is not limited to electromagnetic methods, however, they do comprise the majority of the novel research.

This research work is carried out on behalf of RWE npower, a UK power generation company in conjunction with Nottingham University, a member of the RCNDE. Additional work has been carried out with Imperial College London, University of Warwick and Newcastle University.

1.2. The Engineering Doctorate Scheme

The Engineering Doctorate (EngD) Scheme for non-destructive evaluation (NDE) brings together academic and industrial expertise to solve real-life NDE problems and educate the research engineers. Research engineers are registered students at the participating universities, and in this case, an employee of the sponsoring industrial partner. The intention is that the research engineers are guided by their assigned academic institution, whilst gaining practical experience of industry. The research engineers provide a link between industrial and academic institutions and are ambassadors for the furthering of NDE technology research in an applied setting. The scheme lasts for four years, during which time the research engineers divide their time between working for their sponsor company, furthering their research at the academic institutions and expanding their NDE knowledge through the taught elements of the EngD scheme.

1.2.1. Aims and Objectives of EngD Scheme

The purpose of the Engineering Doctorate is to fill the divide between industrial development of NDE and research in NDE at British universities. It aims to take problems from industrial situations and give them an scientifically rigorous approach to their solution. The constraints and practicalities of industrial developments should be considered and accommodated into a final solution which will raise the standard of industrial NDE developments.

In addition to this improvement to the standard of industrial NDE development, there will be additional benefits to all parties concerned. The research engineer will gain a detailed understanding of a wide range of NDE techniques, an understanding of the state of the art research being realised in the academic community and an understanding of the business needs and drivers of the industrial partner. The industrial partner will gain a highly skilled employee who can drive the quality of their NDE business upwards and will be able to influence future academic research to align with their particular needs. The academic partner will gain focus and an appreciation of the requirements of industry to stimulate future research.

1.3. NDE in the Power Generation Industry

Non-destructive testing is an integral part of safely operating power generation assets. Consequently the power generation industry is one of the largest employers of NDE personnel and one of the main drivers of NDE technology.

The purpose of NDE in the power generation industry has been assessing plant integrity and extending plant life in order to maximise the availability of the asset. Traditionally,

this has focussed on the detection and monitoring of cracks, and particular emphasis is placed on the ability to accurately locate and size ever-smaller defects. The reason for this is the high-energy nature of power generation components. The high temperatures and stresses involved mean that even small defects can rapidly lead to catastrophic component failure. Materials and processes in power generation are well understood, resulting in highly accurate predictions of component life and critical defect sizes. By accurately monitoring sub-critical defects, plant can safely be allowed to continue running without risk from catastrophic failure.

Planning for inspections is key to the power generation industry, as it is simply not practical to inspect every component of a power plant. Knowledge gained from operational experience, metallurgy, chemistry and structural analysis must be utilised to ensure the appropriate items receive the most rigorous inspection methods. The large number of welded joints require high investment in NDE as these are generally considered to be areas of weakness. The continually changing nature of power generation assets, with ongoing modification of existing plant, and new designs and methods, ensures the continuous evolution of NDE within the industry.

A large number of NDE techniques are employed in power generation due to the wide variety of components that require inspection. Below is a list of the different techniques employed, ranked by an estimate of how much they are used in power generation NDE, based on the NDE workload for RWE npower stations[1] and UK customer sites[2].

- Magnetic Particle Inspection
- Conventional Bulk Wave Ultrasonic Inspection

- Visual Inspection
- Dye-penetrant Inspection
- Radiographic Testing
- Phased Array Ultrasound
- Other methods: XRF, Hardness, Thermography, Shearography, Magnetic Flux Leakage
- Eddy Current Inspection
- Ultrasonic Time of Flight Diffraction

As new techniques are established and new problems arise with existing and new-build plant, the various NDE methods will fall in and out of favour, creating a dynamic industry where an understanding of developments is key. The high energy nature of power plant ensures there will always be a significant requirement for NDE in the industry.

A major area of concern within the industry is resources, particularly skilled and experienced manpower. Many technicians learnt their trade and "grew-up" with the large coal (31% of generation) and nuclear power stations (14% of generation) that still form a significant proportion of the UK's generation capacity, despite some being nearly 40 years old[3]. As a consequence of this the age profile amongst NDE practitioners and engineers in general, is such that many are nearing the end of their careers. Action has been taken recently to try to address this problem, by encouraging younger people into the industry through apprenticeship schemes. Whilst this can replace some of the manpower, a lot of experience will be lost, increasing the risk of human error. This is where the Engineering Doctorate scheme is important to the industry as it can give

research engineers a more sound technical knowledge of the techniques employed, reducing the industry's reliance on operator experience to create and validate techniques. Through industrial exposure, research engineers will also be able to provide appropriate solutions to NDE problems that will reduce the chance of operator error.

1.4. RWE npower Company Outline

RWE npower owns and operates a number of power stations within the UK as well as offering technical support to power stations all over the world. The current portfolio consists of eight fossil fuel powered stations (3 coal-fired, 2 oil-fired and 3 combined-cycle gas turbine) as well as a number of combined heat and power installations, hydro-electric stations and wind-farms[4].

Due to the risk of catastrophic failure, injury to personnel, damage to plant and loss of generation income, power plants are subject to stringent regulation and integrity checks. Much of the generation capacity is life expired and must be evaluated regularly to ensure its continued safe running. New plant throws up its own challenges as unforeseen problems manifest themselves as the plant passes through its life-cycle. Consequently NDE forms an integral part of the process to prevent component failure.

NDE within RWE npower is controlled by the Inspection Management Group, which is formed of 18 full time company employees and around 40 contract staff on rolling one-year contracts[5]. The work can be roughly split into two categories:

Outage management – The provision of staff and capabilities for planned station shutdowns. This is usually conventional NDE; ultrasonic testing, magnetic-particle

inspection, etc.).

Specialist inspection – Development and implementation of high integrity inspection methods for specific applications. Which commonly use automated scanning for interrogation by ultrasonic testing, Time of Flight Diffraction ultrasonics (ToFD), phased-array ultrasonics and eddy current testing. Typical applications are the inspection of turbine rotors, high pressure pipe-work and generator retaining rings, which RWE npower undertakes for its own plant as well as plant in Europe, North America, Australia and the Middle East.

1.5. Project Outlines

The main focus of this thesis is electromagnetic methods, but in the course of investigation, other techniques will be considered for specific applications. I have two extensive research projects which reflect the future requirements for NDE within RWE npower, they are "Microstructure mapping of steam turbine blades" and "Assessment of creep damage in main steam pipe-work".

1.5.1. Microstructure mapping of steam turbine blades.

During overhaul, final-stage blades from low pressure steam turbines can develop localised hard spots where a heat-treatment has been incorrectly applied or where a welding operation on a neighbouring blade has caused localised heating. In this particular case, hard spots are a manifestation of a structural change from tempered martensite to untempered martensite. Affected areas of turbine blade are susceptible to stress corrosion cracking and must be identified by non-destructive evaluation prior to return to service. Currently this is performed by mechanical hardness testing, which is a

highly time consuming process. The tip of each blade (an area extending from the free end of the blade to roughly 250mm from the free end) is marked with a 7 x 6 matrix of equi-spaced spots and a number of hardness readings are taken at each spot. This is performed for each of the 192 blades on a turbine rotor and will take around a week to complete. The intention of this project is to create an inspection system that will be able to identify potential hard areas in a time-efficient manner so that these "at-risk" areas can then be mechanically hardness tested.

1.5.2. Assessment of creep damage in main steam pipe-work.

The UK's coal and oil-fired power stations utilise long lengths of pipe-work to transfer steam from the boiler to the turbine. Due to the high-temperature and high-pressure conditions (568°C and 165 bar at Didcot A are typical) [6] under which this pipe-work is operating it is susceptible to creep damage. Although the original pipe-work had been heavily over-engineered, it is now being operated beyond its projected lifetime and more and more areas are considered to be at risk of severe creep damage. Traditionally creep damage is monitored by metallurgical replication, where a transparent copy of the etched microstructure on the surface of the component is made on an acetate slide and examined under a microscope to determine the level of creep cavitation present. This is a time consuming method and will become even more so with the anticipated increase in volume of inspections. There are a number of aspects to be considered in this project, all of which are quite involved. There are several materials to consider, both parent metal and weld metal, all of which have differing creep-degradation microstructural morphology. There are also a large number of NDE techniques that can be, and have been, tried[7]. As a result of this, this project will comprise a feasibility study setting out

the most promising solutions to the problems of detecting at risk areas of parent metal and characterising creep damage and micro-cracking where it occurs. Where appropriate, experiments are performed to assess the suitability of techniques, including bulk and phased array ultrasound, Barkhausen noise, eddy current testing and laser-generated ultrasound, and a plan for future study is proposed. As a result, the results presented in the relevant chapters (Chapters 9 and 10) do not aim to search for a definitive solution to the problem, but do highlight some interesting key trends and scope for future research.

There are two materials used for steam pipe-work which are investigated for this project. The first is a low-alloy ferritic steel, commonly referred to as 0.5CrMoV which has been used in power plant since the 1960's[8]. The second is a martensitic steel, known as Grade 91, which has been utilised since the 1980's[9]. These two materials have similar mechanical properties but behave differently in terms of creep degradation.

A method of characterising the extent of creep-related damage is desirable as a means to replace metallurgical replication. This would need to give as much information as replication does about the creep state of the material at all stages through the life of the component. This would ideally be applicable to both parent material (generalised creep damage in the material bulk) and welds (localised creep damage).

Additionally, a method of detecting micro-cracking in welds is sought. Current ultrasonic testing methods can reliably detect and size macro defects, but lack the resolution to detect the early stages of cracking. Highly focussed ultrasonic inspection techniques are evaluated and proposed to overcome this challenge.

Chapter 2 Background Theory on Electromagnetics

2.1. Background on Electromagnetism

Eddy current theory has its basis in electromagnetism, an area of physics consisting "Electric" and "Magnetic" effects. In order to be able to understand these two effects, it is necessary to look at the property of matter that is common to both of them, namely *electric charge*.

2.1.1. Electrical Characteristics

Conductors can be considered to be an array of positive ions interspersed with "free" electrons (approximately one per atom) capable of moving through the material carrying charge and thus giving the material its conductive characteristic.

All charges have an electric field associated with them, the magnitude of the electric field at any point due to a charge can be calculated using the formula

$$E = \frac{1}{4\pi\varepsilon_0}\frac{Q}{r^2} \qquad (2.1.1)$$ [10]

Where

Q = is the magnitude of the charge

ε_0= is the permittivity of free space

r = is the distance from the charge to the point in the field.

Each charge exerts a force on every other charge, so that for any given pair of charges (q_1 and q_2) the force exerted is given by Coulomb's law.

$$F = \frac{1}{4\pi\varepsilon_0}\frac{q_1 q_2}{r^2} \quad (2.1.2)$$

In conductors, the effect of the free charges are characterised by the *Electric*

Displacment Field, which is a vector field integral to Gauss law concerning the electric field. In differential form Gauss law is simply described

$$\nabla \cdot \underline{D} = \rho \quad (2.1.3)$$ [10]

where $\underline{D}$ is the electric displacement field and ρ is the free electric charge density. This does not include dipole charges bound within the material. In other words, the electric charge density is equal to the divergence of the electric displacement field. This is one of Maxwell's equations (The derivation of these equations can be found in Appendix B).

When an external electric field is applied, the charged particles are subjected to a force causing them to move in the direction of the force with a velocity known as the "drift velocity". However, the electrons will experience multiple collisions with positive ions which will retard the motion in the direction of the force, but won't stop it altogether. So there is a net flow of electrons in the direction of the force, as shown in Figure 2.1. In other words, there is a flow of current. The more free electrons are contained within a material, the greater the flow of electrons so the conductivity of a material is said to be greater.

The collision of the electrons with the positive ions causes the ions to vibrate creating heat within the conductor; the more collisions there are the greater the heating effect becomes. The resistivity of a material is its resistance to current flow, so increasing the frequency of collisions between electrons and positive ions will increase the resistivity. In metals, increased temperature will vibrate the ions more so there will be more collisions and hence greater resistivity.

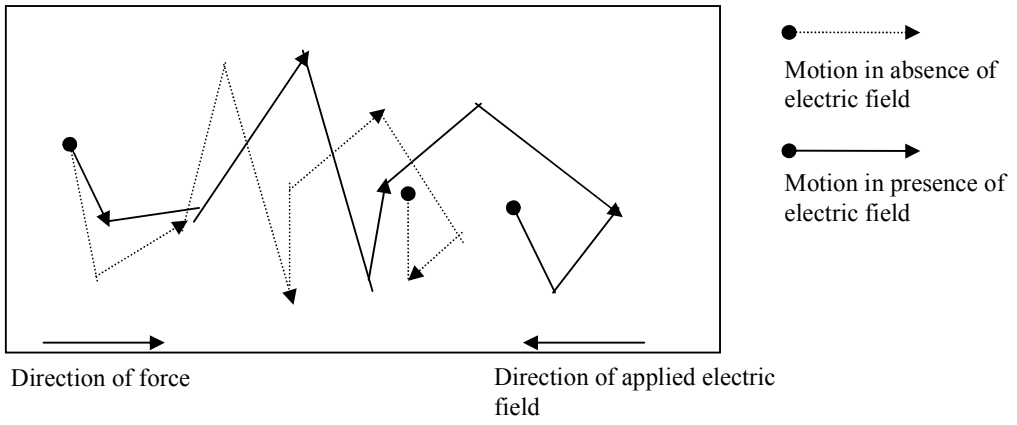

Figure 2.1 – Motion of an electron in a conductor. Where an electric field is applied the end position is further to the right.

2.1.2. Magnetic Characteristics

Every individual charge not only has an electric field associated with it but it also has a magnetic field, these two fields are not entirely separate entities and contribute to the electromagnetic field. What we consider to be the electric field affects charges in its vicinity and what we consider to be the magnetic field affects moving charges and magnetic dipoles.

As with electrical flux, Gauss' theorem can be adapted for the electromagnetic case and forms another of Maxwell's equations. Applicable to static magnetic fields the net magnetic flux is zero because as many field lines enter any Gaussian surface as leave it. Thus there are no sources or sinks of the magnetic field to enclose. In its integral form Gauss' law for magnetism can be written

$$\nabla \cdot \underline{B} = 0 \qquad (2.1.4)$$ [10]

where $\underline{B}$ is the magnetic flux density.

In terms of magnetism it is possible to characterise any atom by a superposition of magnetic dipole moments corresponding to the spin of the atom nucleus and the spin and orbit of the electrons surrounding it. The net magnetic moment of an atom is the sum of all the magnetic dipoles due to the spin and orbit of the various electrons. For many materials the net magnetic moment of each atom is zero; however, by applying an external magnetic field the angular velocities of the electrons will change causing a net change in dipole moment. This net change in dipole moment is called diamagnetism and materials that can only be magnetised in this way during exposure to an external magnetic field are commonly called diamagnetic materials.

In paramagnetic materials, the net magnetic moment of the individual atoms is not zero, even in the absence of a magnetic field. On a macroscopic level however the net magnetisation is zero because of the completely random distribution of the individual atoms' magnetic moments. In the presence of a magnetic field a twisting force will be applied to each dipole, causing a degree of alignment in the direction of the applied field.

A third kind of magnetism is ferromagnetism whereby the distribution of atoms with non-zero magnetic moments is such that they have an overall directional bias and thus a net magnetic moment on a macroscopic scale. This is the case even in the absence of an external magnetic field. In the presence of an applied field they will align in the direction of the magnetic field much more readily than in paramagnetic materials. The ease by which a material becomes magnetised is known as its magnetic susceptibility. Ferromagnetic materials have much stronger dipole moment than diamagnetic or paramagnetic materials. The reason for this is the dominance of the dipole moment from

the electron spin compared to the electron orbit.

Regions of material where the atomic magnetic moments are aligned are known as domains, caused by the interaction of strong neighbouring dipoles. Ferromagnetic materials comprise a large number domains and when a magnetic field is applied to a ferromagnetic material the domains tend to line up, so that the sum of the fields from the ferromagnet and the applied magnetic field is higher in magnitude than the applied magnetic field alone.

Permeability of a material is a measure of the extent to which the magnetisation of a material responds linearly to an applied magnetic field. In calculations it is common to use the relative permeability; the ratio of a material's permeability to the permeability of free space. The relative permeability is closely related to the magnetic susceptibility of the material and is defined as

$$\mu_r = 1 + \chi_m \qquad (2.1.5)$$ [11]

Ferromagnetic materials are very easily magnetised and have a relative permeability much greater than 1, paramagnetic materials have a low response to magnetisation and have a relative permeability of very slightly greater than 1 and diamagnetic materials essentially do not magnetise and have a relative permeability very slightly less than 1.

The concept of domains is very important when discussing ferromagnetic materials and is best illustrated as shown in Figure 2.2. The first arrangement shows the original domain structure in a single crystal, prior to the application of any external magnetic field. Despite being magnetised to saturation the domains are orientated randomly so that the net magnetism is zero. When a weak magnetic field is applied to a

ferromagnetic material the volume of domains preferentially orientated in the direction of the applied field is increased at the detriment of those which are not. This is known as domain wall motion and is shown in the second arrangement of Figure 2.2. Once the applied field is removed the domain wall motion reverses and the material returns close to its original state of magnetism. When a strong external field is applied to the material the domain wall motion reaches the point where it becomes irreversible. Very strong magnetic fields can cause domain rotation, where all the domains begin to take on preferential alignment with the applied magnetic field. This phenomenon is shown in the third arrangement of Figure 2.2.

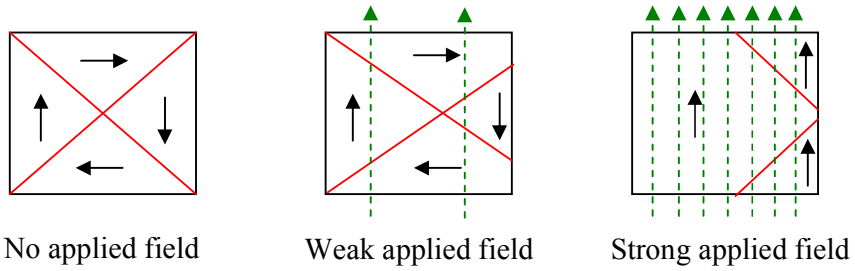

Figure 2.2 – Single crystal domain formation under influence of magnetic fields

The response of a ferromagnetic material to a magnetic field can best be described by a hysteresis curve like the one shown in Figure 2.3. A hysteresis curve shows the variations in characteristics of the material caused by the irreversible domain wall motion and domain rotation.

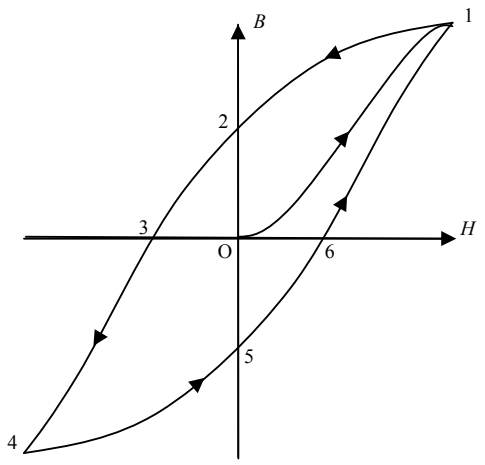

Figure 2.3 – Typical hysteresis curve for a ferromagnetic material.

In its completely unmagnetised state the values of *B* (magnetic flux density) and *H* (magnetic field intensity) are both zero. As an increasingly strong magnetic field is applied (increasing H), the magnetisation builds up causing an increase in B up to the saturation point at point 1 on the diagram. The curve from O to point 1 consists of three regions: An initial curve, an almost linear centre section and a final curve. The initial curve corresponds to the region where the reversal of domain wall motion is possible. The middle section is where the domain wall motion becomes irreversible and the final section is where domain reversal occurs.

When the applied field is removed (*H* drops to zero) a different path is followed from point 1 to point 2. Initially there is some domain wall rotation and then some more irreversible domain wall rotation. At point 2 despite there being no applied field there is still a degree of magnetism retained by the material, this point is the magnetic remanence of the material. In order to further reduce the value of *B* to zero (point 3 on the diagram) an opposing magnetic field must now be applied to cause more irreversible domain wall motion. The strength of this applied field corresponds to the value of *H* at

point 3 on the diagram; this is the coercivity of the material.

Further increases of the opposing magnetic field will eventually cause further irreversible domain wall motion, domain rotation and eventually saturation at point 4. Reducing the applied field to zero (point 5) then increasing it through point 6 back to point 1 will complete the loop via the same processes as followed the initial magnetisation/de-magnetisation procedure.

2.2. Electricity and Magnetic Fields

Before going into the interactions of electric and magnetic fields, it is worth briefly introducing the eddy current test method to put this work into context. In its simplest form an eddy current test consists of a coil of conducting wire with an alternating current passed through it. This is positioned on, or near, the surface of a conducting material to be tested (see Figure 2.4). The variation in the interaction of the electromagnetic field produced between the coil and test material forms the basis of information available from the test. A more thorough explanation will be provided in Chapter 3.

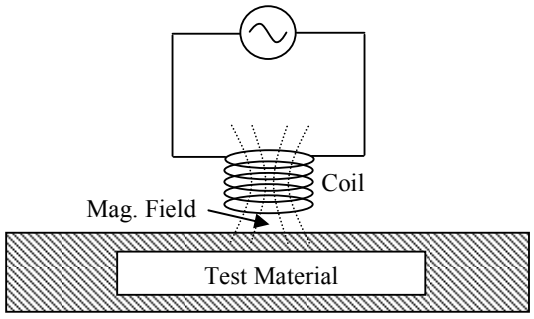

Figure 2.4 – Basic eddy current test arrangement

The electric current passing through a wire creates a magnetic field that consists of lines of magnetic force which exist everywhere parallel to the wire. In other words, they are circles perpendicular to the wire with the wire at their centre.

The magnetic field is characterized by the magnetic flux density B (Webers per square meter or Tesla). The magnetic flux density due to a current element is given by

$$\underline{B} = \frac{\mu_0}{4\pi} \frac{I \; d\underline{l} \times \underline{a}_R}{R^2} \qquad (2.2.1)\,[10]$$

Where I is the current magnitude, $d\underline{l}$ is the length of the current element, $\underline{a}_R$ is a unit vector in the radial direction from the current element and R is the distance from the current element.

The original Ampère's circuit law is a magnetic analogy of Gauss' law, however it is only applicable to the special case where the magnetic field is constant. Maxwell conceived the idea of a displacement current which relates to the changing of electric fields. It is defined as the rate of change of the electrical displacement field. The electrical displacement field is the electric field $\underline{E}$ multiplied by the permittivity of the dielectric it is passing through. Permittivity is a quantity which describes how an electric field is affected by a dielectric medium. Thus the displacement current is given by

$$J_D = \varepsilon_0 \frac{\partial E}{\partial t} \qquad (2.2.2)\,[11]$$

Maxwell then used this to correct Ampère's circuit law for the more general case where the electromagnetic field is changing. Thus Eq. 2.2.2 combines with Ampère's circuit law to become

$$\nabla \times B = \mu_0 J + \mu_0 \varepsilon_0 \frac{\partial E}{\partial t} \qquad (2.2.3)$$

This equation is fundamental to producing any solutions to a dynamic electromagnetic field.

The Lorentz force equation can be used to describe the force acting on a moving charge in an electric field $\underline{E}$ and corresponding magnetic field of flux density $\underline{B}$. A charge q in an electric field $\underline{E}$ experiences a force due to the field given by

$$\underline{F}_E = q\underline{E} \qquad (2.2.4)$$

and a charge moving in a magnetic field of flux density $\underline{B}$ at velocity $\underline{v}$ is given by

$$\underline{F}_M = q\underline{v} \times \underline{B} \qquad (2.2.5)$$

Combining the two to get the Lorentz force equation

$$\underline{F} = \underline{F}_E + \underline{F}_M = q\left(\underline{E} + \underline{v} \times \underline{B}\right) \qquad (2.2.6)$$

The Lorentz force is particularly relevant to EMATs (ElectroMagnetic Acoustic Transducers: these will be explained in Section 8.2) along with the concept of magnetostriction.

2.2.1. Induction

Eddy current testing is based on the concept of electromagnetic induction, first discovered by Michael Faraday in 1831. Faraday discovered that when a current was passed through a conductor any change in the magnetic field surrounding the coil would cause a current to be induced in an adjacent conductor. Thus when an alternating current is applied to a coil, so that the coil's magnetic field is constantly changing, it will induce a similar, but *opposing* alternating current in an adjacent coil (further detail is given in Section 2.1.4). It is this concept of an opposing induced current that is central to eddy

current testing. The strength of opposing current induced is dependent on the conductivity of the material the current is being induced in, amongst other factors.

It was also noted by Faraday that the rate at which the magnetic field changed had an effect on the induced current or voltage. From this he derived what is known as Faraday's Law for an uncoiled conductor: that the induced voltage is proportional to the rate of change of magnetic flux cutting the conductor. That is

$$V_L = \frac{d\phi}{dt} \qquad (2.2.7)$$

Where:

V_L = voltage induced

$\frac{d\phi}{dt}$ = the rate of change in magnetic flux.

More generally this can be written as the differential form of Faradays' law of induction which forms another of Maxwell's equations, where the rate of rotation of the electric field is directly proportional to the rate of change of magnetic flux.

$$\nabla \times \underline{E} = -\frac{\partial \underline{B}}{\partial t} \quad (2.2.8)\,[10]$$

From Eq. 2.2.7, it stands to reason that any factor that increases the rate of change of magnetic flux (i.e. an alternating current of high frequency compared to a low frequency alternating current) will induce a greater voltage. This has important implications in eddy current testing which will be discussed in Chapters 3 and 5. Induction is measured in Henries (H), one Henry is the inductance required to generate one volt of induced voltage when the current is changing at one ampere per second.

2.2.2. Lenz's Law

Following the documentation of Faraday's law of induction, Heinrich Lenz developed his law for determining the direction of the induced current in a loop. Lenz's law states that "an induced current has a direction such that its magnetic field opposes the change in magnetic field that induced the current." So an induced current in a conductor will oppose the change in current that is causing the flux to change (see Figure 2.5). This opposition to current flow is the element of impedance known as the inductive reactance of the component.

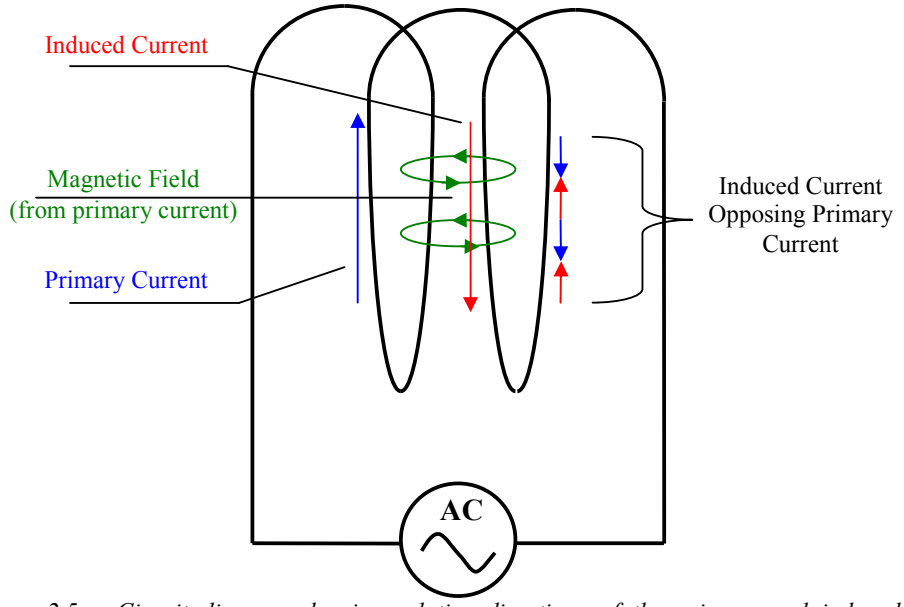

Figure 2.5 – Circuit diagram showing relative directions of the primary and induced current and magnetic field lines for a coil excited by A.C. [12].

2.2.3. Impedance

The impedance (Z) of a circuit is the total opposition to current flow and comprises of three elements. The first of these is *resistance* (R). All circuits have a resistive element which opposes the flow of current. Factors that affect the resistance of a component or circuit include

1. The conductivity of the material used*.
2. The volume of test material affected by the coil's magnetic field.
3. The temperature of the component and the test coil.
4. The current passed through the component.

* The conductivity is often quoted in %IACS (International Annealed Copper Standard), where 1%IACS = 0.58MS/m and 100%IACS = 58MS/m, the conductivity of pure annealed copper.

Factors 1, 3 & 4 will generally remain constant during an eddy current test; in fact all three are related (see Section 2.1.1). Any change will most likely be small but will cause the response to vary slightly making accurate analysis difficult. In an eddy current test coil the resistance can be calculated thus,

$$R = \frac{(\pi \rho d N)}{a} \qquad (2.2.9)\ [13]$$

Where

ρ = the temperature dependent resistivity of the wire (in general, the resistivity of a metal will increase with increasing temperature).

d = the diameter of the coil

N = Number of turns in the coil

a = Cross-sectional area of the wire

The second element of impedance is inductive reactance (X_L). This is the opposition to current flow due to induction in the circuit. This is dependent on many factors including the conductivity, permeability, coil parameters and distance between the coil and test piece. A coil with alternating current passing through it will create this opposition to

flow through self-inductance as per Faraday's law. Since each element of each coil loop will be acted on by the magnetic fields of the loops neighbouring it, these will induce a small opposing current in each loop. Consequently the coil will experience an overall impedance to flow equal to the sum of these individual opposing currents. This reactance will change in the presence of additional external magnetic fields. There is a resulting phase difference where the voltage across the inductor leads the alternating current across it.

When voltage driven by an AC supply is applied to a capacitor the charge that accumulates on each side creates an electric field. This field is the source of the opposition to the flow of current and the capacitive reactance is the third element of impedance. Eddy current circuits will, in general, have a small amount of capacitance, since any adjacent conductors will have a capacitance between them. Thus the coil, the cable and the instrument will all have a small amount of capacitance. In sensitive circuits, particularly at high frequencies, the effects of capacitance can be significant.

It is possible to distinguish between resistance and inductive reactance in a circuit by looking at the time difference between the sine waves of the voltage and current. When there is inductive reactance present in the circuit, the phase of the current will be shifted. The reason for the phase lag can be considered by analogy with the inertia of a large mass being set into motion, where a large applied force causes a slow velocity increase. When a voltage step is applied to an inductor there is a slow build up of the current magnitude in accordance with the formula

$$i = \frac{V}{R}(1 - e^{-t/T_c}) \qquad (2.2.10)\ [13]$$

Where: i = Instantaneous current magnitude

V = Magnitude of constant voltage applied at t=0

R = Resistance in the circuit

t = Time elapsed since application of voltage (seconds)

T_c = L/R, Time constant of the circuit (seconds).

In a purely inductive circuit the current lags the voltage by 90º. This is because the voltage is proportional to the rate of change of the current, thus when the rate of change of current is at its greatest; which is where the current sine wave crosses the zero-axis, the voltage is at its maximum. Consequently there is a 90º phase difference between the two. For a circuit containing resistive and inductive elements, the resulting impedance value is the vector sum of the two elements (resistance and inductive reactance) at a phase angle Θ (see Figure 2.7).

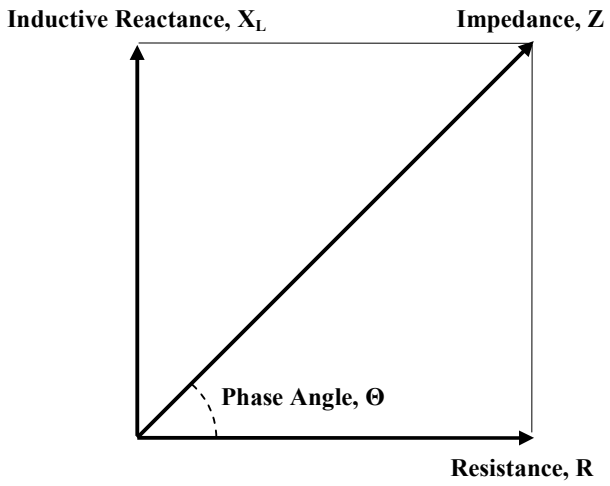

Figure 2.7 – Impedance plane diagram showing the relationship between inductive reactance, resistance, impedance and phase angle.

This chapter has introduced the physical principles that are used in the eddy current test method. The specific interactions of both electrical and magnetic components and how they influence the eddy current test output are described in Chapter 3.

Chapter 3 Electromagnetic Testing: Specific Theory

3.1. Eddy Current Testing Method Principles

The eddy current test method was briefly described in Chapter 2, here it is presented in more detail using the theory presented in Chapter 2. .

3.1.1. Application of Lenz's Law to Eddy Current Testing

The alternating current passed through the eddy current test coil produces a magnetic field that varies in magnitude and can induce a current in a conducting medium within its influence. Lenz's law indicates that this induced current opposes the current/field that caused it and thus the opposing current manifests itself as a measurable impedance in the test coil. Since the phase and magnitude of this impedance will vary with test parameters and test material properties, it can be used to imply the latter. This is the principle of eddy current testing and is illustrated in Figure 3.1. The simplest eddy current test coil arrangement, using a single coil, is known as *absolute*, because the test measurement is the absolute coil impedance measured across the terminals of the coil.

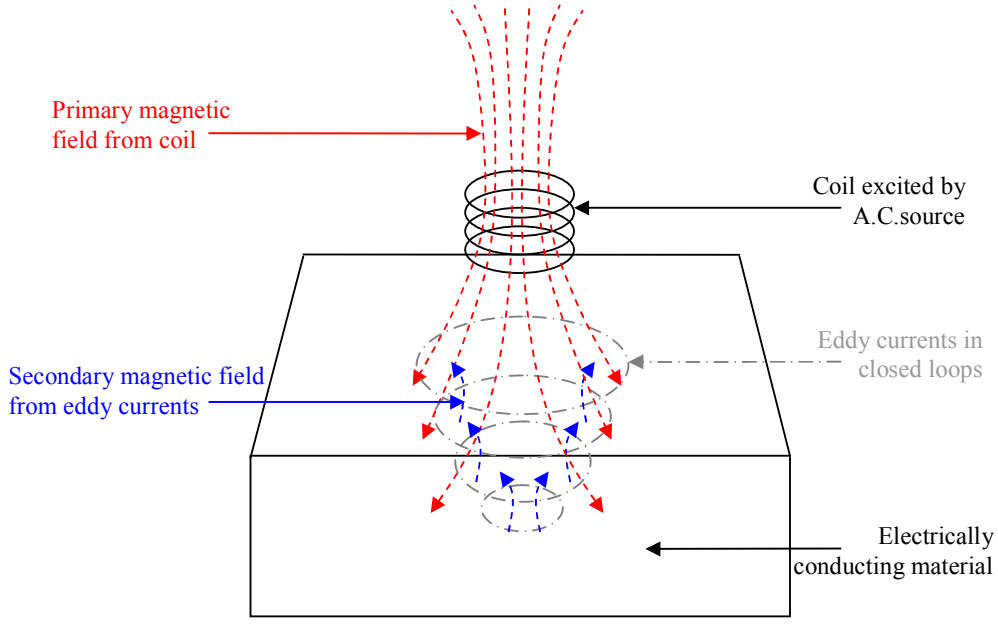

Figure 3.1 – Formation of eddy currents from a coil's magnetic field

3.1.2. Impedance of an Eddy Current Coil

A multiple-turn coil with an alternating current passing through it will have an impedance comprising resistive and reactive elements regardless of whether or not it is acting on a conducting medium. The resistive element corresponds to the resistance of the coil wire, which is frequency dependent. The effect of this frequency dependence is likely to be fairly insignificant in fine wire, where the skin depth, at all but the highest frequencies, is likely to exceed the wire thickness. The reactive part comprises two parts, capacitive and inductive. The winding of the coil, creates a capacitance between each element of each turn; the sum of these capacitances is the total capacitance of the coil. The resulting capacitance is generally small (10^{-9}-10^{-12} Farads), enough to be neglected at all but the highest frequencies. The inductive element of the reactance is also caused by the interaction between neighbouring turns in the coil, this is 180º out of phase with the capacitive reactance. Each turn on the coil creates an alternating magnetic field which induces opposing currents in neighbouring turns as per Lenz's law, this is known as *self inductance*. The resistive element of the coil and the net value of the two reactances form the real and imaginary components of the *unloaded coil impedance*.

When analysing eddy current data, the unloaded coil impedance is often not of interest and is used to normalise impedances measured in the loaded coil case. On an eddy current test instrument this is done using a *null* or *balance* operation with the coil in air. Physically this alters an impedance of a reference part of an internal measurement circuit within the eddy current test instrument. Performing this operation with the coil in the loaded state will normalise all measurements to that particular loaded coil impedance.

When the coil is placed so that a conducting material intercepts the coil's magnetic field the impedance of the coil will change from its unloaded state. The coil's magnetic field induces currents in the conducting material, which is usually analogous to a flat plate. Unlike the interaction between coil turns where the currents flow along the coil wire, in the case where current is induced in a flat plate the currents flow in closed loops in the material. It is the swirling pattern of these currents like eddy currents in fluid flow that give eddy current testing its name. The magnitude and distribution of the eddy currents within the conducting material is dependent on the test frequency, the conductivity of the test material, the magnetic permeability of the test material, the local geometry of the test material and the coil parameters and current.

The induced eddy currents will have their own magnetic field which will oppose the magnetic field that created the eddy currents, thus it will be varying constantly. This magnetic field will induce a current in the eddy current test coil, which will manifest itself as an inductive reactance. Additionally, due to the conservation of energy, the act of generating eddy currents will cause a resistance in the test coil. The amount of magnetic flux coupling the coil to the test piece is termed the *magnetic flux linkage*.

Localised variations in the material under test (which affect the conductivity of the test material), the magnetic permeability of the test material or the local geometry of the test material, will all cause variations in the impedance measured across the eddy current coil. Thus by observing the variations in measured impedance an eddy current test can detect changes in material properties and geometric variations in the material, such as cracks and thickness variation, though the latter is dependent on the *depth of penetration* of the eddy currents, a concept which will be discussed later in this chapter.

3.1.3. Lift-off

Another important factor in the strength of the eddy currents generated in the test material is the distance between the coil and the test surface which is termed *lift-off*. This factor affects the amount of flux linkage between coil and test material, so can also be affected by the incident angle between the coil and the test material. Lift-off causes an exponential reduction in flux linkage resulting in lower test sensitivity, which is usually undesirable. This effect *can be* beneficial as it can be used to measure thin non-conducting coatings on conducting materials. By plotting the impedance at a range of known lift-off distances between the coil and test material, actual coating thicknesses on materials with the same electromagnetic properties can be estimated by measurement of the impedance with the coil in contact with the coating.

3.1.4. Coil Configurations

In eddy current testing the method of generating the eddy currents is the same for all configurations as it is for absolute coil testing. There are however, a number of variations on the configuration for the detection part of eddy current test. Rather than having a common coil for excitation and detection, the detecting coil can be a separate coil, this is known as *transmit-receive* or *driver-pickup*. In this case the receiving coil has no unloaded impedance, so all measurements of impedance are just attributed to the interaction with the material under test; in this case the interrogated area lies between the driver and pickup coil. Other variations on this theme use magnetic field sensors to analyse the variation in eddy current distribution. This can provide improved sensitivity but generally it is more difficult to infer information about material properties due to the lack of impedance data.

Another eddy current test configuration is known as *differential*. This uses two adjacent coils which are wound in opposite directions. The coils are connected in series and the impedance is measured across both coils together. Consequently, when the coils are above identical regions of conducting material their impedances cancel each other out. This makes the pairing insensitive to gradual variations in impedance, which may not be desirable, but sensitive to sudden changes, like cracks. Because the unloaded coil impedances cancel each other out there is no normalising of the data. Differential coils are only effective if the coils are influenced by features of interest at different times, similarly they are only beneficial if structural features causing undesirable signals affect both coils equally at the same time. This is entirely dependent on the orientation of the coils relative to one another.

Common undesirable features that can be suppressed by differential coils are geometric effects. The most common is known as the *edge-effect* where as the eddy currents near the edge of a conducting material they are bound by the physical dimensions of the material and so are redistributed resulting in an impedance change at the coil terminals. This often produces a large unwanted signal on the eddy current test instrument's *Complex Impedance Plane* display, which is the subject of Chapter 5.

3.2. Electromagnetic Waves in Matter

The ability of an electromagnetic wave to pass through a conducting material is dependent on the intrinsic impedance of the medium. It is a complex number dependent on the frequency, conductivity, magnetic permeability and permittivity of the material

[10] and is defined thus:

$$\bar{\eta} = \sqrt{\frac{j\omega\mu}{\sigma + j\omega\varepsilon}} = \left|\bar{\eta}\right| \exp(j\tau) \qquad (3.1.1)$$

It can be seen from Eq. 3.1.1 that the intrinsic impedance contains a real component relating to the magnitude of the impedance and an imaginary component relating to the phase of the impedance, denoted τ.

The intrinsic impedance is closely linked with the *Propagation Constant* $\bar{\gamma}$, this determines the characteristics of how the electromagnetic wave propagates through a material. It is defined in Eq. 3.1.2.

$$\bar{\gamma} = \alpha + j\beta = \sqrt{j\omega\mu(\sigma + j\omega\varepsilon)} \qquad (3.1.2)^{[10]}$$

For a good conductor, where the magnitude of the conduction current density is large compared to the magnitude of the displacement current density, it can be approximated to $\bar{\gamma} = \alpha + j\beta = \sqrt{j\omega\mu\sigma}$ $(3.1.3)^{[10]}$

Like the intrinsic impedance, the propagation constant is a complex quantity consisting of a real part α, the attenuation of the wave and β, the imaginary part, which determines the phase shift of the wave. The quantity α is known as the *attenuation coefficient*, its units are nepers/metre and can be measured from the reduction in field amplitude per unit length which is equal to $e^{-\alpha}$. The imaginary part of the propagation constant, denoted by β, where $\beta = \frac{2\pi}{\lambda}$ is known as the *Phase Constant*.

The definitions for the attenuation coefficient, phase coefficient and thus the velocity of propagation all vary depending on the type of material medium through which the wave is passing. They are defined as follows

Perfect Dielectric, where $\sigma = 0$,

$$\alpha = 0,\ \beta = \omega\sqrt{\mu\varepsilon} \text{ and } \upsilon_P = \frac{\omega}{\beta} = \frac{1}{\sqrt{\mu\varepsilon}} \qquad (3.1.4)\ [10]$$

Imperfect Dielectric, where $\sigma \neq 0$ and $\frac{\sigma}{\omega\varepsilon} << 1$

$$\alpha = \frac{\sigma}{2}\sqrt{\frac{\mu}{\varepsilon}\left(1 - \frac{\sigma^2}{8\omega^2\varepsilon^2}\right)},\ \beta = \omega\sqrt{\mu\varepsilon}\left(1 + \frac{\sigma^2}{8\omega^2\varepsilon^2}\right) \text{and} \upsilon_P = \frac{\omega}{\beta} = \frac{1}{\sqrt{\mu\varepsilon}}\left(1 - \frac{\sigma^2}{8\omega^2\varepsilon^2}\right)$$

$(3.1.5)$ [10]

Good Conductor, where $\frac{\sigma}{\omega\varepsilon} >> 1$,

$$\alpha \approx \sqrt{\pi f\mu\sigma},\ \beta = \sqrt{\pi f\mu\sigma} \text{ and } \upsilon_P = \frac{\omega}{\beta} = \sqrt{\frac{4\pi f}{\mu\sigma}} \qquad (3.1.6)\ [10]$$

The major differences between propagation in matter and propagation in free space are that there is an attenuation effect as the wave passes into and through the material and a change in phase as the wave penetrates deeper into the material. It can be seen from Eqs. 3.1.4, 3.1.5 and 3.1.6 that when the electromagnetic wave passes from a non-conducting region (air or a non-conductive coating) into a conducting medium, there is an increase in the attenuation and a change in the phase. Due to the diffusive nature of eddy currents, for any given depth there will be an eddy current density dependent on the magnetic field strength from the excitation coil. This attenuation is the reason for the *skin-effect,* where the eddy current formation from the magnetic field is concentrated at the surface and decreases exponentially with depth.

Since the decay is exponential, one *standard depth of penetration* is defined as the depth at which the eddy current strength has reduced to 1/e (approximately 37%) of its maximum. It is called the 'standard' depth because that is the depth of penetration in

ideal test circumstances; since these are rarely achieved the true depth of penetration may differ slightly for a given material. At two standard depths the strength is down to 13.5% ($1/e^2$) and at three standard depths it is just 5% ($1/e^3$). The field is attenuated by e^{-1} in a distance equal to $1/\alpha$, so the standard depth of penetration (δ) is

$$\delta = \frac{1}{\alpha} = \frac{1}{\sqrt{\pi f \mu \sigma}} \qquad (3.1.7)\,[13]$$

The phase lag parameter in an eddy current signal is the shift in time between a disturbance detected at the surface and compared with at a distance below the surface. At one depth of penetration there will be a phase rotation of 1 radian/57.3°.

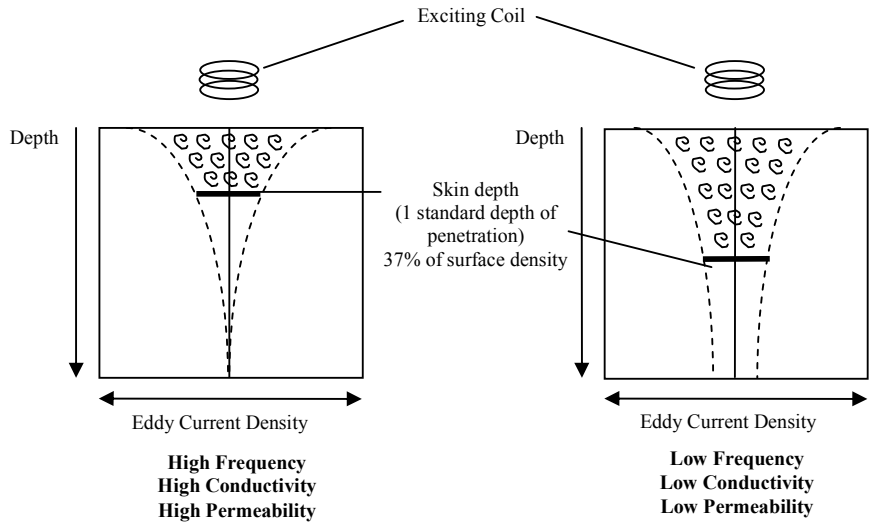

Figure 3.2 – Variation in eddy current density between test variables

When searching for flaws it is important that they are no more than three standard depths of penetration below the surface, otherwise the flaw indication signal will most likely be too weak to be clearly detected. Ideally, they should be located within one standard depth of penetration as illustrated in Figure 3.2.

3.3. Deriving Analytical Solutions to Eddy Current Problems

From the theoretical base of Maxwell's equations (See derivation in Appendix B) it is possible to build up analytical solutions to the eddy current impedance equations. Such solutions were first published by Dodd and Deeds in 1968 and use Bessel functions to derive numerical models for a given set of inputs [14]. These results can be used as a means of calculating the vector potential in a number of regions in the vicinity of an eddy current coil and from this the values of relevant electromagnetic properties can be derived. In this chapter I will explain how the solutions of Dodd and Deeds were derived. Additionally I will use them to derive further solutions for the estimation of normalised impedance values as carried out by Theodoulidis [15]. These solutions are utilised in a piece of software called *Teddy V1.2* [by T. Theodoulidis whilst at Aristotle University of Thessaloniki, Greece] which produces impedance plots for a coil over a two-layer conducting half-space.

3.3.1. Deriving the Dodd and Deeds Solutions

The analytical solutions derived by Dodd and Deeds provide the mathematical basis for most eddy current models. In the interest of brevity I will not describe the derivation of this model – instead I will highlight the key points in the solution. The solutions use cylindrical coordinates. The magnetic field vector $\underline{B}$ is equal to the curl of the magnetic vector potential $\underline{A}$.

$$\underline{B} = \nabla \times \underline{A} \quad (3.3.1)$$ [10]

It can be shown that

$$\nabla^2 \underline{A} = -\nabla \times \underline{B} + \nabla(\nabla \cdot \underline{A}) \qquad (3.3.2)$$

From Ampere's circuit law we know that

$$\nabla \times \underline{B} = \mu \underline{J} + \mu\varepsilon \frac{\partial \underline{E}}{\partial t} \qquad (3.3.3)$$

The current density $\underline{J}$ is related to the electric field by

$$\underline{J} = \sigma \underline{E} \qquad (3.3.4)\ [10]$$

so

$$\nabla \times \underline{B} = -\mu\sigma \frac{\partial \underline{A}}{\partial t} - \mu\varepsilon \frac{\partial^2 \underline{A}}{\partial t^2} \qquad (3.3.5)$$

Adding in the applied current density $\underline{J_0}$ and combining Eq. 3.3.3 and Eq. 3.3.5 we get

$$\nabla^2 \underline{A} = -\mu \underline{J}_0 + \mu\sigma \frac{\partial \underline{A}}{\partial t} + \mu\varepsilon \frac{\partial^2 \underline{A}}{\partial t^2} + \nabla(\nabla \cdot \underline{A}) \qquad (3.3.6)$$

which, according to Dodd's PhD thesis, eventually becomes

$$\nabla^2 \underline{A} = -\mu i_0 + \mu\sigma \frac{\partial \underline{A}}{\partial t} + \mu\varepsilon \frac{\partial^2 \underline{A}}{\partial t^2} + \mu\nabla\left(\frac{1}{\mu}\right) \times (\nabla \times \underline{A}) \qquad (3.3.7)\ [14]$$

Eq. 3.3.7 represents the starting point for Dodd and Deeds solutions as it describes the vector potential of a single turn over a two-layer conducting half-space. The single coil turn is carrying current $\underline{I}$. For this single turn there is no variation in $\underline{I}$ with r or z, only θ; i.e. there is axial symmetry about the z-axis. The vector potential is dependent on $\underline{I}$, so $\underline{A}$ must also only have a θ-component. Since there is only a θ component $\underline{A}$ can be assumed to be a scalar which varies sinusoidally with θ, and using the product rule for differentials this becomes

$$\nabla^2 A = \frac{1}{r}\left(\frac{\partial A}{\partial r}\right) + \left(\frac{\partial^2 A}{\partial r^2}\right) - \frac{A}{r^2} + \frac{\partial^2 A}{\partial z^2} \qquad (3.3.8)\ [14]$$

Expanding this and the right-hand side of Eq. 3.3.7, it can be shown that

$$\left(\frac{\partial^2 A}{\partial r^2}\right)+r^{-1}\left(\frac{\partial A}{\partial r}\right)+\frac{\partial^2 A}{\partial z^2}-\frac{A}{r^2}=-\mu i_0+j\omega\mu\sigma A-\mu\left[\frac{\partial\left(\frac{1}{\mu}\right)}{\partial r}\left(r^{-1}\frac{\partial rA}{\partial r}\right)+\left\{\frac{\partial\frac{1}{\mu}}{\partial z}\right\}\frac{\partial A}{\partial z}\right]$$

(3.3.9)[14]

This is the general differential equation for the vector potential in a linear, inhomogeneous medium with a sinusoidal driving current. This equation can then be used to find solutions to specific eddy current arrangements. In this case, the solution is for a circular coil with an air core and uniform winding density. The coil is located above a two-layer conducting half-space as shown in Figure 3.3.

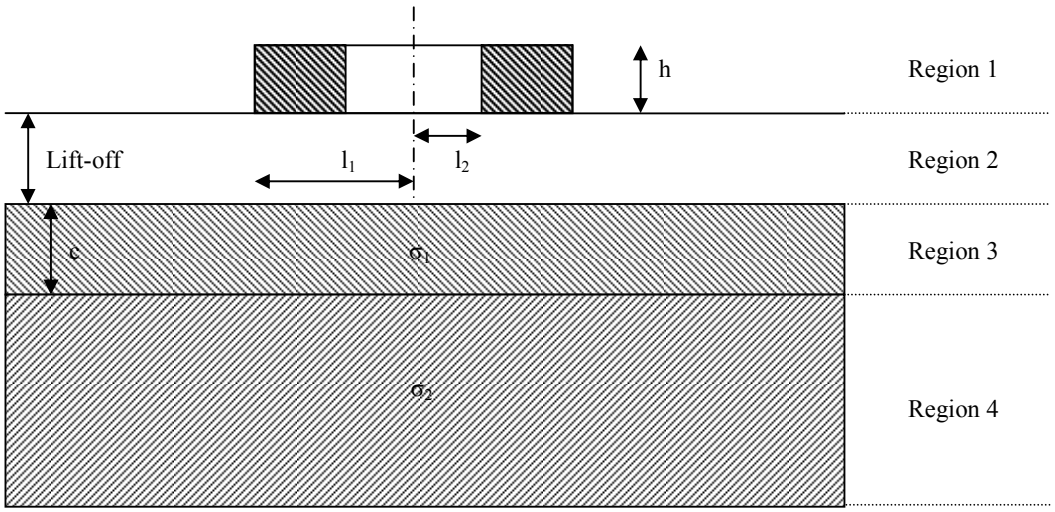

Figure 3.3 – Arrangement of a rectangular cross-section coil over a two layer conducting half-space.

In the case of a homogenous material there is no variation in with r or z, so the final term in Eq. 3.3.9 is zero. Taking I to be the total driving current in the coil, and describing the current using a Dirac delta-function, will make the integral of $\delta(r)$ and $\delta(z)$ equal to 1 at $\delta(0)$ and zero everywhere else. Thus the integral of $\delta(r)$ and $\delta(z)$ are zero except where the coil lies and at the surface of a medium (i.e. at r_o,z_o). Eq. 3.3.9 then becomes

$$\left(\frac{\partial^2 A}{\partial r^2}\right) + r^{-1}\left(\frac{\partial A}{\partial r}\right) + \frac{\partial^2 A}{\partial z^2} - \frac{A}{r^2} - j\omega\mu\sigma A + \mu I\delta(r - r_0)\delta(z - z_0) = 0 \qquad (3.3.10)\ [14]$$

The solution to this linear differential equation for a particular conductor configuration can then be used to build any desired shape of coil by superimposing any number of delta-function coils, provided that the current in each is known.

Using Eq. 3.3.10 as a basis the vector potential can be known for all regions, and from the resulting equations physical phenomena, such as normalised impedance can be calculated.

In a more recent work, Theodoulidis [16] provided more streamlined solutions to the calculation of impedance from the Dodd and Deed solutions. These use a series expansion to replace the integral expressions, resulting in faster computation times and better control of convergence.

3.3.2. Teddy V1.2

As previously mentioned the solutions provided by Dodd and Deeds have formed the basis of much of the eddy current modelling techniques employed since their derivation. In this work Teddy V1.2 will be used for some impedance plane analysis of planar conducting geometries in later chapters of this thesis. The solutions are not modified from their original form and use automated integration routines in FORTRAN based on the QUADPACK integration module [17]. The software requires the following user inputs, from which the Dodd and Deeds equations can be solved to give accurate values of inductance and impedance.

- Input frequency

- Coil height
- Coil outer diameter
- Coil inner diameter
- Number of turns (assumes uniform distribution of turns across cross-section)
- Conductivity of layer(s)
- Relative permeability of layer(s)
- Lift-off distance between coil and conducting medium.

3.4. Probe Design

The basic arrangements of eddy current probes were discussed briefly in Section 3.1.4. There are several sub-variations beyond the absolute, differential and driver-pickup types already mentioned.

Hybrid coils use one coil to induce eddy currents in a material and two or more coils in a differential arrangement to detect the impedance variations. Often the excitation coil is different in design to the detection coils which may form a double-D arrangement as shown in Figure 3.4.

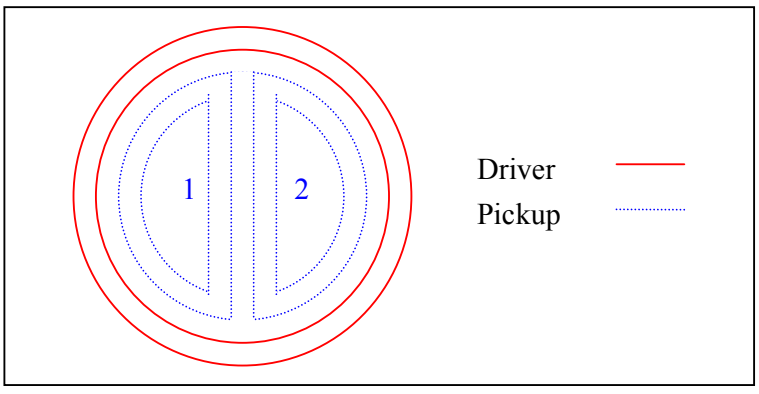

Figure 3.4 – Hybrid coil, double-D design

Array coils consist of a large number of absolute, differential or driver-pickup coils

arranged to give large area coverage with a single probe while still providing excellent sensitivity. Data from the various array channels can be multiplexed and combined in computer software to create plan-view images of a component surface, aiding sizing and positioning of defects.

3.4.1. Coil design

When designing a probe for an eddy current application the most important feature is the coil(s). Coils vary in design (Figure 3.5), the vast majority are constructed of wire wound in a helical manner, whilst others may consist of a flat spiral or *pancake*. It is even possible to use printed circuit board type construction to produce unusually shaped coils. Coils may also be *bobbin* style, where they are designed to be inserted into a test object, or *encircling* where the test object is passed through them.

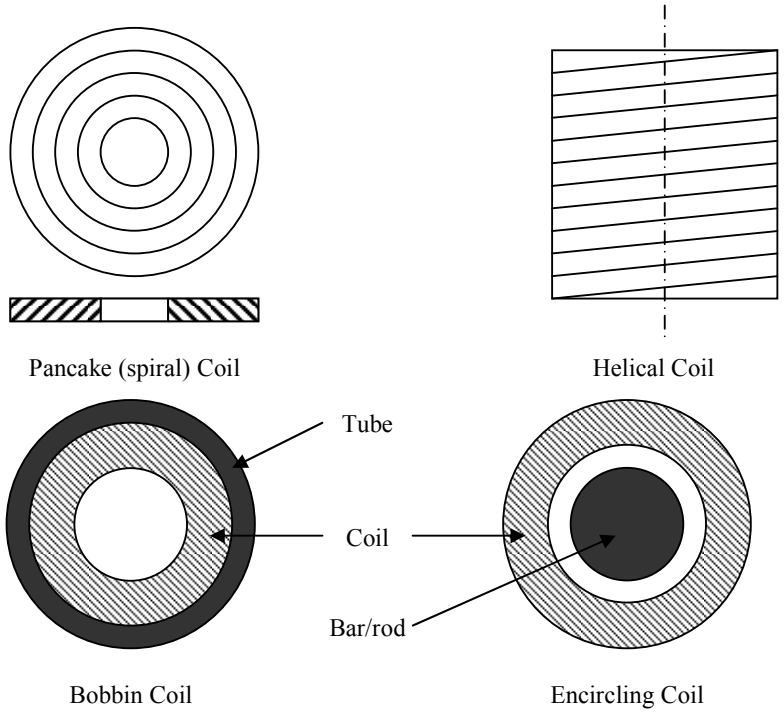

Figure 3.5 – Coil Types

The wire used to make the coils must be non-ferrous in order to avoid the effects of magnetic hysteresis (delayed response to a magnetic field) and should ideally be highly conductive. This keeps the resistance of the unloaded coil to a minimum so that any variation in coil terminal resistance during testing causes a noticeable percentage change in the impedance. Copper is the most common choice.

The coils are wound round a former (normally a dielectric material) which can either be solid to provide extra rigidity, hollow to leave an air gap (necessary on encircling coils) or hollow to permit a ferrite core for *probe loading*. Probe loading uses the ferrite core to concentrate the probe's magnetic field at the centre of the coil. Because ferrite has very low magnetic reluctance the lines of flux concentrate here and the greatest density of eddy currents is generated at the centre, thus reducing the effective footprint of the probe. Probe *shielding* does much the same thing, only using the skin-effect. A conducting shield is placed around the coil circumference preventing the coil's magnetic field from generating eddy currents outside of the probe footprint. Both these methods reduce spurious effects from geometric features by effectively reducing the active probe footprint.

The most important factor to consider is the inductance of a coil; as a general rule this should be high to ensure good sensitivity. The inductance is dependent on several factors including the geometry of the coil, its dimensions, the conductivity of the wire, the magnetic permeability of the core and the test frequency. Coil design is also limited by geometric constraints of the test as well as defect sensitivity. As a general rule, the minimum detectable defect length is the radius of the test coil.

A suitable operating frequency must be selected based on the expected depth of defects, to ensure they lie within one standard depth of penetration, adopting too low a frequency can cause the coils to heat up causing the test parameters to change and thus invalidate the results of a test. There are additional considerations with the frequency which relate to the phase and magnitude of variations on the impedance plane. This is discussed in more detail in Chapter 5.

3.5. Overcoming the limitations of eddy current testing

As with any NDE technique there are a number of limitations with eddy current testing. Some can be overcome to an extent with specialist equipment and some are just not permitted by the laws of physics. The fact that inspection is limited to surface and near-surface defects in conducting media cannot be overcome, but inspections can be designed so that the effects of the following limitations can be minimised.

3.5.1. Lack of penetration (skin-effect)

In the case of non-ferromagnetic materials the depth of penetration can be improved by lowering the test frequency. For ferromagnetic materials a lack of eddy current penetration into the material can only be improved by magnetically saturating the material. This will increase the main which case the material will respond linearly to an applied magnetic field.

Lower frequencies often require larger coils to obtain sufficiently high impedances. The draw-back of this is that the system becomes less sensitive to small defects at the surface. Driving the coils at higher voltages can improve the sensitivity but if the wire is not of sufficiently large diameter then the coils will heat up which will invalidate the

test.

3.5.2. Inconsistent response to ferromagnetic materials

By magnetically saturating the test area, the response to the coil's magnetic field becomes linear. This can be done by using an external magnetic field to saturate the entire area or by using a direct current applied to the coil or a permanent magnet built into the coil for local saturation.

An alternative method of damping the variable signals is to use a differential coil arrangement. Provided both coils are in close proximity to one another they should be affected equally by the non-linear variation. Raising the temperature of the test material above its Curie point will also negate these effects but this is not practical for eddy current testing.

3.5.3. Spurious signal from lift-off

Ideally this problem should be avoided rather than cured. This can be done by maintaining good, consistent contact between the probe and test material. Probe guides/supports or moulded probes may be applicable to assist the inspection. Alternatively, a differential probe can minimise the lift-off signal if both coils are the same distance from the test piece.

3.5.4. Edge-effect and geometric effects

These problems are unavoidable and should be minimised where possible. Probe shielding or loading will reduce the active area of the probe and using a differential probe will minimise the spurious signal caused by the feature.

3.6. Alternative Electromagnetic Techniques

A large number of other electromagnetic testing techniques exist which may prove to be viable alternatives to, or be complementary to, the eddy current method. Background to the following methods, which were ultimately deemed unsuitable for this project, can be found in Appendix D.

- Magnetic Flux Leakage
- Remote Field Sensing
- ACPD
- ACFM
- Meandering Winding Magnetometer (MWM).

An additional two methods, Pulsed Eddy Current and Barkhausen Noise, which are relevant to the second project on creep cavitation are explained below.

3.6.1. Pulsed Eddy Current

A technique that has become more feasible in recent years due to the advances in computing technology and sensor design is pulsed (or transient) eddy current. The concept of using a step function voltage to excite the probe has been around for many years. Where conventional eddy current inspection uses a continuous gated sinusoidal waveform of a specified frequency, pulsed eddy current uses a step-function voltage which contains a continuum of frequencies. The great benefit of this is that the electromagnetic response to the many different frequencies can be measured with a single pulse. Since depth of penetration is frequency dependent, so information from a range of penetration depths can be obtained simultaneously. Consequently, by

observing the data in the time-domain, we have a system analogous to ultrasonics where features nearest the probe are observed prior to those at greater depth.

Another similarity with ultrasonics produces what many consider to be the most useful feature of pulsed eddy current – its improved depth of penetration compared to conventional eddy current. By way of comparison, using a conventional eddy current system, the useful signal within the test material is approximately three times the standard depth of penetration, for a pulsed system it can be as much as ten times.

In pulsed eddy current testing it is beneficial to use a reference or *nulling* signal, similar to some differential coil arrangements in conventional eddy current testing, to improve data interpretation. This signal is representative of the ideal or undamaged state of the inspected component. By subtracting the reference signal only the variations that occur within the test are displayed.

Large amounts of information can be gathered from the acquired data, provided this can be accurately extracted. The method lacks the precision of the conventional eddy current technique and so has its applications in different areas which require relatively lower sensitivity, such as corrosion detection in thin plates.

The fields resulting from pulsed eddy currents can be detected by a receiving probe in a similar manner to a conventional transmit-receive configuration, or by a Hall-effect sensor, located either adjacent to the transmission coil or, for a through-transmission test, on the opposite face of the material being tested. Hall-effect sensors offer better sensitivity for deep defects, at the low frequency part of the spectrum, whereas coils are

better for shallower defects where the higher frequencies are of most significance.

The pulse rise-time and duration determine the frequency content and could typically extend from a hundred hertz to several megahertz. The wave disperses as it penetrates the material and the pulse shape will change since the frequency and thus the wave speed, will vary with depth. Viewing the pulse data in the frequency-domain, further information can be gained from the variation of amplitude and/or phase with frequency. By sampling different delay times within a pulse, specific sections of the spectrum can be evaluated. From the amplitude and phase properties measured parameters such as presence of defects, thickness variations and changes in lift-off can be evaluated for each frequency selected.

3.6.2. Barkhausen Noise

The Barkhausen Noise (or Micromagnetic) NDE technique is a material characterisation method applicable to ferromagnetic metals, which are made up of small magnetic regions called domains. These domains are separated by domain walls which are most easily magnetised in one particular crystallographic direction. Applying an alternating magnetic field to a ferromagnetic material will cause the domain walls to move back and forth as the domains either side of it shrink and grow respectively. This will cause a change in the overall magnetisation of the metal which can be detected by a conducting coil placed nearby. This detection is in the form of an electrical pulse, which will be created for each domain movement. Combining the pulses from all the domain movements gives a stepped signal resembling electrical noise, containing information about the magnetic characteristics of the metal under test. There is a second method of

Barkhausen Noise testing, Acoustic Barkhausen Noise (ABN), which uses ultrasonic transducers to detect the domain movements rather than using a Hall effect (or similar) sensor to detect the change in magnetic field associated with the domain movement.

As with eddy current testing there is a skin-effect preventing deep penetration: typical application depths are 0.01mm to 1.5mm. Two main characteristics will affect the Barkhausen Noise signal; distribution of elastic stresses and the material microstructure.

Due to the phenomenon known as *magnetoelastic interaction*, compressive stresses in the material will cause a reduction in noise intensity while tensile stresses will cause an increase in noise intensity. Modifications to the metal by grinding, shot-peening, carburizing and induction hardening can all be detected by Barkhausen Noise. The MBN method will be discussed in greater detail in Chapter 7.

Chapter 4 Background to Electromagnetic Inspection Technologies

4.1. Introduction

Research into electromagnetic non-destructive testing has always been limited when compared with ultrasonics. Over the years there have been periodic bursts of research in a number of areas including condenser tube inspection, mathematical modelling and most recently, pulsed eddy current. In between these bursts the research has tended to be rather less focussed and has been more focussed on applications, rather than pushing forward the core technology. This is the situation at present and will be the case for my research projects. By way of example, recent research topics have included the use of rectangular shaped coils [18][19][20], measurement of surface cracks in ferromagnetic materials [21] and defect detection in multi-layered structures [22] [23] [24] [25].

This literature review and the accompanying theory sections will cover many aspects of eddy current research and development, to give a comprehensive guide to reading around the subject. Smaller, more focussed literature reviews will accompany the two individual projects. The topics covered here are:

- The history of electromagnetism
- The origins of electromagnetic inspection
- Equipment development and design
- Modelling and simulation
- Alternative electromagnetic techniques

4.1.1. History of Electromagnetism

Of all the non-destructive testing techniques, electromagnetic testing has its origins set furthest back in time. According to McMaster [13], as early as 600BC Thales of Miletus recorded the first observations of magnetic effects, though not until *De Magnate* by W. Gilbert in the 17th century was any scientific experimentation and theory on magnetism formally documented.

The earliest work on research into electricity came from Benjamin Franklin in 1751; *Experiments and Observations on Electricity* [26] featured details of his early studies of electricity. Franklin's work opened up a huge stream of research and in the early 19th century and scientists recognised a link between electricity and magnetism. In 1820 Hans Christian Öersted produced an account of how an electric field affects a magnet in its vicinity, as detailed in Section 2.1.2.

Approximately ten years later Michael Faraday (and concurrently, Joseph Henry) discovered and documented electromagnetic induction – the phenomena central to eddy current testing. In his paper to *The Society* entitled *Experimental Researches in Electricity* [27], Faraday detailed his experiments and explains the concept of induction (See Section 2.1.3 for a full description of induction). A summary of the work done on electrical and magnetic theory by Oersted, Ampere, Lenz, Henry and Faraday was written in 1873 by James-Clerk Maxwell in a *Treatise on Electricity and Magnetism* [28].

4.1.2. The Origins of Electromagnetic Inspection

In 1878 D.E. Hughes recorded his use of electromagnetic induction in a practical

application. In his paper *On the Physical Action of the Microphone* [29] he described his 'sonometer', which measured the imbalance between two pairs of induction coils. In this report he stated that if a coin was placed between one set of coils and an identical coin was placed between the second coil pair then the system will be balanced. However if there is any difference in geometric or temperature characteristics of one coin then there will be an observable difference. This method of measuring an imbalance in induction coils later became the basis for eddy current inspection. Hughes was also responsible for the International Annealed Copper Standard (%IACS), measuring the conductivity of metals relative to copper, to which he assigned a %IACS of 100.

Now that the use of induction coils as a comparative testing tool had been realised, many researchers began to carry out work in developing electromagnetic equipment from the 1920's until the end of World War Two [13]. Most systems were unreliable and thus not accepted by industry but the continued development work of a few companies/institutions (G.E., Magnetic Analysis Corp. and the U.S. Naval Research Laboratory included) gave us practical applications of eddy current testing.

After the end of the war the technology used during the war became available to industry. Oscilloscopes were used to view data, magnetic sensors were employed and the eddy current and magnetometer systems developed by Försters [Institut Dr. Förster GMBH & CO. KG, Baden-Württemberg, Germany] became available to industry; further detail is available in Section 4.2 on equipment development and design.

Eddy current testing has seen a great deal of research, particularly since the 1950's and 1960's when the aerospace and nuclear sectors realised its potential as a surface inspection method. Despite being a well understood inspection mechanism, innovation continues at a rapid pace due to improvements in electronic equipment, new applications and alternative uses of electromagnetism as an inspection tool, such as pulsed/transient eddy current, remote-field eddy current and ACPD (Alternating Current Potential Drop).

4.2. Equipment Development and Design

In its early days electromagnetic testing was a qualitative rather than quantitative technique and to some extent remains so today. Developed from Hughes' 'sonometer' early equipment used calibration standards to facilitate measuring material properties from heat treated condition to the thickness of overlays. Freidrich Förster was an early pioneer of eddy current testing and in 1937 produced a part sorting system using a pair of coils in a differential configuration at the Kaiser-Wilhelm-Institut; imbalances detected in the system were indicated by the deflection of a needle on a galvanometer. Förster recognised the potential for use of the eddy current technique on defect detection in light metals such as aluminium. Förster began to make his own equipment for eddy current testing, such as his 'Sondenkawimeter' which found favour with other researchers and in 1948 his enthusiasm for the technique led him to form a dedicated eddy current equipment manufacturing company in his own name. The vast majority of eddy current testing equipment in existence today has evolved from Förster's original equipment. Förster is still one of the largest eddy current equipment suppliers to industry in the world and continues to develop the latest technologies.

By the early 1940's research was underway using eddy current flaw detection in

industrial applications, Ross Gunn [30] describes using an eddy current method for flaw detection in non-magnetic materials which is capable of detecting flaws that cause a discontinuity in the electrical resistance (i.e. a slot or crack) of the test piece; he was also the first to use eddy current in a driver-pickup arrangement. Equipment development moved on rapidly with the useful frequency range being extended, typically in the range 500Hz to 1kHz.

This and other early developments such as driver-pickup arrangements, automated scanning and recording are summarised in paper from the *Naval Research Laboratory, Washington* [31].

As the technology became more widely appreciated, inspection of more varied components were trialled, Trost [32] gives a summary of testing non-ferrous pipes, bars and *shapes* by eddy current inspection. Armour [33] surmises that many different detectors and methods, including differential coil sorting methods and direct current potential difference testing were available by the mid-point of the twentieth century, but he laments the lack of an adequate current-flow measuring system to realise the full potential of eddy current testing.

The vast majority of the work produced during the 1940's simply detailed people's experiences with the new technology, but a few, including Hastings [34], tried to develop their own improved testing equipment. However, the majority of developments were coming from Förster's and there was a lot of collaboration with researchers, particularly in America. Richard Hochschild spent time working with Förster in Germany and reported back on his experiences with performing impedance analysis of eddy current

tests [35].

Inspection using an oscilloscope to analyse impedance changes rather than a voltmeter had been suggested by W.A Knopp Jnr. [36], but this was only really suited to lab-based testing at that time as researchers became more adventurous in their acquisition of inspection data.

It quickly became apparent that the eddy current testing mechanism could be used to ascertain many pieces of information about the material it was testing. During the 1940s a number of innovations were introduced. Cavenagh [37] wrote of tracing the progress of failure in materials by observing changes in the electric and magnetic properties. Hastings [34] observes the use of eddy currents to detect flaws in ferrous materials and Bowman [38] explains the measurement of thickness of copper and nickel plate in his work. Before the end of the decade even more adventurous applications were being documented, Brenner and Kellogg [39] progressing as far as the inspection of composite coating thickness measurement in 1948.

The basic components of an eddy current testing instrument have changed very little from Förster's early designs, but the equipment has become more accurate and refined thanks to advances in electronics. Oscillators and power supplies were among the first items to be significantly upgraded and upgrades to semi-conductor elements and integrated circuits are amongst the most recent.

During the 1950s and 1960s the use of eddy current inspection methods escalated in the nuclear and aircraft industries as they demanded greater accuracy and sensitivity. Much

of the work was carried out by various agencies of the U.S. Atomic Energy Commission, testing graphite and areas of the reactor core. Probably the most successful application of eddy current in the nuclear power industry was its use on condenser tubes. Using bobbin probes rapid inspection of the vast quantities of tubes was possible.

The number of eddy current testing equipment manufacturers increased significantly during the Fifties and Sixties as the method found favour with the aircraft and nuclear power industries. Two of the giants of the industry Hocking (originally DEB Electronics) and Zetec were formed in 1962 and 1968 respectively and have been producing cutting-edge technology ever since.

The introduction in the 1970's of the microprocessor brought about the most significant developments in eddy current instrumentation. By 1977, NDE specific microcomputers were in use; early examples included the NDE-COMP8 and its successor the NDE-COMP9 in 1980 developed at Oak Ridge National Laboratory, Tenessee. Today computers can combine the signals from multiple eddy current input channels and perform complicated on-line signal processing operations.

4.3. Modelling and Simulation

In the 1940s during the early stages of eddy current testing development many researchers were working on the theoretical basis on which future NDE could produce quantitative results. The most significant work however, came from Dodd and Deeds in the 1960's. Following on the work of Förster, their work began with Dodd's work in 1965 [40] on solving induction problem analytically and culminated in their joint work of

1968 [14] in which the pair produced integral solutions to eddy current problems which form the basis of the majority of subsequent work on modelling eddy current interactions. Most usefully, Dodd and Deeds used a magnetic vector potential formulation to analyse the fields of cylindrical coils and encircling coils. The solutions are integrals of first-order Bessel functions giving the vector potential of the field. The vector potential can then provide electro-magnetic quantities. The solutions would later be refined by other academics because of their limited scope and errors due to mutual inductance at high frequency [16].

Using the analytical solutions of Dodd and Deeds [14] other researchers explored more specific situations such as electromagnetic fields in the vicinity of a surface breaking crack [41] and applications to ferromagnetic materials [42]. The former paper was the first to examine specific defect situations and predict theoretically the eddy current signals caused by the defect.

The most notable subsequent work in the field of eddy current modelling was that of John Bowler, starting with his work on eddy current calculations using Green's functions applied to a half-space [43]. The quasi-static limit permits some simplification of the problem, so that only one scalar is needed to define the field in a homogenous conducting half-space. By modelling the situation as a test applied to a half-space Bowler made the idealization that the frequencies used in eddy current testing are sufficiently low that the displacement current is zero, thus allowing simplification of the problem and solution through the use of Green's functions.

Bowler sought to find solutions to what is described as the "inverse problem" [44]-

modelling defects from impedance responses, and the "forward problem" [45] - modelling the impedance response from a known defect. Much of the modelling work is based on what is known as the Born approximation: If conductivity variations are small, the problem can be linearized by replacing fields inside the conductor with fields in the absence of a flaw [46].

The first case Bowler [47] examined was that of a slot in a conductor; effectively a highly simplified model of a crack. The key to predicting the probe response was to "find the induced source strength at the scatterer for a given incident field". In this particular case it is the slot that was the field scatterer. Bowler had produced a computational model to predict the impedance response due to a slot by determining the electric field produced by the coil in the conducting material in the absence of a flaw and the electric field induced at the flaw. The result was a boundary integral solution for an arbitrary skin depth based on a variant of Green's second theorem, with the flaw represented by an equivalent dipole density.

The probe impedance (ΔZ) due to the flaw can then be given by

$$I^2 \Delta Z = -\int_{coil} \mathbf{E}_{scattered}(\mathbf{r}) \cdot \mathbf{J}(\mathbf{r}) dr$$
$$= -\int_{flaw} \mathbf{E}_{incident}(\mathbf{r}) \cdot \mathbf{P}(\mathbf{r}) dr \qquad (4.3.1)$$

Where $\mathbf{P}(\mathbf{r})$ is the dipole density and $\mathbf{J}(\mathbf{r})$ is the probe current.

This equation is used as the start point in all his subsequent work on eddy current forward problems.

An alternative method was applied to cases where the skin depth was less than the crack dimensions for both ferrous and non-ferrous metals [48]. This used two-dimensional Laplace equations, which are much faster computationally, than vector potential and boundary element methods, but are only applicable in the thin-skinned model, i.e. for high frequencies. This method was expanded to semi-elliptical and epicyclic cracks in the thin-skin model [49].

Some academics produced variations on Bowler's work [50], while others offered their own improvements to various instances of the forward problem. In an attempt to model the response from three-dimensional defects in a layered, conductive media an improvement on the Born approximation known as the *layer approximation* was suggested for this particular problem [51].

Attempts to find solutions to the inverse problem can be split into a number of different approaches; some are already mentioned in application to the forward problem. These approaches include vector potential and boundary integral solutions.

As with the forward problem, the solutions to the inverse problem have their roots in the work of Dodd and Deeds [14] and detailed mathematical modelling has been progressing since the early '90s. The most fundamental study of the inverse problem was to find the solutions for a magnetic field perturbed by a 3-D flaw [52], which gives the Maxwell equations for local conductivity variations in an isotropic conductor. The concept of the inverse problem with an explanation of the Born approximation and an example of how to create an algorithm for inverse problems to be solved iteratively was published a year later [46]. Work on finding inverse solutions where the conductivity and permeability are

changing locally [53] has relevance to my project on detecting material phase changes in steam-turbine blades.

The logical starting point for exploring the inverse solutions for eddy current testing was a surface breaking slot [45] akin to a perfect crack. This was a highly simplified approach and it was assumed that the test sample defect is homogenous to minimise the computation required, so it was not necessary to use a calculation based on an integral formulation. Consequently, the impedance gradient of the response to the slot is determined by the dipole density at the slot surface. Similar studies were carried out for the thin skin region [54] [55]. Burke's model[55] was accurate to within 10% of the true depth and was relatively insensitive to small changes in lift-off and conductivity, provided the slot was uniform and effectively infinite in length. In Harfield's work [54] he explains how the fields near and at the corner of the crack are effectively decoupled, so the solution *(*ΔZ) is the sum of the contributions from all corners, edges and faces.

$$\Delta Z = Z_{corner} + Z_{edge} + Z_{face} \qquad (4.3.2).$$

Harfield [56] then explored solutions away from the thin skinned region, using intermediate frequencies. The technique used describes a scattered magnetic field using a Fredholm integral derived by the Wiener-Hopf technique. The technique required further work and was also applicable to the thin skinned region.

Alternative approaches were explored for describing the influence of surface breaking defects [57][58] using 2-D Laplace equations and the geometric theory of diffraction. The relative benefits of the electric field integral equation method and the magnetic vector

potential method were investigated by Bowler [59]. The conclusion was that although the vector potential method involves the more complicated equation it is in fact easier to deal with and has the greater potential for further specific approximations using this approach.

With many approaches to the solution of the inverse problem solution now available, academics became more adventurous with the situations they were trying to simulate. Embedded defects [60], epicyclic cracks [49] and interaction with a right-angled conductive wedge [61] were all successfully mathematically modelled using the various approaches.

The approaches to the inverse problem are reviewed by Bowler [62] and he notes that progress in the field has meant they give a good approximation to the actual crack shape within one hundred iterations. Another paper by Bowler that year [63] on time domain half-space dyadic Green's functions from current dipole field in a conducting half-space next to a non-conducting half-space has particular relevance to transient eddy current methods. Developments in this field will be discussed later in this section. Variations on the approach to solving the inverse problem continue, the most recent being the TREE method (Truncated Region Eigenvalue Expansion) which can be applied to 3-D coil, axisymmetric geometries and slots in different materials [64].

The boundary integral vector potential solution is examined further and the three cases of volume integral formulation are noted [65]. The three cases are:

For materials where $\mu = \mu_0$. Express the electrical field as an integral over the flaw with

the flaw as the electric source.

For a crack of negligible thickness. Use a surface integral in place of the volume integral.

For an ideal crack. Expand the solutions of the electric field in terms of boundary elements.

Because the solutions derived by Dodd and Deeds were only applicable to air-cored probes, there was a need for solutions for ferrite cored probes, since these are now most common in industry. An eigenvalue method which can be extended to cores and shields that are conducting was duly devised by Theodoulis [66].

Finite element modelling approaches were introduced to try to provide faster solutions to inverse problems [67]. This method was applicable to both non-ferritic and ferritic materials with the latter requiring the use of an additional magnetic source to accurately model the situation. Improvements to the method, including the use of a mixed finite element approximation [68] have continued since.

Neural networks have also been utilised in the solving of inverse problems. Successful fast flaw calculations were achieved by Sikora [69] and adaptive algorithms to estimate flaw characteristics from signals were produced to overcome the difficulties caused by the fact that flaw length, size and width affect the signal in a non-linear way [70].

The use of CIVA/MESSINE to model eddy current configurations has progressed since the turn of the century. This was first demonstrated by Berthiau [71] and the experimental details of this work are shown in a paper by Pichenot [72]. Specific applications have

followed since including the use of ferrite-cored probes over surface breaking flaws in austenitics [73].

4.4. Alternative Electromagnetic Techniques

Much of the research into electromagnetic inspection techniques has focussed on alternative methods of inspection, which follow similar principles to basic flux leakage or EM induction but apply them in different ways. Often these variations use different sensors to evaluate the electromagnetic behaviour of the system under test. Often these alternatives have very specific or limited applications such as Remote Field Eddy Current (RFEC), Alternating Current Potential Drop (ACPD) and Alternating Current Field Measurement (ACFM). Perhaps the most significant development and the one currently receiving the most academic attention is Pulsed Eddy Current (PEC).

4.4.1. Pulsed Eddy Current

Although originally mooted in the 1950's, the pulsed eddy current method saw little development until the 1980's. Its primary advantages were the increased level of penetration afforded by the pulsed input and the depth dependent information it provided about the component. Not surprisingly, its early applications were in coating thickness measurement [74] and the examination of thin-walled tubing [75].

There was a resurgence of research interest in the technique from the 1980's onwards, primarily due to the proliferation of computing power. This enabled greater interrogation of the inspection data as well as improved modelling of eddy current behaviour. Solutions to the transient problem using a steady-state harmonic solution and by a transient time-stepping method were proposed [76], and there was some success,

though required greater refinement was required. Alternatively, integral equations using time-space Green's functions could also be used allowing greater flexibility provided the increased computing power could be provided [77]. With computational tools available, pulsed eddy current was able to extract additional information from an inspection making it a valuable high-end NDE technique. More systems became commercially available and the technique was accepted into regular use in the aerospace industry.

The range of applications of the technique have expanded significantly since the inception of the technique and have extended to corrosion detection [78], deep (>10mm in aluminium) cracking using Hall effect sensors in place of the traditional sensor coil [79], measurement of the thickness and conductivity of conducting coatings over both ferromagnetic and non-ferromagnetic substrates [80] and preliminary attempts to measure individual conducting and non-conducting layers within a multi-layered structure [81]. A similar approach has permitted deep (>8mm) detection of aluminium corrosion in multi-layered structures [22].

Attempts to increase the depth of sensitivity in metals using eddy current are continuing, often using more sensitive sensors to detect the variations in the electromagnetic response of the test. Using highly sensitive detectors such as SQUID magnetometers (Superconducting QUantum Interference Device), small cracks have been resolvable at depths in excess of 5mm in aluminium structures [82].

Recently, a new characteristic of the pulse eddy current signal has been extracted for the purposes of defect classification [83] to supplement the main characteristics, this is time to peak and peak height which define the defect features. This has been termed the

"rising point" and relates to the propagation time of the electromagnetic waves in the target material.

Pulsed eddy current is presently the largest area for research given the massive potential of the technique and its ability to give (some) volumetric information. Combinations with ultrasonic techniques, which often struggle to resolve defects in the near field, could present a rapid and thorough inspection in the future [84].

4.4.2. Meandering Winding Magnetometers (MWM)

MWM arrays were developed and patented by Jentek [Jentek Sensors Inc. Waltham, U.S.A], They were conceived by Prof. James R. Melcher and developed at the Massachusetts Institute of Technology (MIT) in the early 1990s[85]. A prototype MWM system was displayed at the ASNT Spring conference in 1992 and the accompanying paper explains the theory and setup of the system [86]. This work describes how multiple wave-number interrogation with imposed ω-k magnetometers can produce a range of property measurements based on the equations originally devised by Dodd and Deeds [14].

Given the patents on the technology, all further research has come from Jentek Sensors Inc. There are many more potential applications for MWM arrays compared with conventional eddy current because of the greater amount of data acquired and the data interpretation available within the system. The applications have included characterization of degrading thermal barrier coatings on gas turbine blades [87]; measuring ceramic coating thickness, metallic bond coat thickness and porosity. Other applications include monitoring of shot peen quality, permeability measurements as an

indication of fatigue damage [88] and crack and micro-crack detection in ferrous and non-ferrous alloys [89] [90].

4.4.3. Alternating Current Potential Drop (ACPD) and Alternating Current Field Measurement (ACFM)

ACPD was developed in the early 1980s for sizing rather than defect detection[91]. It was born out of limitations of the DCPD system, which was popular in the 1970s [92]. The DCPD method was limited by the current and voltage drifts, temperature issues and thermoelectric voltages [93] although these were largely eliminated later in development [94].

ACPD successfully and accurately sized single cracks in laboratory fatigue specimens [93] and has seen a considerable amount of subsequent research at Imperial College, London. Research into its use on multiple defects and on applying it to real-life situations has had mixed success and its use in industry has been very limited. Other more recent strands of research have focused on analytical expressions of the complex voltage to try and extract depth-dependent information from the system [95].

ACFM has not been the subject of much research since its development in 1990. Most advances have been its application to alternative industrial components [96] and refinement of the technique for one of its original uses – thread inspection [97].

Of the methods mentioned in this section, many have relevance and potential to aid my investigation into suitable methods for detecting microstructural variations, both in steam turbine blades and in creep degrading pipe-work. Due to the flexibility in coil/array design and also the degree to which simulations are readily available,

conventional eddy current is an excellent starting point for the blade microstructure project. MWM also has potential to extract and quantify material properties which could imply material condition (this work was ultimately dismissed in favour of conventional eddy current and the findings of the study placed in a separate document [98]). There is also potential to obtain additional information relating to the electromagnetic properties of materials from DCPD and pulsed eddy current.

Chapter 5 The Impedance Plane

5.1. Introduction

The normalised impedance plane is the most common way for eddy current data to be displayed. Much eddy current data is analysed through the impedance plane, but often it is taken for granted that the behaviour of the impedance matches how it is described in technical manuals. A full understanding of the impedance plane is vital to getting effective use out of eddy current testing; once the relative influence of the complex impedance components measured across a coil are understood, probe design and technique optimisation can be employed to permit effective flaw analysis and material characterisation.

5.1.1. Coil Parameters

In order to assess the behaviour of the normalised impedance plane and to explore the validity of the models a consistent set of probe parameters and reference samples have been chosen. The probe parameters are typical of the pancake coils found in many of RWE npower's eddy current arrays and are summarised in Table 5.1:

Internal diameter(mm)	0.6
External diameter (mm)	2.6
Coil height (mm)	0.65
Number of turns	264
Design Frequency (kHz)	100
Unloaded coil impedance (Ohms) (manufacturer's reading)	48
Unloaded coil phase (Deg) (manufacturer's reading)	66

Table 5.1 – Coil parameters

5.1.2. Test Samples

The samples chosen gave a range of conductivities across the ferromagnetic and non-ferromagnetic range. A total of twelve small disc-shaped samples were used; eight were from a Hocking conductivity calibration sample (Type 33A151) and four were from a Fischer ferrite measuring calibration sample (No reference/part number supplied), they are listed in Table 5.2.

Copper (annealed)	Non-ferromagnetic
Aluminium (Al1200)	Non-ferromagnetic
NiAg (48%Cu, 42%Zn, 10%Ni)	Non-ferromagnetic
Aluminium (Al7075)	Non-ferromagnetic
300 series stainless steel	Non-ferromagnetic
Carbon Steel	Ferromagnetic
400 series stainless steel	Ferromagnetic
Ferrite (65%Fe, 15%Mn, 10%Zn)	Ferromagnetic
Base (94%Ni, 6%Fe)	Ferromagnetic
12.4FN (62%Fe, 24%Cr, 12%Ni)	Ferromagnetic
35.0FN (69%Fe, 23%Cr, 5%Ni)	Ferromagnetic
122.4FN (90%Fe, 8%Cr)	Ferromagnetic

Table 5.2 – Test samples

For each sample it is important to know the conductivity and the approximate relative permeability over the frequency range 100 kHz – 1MHz. For the non-ferromagnetic samples the relative permeability is assumed to be approximately 1. In order to measure the conductivity of the non-ferromagnetic samples a 60-500 kHz conductivity measuring probe (Hocking/GE U.K. 47P001) was used, calibrated against the 100%IACS annealed copper. Such a method is not suitable for ferromagnetic samples so a d.c. potential drop method was used instead.

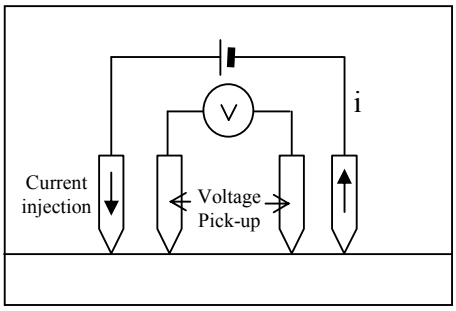

Figure 5.1 – Diagram of a 4-point DCPD measurement system

A four-point measuring system [95] as illustrated in Figure 5.1 was used to measure the transfer resistance between two points on the samples; this value and the sample thickness are then used in the following formula

$$\sigma = \left(\frac{1}{\pi R}\right)\left(k_1^{\beta} + \left(\frac{k_2}{T}\right)^{\beta}\right)^{\frac{1}{\beta}} \qquad (5.1.1)\ [99]$$

Where R is the resistance associated with the potential drop measured, T is the thickness of the sample in metres, and β, k_1 and k_2 are geometric constants dependent on the probe. In this case $\beta = 3$, $k_1 = 2000/3$ and $k_2 = \ln(3)$. Table 5.3 shows the conductivity values for each of the 12 samples.

Sample	Conductivity	
	%IACS (International Annealed Copper Standard)	MS/m
Copper	100	58.00
Al1200	61	35.40
NiAg	9	5.20
Al7075	34	19.80
300 series stainless	2	0.80
Carbon Steel	2	1.16
400 series stainless	2.3	1.36
Ferrite	<1	0.40
Base	30	17.4
12.4FN	1	0.58
35.0FN	1	0.58
122.4FN	1.25	0.70

Table 5.3 – Measured conductivities of the 12 test samples

5.2. Impedance Planes

5.2.1. Impedance Planes from Literature

Figures 5.2, 5.3 and 5.4 show three normalized impedance plane diagrams from various educational sources. For the moment I will just concentrate on the non-ferromagnetic region of the impedance plane. In Figure 5.2 the impedance relative to air (the unloaded coil condition) varies in terms of resistance and inductive reactance. At low conductivities the increasing resistive part dominates but at higher conductivities the reducing inductive reactance dominates. The lift-off curve follows an almost mirror-image of the conductivity curve along an axis from air to a given conductivity (in this case representative of probe in direct contact with brass). Figure 5.3 shows a very similar situation with the addition of a crack impedance line going straight from a point

on the conductivity curve (representative of probe in direct contact with aluminium) towards air.

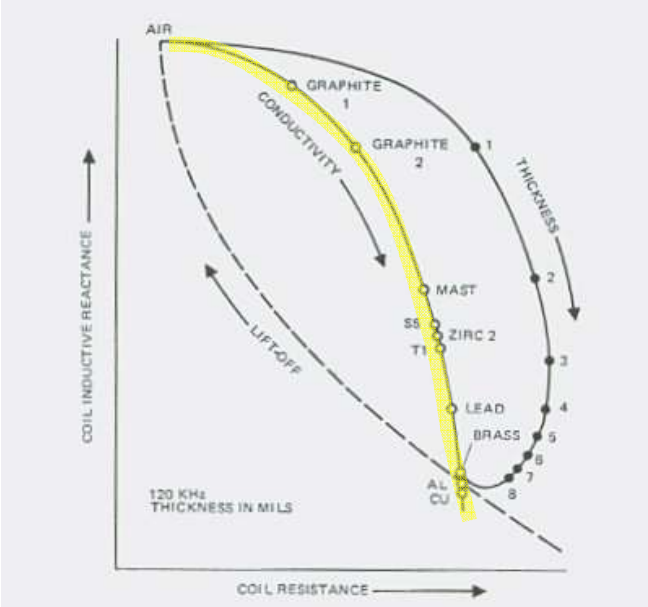

Figure 5.2 – Diagrammatic normalized impedance plane from Zetec eddy current instruction handbook, showing conductivity curve and thickness and lift-off curves for brass resulting from relative impedance changes across an eddy current testing coil. [100]

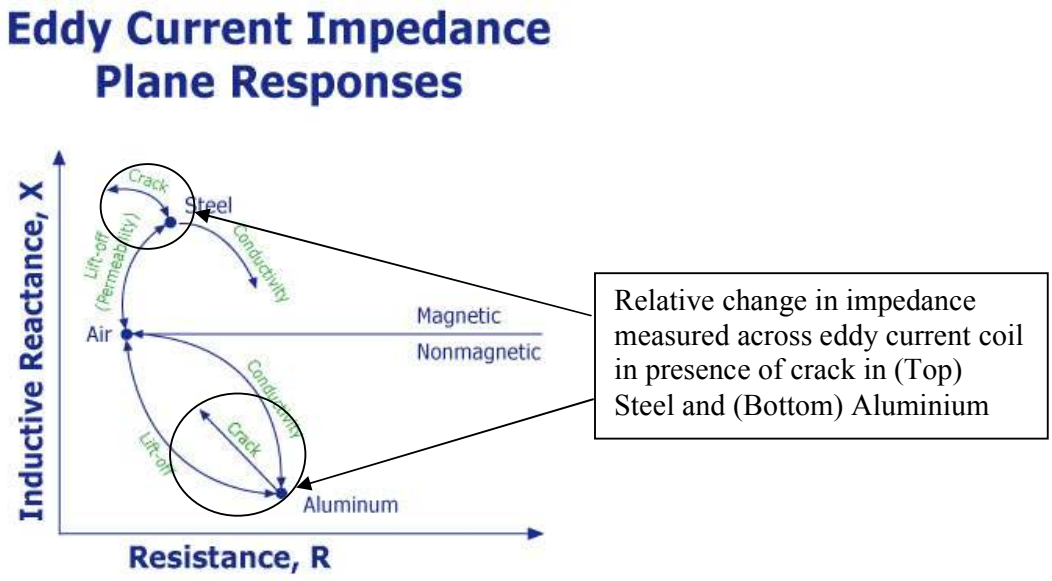

Figure 5.3 – Diagrammatic normalized impedance plane from NDE-ed.org, showing relative impedance changes across an eddy current testing coil with varying conductivity, lift-off and in the presence of surface-breaking defects for both magnetic and nonmagnetic cases [101]

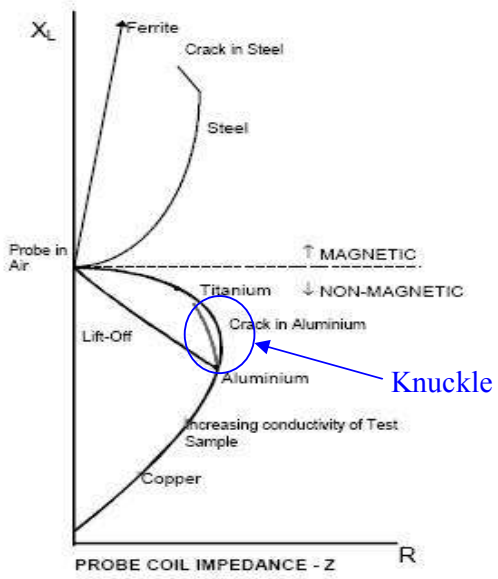

Figure 5.4 – Diagrammatic normalized impedance plane showing relative impedance changes across an eddy current testing coil with varying conductivity, lift-off and in the presence of surface-breaking defects for both magnetic and nonmagnetic cases [102]

In Figure 5.4 the situation is slightly different. This time the path of increasing conductivity reaches a "knuckle" then curves back on itself in the R-plane and the crack signal moves toward a point on the conductivity curve away from the unloaded coil (air).

Returning to the theory of eddy currents, for an unloaded coil in air the complex impedance measured across its terminals should have virtually no resistance if the coil itself is highly conducting. The inductive reactance should be solely due to the self-inductance of the coil. As the coil is moved near to a conducting medium, the coil's magnetic field will induce eddy currents in the medium. The energy given up to create these eddy currents will manifest itself as an increase in resistance across the coil terminals. The opposing voltage generated in the coil by the induced eddy currents will

reduce the overall inductive reactance across the coil terminals. This overall reduction will increase with increasing conductivity and/or frequency. This explanation covers the cases shown in Figures 5.2 and 5.3 but not Figure 5.4. The reason for the curve bending back on itself relates to the skin-depth of the eddy currents generated in the conducting medium. As the conductivity rises, the skin depth reduces and so the area through which the eddy currents circulate is reduced, thus increasing the effective resistance of that medium and so the resistive element of the coil impedance begins to reduce as weaker eddy currents are generated in the test piece. The inductive reactance and the skin effect are also frequency related, so variations in frequency will have a similar effect to changes in conductivity. Therefore the differences in the conductivity curves of the three diagrams could be apportioned to using different operating frequencies. Further evidence of this case is shown in Figure 5.5, which shows the conductivity curve from *air* to *copper* for a 50Ω coil. The plot to the left is at 50kHz and has the knuckle present, whereas the image to the right, at 5kHz does not.

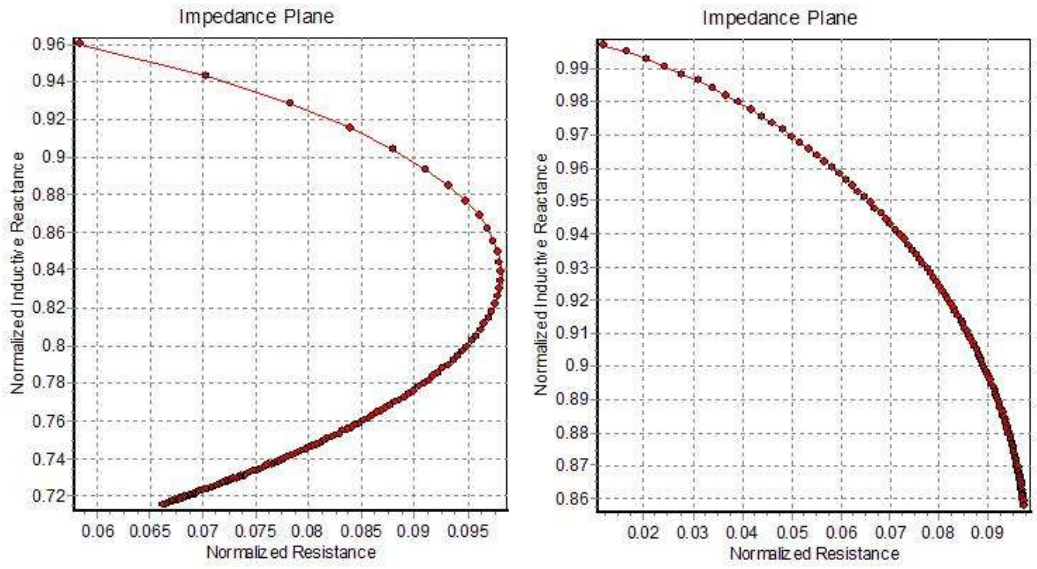

Figure 5.5 – Impedance plots produced with Teddy 1.2 for a 50 Ω coil, showing (left) a knuckle on the conductivity curve at 50kHz, but (right) no knuckle on the conductivity curve at 5kHz.

In the ferromagnetic region, the impedance plane becomes more complicated. Again there is an increase in the coil resistance when it is brought near a conducting medium, but this time the normalised inductive reactance increases from that of the unloaded coil. In this region the effects of permeability dominate and concentrate the coil's magnetic field, causing an increase in flux linkage and thus an increase in the inductance measured across the coils. A similar trend for conductivity occurs in this region as for the non-ferromagnetic region. However, due to the increased electromagnetic coupling from the increased permeability there are stronger eddy currents generated in the test piece and so the resistance across the coil terminals increases. This increase is barely noticeable at high permeability values since the inductive reactance element dominates and distorts the conductivity curve. The greater the permeability influence, the less pronounced the variations due to conductivity; this is often exacerbated by the fact that many high-permeability materials have low conductivity. Figure 5.6 shows an impedance plane created in Teddy V1.2 for a non-ferromagnetic material (relative permeability 1, conductivity 58 MS/m) and a ferromagnetic material (relative permeability 50, conductivity 1.16 MS/m). The lines shown are decreasing lift-off from air towards the material for a range of frequencies from 10 kHz to 6MHz. For the non-ferromagnetic material, the impedance values mark out a curve which begins left-to-right at low frequency and then bends back on itself at high frequency. For the ferromagnetic materials the curve arcs gently from left-to-right as frequency increases.

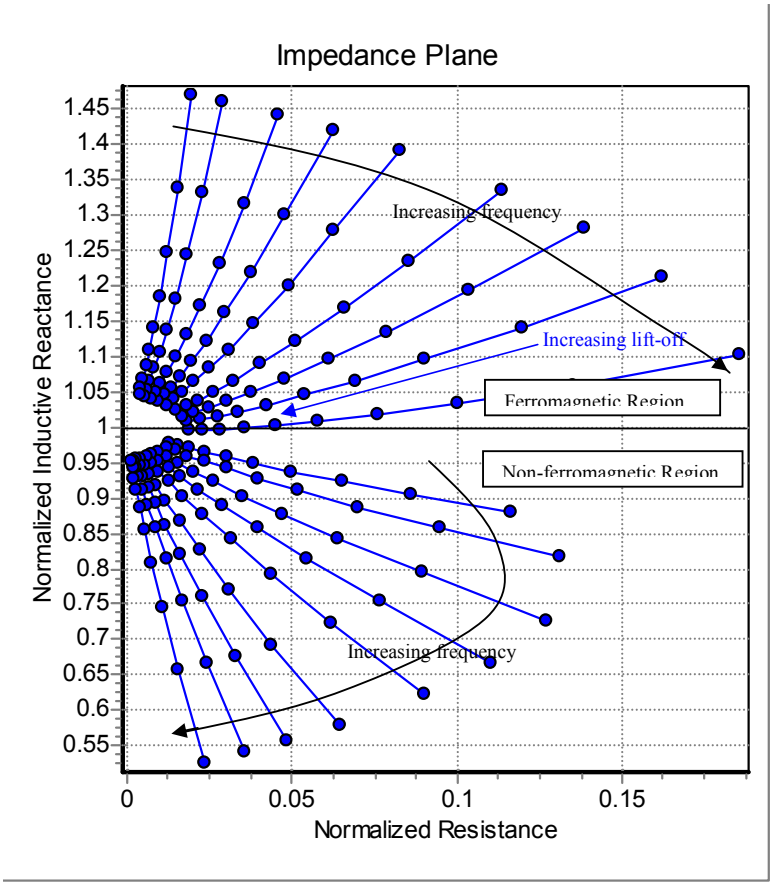

Figure 5.6 – Variations in impedance with operating frequency for ferromagnetic and non-ferromagnetic samples, simulated in Teddy V1.2. Lift-off lines (in blue) generated from calculations at zero lift-off to 1mm lift-off in 0.1mm steps.

Having established that the behaviour of the normalised impedance plane described in educational texts is in qualitative agreement with the theory described here in terms of conductivity, magnetic permeability and frequency, the next stage is to see how well it fits with real eddy current data and with simulations. Once this is established the accuracy of the simulation can be ascertained.

Figure 5.7 shows the impedance plane produced by Zetec's EddyView software, driving a 2.6mm diameter pancake coil at 300 kHz through an eddy current acquisition unit (Zetec MS5800, Canada). Four of the ferromagnetic materials have been separated to

avoid the display being too congested. The lines show the lift-off curves from each of the twelve test samples. The display actually shows normalised complex voltage rather than impedance, but the two follow the same trend. The scale is 10V from the top of the display to the bottom and from the far left to the far right. The display can be freely rotated and was set by the operator so that it resembled the theoretical impedance planes in the text. This display is only suitable for comparing general behaviour of the impedance plane, not for producing exact values to compare with simulations. In order to achieve this, I measured the actual impedance of the coil in contact with each of the test materials using a complex impedance analyser.

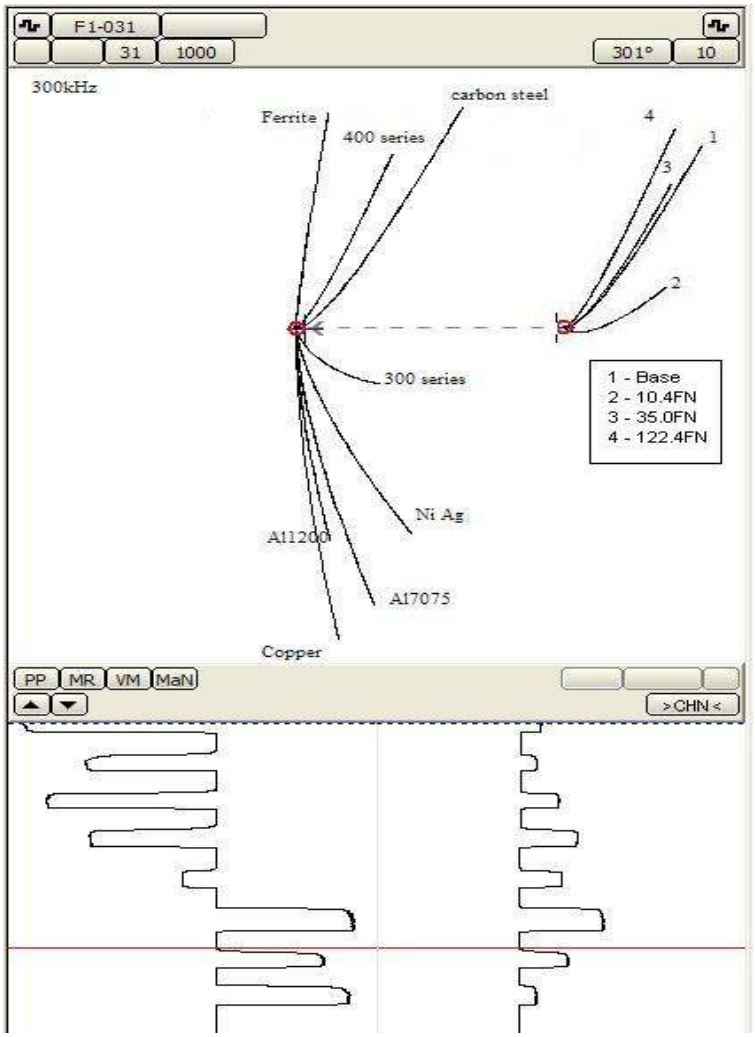

Figure 5.7 – Impedance plane for 12 test samples at 300 kHz produced in EddyView

5.2.2. Impedance Plane from Measurements

A complex impedance analyser (HP, U.K. 4192A LF Frequency Analyser, 5Hz-13MHz) was used to measure the impedance of 2.6mm diameter coil identical to the one used to produce Figure 5.6 in contact with each of the twelve test samples. Values of resistance, inductive reactance and capacitive inductance were recorded for each sample and then normalised to the impedance of the unloaded coil in air. Values recorded at 300 kHz are shown in Table 5.4 and the normalised plane is displayed in Figure 5.8. There is a potential error on the measurements due to the addition of a short length of copper wire at each end of the coil to allow it to be inserted into the analyser's contact points. This wire has a small effect on the resistance of the coil, however this will be cancelled out by normalising the results, since it will affect the resistance in both the loaded and unloaded condition.

	Z (Ohm)	Theta (deg)	R (Ohm)	XL (Ohm)	XC (Ohm)
Unloaded	129.1	80.8	20.7	42.5	-0.002614
Base	160.4	77.7	34.3	52.2	-0.00213
10.4FN	140.7	76.8	32.2	45.6	-0.002438
35.0FN	155.6	78.4	31.3	50.8	-0.002187
122.4FN	162.5	79.1	30.7	53.2	-0.002092
Copper	97.2	73.6	27.5	53.2	-0.003575
Al1200	99.9	73.3	28.9	31.1	-0.003487
NiAg	102	72.3	31	31.9	-0.003431
Al7075	112.4	73	33	32.4	-0.003104
300 S/S	127.3	76.7	29.3	35.8	-0.002689
Carbon Steel	160	78.4	34.1	41.3	-0.002086
400 S/S	163.4	77.7	33.1	52.1	-0.002124
Ferrite	173.5	83.9	21.2	53.3	-0.001998

Frequency (Hz)	100000
Angular Frequency (rad/s)	628318.5

Table 5.4 – Measured Impedance data at 300 kHz.

The data displayed in Figure 5.8 has been normalised as follows;

$$X_{normalised} = \frac{X_c + X_L}{X_{Unloaded}} \qquad (5.2.1)$$

$$R_{normalised} = \frac{R - R_{Unloaded}}{X_{Unloaded}} \qquad (5.2.2)$$

The reason for this is to make the data comparable to the output from *Teddy V1.2* which uses this method of normalisation.

Using the parameters listed in Table 5.1 and an operational frequency of 100 kHz, impedance plots of the lift-off curves for each of the twelve materials were produced in Teddy V1.2 using the conductivity values from Table 5.3. These are shown in Figure 5.9. There was good agreement in the trends between the measured data and simulated data for the non-ferromagnetic materials, albeit with an off-set. The typical off-set in the Resistive plane was 0.02Ω and in the Reactive plane was around 0.1Ω. The unloaded coil inductive reactance was 128.4 Ω compared to the measured 127.4Ω.

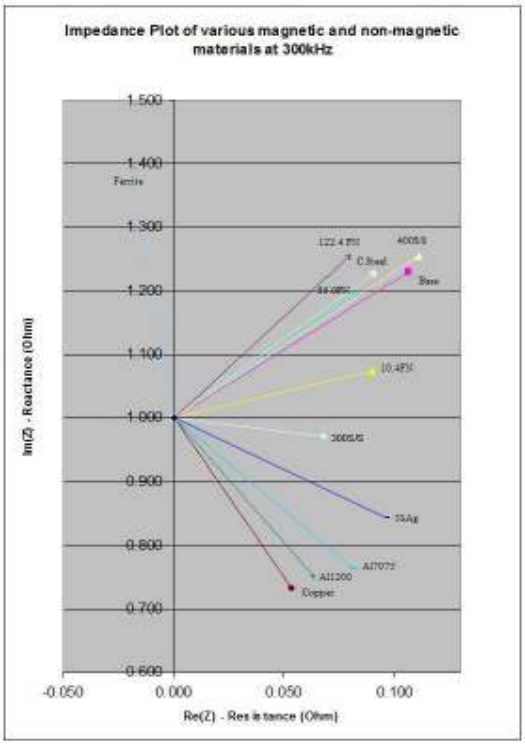

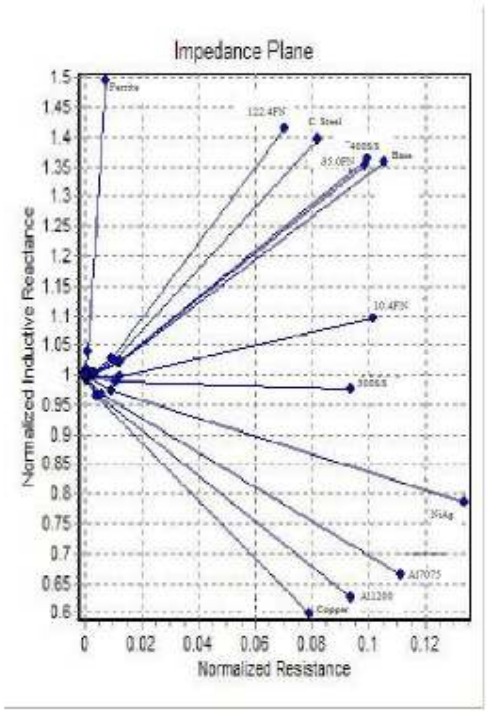

Figure 5.8 (left) – Measured normalised impedance for 12 test samples at 300 kHz

Figure 5.9 (right) – Teddy V1.2 simulation data for test samples at 300 kHz.

Taking the off-set into account, plots were made for ferromagnetic materials, using known values of conductivity and approximated values for the permeability. It was decided that making exact measurements of relative magnetic permeability was not practical because the permeability is field/frequency dependent and therefore estimation by hysteresis may not be truly representative. Using the approximated values of relative magnetic permeability listed in Table 5.5 a good agreement between measured and simulated data could be achieved. There does appear to be a fairly consistent offset between the two sets of values which does differ slightly between ferromagnetic and non-ferromagnetic materials. For all materials the offset on the imaginary axis is around 0.14Ω and on the real axis the offset is 0.01Ω for ferromagnetic materials and 0.03Ω for non-ferromagnetic materials. Some example values are shown in Table 5.6

Sample	Magnetic Permeability (in range 100Khz-300kHz0	
	Relative	Absolute (NA^{-2})
Copper	1	1.257×10^{-6}
Al1200	1	1.257×10^{-6}
NiAg	1	1.257×10^{-6}
Al7075	1	1.257×10^{-6}
300 series stainless	1.2	1.508×10^{-6}
Carbon Steel	32-38	4.022×10^{-5} - 4.777×10^{-5}
400 series stainless	80-100	1.006×10^{-4} - 1.257×10^{-4}
Ferrite	5000	6.285×10^{-3}
Base	500	6.285×10^{-4}
12.4FN	2	2.514×10^{-6}
35.0FN	14-17	$1.760 \times 10^{-5-}$ - $2.137 \times 10^{-5-}$
122.4FN	60	7.542×10^{-5}

Table 5.5 – Magnetic permeability values for the 12 test samples

Material	Real Axis (resistance) - Ω			Imaginary Axis (Reactance) - Ω		
	Actual	Model	Diff.	Actual	Model	Diff.
Copper	0.05	0.08	0.03	0.73	0.60	0.13
Al1200	0.06	0.09	0.03	0.75	0.63	0.12
Al7075	0.08	0.11	0.03	0.76	0.65	0.11
122.4FN	0.08	0.07	0.01	1.25	1.42	0.17
C. Steel	0.09	0.08	0.01	1.23	1.4	0.17
Base	0.11	0.13	0.02	1.23	1.36	0.13

Table 5.6 – Comparison of some measured and simulated impedance values

Accepting that the Teddy V1.2 simulation gives a good analogy of the measured impedance data albeit with numerical offsets due to simplifications in the model, this can be used to ascertain how altering various parameters affects the impedance plane. This is crucial to optimising eddy current inspection parameters for specific inspections.

5.3. Parameter Variation

In this section I will explore what effect varying frequency, conductivity and magnetic permeability has on the impedance plane by varying the inputs in Teddy V1.2. Where possible I will compare the results with experimental data. All probe parameters remain as set in Table 5.1.

To begin with, I will look at the variation with frequency in both the ferromagnetic and non-magnetic region. In the magnetic region, the conductivity is set to 2%IACS and the relative magnetic permeability to 100. In the non-magnetic region the conductivity is set to 10%IACS and the relative magnetic permeability to 1. The frequency was varied from 10 kHz to 5MHz. In Figure 5.10 the lift-off lines represent calculations made for 10 kHz, 50 kHz, 100 kHz, and 500 kHz, 1 MHz and 5 MHz.

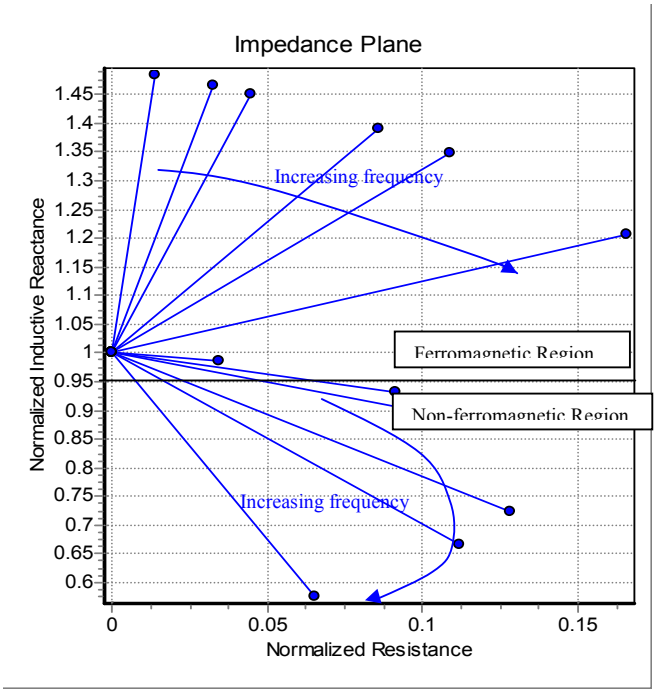

Figure 5.10 – Impedance simulation showing variation in impedance with changing frequency for ferromagnetic and non-ferromagnetic materials

To replicate this test using experimental measurements would risk damaging the coil through excess heating at low frequencies. This could cause inaccuracies in the readings. In order to demonstrate the effects of frequency variations, I repeated the measurements for the twelve test samples at 200 kHz and 100 kHz. Figures 5.11 and 5.12 show simulation and measured data for 100 kHz and 200 kHz respectively.

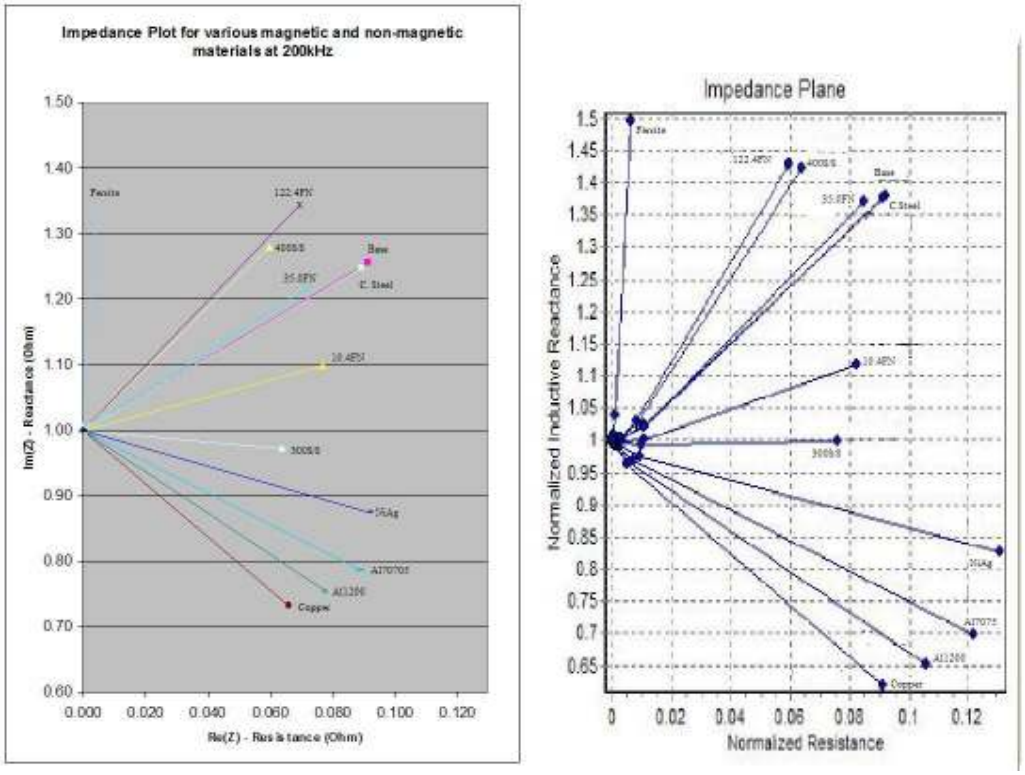

Figure 5.11 – Simulated and measured impedance at 200 kHz

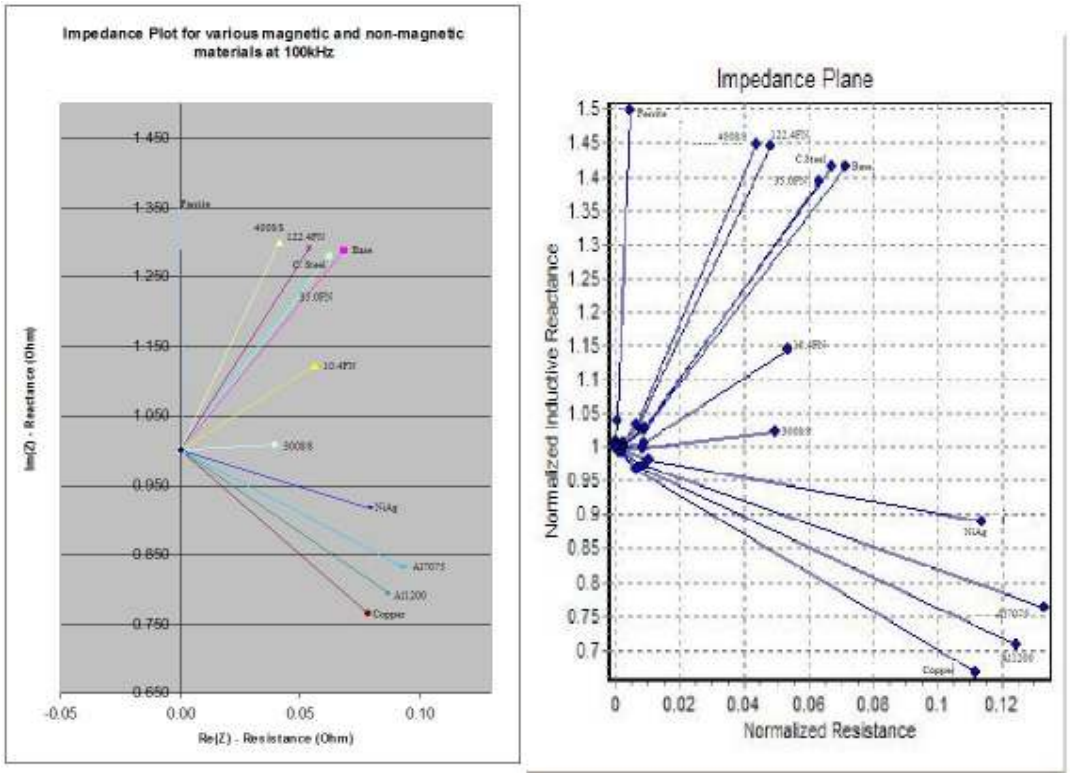

Figure 5.12 – Simulated and measured impedance at 100 kHz

There are a number of points of interest here. As expected, in the non-magnetic region the frequency does shift the position of the various metals along the conductivity curve; the higher the frequency, the further away from the unloaded coil impedance. In the ferromagnetic region, an increase in frequency will increase the resistive element of the impedance, so materials shift left-to-right as the frequency increases. In the diagrams, the change in frequency seems to shift the display's resistance element, causing a decrease in resistance with frequency. On closer inspection, this is due to the frequency dependent nature of permeability, causing the relative positions of materials to change.

Keeping the frequency constant at 300 kHz and varying the conductivity from 0 to 100%IACS produces the bottom curve shown in Figure 5.13 for non-magnetic materials. For ferromagnetic materials, with a relative permeability of 10, the top curve is produced.

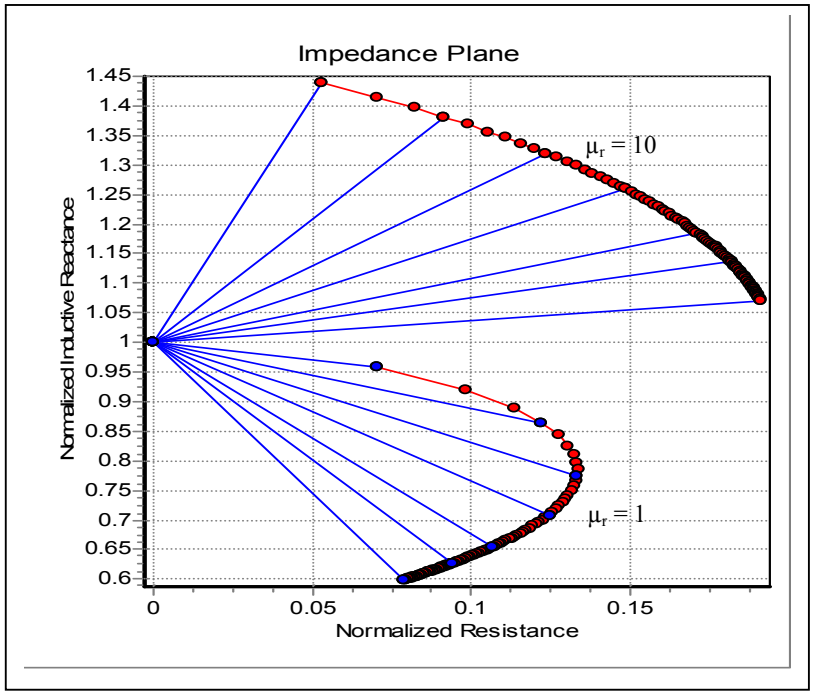

Figure 5.13 – Conductivity variation for materials at 300 kHz.

This may appear to be a different form of curve to the bottom curve, but if we look at more curves for other values of relative permeability (Figure 5.14), it becomes evident that the curve is the same but shifted upwards by the increase in inductive reactance. The curve also becomes shortened with increasing relative permeability and almost becomes a straight line at high values. This is illustrated by the blue arrow in Figure 5.14 which shows the extent of the range for $\mu_r = 1000$. This straighter area of the curve is the region of most interest in ferromagnetic materials as they generally have very low conductivity.

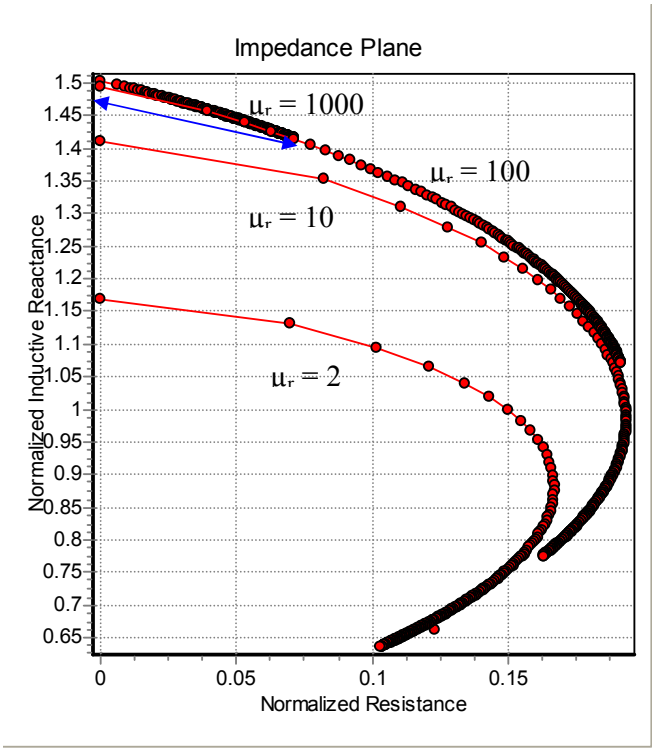

Figure 5.14 – Normalised impedance plane simulation showing conductivity curves from 0-100 %IACS at 300 kHz for varying relative permeability (shown adjacent to curves). Blue arrow shows extent of μr = 1000 curve to distinguish it from the μr = 100 curve.

From Figure 5.14, it begins to become apparent what happens when relative permeability increases. The inductive reactance of the coil increases with permeability

until it appears to reach a maximum value. The variation in the resistive element of impedance decreases as the relative permeability increases.

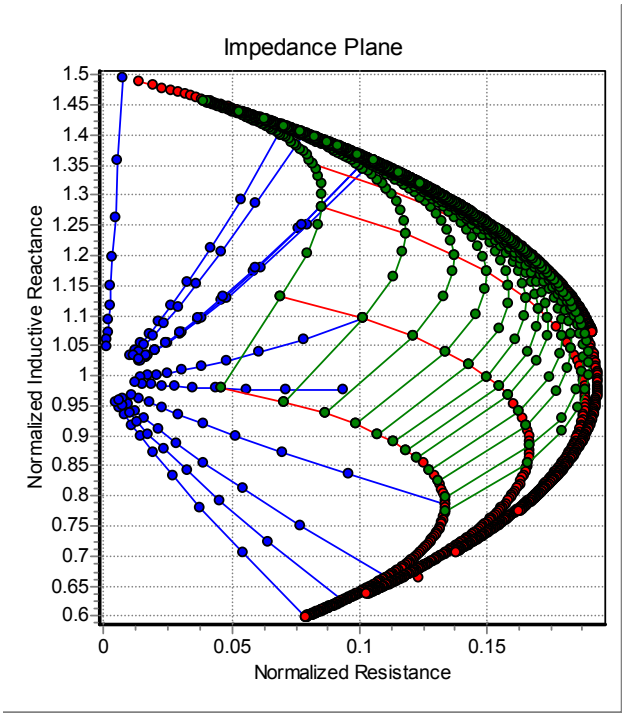

Figure 5.15 – Normalised impedance plane simulation showing variation in conductivity and permeability at 300 kHz. Conductivity variation curves at constant permeability are shown in red and permeability variation curves at constant conductivity are shown in green.

Looking in more detail, Figure 5.15 shows both conductivity and permeability being varied at 300 kHz. These overlay the impedance plane (in blue) of the twelve test samples for reference (see Figure 5.9). The curves that begin left-to-right are conductivity curves for set permeability (1,2,5,10,100 and 1000) and the curves that begin top-to-bottom are permeability variations for constant conductivity (0.5-10 %IACS).

It can clearly be seen from producing plots like Figure 5.15 where the areas of greatest sensitivity are, where the grid lines are far apart. To achieve the best results from eddy

current testing the inspection should be designed to operate within these areas of higher sensitivity wherever possible. Similarly, there are regions where there is very little impedance change with material parameters. This is particularly true for materials with high permeability. Knowledge of areas of greatest sensitivity on an impedance plane is essential in designing eddy current-based inspections.

5.4. Conclusions

From the simulated and measured data we can see how the impedance of the coil responds to differing inspection conditions and there is good agreement with the theoretical impedance planes from the literature and the model based on Dodd and Deed's solutions. It is worth noting that when comparing the simulated data and the recorded data, there is a large disagreement between the two sets of values, particularly at 200 kHz. Additionally, although in general the relative positions of materials on the impedance planes is the same for measured and simulated data, this is not true for all ferromagnetic materials at all frequencies.

There are several possible explanations for this, the first being that the simulation model is simplified and idealised. Additionally, the values of conductivity and permeability used to create the simulation are not entirely accurate. Conductivity measurements may have errors up to 2%IACS and the permeability is estimated and frequency dependent. The degree of variation in permeability with frequency is dependent on the material and its magnetic history. The permeability increases with H, up to a limit; the magnetic saturation point of the material, after which it is constant. Since in eddy current testing the applied field is alternating, the permeability never achieves this constant state. The permeability of some materials, such as ferrites, may not vary at all, whereas others,

such as nickel alloys, may vary non-linearly by a factor of 10 over a frequency range of 1-100kHz. [103]. With this in mind the simulation used here gives an at least acceptable approximation of the eddy current problem and as such is a valuable design tool. However, any predictions need to be supported by experimental trials.

Another essential point to take from this work is how well the impedance plots of the industrial instruments compare with the measured data from the impedance analyser. As long as variations between the two are only small and they follow the same trend then it is valid to use information gained from impedance measurements to design inspections using the industrial instrument. RWE npower use the Zetec MS5800 eddy current array hardware which produces adequately consistent impedance plots compared with the impedance measurements as shown in Figure 5.16 below.

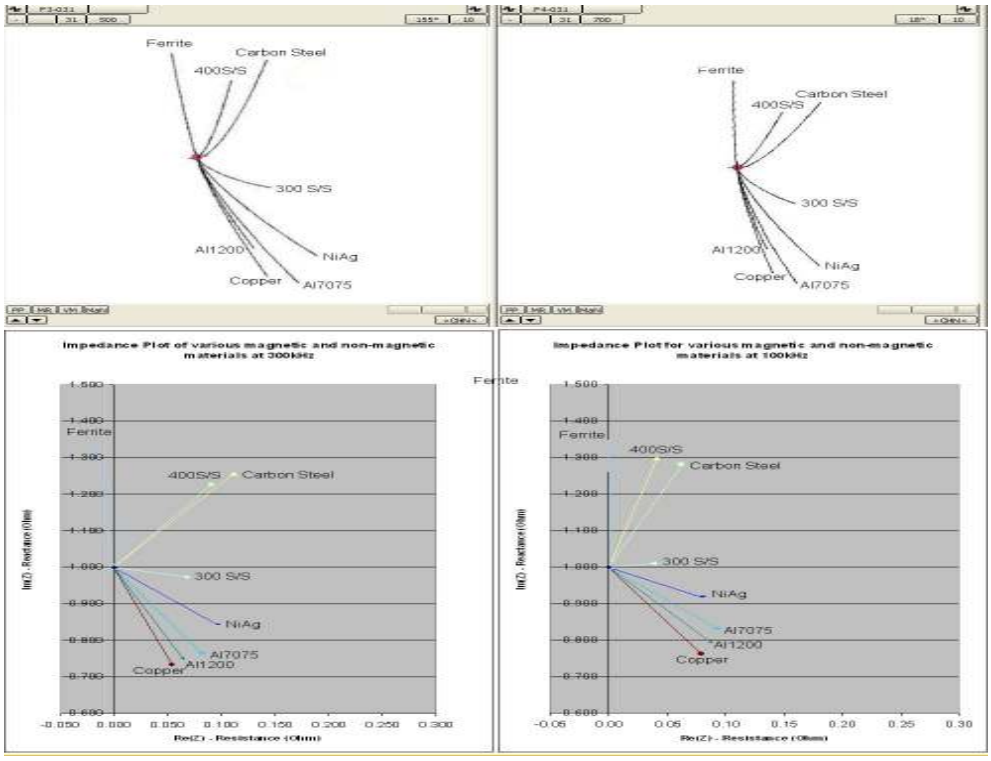

Figure 5.16 – Comparison between MS5800 impedance plane (top) and impedance analyser data (bottom)

The impedance planes on the left show data at 300kHz and the data on the right is taken at 100kHz; the differences between the two are small and the most important feature is that the eight reference materials are in the same positions relative to one another. The relative positions of the reference materials are slightly further apart in both cases for the 300kHz data in both amplitude and angular separation. As a general rule it does appear that the MS5800 gives a good representation of the true coil impedance, though it is worth noting that there are occasionally discrepancies in the amplitude of signals as can be observed with the Al1200 reference material.

The understanding of the effect of material parameters on the normalised complex impedance plane is a vital component in designing an inspection for detecting microstructural variations in ferromagnetic steels. This helps to not only identify what variations are causing changes in the measurable impedance of an eddy current coil, but also how to design the inspection to maximise sensitivity and effectively extract the relevant information.

Chapter 6 Microstructure Mapping of Steam Turbine Blades

6.1. Introduction

Some large steam turbines used in power generation consist of three pressure stages, the high pressure (HP) turbine, the intermediate pressure (IP) turbine and one or more low pressure (LP) sections (See Figure 6.1).

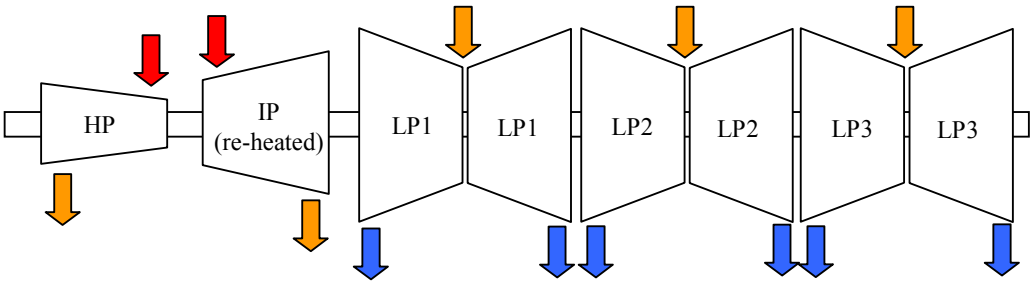

Figure 6.1 – Diagram of turbine train showing inlet and outlet positions of each stage

Each section consists of a number of rows of blades known as stages, these increase in blade length from the inlet to outlet. The reason for this is that efficiency is dependent on the ratio of steam velocity to blade velocity. The steam passing through the stages of the LP turbine expands very rapidly and accelerates to achieve supersonic velocities, thus as the steam gets faster the blades must get longer so that their velocity increases. The form of the LP blades is long and highly-twisted in design to conform to the three-dimensional flow characteristics of the steam. The steam enters the turbine train in the high pressure turbine at approximately 568°C and 165 Bar, in this superheated state it is saturated dry steam. The steam expands through the high pressure turbine giving up its heat energy and dropping in pressure as it rotates the turbine. It is reheated in the boiler before passing into the intermediate pressure turbine and then directly into the low pressure turbines. The low pressure section of a turbine operates at relatively low temperatures and by the final stage of the turbine temperatures are below 60°C and the moisture content at this point can be as much as 12% [Based on RWE npower plant data

from 2008]. The corrosive nature of this environment means there is a risk of stress corrosion cracking in the blades [104]. Ordinarily this risk is low, but it is increased considerably in regions where the turbine blades are abnormally hard due to microstructural phase-changes and a failure has occurred in the past at RWE npower's Didcot A power station, see Figure 6.2. The instance seven years ago, saw a blade cracked due to this mechanism and a section of it detached, damaged neighbouring blades and unbalancing the rotor [105]. Recently, further cracked blades have been detected prior to failure; all cracks were located in areas that were much harder than normal. These hard regions are often created accidentally during turbine refurbishment by heat impingement from gas torches or from the slipping of heating blankets, which are used for heat treatment [106]. The acceptability threshold imposed on these blades is 390Hv (hardness measured by a Vickers test), so any regions of higher hardness need to be identified. The area considered most at risk is the final 250mm of the 1.2 metre turbine blade (this tip section is shown in Figure 6.3 cut off from the rest of the blade). The blades are made from 12% chrome steel (usually FV566 specification) and are ferromagnetic. Note: for ease of reading, this material will be referred to as 12Cr for the rest of this document. They would be ground to a surface finish of 10CLA (Centre Line Average – the arithmetic mean deviation of the surface profile in micro-inches) or better prior to hardness testing. Hardened regions vary in size from approximately 5mm x 5mm up to 50mm x 50mm in the most extreme cases.

Figure 6.2 – Image of the Didcot A failure, inset -the failed turbine blade tip.

Normal procedure is to inspect the at-risk area of each turbine blade with a mechanical hardness tester [107]. This is done by marking a 7x6 matrix of spots spaced at 20mm intervals along the blade and 10mm across the blade and taking multiple hardness readings at each spot. There are two last-stage sets of blades for each rotor, one at each end of the rotor, consisting of 96 blades each. Assuming a minimum of three hardness readings are taken per spot the total number of readings per rotor is around 25,000, which will take at least five days to complete.

In order to reduce the time spent on hardness testing the rotors, it is hoped that a fast screening method can be employed to identify the transformed regions which will then be hardness tested mechanically to give an absolute value of the material hardness.

Ideally, an inspection that produces a hardness profile of the blade with one or two passes would be required. The problem here is that no 'truly non-destructive' technique can measure hardness directly; hardness is a relative measure of material flow under load which can only be measured directly by mechanical methods, which although they cause little damage to a component are not truly non-destructive. It is known that a change in hardness/microstructure of a material may alter its values of electrical conductivity and magnetic permeability [13], both of which have a strong influence on eddy current impedance tests.

Figure 6.3 – A typical turbine blade tip to be hardness tested. The left end is the very end of the blade and the right end is where it has been cut from the rest of the blade.

6.2. Literature Review

Information on hardness testing by NDE methods is fairly restricted with mostly electromagnetic methods proposed as a viable alternative to mechanical hardness testing. One exception is the proposed use of thermal waves which can detect variations in the

local thermal conductivity associated with some hardness variations [108].

Although attempting to produce a hardness profile of a turbine blade using eddy currents has not been documented before, there have been a number of relevant papers produced [109][110]. The hardening of 12Cr steel has been of interest for many years particularly in the nuclear electric industry and consequently there have been several studies into this particular problem [111][112].

From our [RWE npower's] experience, localised hardening of 12Cr steel turbine blades occurs during component overhaul. There are two main sources of this hardening: One is from errors in post-weld heat treatment when replacing blade tips and the second is from accidental flame impingement during work on neighbouring blades.

Flame hardening, performed in a controlled manner, is often used to harden turbine blades and has the benefit of providing greater resistance to impact, thus increasing the lifetime of the component. To achieve the hardness a non-equilibrium heat and immediate cool process is used. This produces a surface hardening due to the transformation of austenite (or tempered martensite) to untempered martensite, without changing the properties of the rest of the component [112]. What needs to be controlled is the level of hardness, the depth of the hardening and, probably the most crucial of all, the residual stress.

Obviously in the situation we are dealing with the hardening is not a controlled process. If it was, it would be necessary to control the elastic residual stresses at a moderate level, because the flame hardening can induce high tensile stresses which make the steel

susceptible to stress corrosion cracking [113][114]. It is this susceptibility that is the primary driver for identifying any areas that may be hardened.

In order to utilise the best possible method for detecting the hardened areas encountered in the 12Cr turbine blades, it is beneficial to understand what is going on metallurgically. The original austenitic structure of the 12Cr material is relatively weak and is strengthened and hardened through a heat-quench process which transforms it into the unstable martensitic phase (shown on a TTT diagram in Figure 6.4 and on a micrograph in Figure 6.5), which is extremely brittle. Martensite is a single-phase, body-centred-tetragonal (BCT) structure with almost no ductility. This lack of ductility is due to the effectiveness of the interstitial carbon atoms hindering dislocation movement in the BCT structure which itself has few slip systems [115]. The blade material is then tempered (heat treated below the eutectoid) to form a tempered martensite structure, which has better ductility than, and comparable strength to, the martensitic phase. Tempered martensite contains a cementite phase within a continuous ferrite matrix. The tempering process softens the blades by relieving the stresses in the martensite structure. In the case where a newly hardened region has formed on the blade due to an accidental heating operation there is a return to the untempered martensite phase with reverse temper embrittlement.

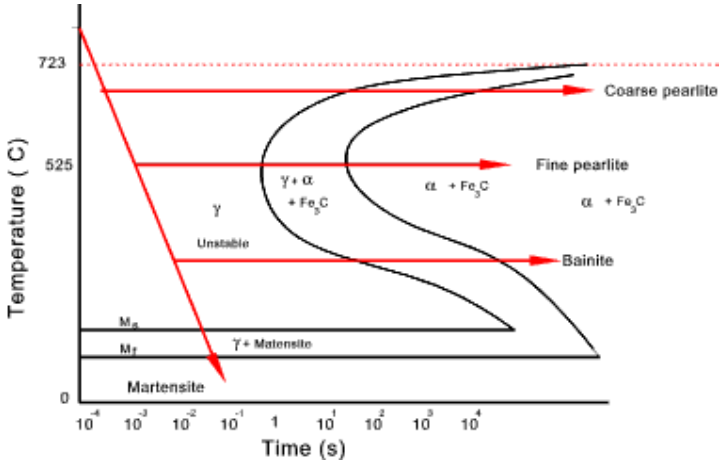

Figure 6.4 Time-Temperature-Transition diagram for carbon steel showing formation of Martensitic phases [116].

The phase transformation during the heating-cooling cycle of incidental or deliberate flame hardening produces a tensile stress, and a thermal compressive stress will occur during cooling [117]. The tensile stress is due to trapped carbon atoms in the set of octahedral sites, which produce the tetragonality of the martensitic crystal structure and create substantial tensile strains with displacements of the nearest neighbour iron atoms [112]. Thus the higher the heating temperature and the more rapid the cooling, the higher the residual stress and the higher the hardness.

Martensite differs from austenite in having higher electrical conductivity and magnetic permeability [118] and it is likely that there will be a change in electrical conductivity and magnetic permeability between tempered and untempered martensite also. This would provide a useful indication detectable by an electromagnetic technique. Identifying areas 'at-risk' of stress corrosion cracking by evaluating the extent to which a martensitic transformation has occurred, may prove more reliable than hardness testing.

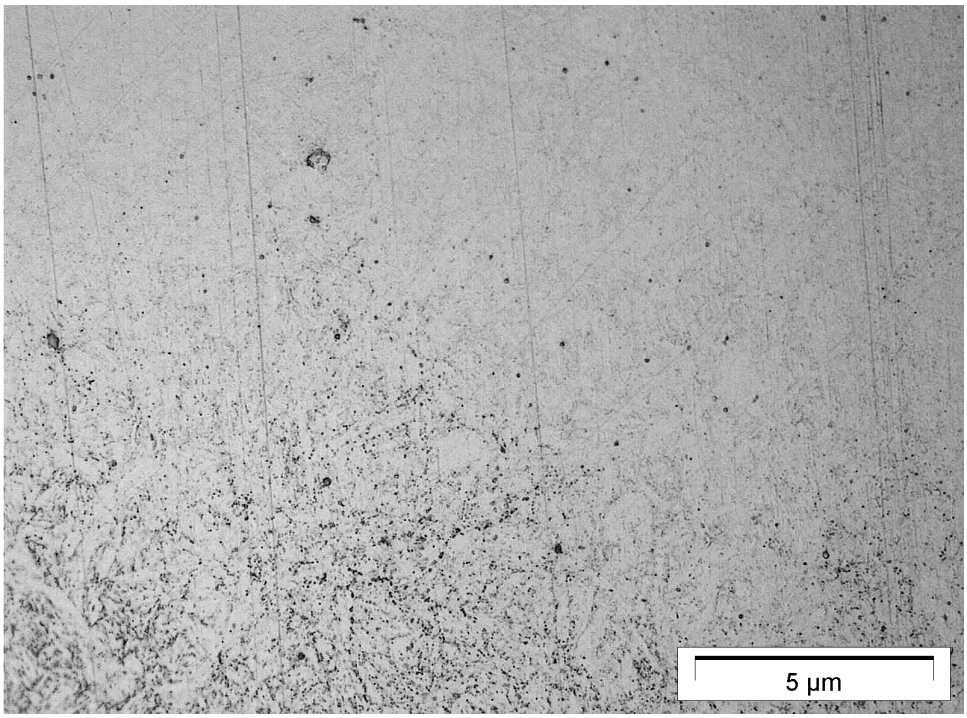

Figure 6.5 – Microstructure difference between tempered martensite (bottom) and non-tempered martensite (top).

Attempts have been made to directly measure conductivity using eddy current measurements [119]. In that study an inverse solution to the problem was devised and then tested on experimental data. Although there was correlation between the probe impedance and the conductivity of the metal under test, it was actually linked most closely to some average of the conductivity profile. This 'average' was not established during the course of that investigation. The report concluded that only in certain cases could this model be used to infer conductivity from impedance measurements due to the diffusive nature of the wave equation involved.

More recently some successful measurements of conductivity and permeability have been made [120]. Although not entirely accurate, good estimations of these values were made when examining porous metals. Research at other institutions is continuing on

developing forward problem solutions to better refine the estimation of these characteristics [121].

The use of eddy current impedance analysis for material characterisation rather than defect detection has seen a fair amount of work in recent years, particularly in trying to measure mechanical properties and metallurgical characteristics such as decarburising [110]. Primarily this has been aimed at establishing tensile properties and/or material hardness. Successful work on characterizing cast iron [122][123] using impedance analysis has shown the feasibility of the method. Another successful method has been the employment of coercivity measurements/ Barkhausen Noise in determining hardness of austenitic stainless steels [124].

The most relevant paper on the relationship between mechanical microhardness and impedance variations is by Zergoug *et al*. [109]. The major difference being that the research for this project is based on hardness on a macroscopic level and I am aiming to isolate a small band of hardness in a particular area on a specific material. In their work, Zergoug *et al.* are able to confirm reasonably good correlation between eddy current impedance measurements and the microstructural variations associated with increases in hardness. My work has been refining this into a rapid scanning system for a relatively small hardness range on a real-life application.

6.3. Choice of Method

In order to choose the most appropriate NDE method for detecting the local phase-transformed/hardened areas it is worth reviewing exactly what we are trying to detect and the benefits we are seeking over the current method employed.

Although historically what we have tried to detect is a variation in hardness, this is just a manifestation of a phase transformation from tempered martensite to un-tempered martensite. This phase transformation causes an apparent change in material electrical conductivity and/or magnetic permeability, which gives a total of three potentially detectable characteristics associated with this inspection problem. The current method of utilising mechanical hardness testing is too labour intensive and is insensitive to small regions of untempered martensite because of the lack of 100% coverage. However, it is a useful validation tool and is likely to be utilised as part of a validation of a new rapid screening method.

The damaged regions are caused by heat impingement on the blade surface, so any indication of the transformation is likely to be strongest at the surface, so volumetric techniques are largely redundant. The lack of discontinuities discounts many of the surface inspection techniques available. Surface ultrasonic inspection can be discounted on the basis that there is no appreciable bulk sound velocity/attenuation variation associated with the transformation.

Thermography has potential but is impractical due to the physical constraints of testing the rotor. It is also impractical for re-testing after the blades have been ground for mechanical hardness testing, due to the change in emissivity.

Accurate measurements of material phase are confined to lab-based instrumentation which leaves us with electromagnetic techniques as the most viable option. ACPD/DCPD would have the potential to measure the variation in conductivity;

however the technique does not lend itself well to rapid scanning with good spatial resolution. Additionally, conductivity measurements require accurate measurement of material thickness which varies in two dimensions across the blade. ACFM would also be a potential technique, however it offers no advantage over the eddy current method because of the easy access to the component surface.

So the potential options could be:

Eddy current scanning

Meandering Winding Magnetometer (MWM) measurements

Pulsed Eddy Current

Magnetic Barkhausen Noise

6.4. Potential Methods

Eddy currents have been used for the purposes of hardness testing for some years. In small component manufacture (i.e. bolts) the surface condition (hardness, heat treatment etc.) of a component is checked by passing the component through an encircling eddy current coil. The coil impedance is compared with the impedance of an identical coil containing an "ideal" component as a comparator. Through analysis of the impedance difference, it can be deduced whether the difference in components is due to size, material composition or heat treatment and whether any difference is within tolerance. For example, some component tests using a differential eddy current arrangement will have an alarm zone marked around the null point on an impedance display, within which all components are acceptable. Should a component cause the impedance to change such that it no longer falls within this zone, the component is unacceptable. Depending

on the size, shape and material of the component, the test can be arranged such that a movement in a particular direction on the impedance plane is indicative of a particular material property variation (i.e. case hardening). The direction of this movement is however entirely dependent on the parameters specific to the test and the orientation of the impedance display. It would not be practicable to use a similar method on turbine blades since they cannot be passed through an encircling coil due to them being attached to the rotor and having very little clearance. If they could be removed and passed through a very large coil, this would assess the blade as a whole blade and thus would not provide sufficient information of the exact location of any phase changed areas.

A change in material hardness may also manifest itself as a change in material electrical conductivity and in some cases, a change in magnetic permeability. The electrical conductivity and magnetic permeability are also affected by material composition, residual stress, heat treatment and surface condition amongst other factors, though some have a relatively greater impact on one than the other. In this case the residual stress and heat treated condition are closely linked to the material characteristic change that is sought. Thus, in order to obtain as good a correlation as possible between the phase change/hardness and impedance it is necessary to minimise the effects of the other significant factors, composition and surface condition.

The surface condition should be uniform for all blades to be tested. The current testing method requires a 180 grit (63CLA) finish on the blades prior to testing which would provide a clean and consistent surface for eddy current testing. To minimise the geometric effects of the surface, I propose using fully-conformable sensors and arrays. The impact from variable material composition could be minimised by the use of a

calibrating standard and/or using a differential signal.

A semi-flexible eddy current array probe was built by Zetec for RWE npower for inspecting steam turbine blades for welding defects, but had limited success. There was too much variation in lift-off between coils to obtain the necessary sensitivity and the connections to the coils kept breaking because of the flimsiness of the design. However, during trials with this array probe it was noted that the heat affected zone (HAZ) of the welded blades (being of identical composition but different microstructure and hardness) was visible on an eddy current C-scan (a 2-D surface plot of eddy current signal amplitude in either X or Y plane) of the inspection. This suggests that there is a chance that a C-scan map of microstructural variation could be produced provided the effects of non-relevant influences can be minimised.

The use of Magnetic Barkhausen Noise to detect the embrittled areas was investigated in conjunction with Newcastle University. The results, which can be found in Appendix G, show that there was a lack of consistent trends produced and consequently the method was dismissed. The inconsistency arose from the sensitivity of the Barkhausen Noise method to component surface preparation and the inability of the probe to conform to the blade surface. Since neither of these can be practically negated, it was not deemed appropriate to proceed with this line of investigation. Data gathered from the tests is used as supporting information in the proceeding work.

Pulsed eddy current testing was also explored at Newcastle University. The technique did not lend itself well to this particular inspection since this method is detecting an effect that is greatest at the material surface. Further details are given in Appendix G

and data from the investigation is used as supporting evidence for the eddy current technique.

Having dismissed magnetic Barkhausen noise and pulsed eddy current as being unsuitable, two methods are left for further investigation; conventional eddy current and Meandering Winding Magnetometer measurements. In order to focus in on the most appropriate method, some initial trials using the two proposed techniques were implemented to establish which, if any, was the most appropriate to persevere with. Ultimately the MWM method proved to be too slow compared to the eddy current method, the MWM experimental findings are given in a separate document [98]. The approach to this project is to establish whether or not the microstructural phase change from tempered martensite to untempered martensite affects the electrical conductivity and/or magnetic permeability of the material and if it does, how it affects both and to what extent. Once this is established it is necessary to minimise influence from all other factors that may cause a change in test impedance so what is left is just the conductivity/magnetic permeability variations associated with the material phase change.

6.5. Test Samples

Prior to conducting any tests to check the suitability of the proposed methods for this inspection, a range of test samples were required. The details of each one are as follows:

Samples A-E are slices of FV566 12Cr blade root which have been heat treated to produce a range of hardnesses. In non-hardened areas the hardness varies from 290Hv to 380Hv. They have the same material composition as shown in Table 6.1. Samples

measure approximately 100mm x 40mm x 8mm.

Element	Cr	Ni	Mo	Mn	Si	V	C	Cu
Wt %	12.0	2.37	1.25	0.54	0.32	0.21	0.13	0.12

Table 6.1. Composition of blade sections (Bodycote chemical analysis)

Sample A. 338Hv – Non heat-treated blade section.

Sample B. 436Hv - 30 minutes at 1050°C, then air-cooled at room temperature (approx. 3 hours to reach room temperature).

Sample C. 318Hv - Tempered at 680°C for three hours, then air-cooled at room temperature (approx. 2 hours to reach room temperature).

Sample D. 360Hv - Tempered at 610°C, then air-cooled at room temperature (approx. 2 hours to reach room temperature).

Sample E. 390Hv - Tempered at 560°C, then air-cooled at room temperature (approx. 2 hours to reach room temperature).

Samples F-O are ex-service blade tips (final 250mm as shown in Figure 6.1.1.2), all are of the same composition as shown in Table 6.2. They are marked with 42 spots from the 7x6 hardness measuring matrix and values at each spot as measured using a GE Inspection Technologies TIV hardness tester have been recorded.

Element	Cr	Ni	Mo	Mn	Si	V	C	Cu
Wt %	11.9	2.23	1.52	0.61	0.18	0.33	0.11	0.06

Table 6.2. Composition of ex-service blades (Bodycote chemical analysis)

Sample F. Blade tip, hardened region approximately 40mm x 25mm @ 430Hv.

Sample G. Blade tip, hardened region approximately 30mm x 20mm @ 410Hv.

Sample H. Blade tip, hardened region approximately 20m x 20mm @ 400Hv.

Sample I. Blade tip, no hardened region.

Sample J. Blade tip, no hardened region.

Sample K. Blade tip, no hardened region.

Sample L. Blade tip, no hardened region.

Sample M. Blade tip, no hardened region.

Sample N. Blade tip, no hardened region.

Sample O. Blade tip, no hardened region.

Sample P is a full length blade provided by British Energy for 'blind' trials. Material specification is as per Table 6. 1.

Sample P. Blade with three flame-hardened regions on trailing edge @ 430-500Hv.

Sample Q. Small section of 12Cr material with 5mm x 5mm hardened region @ 500Hv created by creating molten pool with a TIG welder. Composition is as per Table 6.1.

Sample Z. Carbon steel reference block, Hocking 29A028 (S/N 312167/07)

6.6. Conventional Eddy Current Testing (ECT)

For these tests a Zetec MS5800 eddy current acquisition unit is used, along with a semi-flexible 64-element absolute coil probe (ECP1), shown in Figure 6.6. The probe contains two rows of 32 coils with a slight offset between the two rows. The air-cored coils are circular and flat with a 2mm outer diameter, 0.2mm internal diameter and 264 turns. The design operating frequency for these coils is 500kHz. A second probe (ECP2) shown in Figure 6.7 was built by Zetec for RWE npower, using the same coils but only using a single line of 56 coils adjacent to each other which could cover the full width of a turbine blade with one pass. A third array probe (Figure 6.8), also built by Zetec, had a fully flexible housing and consisted of 22 magnetically-backed coils in a

transmit-receive arrangement. These coils were 5 mm in diameter, had 250 turns and were optimised to operate in the frequency range 50-300kHz. Also used was a Hocking single-element, 500 kHz absolute coil pencil probe, type 106P4 (ECP4).

The eddy current probes are operated using a Zetec MS5800 eddy current acquisition system which is controlled via a laptop computer running Zetec EddyView 1.6Q2 software. When using an array probe a Zetec AATX145A multiplexer is also required. The software allows the data to be viewed as individual X-Y strip-charts for each channel, as a combined C-scan of all channels, and as corresponding impedance planes for either individual or combined channels.

Figure 6.6 - Semi-flexible array probe ECP1

Figure 6.7 - Semi-flexible array probe ECP2

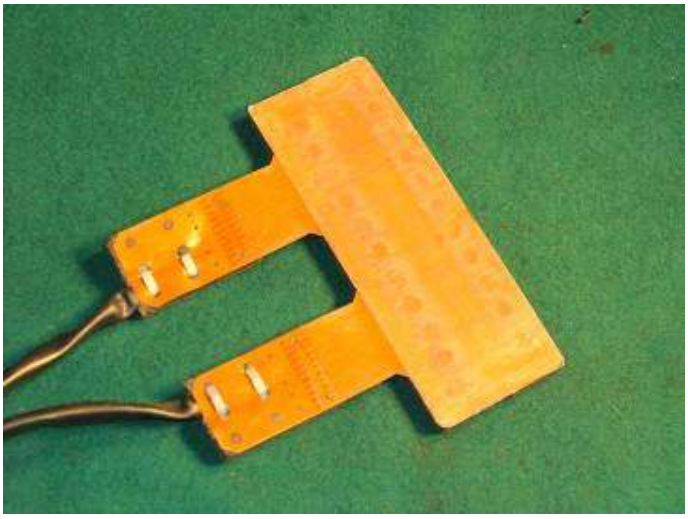

Figure 6.8 - Fully-flexible array probe ECP3

6.6.1. Experiment ECT 1

Equipment: *Zetec MS5800 with ECP4 probe.*

Reference: *Nulled on Sample A, phase rotated so lift-off is centre to left on impedance plane.*

Key parameters: *500kHz at 3V input with 38dB gain.*

Samples: *A-E.*

In order to verify whether the eddy current method has the potential to detect microstructural differences in 12Cr blade material, a simple test was conducted using a single-coil eddy current pencil probe. The probe was placed vertically on the face of Sample A and the system was nulled. An acquisition was started and the probe was held on each of the five samples (A-E) in turn for approximately 5 seconds.

With the lift-off component of the eddy current signal set to horizontal (centre to left), it is evident from the results in Figure 6.9 which shows the vertical component of the complex normalised voltage of the coil response drops with increasing hardness. Analysis of the impedance plane suggests this is an increase in conductivity and/or a drop in magnetic permeability.

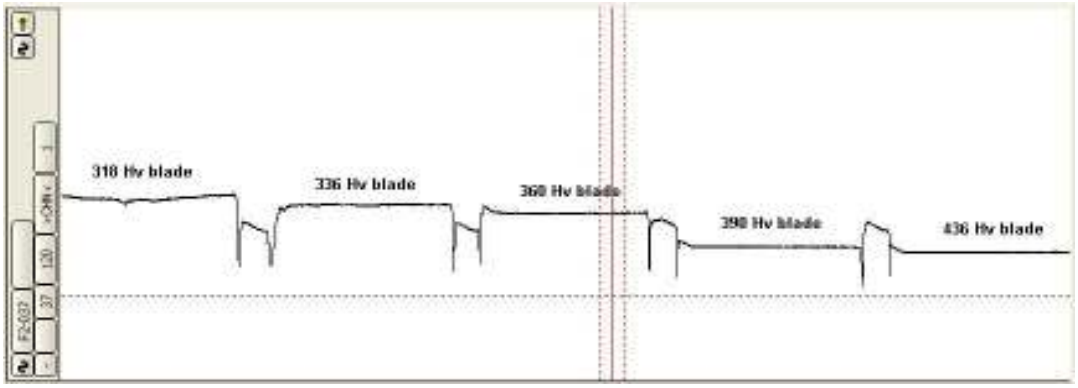

Figure 6.9 - Eddy current response to varying levels of hardness in Samples A-E at 500kHz.

There appears to be a more pronounced drop in the normalised vertical component of the voltage between the blades that are under the hardness threshold and those that are over it, as indicated by the steep slope in the middle of Figure 6.10. There is also a large increase in the rate of change in voltage near the threshold value.

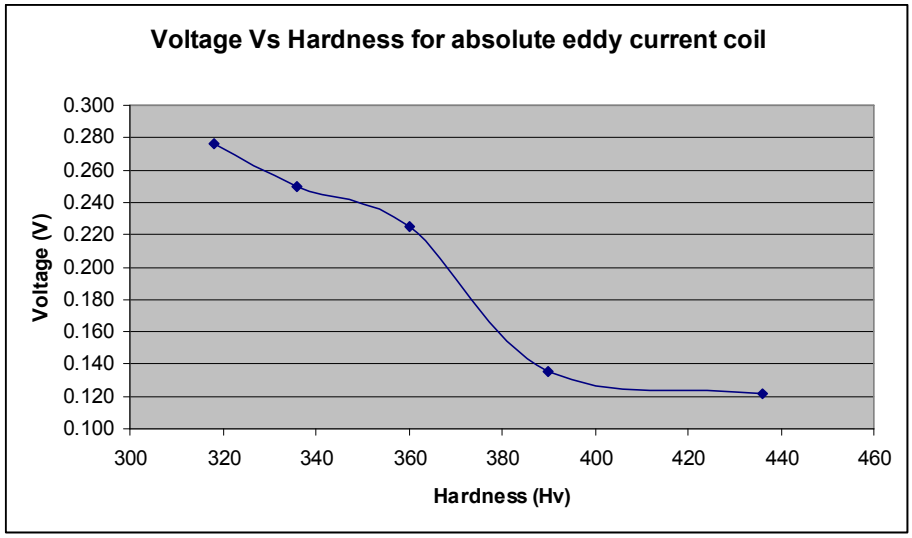

Figure 6.10. Eddy current normalised voltage vertical component vs. hardness

6.6.2. Experiment ECT 2

Equipment: *Zetec MS5800 with ECP1 probe.*

Reference: *Nulled on Sample F away from tip end, phase rotated so lift-off is centre to left on impedance plane.*

Key parameters: *500kHz at 3V input with 38dB gain.*

Samples: *F.*

The results of ECT 1 suggest that an eddy current system could detect the microstructural change in 12Cr. The next stage is to expand this to an eddy current array to permit rapid scanning of blades and the production of a C-scan image to highlight phase transformed areas. Probe ECP1 was placed on the concave surface of Sample F away from the tip end of the blade and nulled. An acquisition was then started and the probe was then scanned towards the blade tip, producing the C-scan shown in Figure 6.11, which has had an approximate overlay of measured hardness put over it. The colours are representative of the vertical voltage component with blue at the lower end

of the scale (-0.3V) and red at the high end of the scale (+0.3V). A sample strip chart of the normalised vertical voltage component from one of the coil channels passing through the hardened region is shown in Figure 6.12.

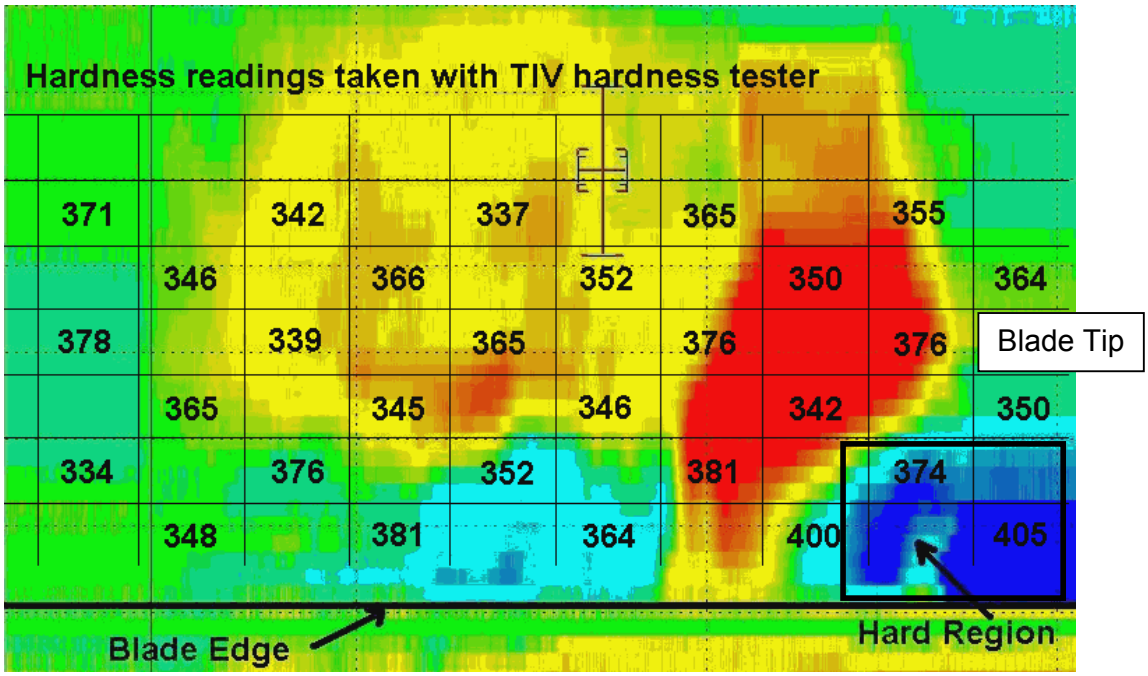

Figure 6.11 - C-scan of ex-Didcot blade (Sample F) with mechanical hardness readings for comparison. Hardened/transformed regions appear in dark blue, light blue region located at bottom-centre may be spurious or on the borderline of transformation .

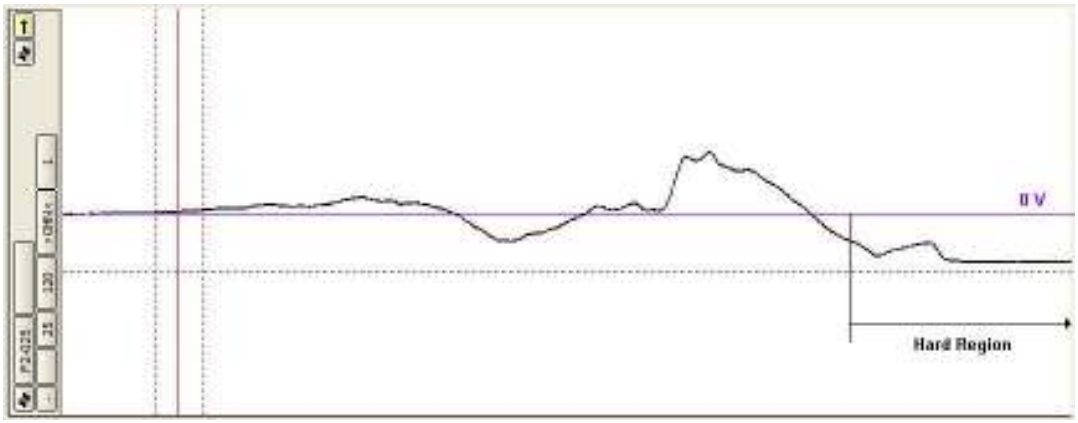

Figure 6.12. Pencil probe response to ex-Didcot (Sample F) blade

Again, initial results were encouraging, the region of blue at the bottom right corner of the image corresponds to a small area of the blade where the hardness exceeds the

390Hv threshold. The area over the hardness threshold matched well, although the rest of the blade was a little less distinct. It is difficult to make a direct comparison of hardness value to voltage due to the variation in reading consistency experienced with such hardness testers. However, as was illustrated in Figure 6.10 there is a far greater variation in the voltage change as the curve passes over the threshold value for hardness associated with the phase transformation, which should allow for easier identification of true embrittled areas from uncontrolled variations in probe response.

6.6.3. Experiment ECT 3

Equipment: *Zetec MS5800 with ECP3 probe.*

Reference: *Nulled in air.*

Key parameters: *500kHz at 3V input with 38dB gain.*

Samples: *F, Hocking Reference Block 33A151.*

To better understand the signals observed in ECT 2, they need to be put in context of the whole impedance plane. To achieve this ECP3 was nulled in air then placed on each of the eight materials on the 33A151 reference block in turn and then onto a hardened and non-hardened area of Sample F. The resultant complex normalised impedance plane is shown in Figure 6.13. It can be seen that the change from tempered martensitic to martensitic 12Cr results in an increase in the resistive component of the coil impedance and a small reduction in the inductive reactance component. The magnitude of the change from tempered martensitic to martensitic 12Cr is 0.29V for this coil/frequency combination. This is a small, but detectable variation which will be put into context later in Experiment ECT 10.

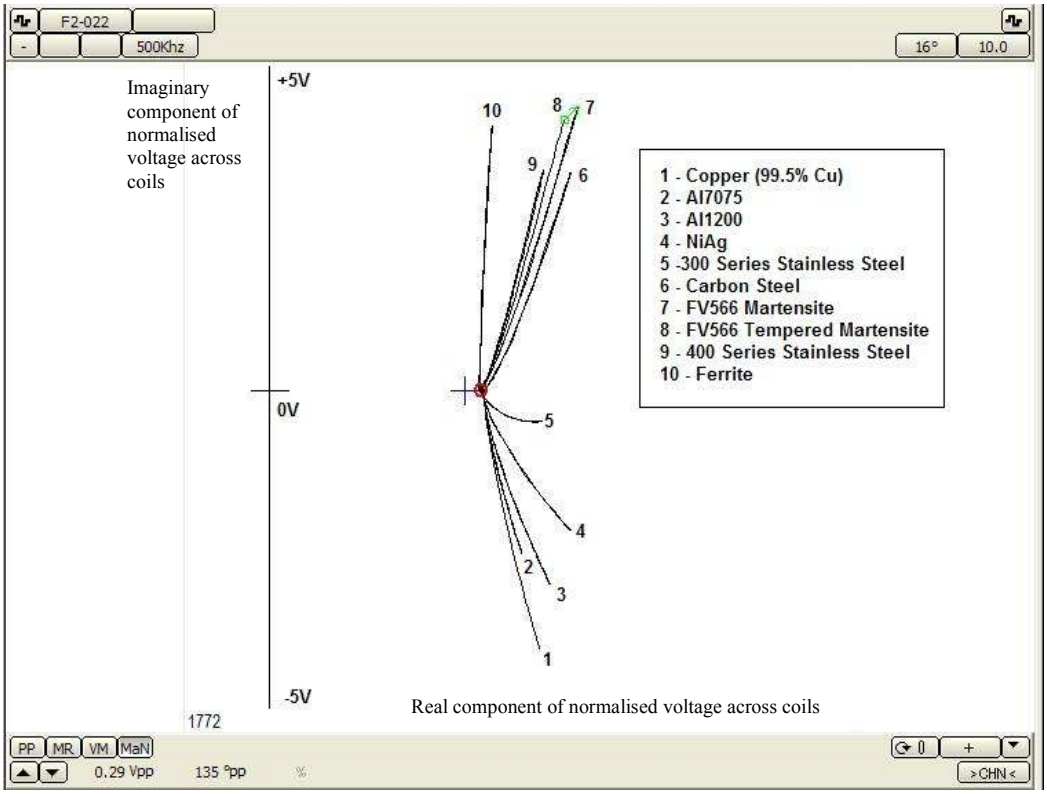

Figure 6.13 – Normalised and rotated impedance plane showing lift-off curves for martensitic and tempered martensitic 12Cr relative to other common metals.

6.6.4. Experiment ECT 4

Equipment: *Zetec MS5800 with ECP1 probe.*

Reference: *Nulled on each blade away from tip end, phase rotated so lift-off is centre to left on impedance plane.*

Key parameters: *500kHz at 3V input with 38dB gain.*

Samples: *P and full turbine rotor from Didcot A power station..*

The results of ECT 2 were encouraging, detecting the exact area of phase transformed material using a rapid scanning technique that produces results in a very easy to interpret display. The next stage was to see whether the technique would work on other test samples. Sample P and the full turbine rotor were available and the same technique that

was used for ECT 2 was employed. The technique was able to detect the phase transformed areas on Sample P and also on a number of blades on the turbine; however, a spurious signal was detected on Sample P to the left of the first embrittled area on the C-scan (Figure 6.14). The C-scan images displayed show a differential signal output which normalises the coil outputs for each position to their own output at the position of a reference cursor on the C-scan. For each image (Figures 6.14 – 6.17) the cursor has been moved to the position where the detection of the phase transformed regions is at its best. The advantage of using this feature is that every blade is normalised to itself, so subtle material variations between different blades/rotors are removed. Clearly, care must be taken that the reference line is at a position where the blade material is fairly homogeneous all across its width. The advantage of this method is that the cursor can be moved during the data analysis stage and moving the cursor across the full scan length should indicate any localised variations.

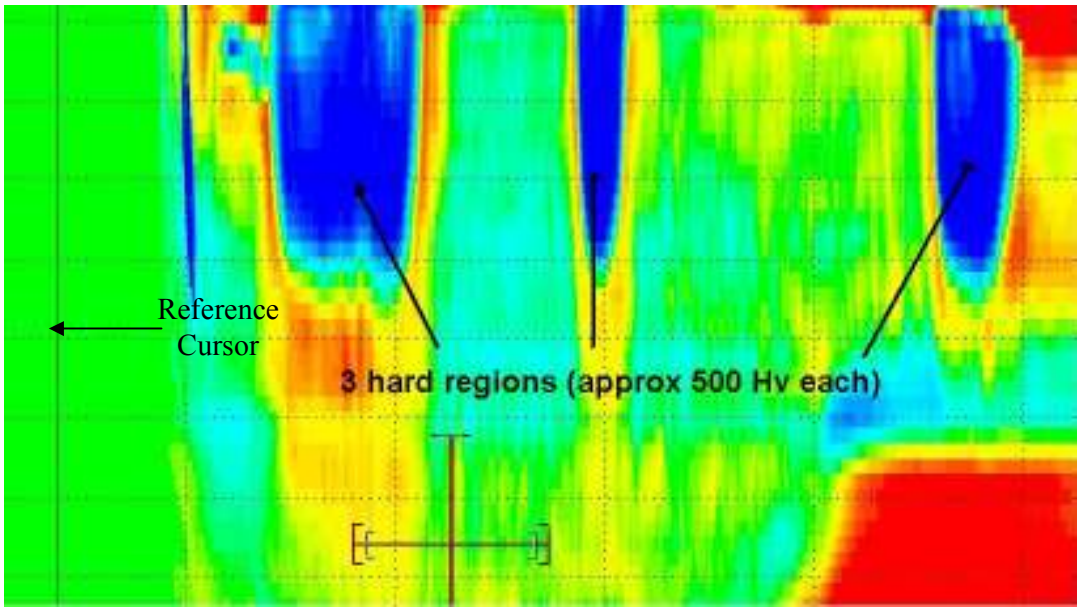

Figure 6.14 - C-scan of the British Energy flame-hardened blade (Sample P) using array eddy current ECP 1 at 500 kHz.

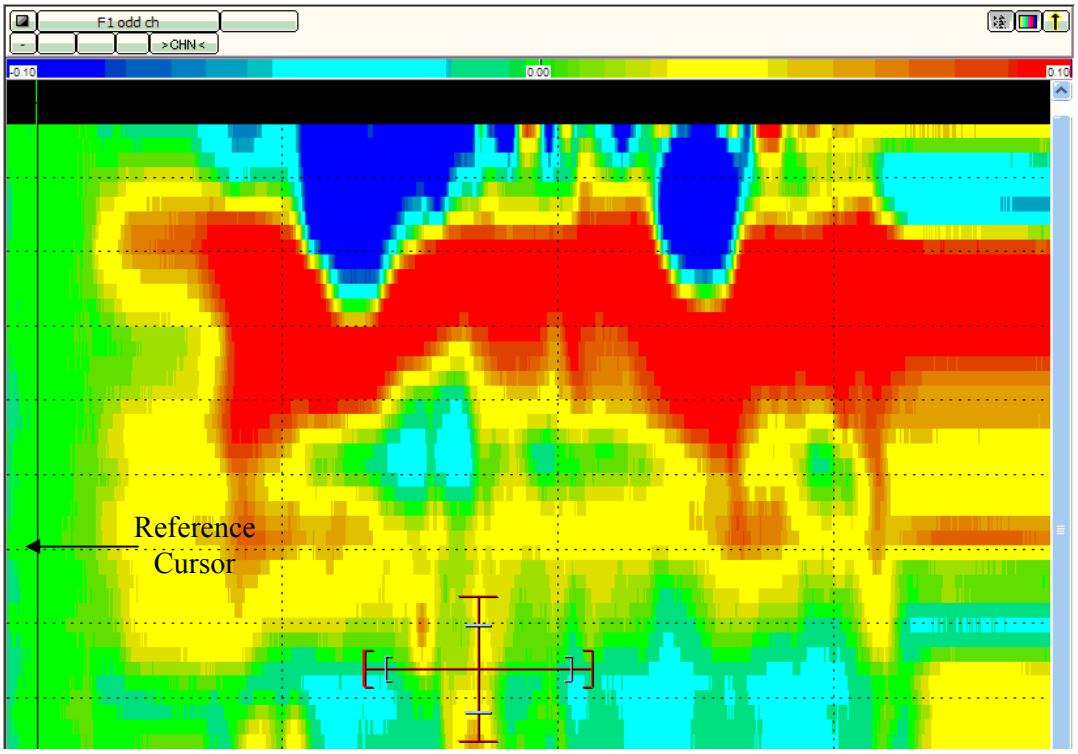

Figure 6.15 - Blade inspection with 2 hard spots on trailing edge using eddy current array ECP 1 at 500 kHz

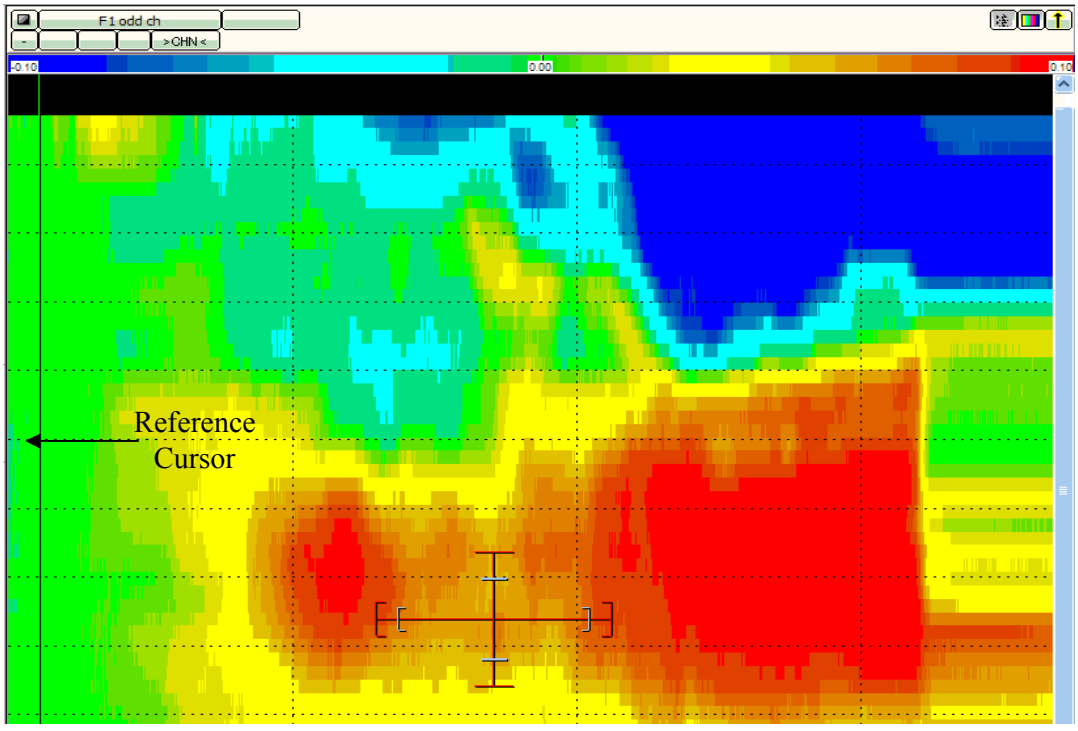

Figure 6.16 - Blade inspection with one large hard area on trailing edge using eddy current array ECP 1 at 500 kHz

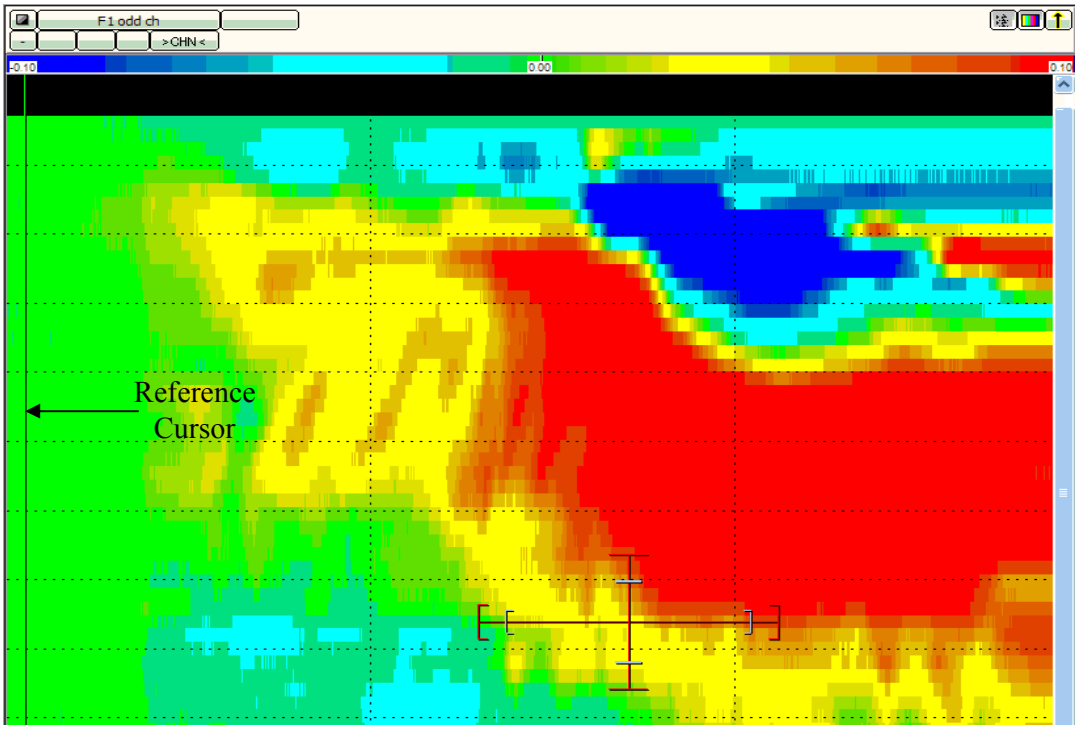

Figure 6.17 - Blade inspection showing hard area in from trailing edge using eddy current array ECP 1 at 500 kHz

6.6.5. Experiment ECT 5

Equipment: *Zetec MS5800 with ECP1 probe.*

Reference: *Nulled on each blade away from tip end, phase rotated so lift-off is centre to left on impedance plane. Reference cursor at sample 30.*

Key parameters: 100, 300, *500, 800 and 1000kHz at 3V input with 38dB gain.*

Samples: *F, I, P.*

The next essential stage in validating this technique is to check the repeatability of the technique. In order to make an accurate comparison the nulling operation needs to be standardised for all blades. Use of the reference cursor to produce a differential C-scan removes some of the importance from the nulling operation; however it is important to ensure that the coil response is constant across the array. A reference sample was made

using a section of 12Cr material with consistent hardness across its width.

Four additional frequencies have been introduced to this test to observe how the probe behaves away from its optimum frequency and whether this will have a bearing on repeatability.

For each sample, the array was nulled on the reference sample and the blade section was scanned for 250mm from its tip end. Each blade was scanned four times, with normalised vertical voltage components measured at sixteen set positions on each blade. The gain settings, phase rotation and reference cursor position were kept constant for all tests.

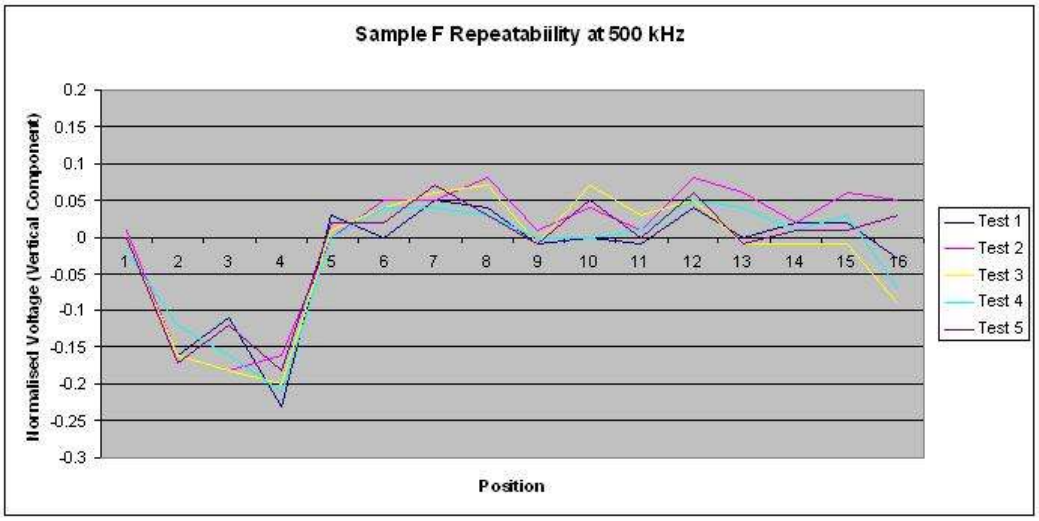

Figure 6.18 – Repeatability at 500 kHz for Sample F

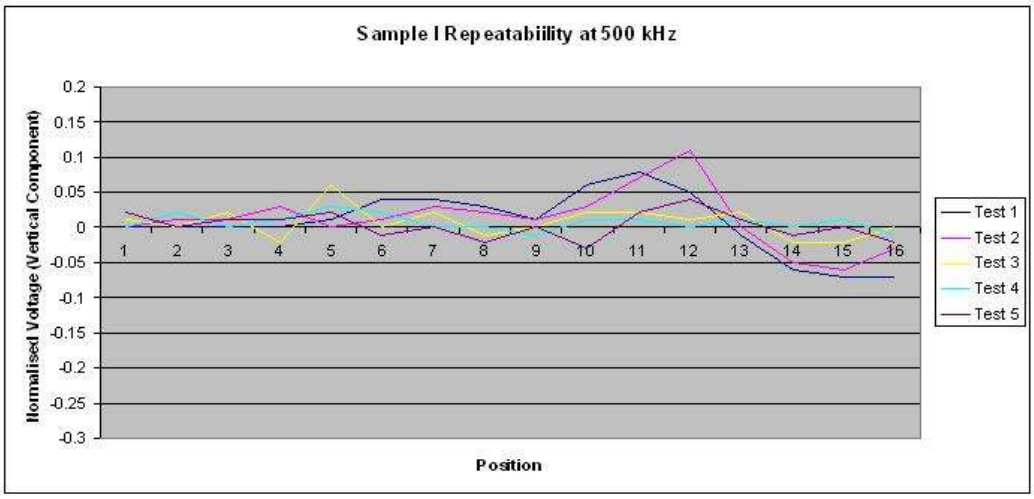

Figure 6.19 – Repeatability at 500 kHz for Sample I

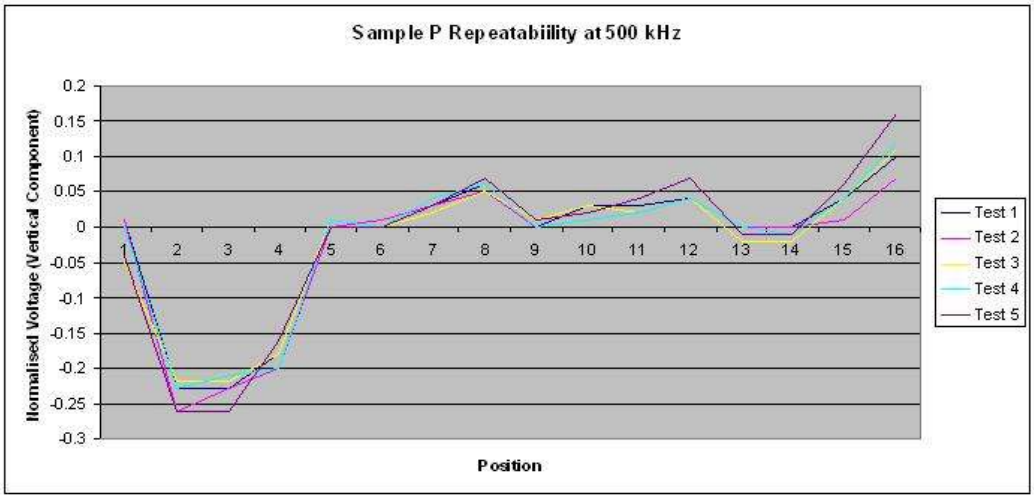

Figure 6.20 – Repeatability at 500 kHz for Sample P

The results in Figures 6.18-6.20 show that the technique has reasonable consistency in terms of general trends but that there are areas where there is increased variation which could lead to spurious results and or missed indications. The variation is most likely due to small variations in positioning, leading to detection of different electromagnetic properties. The average standard deviation for each measurement point in these results is 0.017V over a range of 0.42V, which is 4.0%. Figure 6.21 shows an instance where the detection of the embrittled areas is poor and Figures 6.21 – 6.23 all show areas where spurious indications are present.

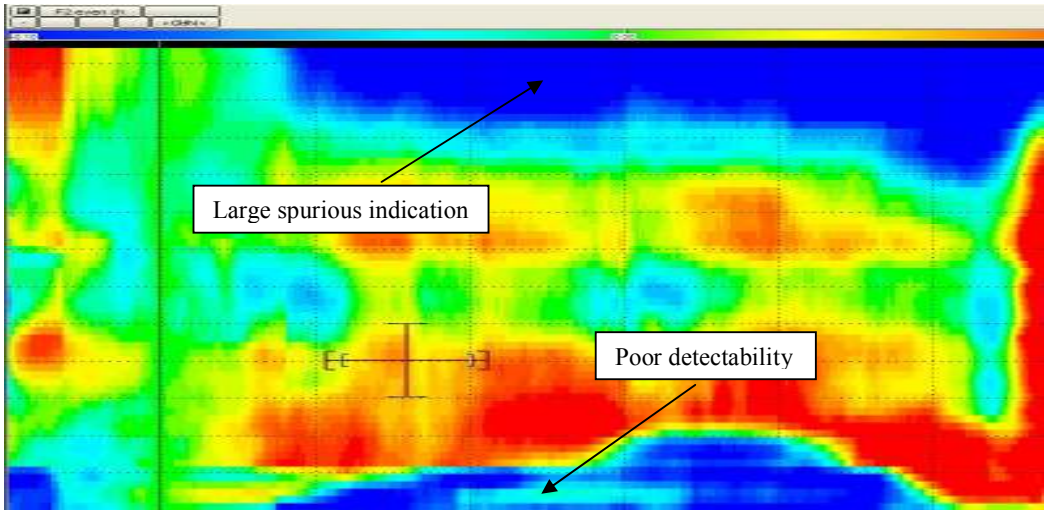

Figure 6.21 – Poor detectability and spurious indications on Sample F at 500 kHz

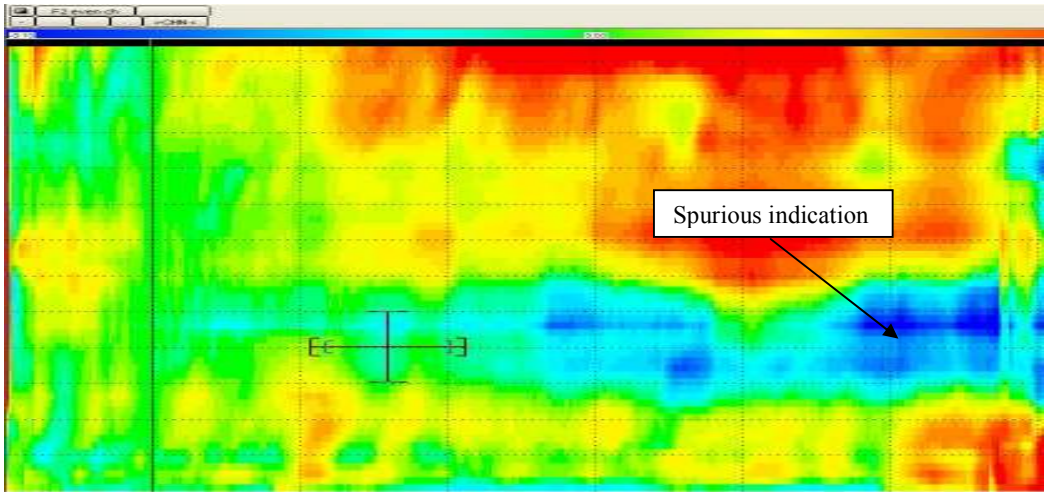

Figure 6.22 – Spurious indications on Sample I at 500 kHz

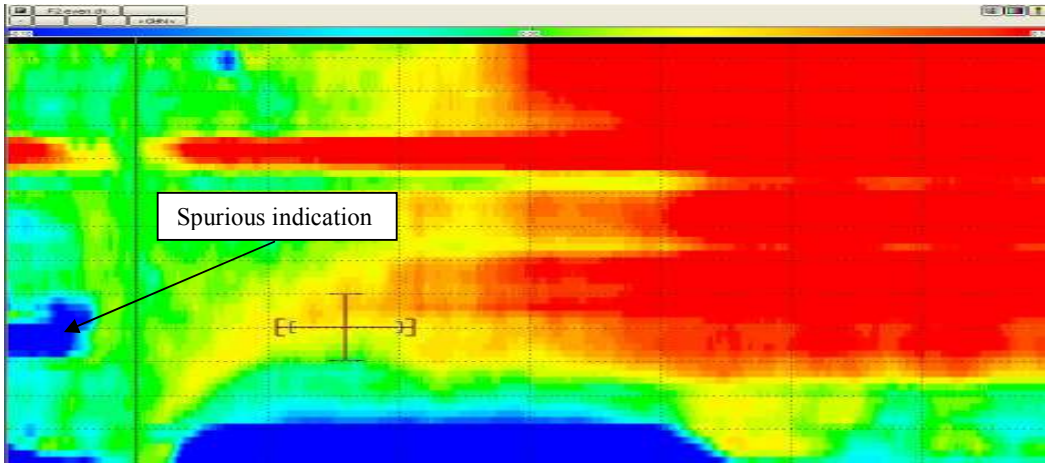

Figure 6.23 – Spurious indications on Sample P at 500 kHz

It is evident from Figure 6.24 below that as the operating frequency is lowered from the optimum value of 500 kHz, the repeatability becomes worse. This is because the magnitude of the eddy current response to martensitic regions will reduce but there will still be significant variation due to geometric effects; thus the variation as a percentage of the total response will be greater. Sample F is shown as an illustration.

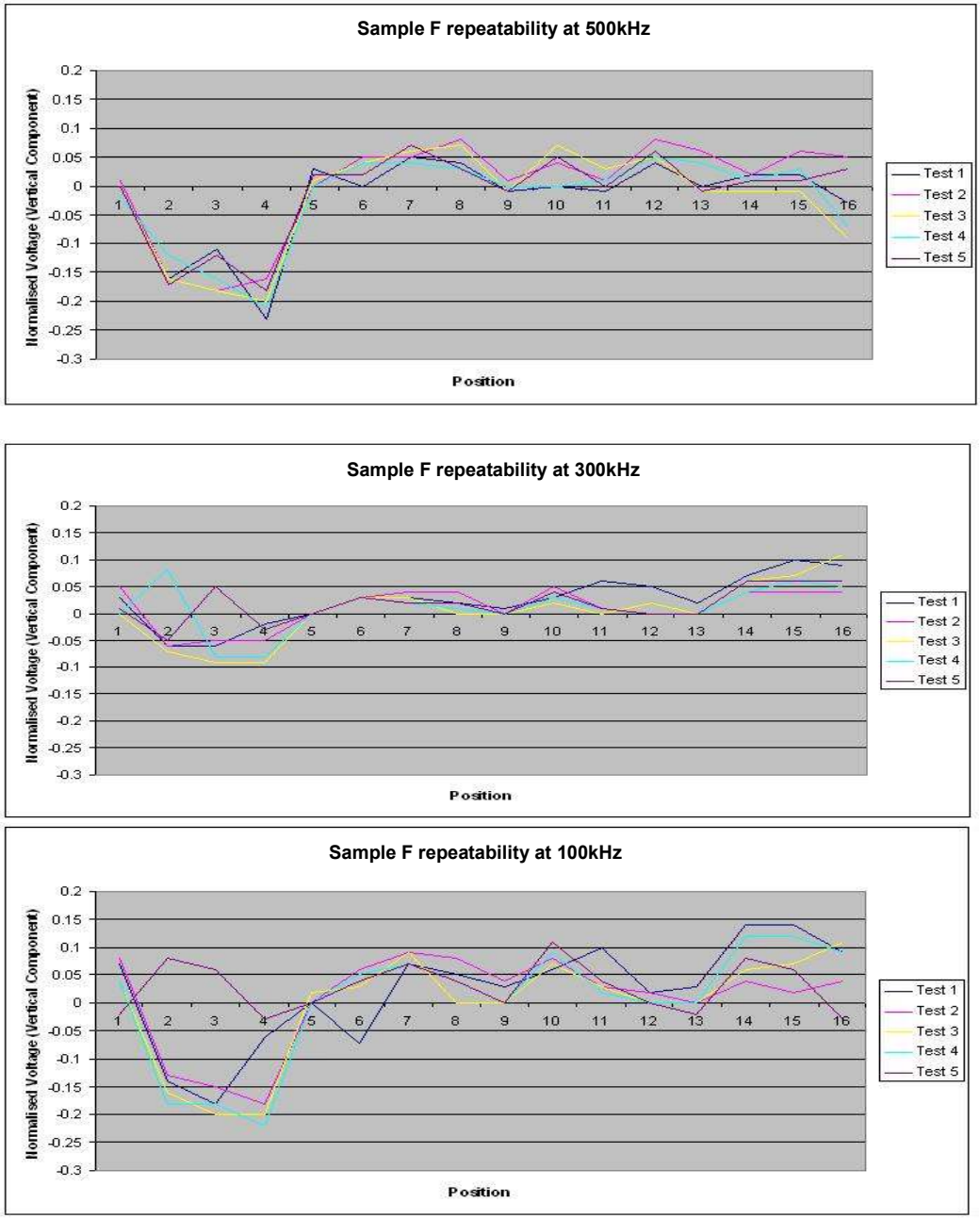

Figure 6.24 – Decrease in repeatability as frequency drops from probe optimum

Similar, but more significant variations were observed at the higher frequencies (not shown). This can be explained by the greater variation in magnetic permeability at high frequencies. The same trends are true of the data collected for Samples I and P, which is reflected by the average standard deviations recorded for each frequency across all measurement points. This is shown along with the voltage range of the results in Table 6.3.

	1000KHz	800KHz	500 kHz	300 kHz	100 kHz
Average Std. Dev.	0.046	0.034	0.017	0.013	0.027
Range of variation	0.74	0.60	0.42	0.24	0.51
Std. Dev as % of Range	6.2	5.7	4.0	5.6	5.2

Table 6.3 – Repeatability statistics as the frequency varies from probe optimum

It is worth noting that there is a marked change in the sensitivity to the phase transformation with the change in frequency. Taking position 4 on Sample F as an example of a phase transformed region; at 500 kHz the normalised voltage is -0.23V, at 300 kHz it is just -0.09V and then at 100 kHz the magnitude increases to -0.22V. This would indicate that the test is very sensitive to operational frequency. This is to be expected and there are several possible reasons:

- The change in frequency changes the phase between lift-off and the phase-transformation signal, resulting in an increase or decrease in the vertical normalised voltage response.
- The variations due to magnetic permeability may be sensitive to frequency – this is the most likely reason.
- The impedance/frequency combinations may be more/less sensitive to the range of conductivity and/or magnetic permeability across the samples.

With the above points in mind and given that the repeatability of the inspection is not as reliable as it needs to be, it is necessary to review the design of the array and use impedance plane simulation to produce a better optimised probe design.

6.7. Designing the eddy current array

The last-stage steam turbine blades I have been attempting to identify microstructural phase changes in, originally had a tempered martensite structure when they entered service. During heating operations in the overhaul process, some areas may experience a reverse-tempering process which can lead to embrittlement. Metallurgically, the blade undergoes a phase transformation from tempered martensite to untempered martensite. In other words, it is going from a stress-relieved state to a stressed state.

Generally stress-relieving processes will increase the conductivity of a material. This is because the heat treatment will remove many of the obstacles to electron flow, such as interacting dislocations and alloying particles [13]. Thus, it would be expected that the untempered martensite regions would be lower in conductivity than the tempered martensite. However, in initial tests for this project it appears that the reverse is true. In ECT 3 an increase in the resistive component of the complex impedance and a reduction in the inductive reaction were observed when moving from a tempered martensite region to a non-tempered martensite region, suggesting that the embrittled, untempered martensite has higher conductivity than tempered martensite. This can be explained by the specific nature of the material involved.

In its tempered state, martensite has a body-centred tetragonal (BCT) structure consisting of a continuous α–ferrite matrix containing finely dispersed cementite (Fe_3C)

particles. In its untempered state, martensite still has a BCT structure, it is a single unstable martensite phase, supersaturated with carbon [115]. This concentration of carbon in untempered martensite increases the hardness of the material as the interstitial carbon atoms hinder dislocation motion. This has some effect on decreasing the conductivity but it is not as significant as the effect of the finely dispersed cementite particles. A greater number of smaller particles offers more resistance to electron flow than a few larger ones [13]. Thus as the phase changes from tempered martensite to untempered martensite and the finely dispersed cementite particles are assimilated into the single martensite phase, the impedance to electron flow decreases and so conductivity will increase.

Based on the results of ECT 3, the impedance change associated with the change in microstructure is approximately as shown in Figure 6.25 on a simplified, normalised complex impedance plane.

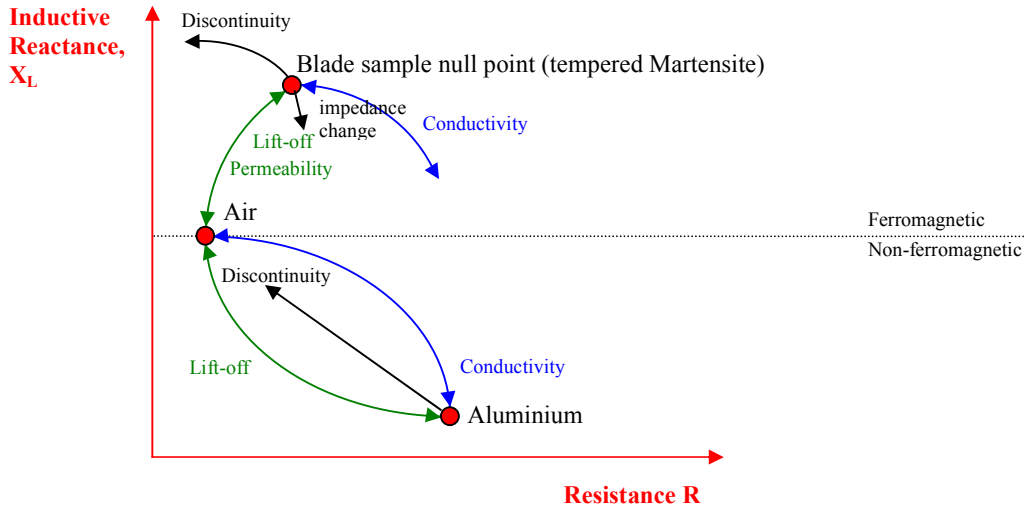

Figure 6.25 – Diagrammatic view of impedance change due to embrittled region at 500kHz

Obviously the operation is taking place in the ferromagnetic part of the impedance plane where magnetic permeability has some influence and relative magnetic permeability is

above unity. To improve the inspection, it was necessary to understand the magnitude of the effect of permeability.

6.7.1. Experiment ECT 6

Equipment: *Lab-based PEC inspection system from Newcastle University with circular coil probe: 18mm diameter, 5.5mm height, 500 turns, ferrite core.*

Reference: *Air.*

Key parameters: *Excitation repetition frequency: 500 Hz.*

Samples: F-H.

Pulsed eddy current measurements were made by M. Morozov at Newcastle University on the tempered martensite and non-tempered martensite regions of Samples F, G & H. The following parameters were measured to assess the relative influence of conductivity and magnetic permeability in the samples.

Response:

- *Difference signal $\Delta B_Z = B_Z - B_{AIR}$ dependent on magnetic permeability and conductivity;*
- *Normalised difference signal $\Delta B_Z^{NORM} = B_Z/max(B_Z) - B_{AIR}/max(B_{AIR})$ mainly proportional to the electric conductivity of the material, where B_{AIR} is the reference signal obtained in air;*

Features:

- *Max value of ΔB_Z reflecting magnetic permeability and conductivity*
- *Peak value of ΔB_Z^{NORM} mainly proportional to the electric conductivity of the material.*

For each sample, region 2 is the tempered martensite region and region 1 is the non-

tempered martensite region. In Figure 6.26 the B1 prefix refers to Sample F, B2 refers to Sample G and B3 refers to Sample H.

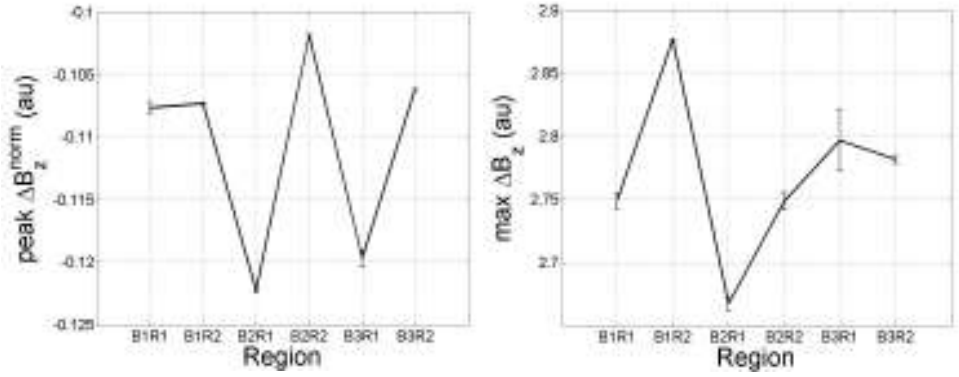

a) b)

Figure 6.26 - a) PEC Peak value of normalised difference signal ΔB_Z^{NORM}, b) Max value of absolute difference signal ΔB_Z

Generally speaking Figure 6.26 a) is representative of the conductivity of the component and Figure 6.26 b) is representative of the magnetic permeability. The further the B_z peak is from B_{air} the higher the conductivity, since the peak value is normalised to air a larger negative ΔB_z value indicates a higher electrical conductivity. From this is appears that in all cases the conductivity increases from the tempered regions to the non-tempered regions, which is in agreement with all previous theory and experiments. On B1 (Sample F) the increase appears to be small, however the peak value of ΔB_Z^{NORM} for B1R1 is unusually high compared to the other samples.

The trend shown in Figure 6.26 b) is representative of the relative magnetic permeability. In this instance there appears to be no consistent trend to the data, suggesting that the permeability may increase or decrease with microstructural change from tempered to non-tempered martensite. There are potential implications from this. Reverting back to the impedance plane work from Figure 5.15; if the relative magnetic

permeability is below 100, then the permeability could dominate over changes in conductivity in the 1-4% IACS range. The magnitude of the relative magnetic permeability change is critical to determining the degree of influence of any variation on the impedance, however it is not practical to measure it on these discrete regions. Consequently, it may be necessary to reduce the effects of permeability by magnetic saturation in order to leave the more consistent conductivity variations as the dominant effect.

6.7.2. Experiment ECT 7

Equipment: *Lab-based DCPD measurement system from Imperial College using 4-point DCPD probe.*

Samples: *F-H*.

In order to quantify the magnitude of the change in conductivity, DCPD was used to measure the conductivity of tempered and non-tempered martensite regions of blade Sample F. The methodology and equipment for this was the same as used for measuring the conductivity of the reference samples in Section 5.1.2. The measured values for each microstructural phase are shown in Table 6.4.

Material	Measured Conductivity (MS/m)	Maximum variation (MS/m)
Tempered Martensite	1.5	+/- 0.75
Untempered Martensite	2.0	+/- 0.75

Table 6.4 – Conductivity values of martensitic phases measured with DCPD

There is a large error band on each measurement due to the DCPD measurements being taken across an area of non-constant thickness. Unfortunately this can only be overcome by cutting the samples which would render them useless for method verification. This

means the values obtained are not suitable for accurate modelling of the situation, however it does give an indication of the region of a conductivity curve that is of most interest: <3MS/m. Despite the large error bands this data supports the argument that the phase change from tempered to untempered martensite does increase the localised conductivity of the turbine blade.

6.7.3. Experiment ECT 8

Equipment: *Zetec MS5800 with ECP2 probe.*

Reference: *Nulled on each blade away from tip end, phase rotated so lift-off is centre to left on impedance plane.*

Key parameters: *500kHz at 3V input with 38dB gain.*

Samples: *F, G, H & P.*

Note: ECP2 probe replaced ECP1 probe, due to damage being suffered by the former. Coils are identical on both probes so change of probe should not affect continuity of results.

In order to remove any influence from permeability a strong permanent magnet (0.34 Tesla) was placed on the underside of the test sample (Sample F, initially). By magnetically saturating the material under test the relative permeability is reduced to unity, the same for non-ferromagnetic materials. As per ECT 2 the probe was nulled on a non-embrittled region which was magnetically saturated. With the lift-off set centre to left on the screen the probe was passed over the embrittled area (also magnetically saturated) and the impedance change shown in Figure 6.27 was observed.

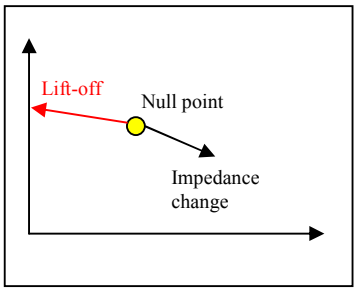

Figure 6.27 – Diagrammatic view of impedance change observed with magnetically saturated embrittled region at 500kHz

Superimposing this onto the full impedance plane, Figure 6.28 shows that, in the absence of permeability effects, there is a change in impedance consistent with a conductivity increase (Figure 6.28).

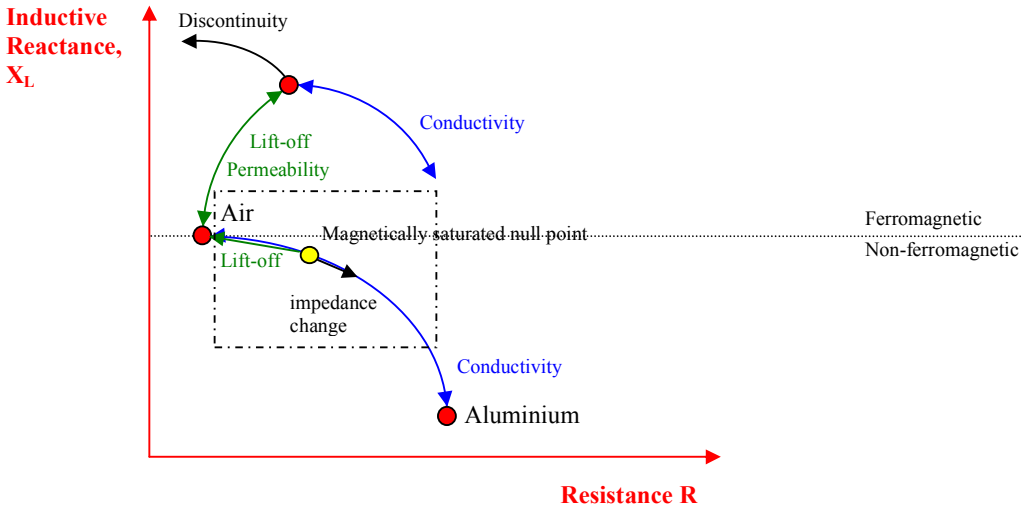

Figure 6.28 –Diagrammatic view of impedance change due to magnetically saturated embrittled region at 500kHz

The test was repeated for Samples G, H and P; the magnitude of the normalised complex voltage for each blade is recorded in Table 6.5.

Sample	Signal Magnitude (V)
F	0.51
G	0.32
H	0.35
P	0.63

Table 6.5 – Normalised Voltage magnitude change between tempered and non-tempered regions

Magnetically saturating the test piece would nullify the permeability-related inconsistencies exposed in ECT 6. With the relative magnetic permeability reduced to unity, the voltage magnitudes are still large enough to be detected by the eddy current system but are in-plane with the lift-off. If the lift-off could be negated, practical considerations* meant that magnetically saturating each blade during inspection would not be appropriate, however the important conclusion from this test is that the signal change due to conductivity is significant enough by itself to be detectable.

* A permanent magnet large enough to saturate the blade fully would be too big to fit into an eddy current array and placing a magnet directly onto the blade would not produce a uniform field across all coils in the probe.

6.7.4. Experiment ECT 9

Equipment: *Zetec MS5800 with ECP3 probe.*

Reference: *Nulled on each blade away from tip end, phase rotated so lift-off is centre to left on impedance plane.*

Key parameters: 51Ω *@125 kHz at 3V input with 38dB gain.*

Samples: *F, G, H & P.*

ECP3 Coil: 5mm OD, 0.1mm ID, 2mm high, 250 turns.

A third coil array was designed, this time incorporating magnets to reduce the effective permeability. Coil frequency was kept low to minimise frequency dependent permeability fluctuations and to operate in the higher sensitivity region of the impedance plane for low conductivity, medium permeability metals. A frequency range of 50kHz to 300kHz was deemed appropriate and further details on the frequency choice are given

in ECT10. The design was a trade-off between coil size and magnet strength. It was decided that the maximum coil size to allow for sufficient resolution and more importantly, to maintain good contact with the varying contours of the blade, was 5mm diameter. The eddy current array had the permanent magnets housed behind the coils. This was a much weaker magnet (0.13 Tesla) than that used in experiment ECT 8, consequently the material was not magnetically saturated, though the relative permeability was reduced. Theoretically, this will reduce the magnitude of the permeability influenced fluctuations. Figure 6.29 shows the change in coil impedance relative to lift-off experienced as the coil was passed over the embrittled area. The magnitude of the vertical drop in complex voltage was 0.50 V.

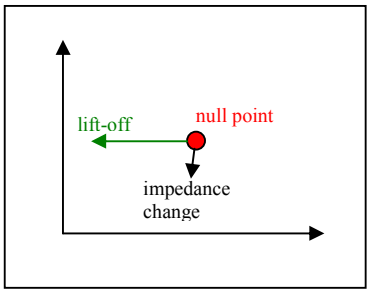

Figure 6.29 – Diagrammatic view of impedance change observed with partially magnetised coil over embrittled region

Viewing this change on the full impedance plane (Figure 6.30) suggests that there is still a strong change due to conductivity and a diminished change due to permeability.

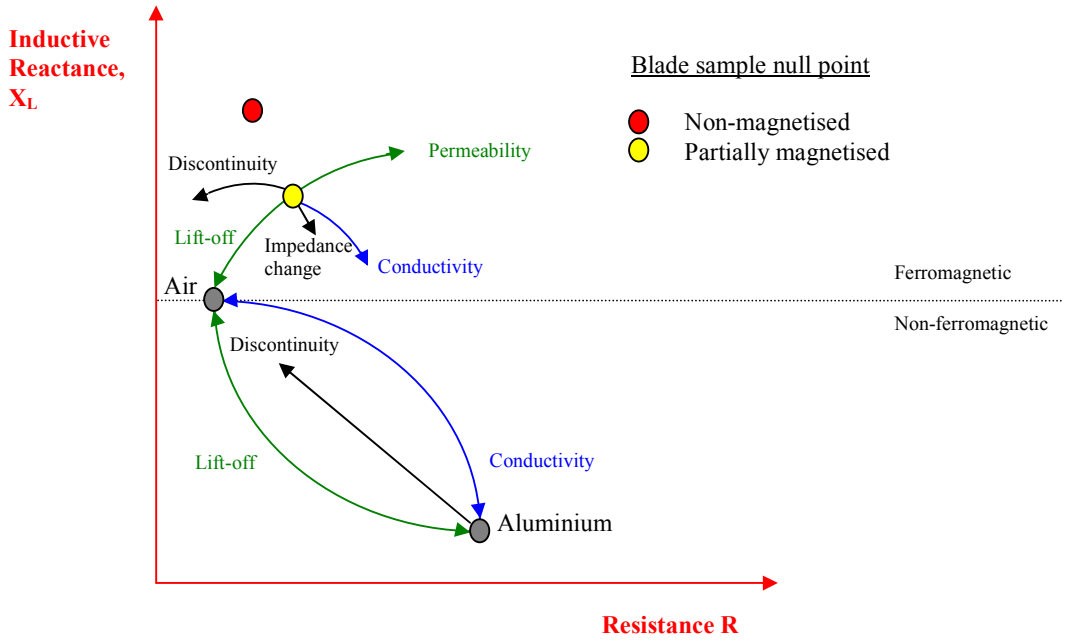

Figure 6.30 – Diagrammatic view of impedance change of partially magnetised coil due to embrittled region

Figure 6.31 shows the impedance plane data from the test with the impedance lift-off curves for eight reference materials included. It can be seen that the magnetised coils cause a significant reduction in the inductive reactance components for the ferromagnetic materials, indicating a reduction in the relative magnetic permeability.

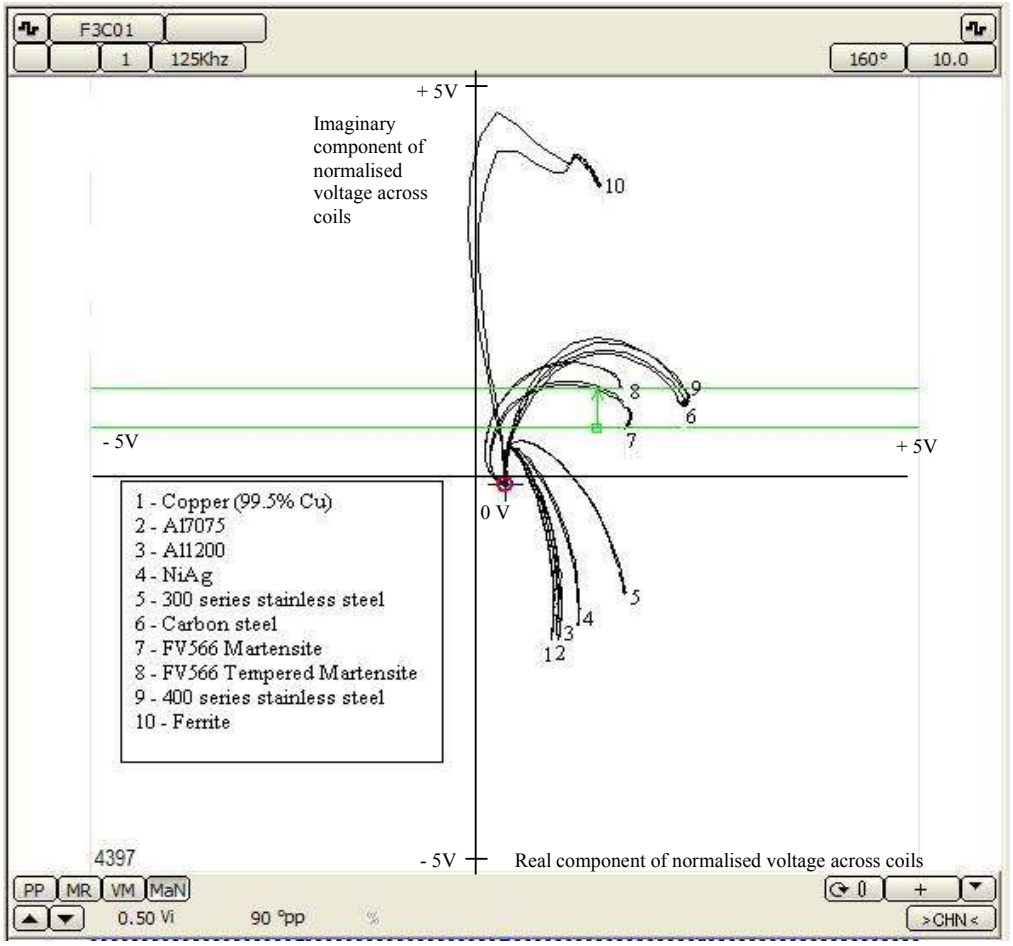

Figure 6.31 – Measured voltage (follows same trend as impedance) plane showing lift-off curves of partially magnetised coil due to embrittled region and reference materials. Green lines show extent of vertical voltage component change between tempered and non-tempered martensitic samples

From the results above it would appear that there is a strong, discernable signal change between the eddy current test response to the martensitic 12Cr and tempered martensitic 12Cr, when the effects of magnetic permeability are minimised. The rapidly changing orientation of the lift-off curve is potentially problematic, though this will be mostly eliminated since the magnets will cause the flexible array to conform to the blade surface tightly. Control of the impedance plane rotation should further negate this problem. Consequently, it would appear that this is a suitable way of testing the blades provided it can be proven to be reliable and repeatable.

6.7.5. Experiment ECT 10

Equipment: *Zetec MS5800 with ECP3 probe.*

Reference: *Nulled on each blade away from tip end, phase rotated so phase-transformation signal is vertically downwards on impedance plane. Reference cursor on C-scan set at 30mm along scan.*

Key parameters: *50-300 kHz at 3V input with 38dB gain.*

Samples: *P.*

The choice of frequency for the test is a vital consideration. Recalling Figure 5.15, it is possible to roughly highlight the area of interest on the impedance plane. From ECT 7, it is known that the approximate conductivity range is 0.75-2.75MS/m (1.3 – 4.75%IACS). The relative permeability with the magnet in place appears to be quite low from the evidence of ECT 9, most likely $\mu_r < 10$. Figure 6.32 below shows a similar display to the figure from Chapter 5, but using the ECP3 coil parameters and displaying the impedance plane at 50, 100, 200 and 300 kHz, with the area of interest marked by a red circle on each plot. It is known that reducing the frequency will tend to concentrate the low-conductivity regions near the bottom end of the conductivity curve, i.e. nearer to air and this is evident in the impedance plots. Thus it is likely that sensitivity can be improved by operating at a lower frequency, though experimental data is required to find the absolute optimum, as although the relative difference appears to improve with reducing frequency, the coil impedance and thus the overall amplitude will reduce, so a balance must be sought.

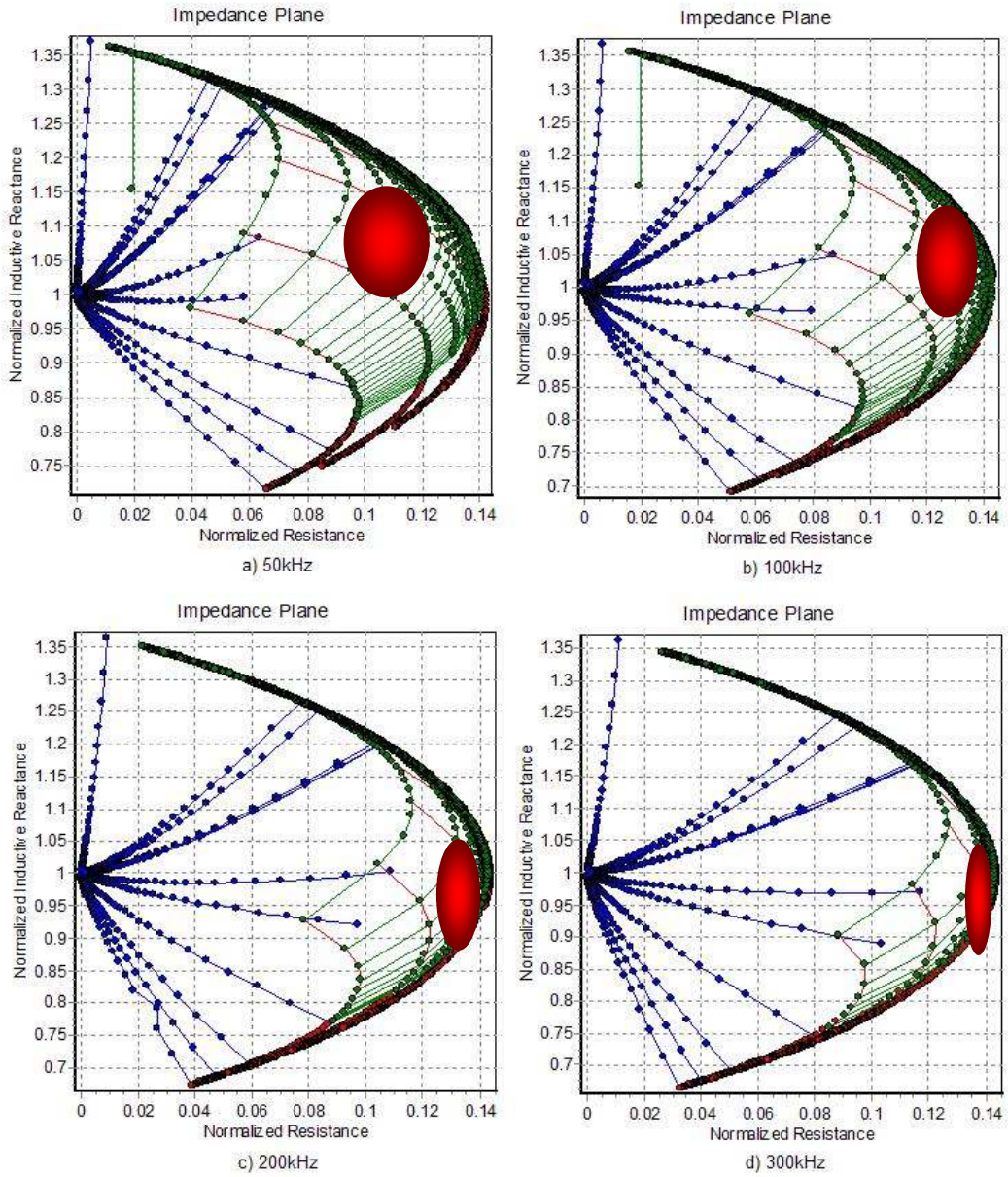

Figure 6.32 – Impedance planes produced in Teddy 1.2 showing area of interest (red circle) at a) 50kHz, b) 100kHz, c) 200kHz and d) 300 KHz operational frequency. Red lines show conductivity curves, green lines show relative permeability curves and blue lines show lift-off curves of 12 reference materials as specified in Table 5.2.

The eddy current array using magnets at the centre of the coil has an operating range of 50 – 300 kHz, providing a range of frequencies to establish sensitivity trends below 300

kHz. An encoded scan of Sample P, starting from the blade tip and running 250mm, was recorded at 25 kHz intervals over the full operational range of the probe. The C-scan reference cursor was set to 30mm and a normalised voltage reading was taken at 100mm along the blade, a distance of 1 mm in from the blade edge. Thus the recorded voltage was the vertical normalised voltage shift from point (30,1) to point (100,1) which are known tempered and non-tempered martensite regions respectively. The recorded voltage shifts for each frequency are shown below in Table 6.6.

Operating Frequency (kHz)	Normalised Voltage Displacement (V)
50	0.29
75	0.40
100	0.47
125	0.40
150	0.47
175	0.53
200	0.47
225	0.49
250	0.43
275	0.38
300	0.34

Table 6.6 – Normalised voltage displacements with varying frequency using probe ECP3 on phase transformed regions of Sample P.

There are a few fluctuations in the data but in general, the best response is at 175 kHz and the worst response is at the extremes of the frequency range. The coils will operate

most efficiently where the coil impedance matches that of the connections allowing maximum energy transfer, as the frequency changes from the centre frequency the impedance will change slightly and the coil response will thus be reduced.

6.7.6. Experiment ECT 11

Equipment: *Lab-based PEC inspection system operated in time-harmonic mode from Newcastle University with circular coil probe: 18mm diameter, 5.5mm height, 500 turns, ferrite core.*

Reference: *Air.*

Key parameters: *Excitation frequency: 100, 500 & 1000 Hz.*

Samples: F-H.

In ECT 10, it was determined that the best operational frequency for this test is 175 kHz, using probe ECP3. Assuming that the relative magnetic permeability is reduced to approximately 5 and the conductivity is approximately 2MS/m, the depth of penetration for this test is just 0.38mm according to Equation 3.1.7. To observe whether there is a variation in the trends observed in eddy current response with depth of penetration, some low frequency measurements were made. These use a large PEC coil operated in time-harmonic mode, which is too large to be practical for scanning the blades but was sufficient for spot measurements on a tempered and non-tempered region of samples F, G & H. The probe was operated at 100 Hz, 500 Hz and 1000 Hz, which assuming a relative magnetic permeability in the region of 50, would penetrate to a depth of 5mm, 2.25mm and 1.6mm respectively. The absolute value of the time-harmonic eddy current response is shown in Figure 6.33, showing a consistent trend across all four frequencies for Sample F (B1), but inconsistencies for Samples G and H (B2 & B3). At the least

penetrating frequency, 1000 Hz, the trend between the tempered martensite (R2s) and the martensite (R1s) is consistent with the largest response coming from all the R2s. The difference is least significant for Sample H (B3) and it is this sample that shows the most frequency-dependent variation.

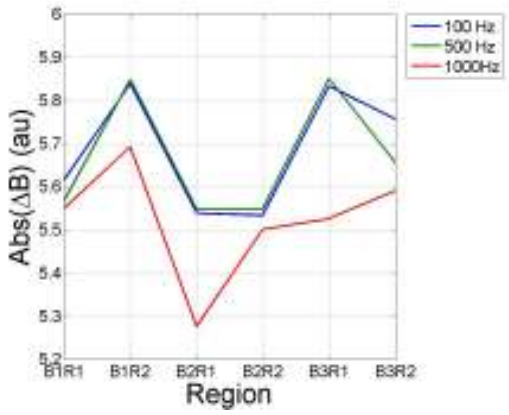

Figure 6.33 – Time harmonic eddy current response to samples F, G and H at low frequencies

It would seem likely that the phase transformation in Sample F goes deeper than for Sample G and Sample H. Since the transformation is likely to be greatest at the surface due to the larger thermal transients experienced, it would seem appropriate to keep the frequency in the kHz range to concentrate the field in the appropriate area.

6.8. Optimum Design

From the results of the experiments in section 7 of this chapter, the following test parameters were derived as being the most appropriate:

- Use of fully flexible array ECP3.
- Use of magnetically-cored coils to reduce influence of magnetic permeability variations.
- Operational frequency of 175 kHz.
- Impedance plane phase should be rotated so that impedance change associated with material phase transformation is vertically downwards.

- Martensitic regions will produce a normalised voltage shift relative to tempered martensitic regions in excess of -0.3V. This should be the gate settings for the C-scan.

Having established that these parameters give the most sensitive inspection, the next stage was to quantify how repeatable the technique was and whether the achieved level was acceptable. Additionally, the spatial resolution of the test using this array needed to be quantified. Finally, field trials were carried out to fine-tune the inspection technique and to produce a working inspection procedure.

6.8.1. Experiment ECT 12

Equipment: *Zetec MS5800 with ECP3 probe.*

Reference: *Nulled on each blade away from tip end, phase rotated so phase-transformation signal is vertically downwards on impedance plane. Reference cursor on C-scan set at 30mm along scan.*

Key parameters: *125, 175 & 225 kHz at 3V input with 38dB gain.*

Samples: *F-P.*

Repeatability is quantified in the same way as it was in experiment ECT 5, taking five scans of each of the sample blades. Encoded scans were made along the blade, from 250mm down the blade up to the blade tip. Using a reference cursor at a constant position (30mm along x-axis), vertical normalised voltage readings were taken at sixteen set positions on the blade as shown in Figure 6.34.

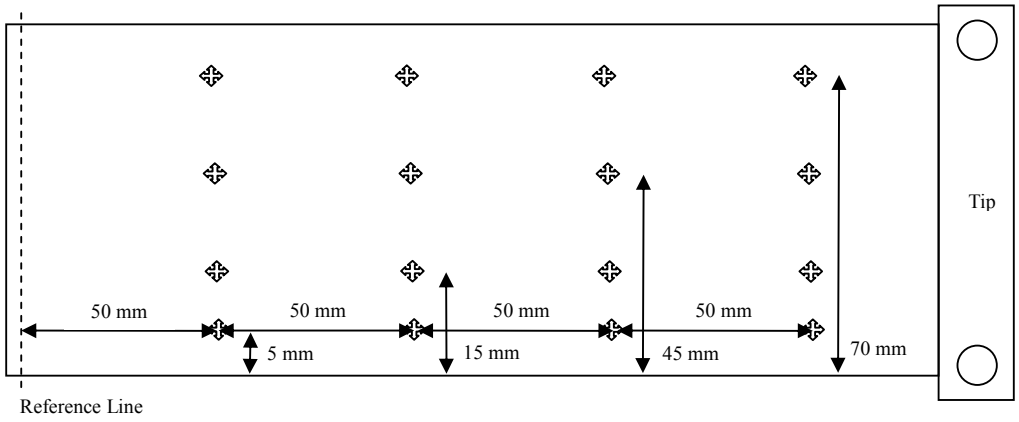

Figure 6.34 – Schematic showing position of repeatability readings taken.

The positions across the blade (y-direction) were selected so that the first is right in the middle of the location of most of the martensitic regions, the second is on the boundary of most martensitic region, the third is roughly half way across the blade and the last is near the far side of the blade.

Figures 6.35 – 6.39 show examples of the levels of consistency achieved between the samples at 175 kHz.

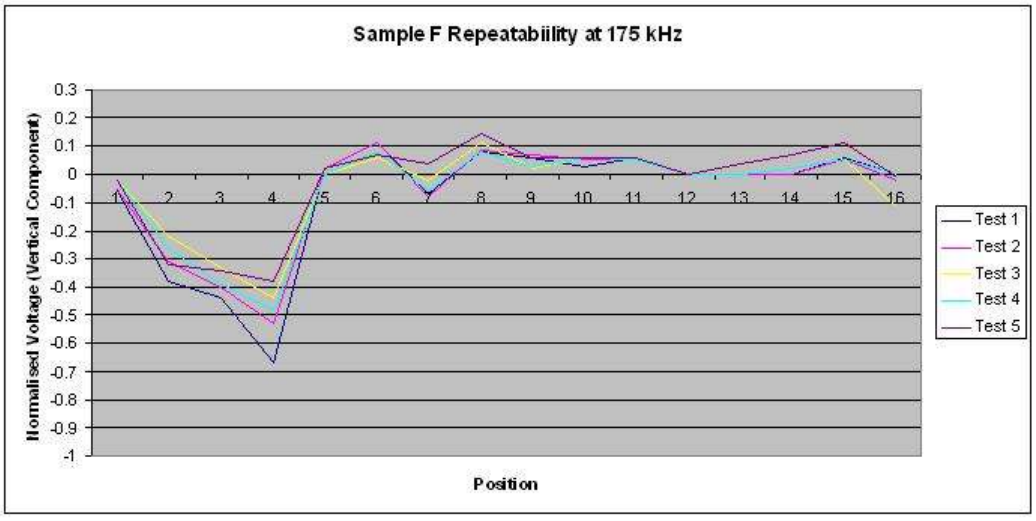

Figure 6.35 – Repeatability of scans on Sample F at 175 kHz

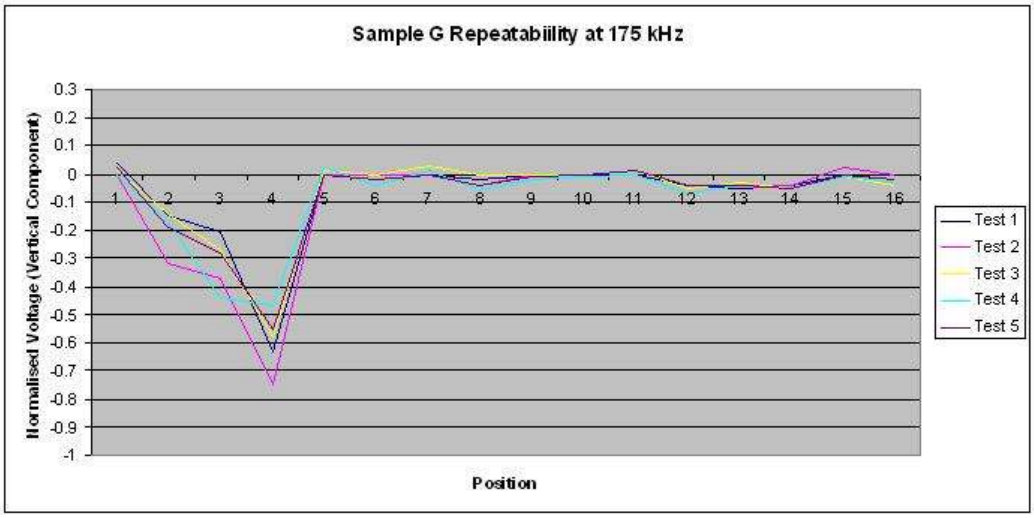

Figure 6.36 – Repeatability of scans on Sample G at 175 kHz

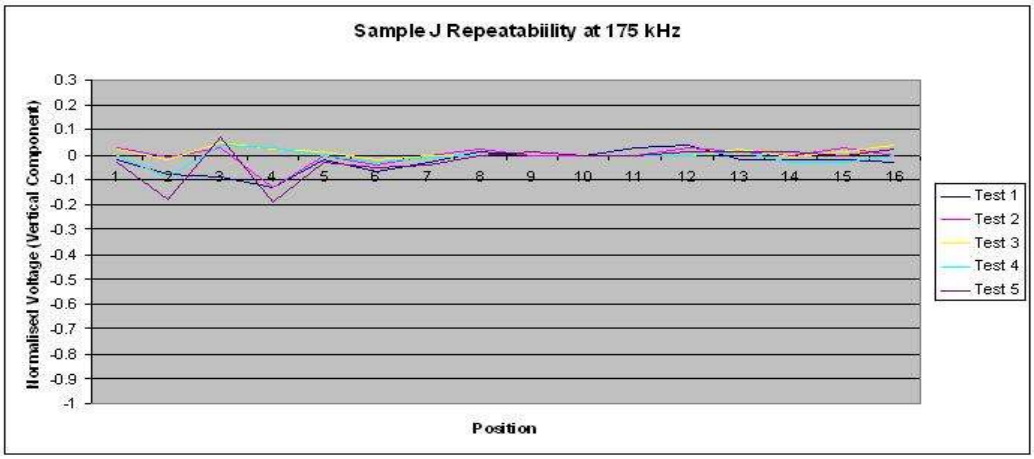

Figure 6.37 – Repeatability of scans on Sample J at 175 kHz

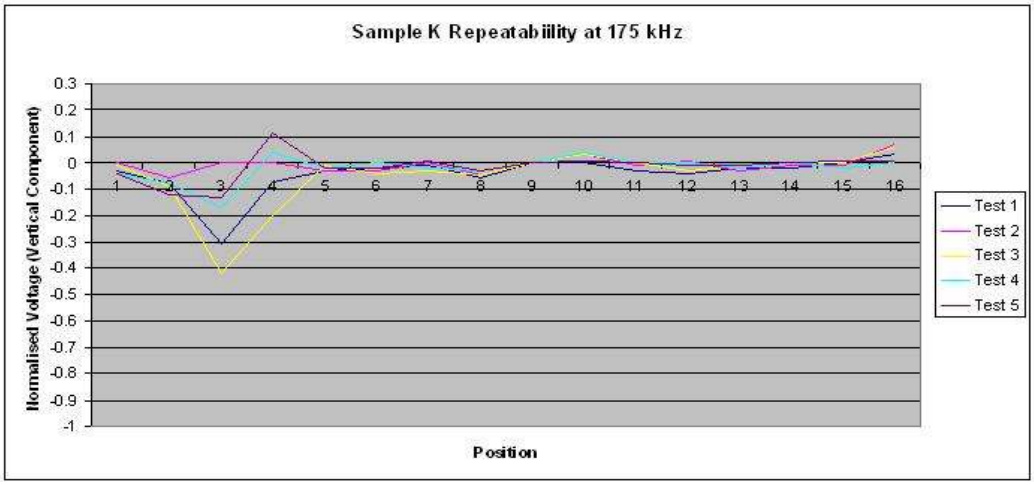

Figure 6.38 – Repeatability of scans on Sample K at 175 kHz

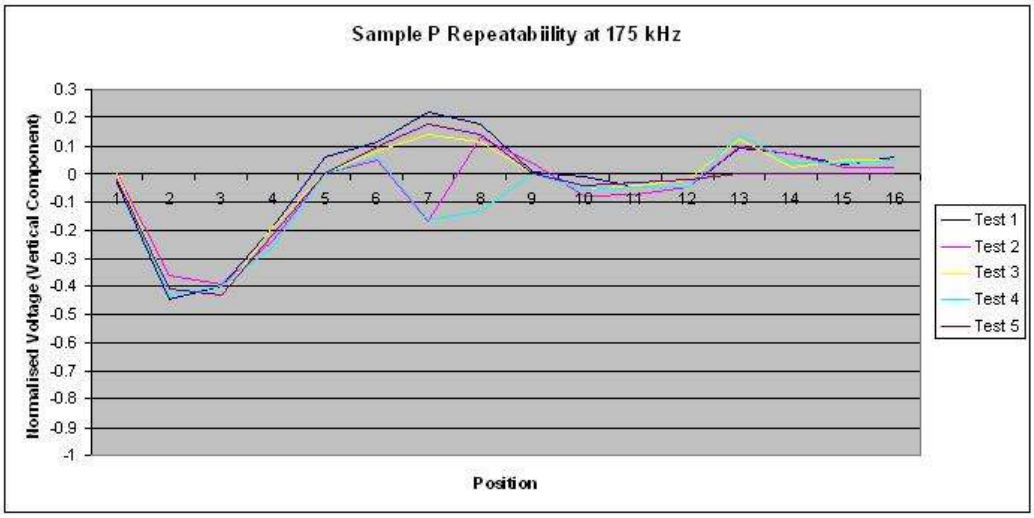

Figure 6.39 – Repeatability of scans on Sample P at 175 kHz

At first glance the repeatability looks good and comparable to that achieved with ECP2 in experiment ECT 5. Again there are a few areas of notable variation, which can be attributed to small variations in coil positioning leading to measurement of different electromagnetic properties and/or lift-off variations. The average standard deviation over all the samples is in fact 0.0285 V, which is similar, but slightly higher than the best achieved in ECT 5. It is however, important to consider that the overall range of values is 0.97V, so when the standard deviation is expressed as a percentage of the total range, it is just 2.93% compared to 4.00% which was the best achieved with probe ECP2.

As is illustrated by Figures 6.40 – 6.42, there are far fewer spurious indications observed, compared to the results of ECT 5 and the system can be set so that the C-scan hides much of the noise in local material fluctuations. In the figures the gate is set to -0.3 V and anything below that threshold is a solid blue colour on the C-scan. Anything highlighted in this manner will either be phase transformed and worthy of further investigation or will represent an edge effect as the coils crosses the edge of the blade. This edge-effect is almost impossible to eliminate but is identifiable by performing two

scan passes on each blade, with the probe edge following the leading edge on the first pass and following the trailing edge on the second. By doing this it can be ensured that no edge-effect will occur on both scans, but any other features that do appear on both are likely to be phase transformations.

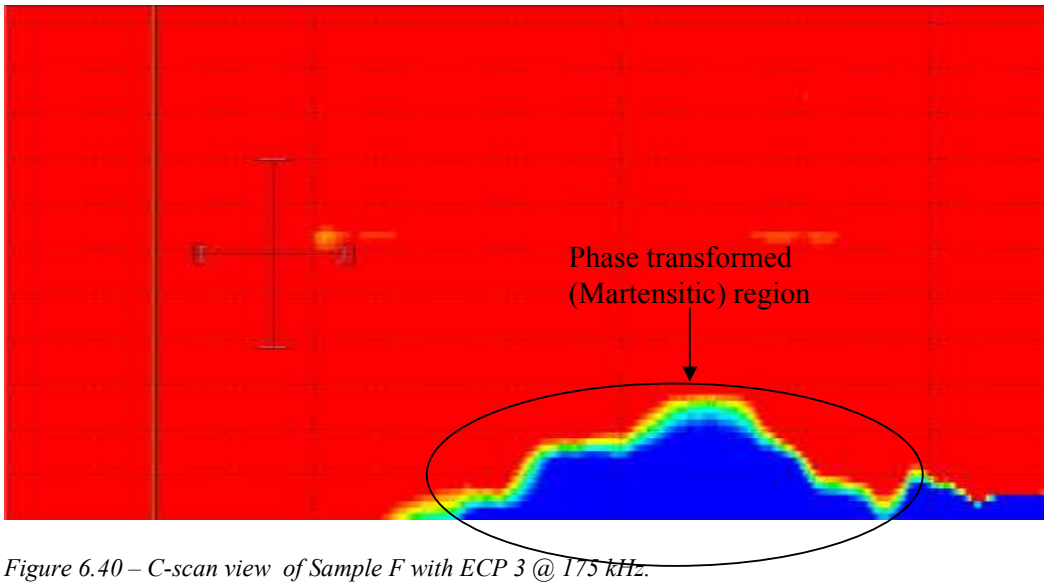

Figure 6.40 – C-scan view of Sample F with ECP 3 @ 175 kHz.

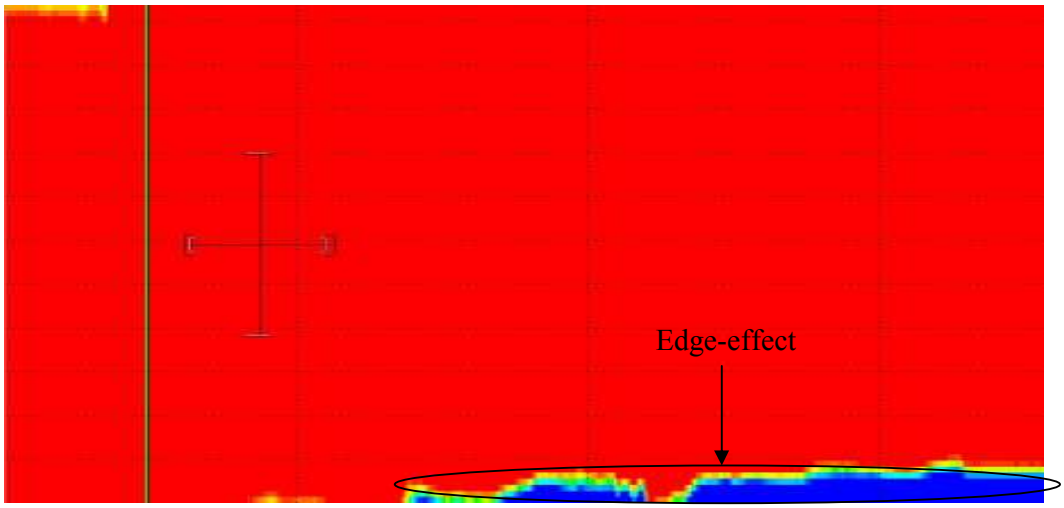

Figure 6.41 – C-scan view of Sample I with ECP 3 @ 175 kHz

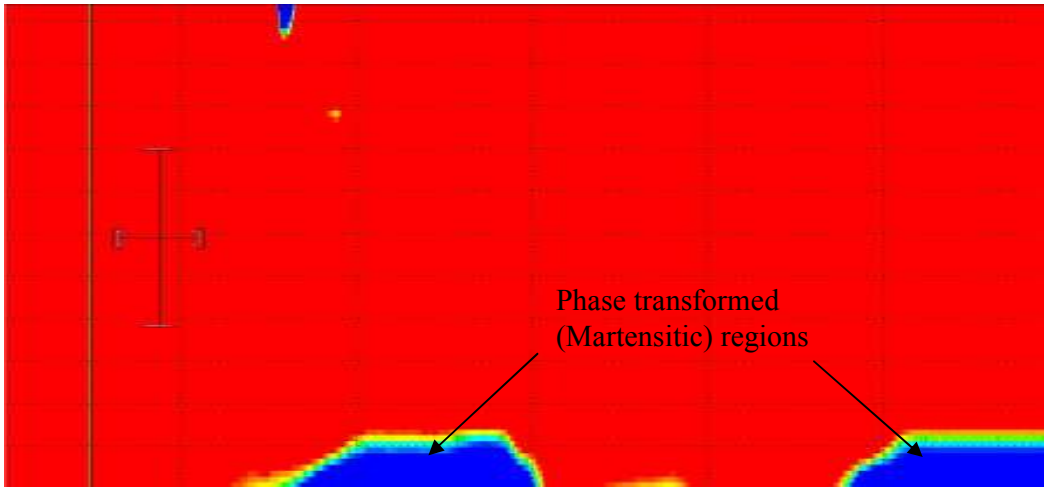

Figure 6.42 – C-scan view of Sample P with ECP 3 @ 175 kHz

6.8.2. Experiment ECT 13

Equipment: *Zetec MS5800 with ECP3 probe.*

Reference: *Nulled on each blade away from tip end, phase rotated so phase-transformation signal is vertically downwards on impedance plane. Reference cursor on C-scan set at 30mm along scan.*

Key parameters: *175 kHz at 3V input with 38dB gain.*

Samples: *K.*

The spatial resolution of the probe is determined by the probe geometric features. Probe ECP 3 consists of twenty-two transmit-receive coils, which are 5 mm in diameter with a 9 mm centre-to-centre off-set. There are two rows of eleven coils, thus each row can operate ten pairs of transmit-receive channels. The two rows are off-set by 4.5 mm, so this effectively halves the scanning gap between the channels to 4.5 mm across the blade. Along the blade, the resolution is again determined by the coil diameter, so in theory this will be 5 mm.

To establish whether these assumptions are correct and to determine the minimum detectable defect size, a scan was set up using a homogenous blade sample (Sample K) and some 2 & 5 mm wide strips of aluminium tape as illustrated in Figure 6.43. The aluminium is significantly different in terms of electromagnetic properties, so should be easily identifiable, a 2 mm strip is used as it is significantly smaller than the probe diameter. Figure 6.44 shows the resulting C-scan as the probe is passed over the horizontally and vertically oriented tape. In both orientations the detected area appears to be almost 10 mm wide, despite the strips actually being much smaller, so the technique will tend to oversize in steps of 5 mm with a resolution of 5 mm x 5 mm. The minimum detectable defect size is approximately 2 mm x 2 mm, which manifests itself as a 5 mm wide indication. This indication is only just detectable, however it is worth noting that the normalised voltage response from the aluminium is larger than the martensitic phase transformation; despite this, the technique should comfortably detect areas of 5 mm x 5 mm. This is superior to the 20 mm x 10 mm areas which can potentially be missed by the mechanical hardness testing measurement grid system.

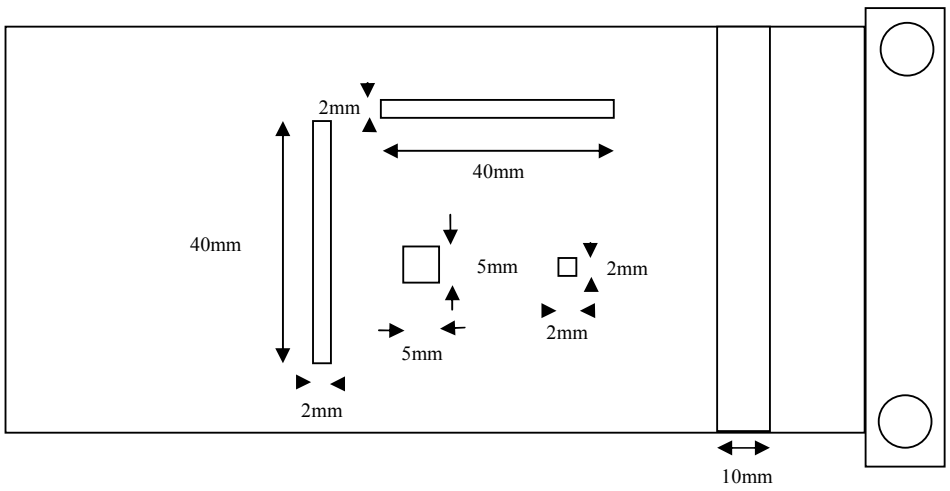

Figure 6.43 – Schematic showing positions and dimensions of aluminium tape on Sample K.

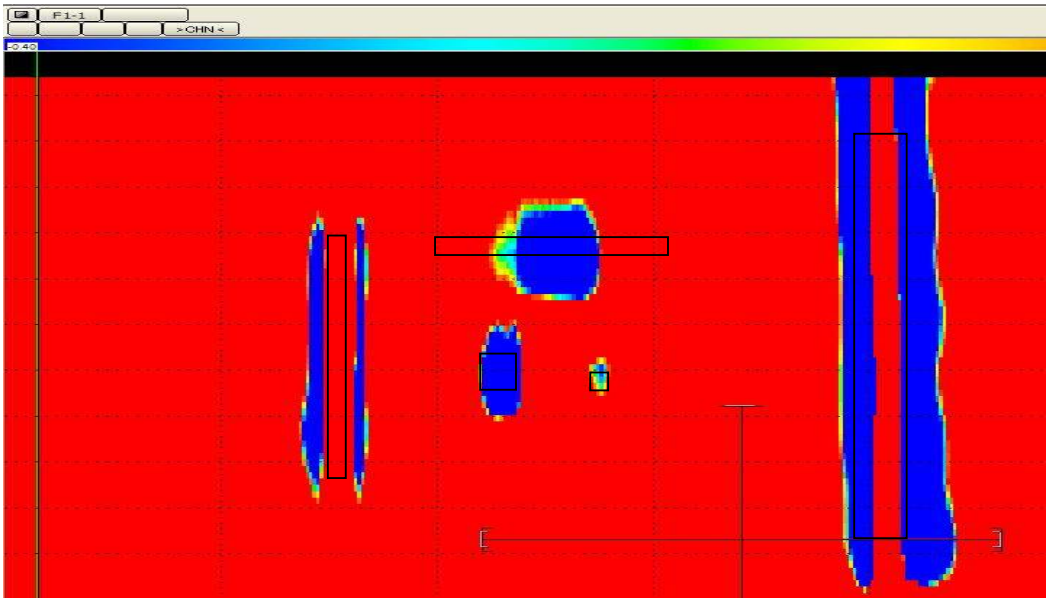

Figure 6.44 – C-scan showing eddy current response to aluminium strips on Sample K.

6.8.3. Experiment ECT 14

Equipment: *Zetec MS5800 with ECP3 probe.*

Reference: *Nulled on each blade away from tip end, phase rotated so phase-transformation signal is vertically downwards on impedance plane.*

Key parameters: *175 kHz at 3V input with 38dB gain.*

Samples: *Tilbury LP rotors.*

With the sensitivity, repeatability and spatial resolution all quantified, the final test was a full field test on a rotor due for overhaul. The rotors contained a total of 180 FV566 last-stage blades, which were tested on the inside (concave side) and the outside (convex side) of form. The scanning patterns employed are shown below in Figure 6.45. On the inside of form there are two scan passes, from 250mm down the blade towards the blade tip. One pass keeps the probe in line with the trailing edge of the blade, the second keeps the probe in line with the leading edge. This ensures that lift-off signals from any specific part of the blade are only visible on one of the two scans, whereas any

significant indications should be visible on both scans.

(inside of form)

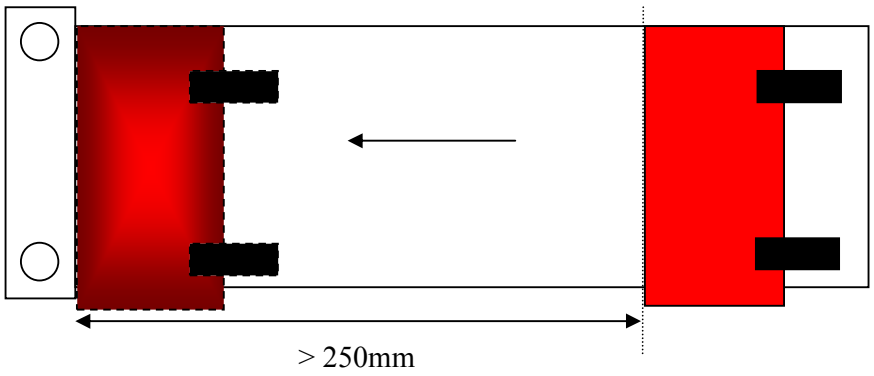

Figure 6.45a – Scan pattern for inside of form, in line with leading edge

(inside of form)

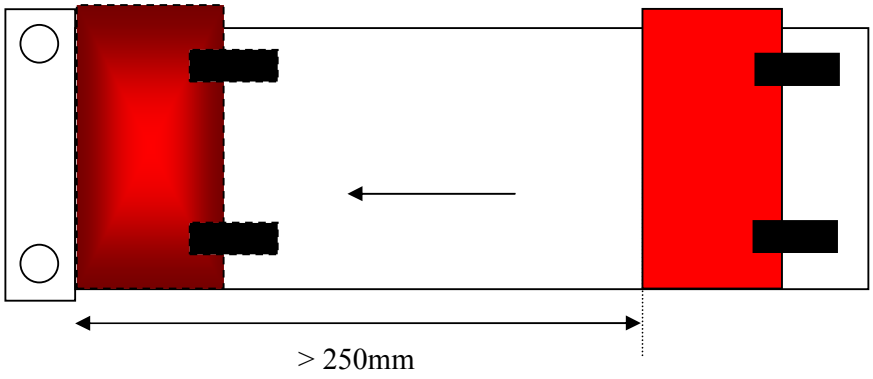

Figure 6.45b – Scan pattern for inside of form, in line with trailing edge

(back of form)

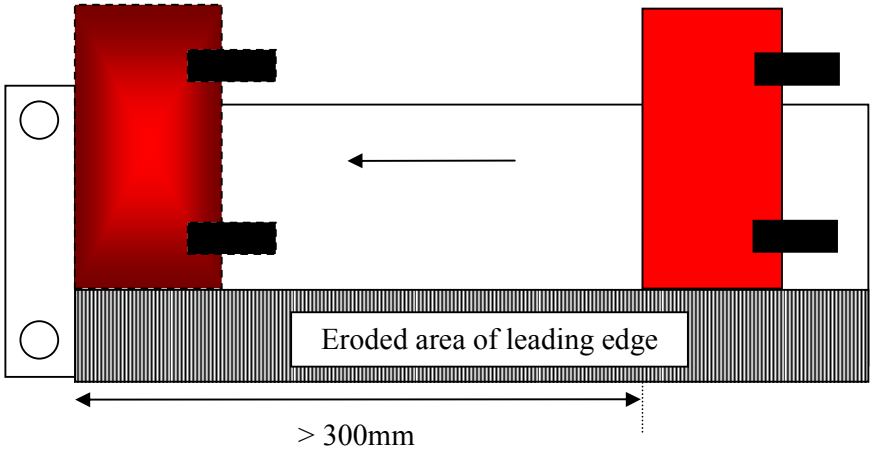

Figure 6.45c – Scan pattern for outside of form, in line with leading edge

A total of 20 blades were subsequently checked by mechanical hardness testing using a GE IT TIV portable hardness tester. This included 13 blades which had been flagged for investigation by the eddy current technique plus another 7 chosen at random. The blades tested had a geometric modification whereby an arc of material was removed form the trailing edge, which caused an additional area of edge-effect on some of the scans. Figure 6.46 shows a C-scan of a blade with this geometric modification shown on an overlay. Figures 6.47 and 6.48 show C-scans of suspected areas of non-tempered martensite, which were subsequently verified by mechanical hardness testing.

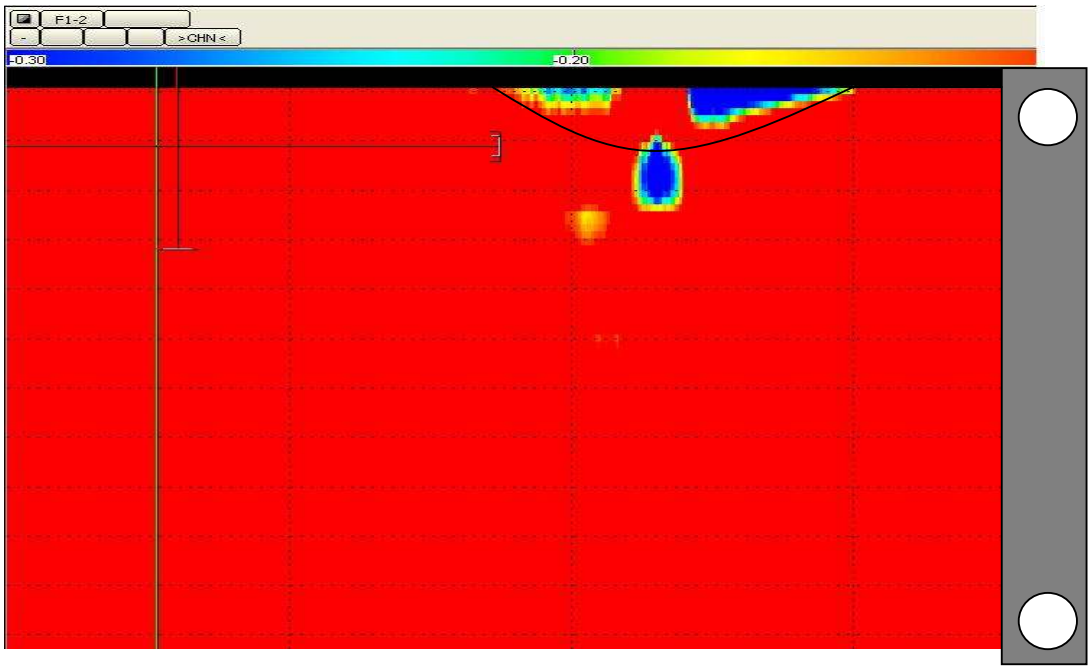

Figure 6.46 – C-scan showing eddy current response from geometric modification

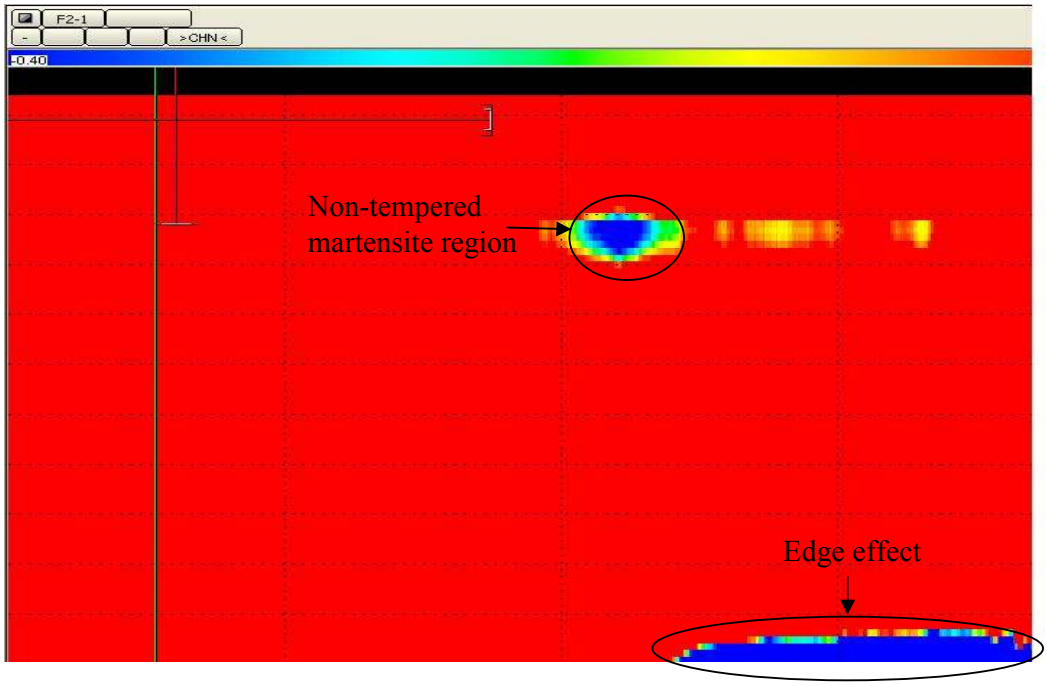

Figure 6.47 – C-scan showing localised region of non-tempered martensite

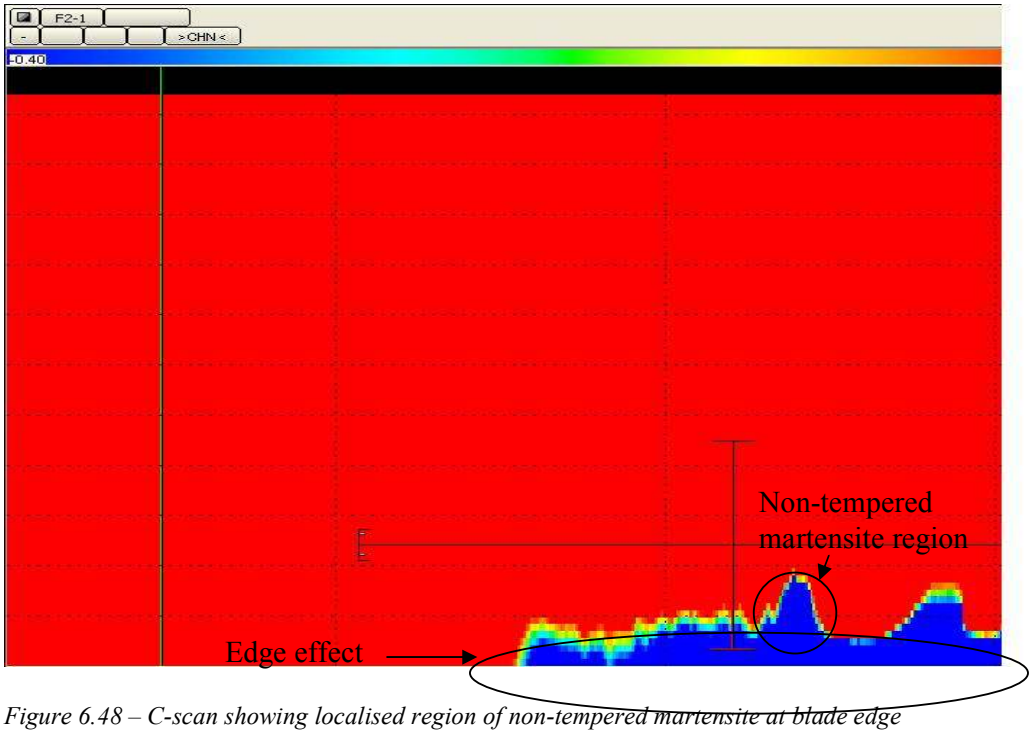

Figure 6.48 – C-scan showing localised region of non-tempered martensite at blade edge

Of the 20 blades validated with mechanical hardness testing, 7 were not flagged by eddy current and were successfully verified by mechanical hardness testing, 6 were flagged up by the eddy current and were subsequently found to have hardness above the threshold

value, 5 were flagged up by eddy current and were found to be within 10Hv of the threshold and two were flagged and found to contain no hardened areas at all, this data is summarised in Table 6.7.

	Number of Blades	Percent of Total
Non-flagged blades below threshold	7	35%
Flagged blades above threshold	6	30%
Flagged blades < 10Hv below threshold	5	25%
Flagged blades > 10Hv below threshold	2	10%

Table 6.7 – Summary of results of site trial validation

In terms of accuracy of results, Table 6.7 shows that 65% of the results were in full agreement, 25% were on the margin of the threshold and 10% of the results were spurious. No hardened areas were found that were not identified as non-tempered martensite by the eddy current technique.

Given the inaccuracies inherent in portable mechanical hardness testing and that the threshold of 390Hv is an approximation of the true hardness where a martensitic transformation occurs, it is reasonable to assume that it is better to detect those areas where the hardness is just below the threshold than not to detect them at all. Taking that into consideration there is only a 10% rejection rate on these results, which should reduce with increased operator experience. This is however, a very limited sample, so no firm conclusions on the reliability can realistically be drawn until more rotors become available for test. Around 200 samples, from no fewer than four rotors, should be a sufficient sample set for confidence in the technique.

6.9. Conclusions

The experiments in the preceding chapter have helped develop a working solution capable of detecting the material phase transformation from tempered to non-tempered martensite associated with an increase in blade material hardness. This technique reduces the time required to carry out an inspection from 5 days to 1.5 days, which is a huge effiency improvement. Whilst further site trials are required to increase confidence in the technique, it appears that using the normalised voltage response of eddy current arrays it is possible to produce C-scans corresponding to the phase change in 12% Cr last-stage turbine blades. The technique now has been added to RWE npower Inspection Management's list of specialist inspections with an approved procedure/technique sheet [125].

The following conclusions from the experimental work summarise the technique's key parameters and technical capabilities. There is a material phase transformation detectable by the eddy current method that is strongest at the component surface. The electrical conductivity change associated with this material phase transformation is approximately 0.5 MS/m in the range 0.75-2.75 MS/m. The electrical conductivity change is accompanied by a change in magnetic permeability, however this latter change is variable in its magnitude and direction.

Using magnetically-backed coils the effects of magnetic permeability can be minimised, leaving conductivity as the dominant effect. When incorporated into a fully-flexible array, the magnetic coils keep the probe conformed to the blade profile, practically eliminating lift-off. The optimum operating frequency is 175kHz, giving a standard

depth of penetration of < 0.85 mm (based on worst case where $\mu_r = 1$).

When carrying out the inspection the complex impedance plane phase is rotated so that it gives an impedance/voltage response vertically downward when going from a tempered to non-tempered region of martensite on FV566 material blades. The response to non-tempered martensite region is in excess of 0.3 V in the negative direction. Consequently C-scan gates are set so that all normalised voltage responses above -0.3 V are red (acceptable) and all responses below -0.4 V are blue (unacceptable).

The average standard deviation between scans (based on 10 samples with 5 scans per sample) is 2.93%. There is a minimum reliable detectable defect size is 5 mm x 5 mm and the sizing resolution limited to 5 mm steps.

The initial field trial validation yielded no missed defective areas and a 10% spurious indication rate, however the sample population was too small to reach any definite conclusions on the false-call-rate. The inspection is currently at TRL (Technology Readiness Level) 3, based on the fact that although the system prototype has been tried in the laboratory and in the field, the proof of concept is not yet robust. Consequently the system requires more extensive field trials and subsequent revisions before it is fully validated and rises to higher TRL levels. Opportunities for such trials are currently rare due to a drop in importance of the technique due to long inspection cycles and obsolescence on some machines, so the process is on-going.

Chapter 7 Detection of Creep Damage in Steam Generation Pipe-work

7.1. Introduction

A logical next step from the successful work on detecting microstructural variations in a Martensitic steel is to explore the use of the eddy current technique on other Martensitic metals. In modern, steam driven power generation assets Grade 91, (also known as P91 when in pipe form) steel is used due its excellent strength performance at high temperatures. Grade 91 is a martensitic steel whose main alloying elements are 9% Chromium and 1% Molybdenum. It is extremely brittle in its untreated state; it must be tempered prior to entering service and carefully heat-treated during the fabrication of weldments.

Grade 91 is very resistant to creep damage, but it has now been in use on plants for over 25 years and some components are showing signs of deterioration. Under normal operating conditions, good quality Grade 91 should be fit for several hundred-thousand operating hours. Unfortunately, occasionally errors in the production of P91 and P91 weldments can lead to the material being unfit for prolonged use. The unsatisfactory material is often caused by improper heat treatment and occasionally by poor control of the alloying elements. The former problem often manifests itself as an increase or decrease in the material hardness. The material is often checked for high hardness during the fabrication process as it is well understood that the material will be brittle if tempering and/or post-weld heat treatment have not been correctly implemented. On occasions the material entering service is in fact too soft, which results in a notable decrease in its ability to withstand creep. This may not be evident for some time into the component's operational life, but can lead to very premature creep-life expiry. Detection of this poor quality Grade 91 in newly fabricated components is a logical

progression to the work on steam turbine blades. The metallurgical transitions are very similar in the two cases and it is likely that the technique will translate across very easily. This will be investigated in Section 10.1.

Following on from that work is a study into the detection of in-service creep damage in Grade 91 pipe-work using NDE methods. This will be expanded to cover potential methods of detecting creep damage in 0.5CrMoV pipe-work; this material pre-dates Grade 91 but is still in widespread use and is mostly being operated beyond its design life. A theoretical look at the potential for other non-destructive methods to be used for this problem is included later in the chapter.

As well as there being two material types for which creep degradation is a concern there are also two distinctly different creep issues. The first is creep damage in the vicinity of weldments, henceforth referred to as localised creep. This is generally the type of creep of most concern as it forms bands of high density cavities which coalesce to form cracks on or near the fusion face. This will be described in more detail later in this section. The second type of damage is volumetric creep affecting the parent material; cavitation levels are far lower but become critical at much lower concentrations. It has historically been accepted that this type of damage is much less of a concern than damage at weldments, since welds are more highly stressed and therefore more likely to fail first. The age of some of the UK power industry's pipe work now means that concern for volumetric creep is increasing.

7.2. Background on Creep

Creep in metals is a very well understood concept in metallurgy where there is a combination of elevated temperatures and material stress which, below the yield strength or ultimate tensile strength, cause a time-dependent degradation of the metal which eventually leads to failure. The strain-rate of the material governs its creep behaviour and degradation.

The strain rate in creep is in general dependent on four factors,

- The applied stress
- The material temperature
- Structural parameters (grain size, dislocation density etc.)
- Any existing creep degradation in the material.

There are three stages in the creep process [115]

- Primary creep – Strain rate decreases as strain increases
- Secondary creep – Steady state – strain rate is constant (approx. 5% of the sum of primary, elastic and steady state strains)
- Tertiary creep – Strain rate increases very rapidly with strain

The first two stages cause little physical damage and are barely detectable. It is the third stage where the serious material degradation occurs and where the rate of creep strain is variable. During creep degradation the material changes in two ways; changes in microstructure without decohesion, and changes in the level of internal damage (i.e.

cavitation nucleation) with no associated microstructural change [126]. Although these two changes run simultaneously, one will always be dominant at any given time and this will dictate the stage of the creep damage in the material.

Depending on the creep rate and applied stress there are two types of creep cracking. The first is transcrystalline cracking which occurs at high creep rates. In this mechanism cracks are formed at inclusions in the material matrix which gradually link up to form macro-cracks. The second type of cracking, which is relevant to the situation investigated in this work, is intercrystalline cracking. This occurs at much lower creep rates and results in the formation of cavities and crevices at grain boundaries and interfaces. These occur at the boundaries which are aligned at approximately 45° or 90° to the applied stress and will eventually join to form micro-cracks.

There is some debate on where in a component the creep damage is likely to be greatest. For the thick-walled pipe that we will be dealing with, Dobrzański [126] suggests that the greatest level of cavity and crevice formation occurs at the surface of the material while in the work of Parker [127] greatest damage was observed at the mid-wall of a pipe.

7.3. RWE npower Creep-life Management

7.3.1. Overview

RWE npower employ a number of methods to effectively manage the creep degradation of it main steam pipe-work and headers. Current policy is the same for both 0.5CrMoV and modified 9Cr materials despite there being differences in the manifestation of creep damage between the two.

The RWE npower creep life review for each plant is used to identify sections of pipe-

work and headers for inspection during major outages based on operational conditions. Using thermocouple data and taking an average operating temperature over the period between outages (typically four years) any area that is expected to be 80% or more creep life expired at the time of the next outage, is flagged for inspection. These calculations are based on lower-bound material properties to give the worse-case scenario. In addition to plant identified in this manner, any previously inspected areas that require further monitoring or re-inspection are also included in the inspection program.

The tools currently available for assessing the creep degradation of the material are as follows:

- Metallurgical Replication
- Hardness Testing
- Material Composition Analysis
- Wall Thickness Measurements
- Magnetic Particle Inspection
- Ultrasonic Inspection
- Creep Pip Measurement*

* Only available at limited locations. Measured during each outage period.

Not all methods are used at all locations and their significance may change dependent on location. This will be discussed in more detail in the sections applicable to each location type. Here is a brief explanation of each technique employed:

- **Metallurgical Replication** - This is an assessment of the microstructure of the material, with particular emphasis on the concentration of creep cavities present

within the material. Creep cavities are voids of the order of 1μm in diameter which form along the boundaries between grains. The cavities are visible on micrographs following etching using 2% Nital (2% Nitric Acid in Methylated Spirit) under an optical microscope at 500x magnification. Cavitation levels are measured by sampling areas of 1/15th of a square millimetre, counting the number of cavities present and then multiplying by 15 to give a value of cavs/mm^2. The significance of the cavitation levels varies dependent on the location of the damage and often a *peak* value and an average *background* level will be quoted for a given area. For parent material the flag for further assessment of the material is approximately 150 cavs/mm peak and 90 cavs/mm background. This is the current standard method of quantifying creep damage at RWE npower, so will be used as the comparative reference for the work in Chapters 9 and 10. **Applicable to localised and volumetric damage**.

- **Hardness Testing** - Hardness measurements are taken in the parent metal at all replication areas and around 200-300mm from the weld fusion lines. The significance of the results is questionable due to the significant variation in readings experienced with portable hardness testers. However, it is generally accepted that areas of parent material that are significantly softer than surrounding areas are more likely to experience severe creep degradation. **Applicable to localised and volumetric damage**.

- **Material Composition Analysis** - X-ray diffraction (XRD) is used to analyse the material composition of the parent material at the same locations as the hardness tests. It is considered that areas of particularly low (compared to the

specification) chromium are likely regions for creep degradation. **Applicable to volumetric damage**.

- **Wall Thickness Measurements** - These measurements serve two purposes. The first is to check for any thinning of the pipe as an indication of the material creeping significantly. The second relates to the ovality of the pipe, which can cause excessive stress making the risk of failure much greater. **Applicable to volumetric damage**.

- **Magnetic Particle Inspection** - This tests for any surface breaking defects in the pipe-work. Inspections are limited to bends, weldments and regions adjacent to welds which are considered to be most at risk. **Applicable to localised and volumetric damage**.

- **Ultrasonic Inspection** - This tests for any significant defects in the volume of the pipe-work. This is restricted to the weld volume and HAZ, particularly around the fusion faces. Inspection uses single-element pulse-echo ultrasound as well as ToFD and phased array as appropriate. **Applicable to localised damage.**

- **Creep Pip Measurements** - Creep pips are small metal studs, located equidistantly around the pipe circumference. Through accurate measurement of their separation a strain rate of the material can be calculated. This can be used to gauge whether the creep rate is constant or increasing. **Applicable to volumetric damage**.

7.3.2. Welds

Welds are considered to be the most at-risk area of 0.5CrMoV and Grade 91 pipe-work. There are a number of reasons for this, including thermal stressing, differing weld/parent composition and thermal variations in microstructure. Welds are categorised on a scale A-E, with category A being an extremely high risk which requires immediate attention and E being a very low risk weld. The weld categories are based on previous inspection data, physical location, thermocouple data, operational hours, repair history and weld material. Consequently, the weld category will change for each weld during its lifetime. Category A welds are an immediate threat, category B welds require repair and/or inspection at the next outage and category D and E welds will be inspected periodically.

The extent of inspection required for a weld is determined by its current category and its inspection history. Generally, this will comprise of MPI on the surface and UT of the fusion faces looking for macroscopic creep cracks and metallurgical replication of the weld, HAZ and parent. The replication of the parent material is usually adjacent to the weld, but in higher risk areas additional replicas may be taken at 10mm, 20mm and 30mm up and downstream of the weld.

Welds are divided into regions based on historical cracking locations, these are know as the Type I Type II, Type III, Type IIIa and Type IV regions. Figure 7.1 shows a schematic of a weld geometry and the five regions. The regions of most interest from metallurgical replication of welds are the Type III, IIIa and IV regions. Creep cavitation levels are measured in each region, with peak and background values measured.

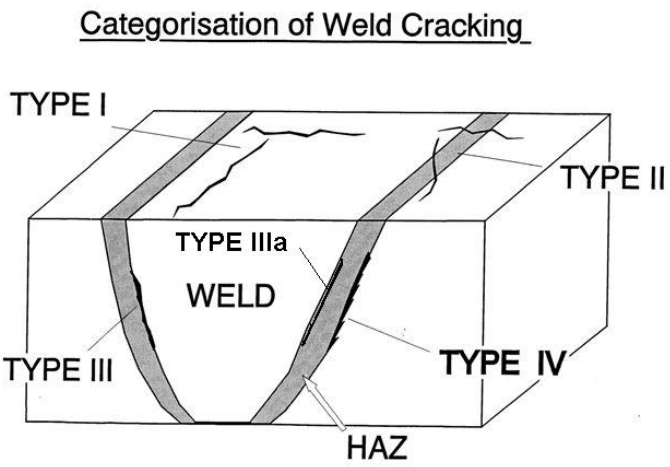

Figure 7. 1 – Schematic showing cracking locations on large butt welds

The areas where creep cracks occur tend to have finer grains than the parent material and the density of cavities increases accordingly. Consequently the cavitation levels that are considered dangerous are much higher than for parent material. A low level of cavitation would be a peak of up to 400 cavs/mm, medium would be up to 800 cavs/mm, high would be up to 1200 cavs/mm and anything above this would be classified as "very high". Once cavitation levels have reached the high level, the cavities will begin to coalesce and eventually micro-cracks will form.

Metallurgical replicas will be taken at three positions around the circumference of the weld on both the upstream and downstream sides. Where metallurgical replicas have been taken, hardness testing and material analysis are taken as a matter of course. High risk welds will be inspected using manual pulse-echo ultrasonic inspection, occasionally using ToFD to size known defects.

7.3.3. Pipe-work Bends

After welds, the next most at-risk region of the main steam pipe work is the bends due to the additional stresses and wall thickness variations. The whole bend is inspected with MPI to check for any surface breaking defects. Metallurgical replication, hardness,

material analysis and ovality checks are made at six positions on the extrados, intrados and neutral-axis of the bend. Cavitation levels that are considered dangerous start at 150 cavs/mm, as with all parent material.

7.3.4. Headers

Headers are treated in the same way as pipe-work, but have additional welds and stress raisers which may increase their risk of failure by creep damage. Inspection methodology is the same as per pipe work.

7.3.5. Pipe-work Straights

Straights have always been considered low-risk compared to welds and bends. This may still be true, but the number of service hours accumulated by some plants means that parent material is reaching the end of its creep life, based on conservative estimates. Testing of straights would be difficult to focus and metallurgical replication would be very time-intensive. Screening or sampling methods need to be implemented to help address this problem.

7.4. Creep in Power Generation Steels

7.4.1. 9Cr 1Mo (Grade 91)

Grade 91 steels are ferritic-martensitic steels used in high temperature applications such as power generation pipe-work and headers. Power stations began using Grade 91 steels (see composition in Table 7.1) in place of traditional 0.5CrMoV steels in the 1980's due to their excellent elevated temperature strength and creep behaviour [128]. Since Grade 91 has not been around as long as the older 0.5CrMoV steels, its long term behaviour is not as well understood. The main risk associated with ferritic-martensitic steels is that

the long-term creep strength will fall below the level assumed for design leading to failure [129]. Grade 91 steels have non-equilibrium (thermodynamically unstable) microstructure resulting in them undergoing severe microstructural changes from their manufactured state through their service life.

Wt%	C	Mn	P	S	Si	Cr	Mo	V	Nb	N	Al	Ni
Min	0.08	0.3			0.2	8.0	0.85	0.18	0.06	0.03		
Max	0.12	0.6	0.02	00.1	0.5	9.5	1.05	0.25	0.10	0.07	0.04	0.4

Table 7.1 Composition of Grade 91 steel

Niobium and Vanadium are strong carbide formers; this allows the Molybdenum to remain in solid solution, thus maintaining mechanical strength [130]. Grade 91 is normalized and tempered prior to use which gives it a tempered martensite structure with precipitation of $M_{23}C_6$ carbides (M in this notation signifies *Metal*, a combination of Chromium and Molybdenum and C signifies *Carbon*) and Niobium rich MX carbo-nitrides. The microstructure of Grade 91 consists of lath, block and pocket martensite with a high density of dislocations and carbonitrides. A fine dispersion of these carbonitrides provides excellent creep strength and toughness [131]. These precipitates form on boundaries during tempering and stabilise the lath martensite structure and improve the creep strength through precipitation hardening [128].

Once the material has been subjected to long-term creep damage the microstructure evolves into large, dislocation-free cells and coarse particles [128]. Coarsening of the secondary, carbide phases along with the depletion of Mo associated with the precipitation of the Laves phase (a brittle Fe_2Mo or Fe_2MoW phase) is regarded to be the main degradation process in Grade 91 [132]. The withdrawal of Molybdenum from the

matrix reduces the solid solution strengthening which is not compensated for by the precipitation hardening resulting from the presence of this phase. Also detrimental to the creep strength of the material is the formation of the deleterious Z-phase. Z-phase is a nitride particle with a high Cr and V content which forms and coarsens at the expense of the MX particles which are creep-resisting. The presence of these phases results in a decrease in parent material toughness and can be correlated with a decrease in hardness [133], though this reduction is small.

It is suggested that the onset of tertiary creep is associated with the coarsening of dispersed precipitates such as M_7C_3 carbides and this process is accelerated by applied stress [132]. Like 0.5CrMoV metals, there also appears to be a presence of voids and micro-cracks in later creep degradation [130], although this has not always proved to be the case [133]. It may also be the case that voids are more likely to occur at depth rather than on the surface of the material [134] and that these grow to the size of grains rather than increasing in number and coalescing. It is also reported that the martensite laths increase in length during the creep process and that there is a change in the dislocation density; both of these are correlated with hardness. While there is a link between hardness and creep for Grade 91 it is dependent on applied temperature and stress [133]. It is suggested that the relationship between hardness and life-fraction may even be linear for the range 20-90% life expiry [134].

Welding of Grade 91 results in the formation of a heat affected zone (HAZ) which has a significantly different structure, and thus properties, compared to the parent material. During welding, the temperatures can exceed 900°C and a large extent of the material will be made up of martensite. Due to the short thermal cycle the precipitates are not

fully dissolved and consequently, during the post-weld heat treatment, there is not significant reprecipitation of carbides, and the resulting microstructure is very different from it original state. Consequently the carbides coarsen reducing their strengthening effect and a soft fine-grained region is formed on recrystallisation. At higher welding temperatures with a longer thermal cycle the carbides are able to reprecipitate leaving a coarser grained structure with a similar carbide distribution to the original state. Where there is no reprecipitation of MX carbo-nitrides the creep strength of the material is significantly reduced [132]. Inspecting this area for hardness variations is very difficult due to its narrow width, making creep evaluation by this method unreliable [134].

7.4.2. 0.5CrMoV

Many of the low-alloy ferritic steels used in the power generation industry have good resistance to creep, however they will suffer long-term degradation in their ability to withstand creep due to the high temperatures and pressures that they are exposed to. These materials are commonly used in superheater pipe-work, headers and tubes, so will experience temperatures around 570°C and pressures approaching 170 bar; they are designed for a working life of >100,000 operational hours. Much of the main steam pipe work systems at RWE npower plants is made from 0.5CrMoV. This material was developed more than forty years ago and has reasonable creep strength as well as a high tensile strength. Its composition is shown below in Table 7.2.

Wt%	C	Si	Mn	P	Si	Cr	Mo	Ni	V
Min	0.10	0.10	0.40	-	-	0.30	0.50	-	0.22
Max	0.15	0.35	0.70	0.03	0.03	0.80	0.70	-	0.28

Table 7.2 – Chemical composition of 0.5CrMoV

When forming welded joints between 0.5CrMoV components a 2.25Cr1Mo filler is

generally used for historical reasons relating to its improved resistance to re-heat cracking compared to 0.5CrMoV consumables. The composition of the 2.25Cr1Mo weld consumable can be seen in Table 7.3.

Wt%	C	Si	Mn	P	Si	Cr	Mo	Cu	Sn	As
Min	0.05	-	0.50	-	-	2.00	0.90	-	-	-
Max	0.10	0.015	0.90	0.02	0.50	2.50	1.20	0.15	0.01	0.035

Table 7.3 – Chemical composition of 2.25Cr1Mo

During the component lifetime the creep degradation will cause changes in microstructure including decomposition of pearlite/bainite, precipitation of carbides and the formation of internal cavities [126]. Dobrzański describes the varying stages of creep cavitation in 0.5CrMoV steels and makes an estimation of the level of creep life expiry associated with each:

- No damage. (<50% life expired).
- Development of cavities - Presence of single cavities at grain boundaries. (60% life expired).
- Development of cavities - Presence of a few cavities along grain boundaries. (60% life expired).
- Growth of cavities - Cavities oriented at grain boundaries 45° or 90° to main stress axis. (70% life expired).
- Growth of cavities - Chains of cavities at grain boundaries. (70% life expired).
- Growth of cavities - Coalescence of cavities. (80% life expired).
- Growth of cavities - Surface intercrystalline crevices encompassing a single grain. (80% life expired).
- Formation of microcracks - Surface intercrystalline crevices encompassing several grains. (90% life expired).

- Formation of microcracks - Surface intercrystalline crevices encompassing at least a dozen grains. (90% life expired).
- Formation of macrocracks. (≈100% life expired).

Nucleation of cavities is likely to be connected with grain boundary slip and with decohesion of the interfacial matrix. It has been proposed [126] that dislocations along slip planes build up and become "stacked" thus forming cavities.

Late on in a material's creep life, it is unclear how exactly the extent of damage propagates. Once nucleation of cavities has begun, the damage process accelerates the nucleation of new cavities. One theory [126] is that because the cavities tend to form along grain boundaries orientated at 45° or 90° to the principal stress, ultimately as more and more cavities form these appear to be aligned in chains. These aligned cavities often touch each other and coalesce as the material bridges between them break down. Ultimately these form micro-cracks which reduce the overall strength of the material making it liable to fracture and failure. Alternatively there may be a volumetric growth of existing cavities rather than an increase in cavitation density [135]. Either way the eventual outcome is the same with the microcracks joining to form macrocracks prior to total material failure.

In addition to the nucleation and coalescence of cavities other metallurgical changes occur reducing the overall creep strength of the material [136]. These include:

- Formation of precipitate free zones near grain boundaries and the formation of coarse carbides.
- Formation of molybdenum rich carbides which depletes this vital element from the

matrix

- Recovery of dislocations (annihilation and rearrangement)
- Increase in inter-particle spacing of carbides due to coarsening.

Although creep failure can potentially occur at any point in the 0.5CrMoV pipe-work system, logically it is more likely to occur in locations where there are significant additional stresses, such as bends, branches and welds. Statistically the most likely failure location is in the intercritical (fine-grained) HAZ.

Welds represent the most likely locations for failure due to creep. In 0.5CrMoV pipe-work these weldments mostly use a 2.25Cr 1Mo filler which is more creep resistant in its virgin state but less so after welding. The most common failure mechanism [137] is type IV cracking, where cracking develops in the intercritical heat affected zone (ICHAZ). Creating weldments such as these requires a significant amount of preheating to prevent the formation of very brittle structures. Consequently the HAZ will contain a variety of microstructures including areas where austenite grains grow. The regions nearest the weld itself will obviously be subjected to the highest temperatures, causing the formation of coarse-grained austenitic structures adjacent to the fusion boundary. Further away from the fusion boundary the grain size will reduce with distance; the structure here will be bainitic due to the relatively rapid cooling rates. Adjacent to the fine-grained bainite is the intercritically transformed region where fine grains (approx. 5μm) of ferrite are formed because the peak temperature is insufficient for full transformation to austenite.

Currently RWE npower use surface replication to assess creep damage by counting

cavity density adjacent to welds and also on bends (see Section 7.2). This technique does give a good indication of the amount of creep damage a component has developed but it is unclear whether or not this method gives an accurate representation of the through wall extent of cavitation. The method is also very time consuming in both creation of replicas and in replica diagnosis.

Material failure due to creep is closely related to the accumulation of lattice defects such as dislocations, which accumulate to form grain boundary cavitation. Although grain boundary cavitation is one of the most visible characteristics of time-dependent damage due to creep, other features may be able to able to assist in the evaluation of the creep life exhaustion of a component. Potential features include:

- Strain rate measurement
- Magnetic domain analysis
- Material hardness
- Carbide/precipitate detection and analysis.

Through reliable evaluation of the accumulation of material degradation prior to the onset of cracking, the material life can be planned into replacement schedules with a low risk of failure. The early detection of fatigue damage, which is similar to creep damage in that is has potentially-detectable damage pere-cursors, has been investigated using magnetic NDE methods [138] and has shown promising results.

A number of NDE methods, mostly magnetic and ultrasonic have been suggested for creep damage detection and trialled with varying degrees of success [139][140][141]. Due to the complex nature of the creep process and the microscopic nature of the tell-tale

indications of damage it is unlikely that one method alone will give sufficient confidence to fully evaluate the creep condition of a material; however, it is possible that a combination of techniques will provide a suitable inspection protocol that is as reliable and faster than the current method of replication.

7.5. Possible Methods

The yield strength of a material can be enhanced by the presence of obstacles which impede the dislocation movement in the material under load. The obstacles can be dislocations, dissolved atoms, precipitates, grain boundaries and even cavities which cause localised additional residual stresses in their vicinities. Detection of such obstacles should give some indication of the material's ability to resist creep damage.

Because we are dealing with creep damage in a ferromagnetic material, there is a potential to use magnetic and micromagnetic techniques to evaluate the problem. Parameters of micromagnetic techniques are mainly influenced by temperature and load induced microstructural changes [139], such as the changes experienced in long-term creep life degradation.

Magnetic domains in ferromagnetic materials are always magnetised to the saturation point of the material, but are usually oriented so that the net magnetism of all the domains is zero. In this state the metal would be regarded as unmagnetised. The ferromagnetic material can become magnetised in the presence of a magnetic field; in such cases the domains become aligned in the direction of the applied field, thus the net magnetism becomes equal to the sum of the magnetism of all the domains. The

alignment of domains occurs by movement of Bloch walls (a thin transition region between domains of different magnetism values); magnetism rotates through the plane of the Bloch wall. Domains orientated parallel (or almost parallel) to the magnetising field increase in size and the other domains cease to exist. This process does not occur instantaneously but in a stepped manner due to microstructural obstacles in the material "pinning" the domains [142]. Kim [143] reports that although grain boundaries have an effect on pinning of domain walls, the more dominant pinning effect comes from the cementite particles in steels.

The varying structure and precipitates of Grade 91 with degradation make it likely that the magnetic properties of the material will vary in some way; most likely through the pinning of domain walls by fine precipitates. In a recent study it was discovered that there was detectable variations in coercivity, remanence and magnetic Barkhausen noise (MBN) [144]. The magnetic characteristics of the metal changed during the three phases of creep. During primary creep the remanence and coercivity increased and the MBN peak (rms) value decreased. This is most likely associated with the formation of new precipitates increasing the pinning density. In secondary creep, as the carbides coarsen rather than increase in number, the pinning density will drop and this is reflected in a decrease in the relative coercivity and remanence and an increase in the MBN peak. In the tertiary stage, there is a decrease in coercivity and remanence as well as a reduction in the MBN peak. It is suspected that this is due to the demagnetising field from the large non-magnetic carbides decreasing coercivity and remanence and the formation of microcracks restricting domain movement, thus reducing peak MBN [144].

7.5.1. Hysteresis Measurements

The coercivity and residual flux density of ferromagnetic materials are both influenced

strongly by lattice defects and hence by plastic deformation. The coercivity of the material depends on the density and distribution of lattice defects such as micropores/cavities [145] since both are linked to the movement of the Bloch walls. Several potential methods for measuring the magnetic properties have been investigated [146], including magnetic Barkhausen noise, measurement by SQUID (superconducting quantum interference devices) and by magnetic hysteresis methods.

The basic relationship between dislocation density (ρ) and initial magnetic susceptibility (χ_0) and coercivity (H_c) is given in Eqs. 7.3.1 and 7.3.2 [147].

$$\chi_0 \propto \frac{1}{\sqrt{\rho}} \quad (7.3.1)$$

$$H_c \propto \sqrt{\rho} \quad (7.3.2)$$

Thus, theoretically the dislocation density can be determined from magnetic measurements, though in practice the complex stress condition makes results unreliable [146]. Since there is considerable reorganisation of the dislocations during the creep process the behaviour of the magnetic flux density and coercivity is unlikely to be consistent throughout the process as was observed in work on monitoring fatigue life [148].

Govindaraju [140] suggests that magnetic properties vary at different rates during the creep deformation process due to microstructural evolution, including cavity nucleation, but it should be able to evaluate damage within each creep regime. In the primary stage of creep there is an increase in the density of dislocations and nucleation of cavities at grain boundaries which pin magnetic domains. This will increase the coercivity [149] during plastic deformation. In the steady state creep regime the growth of cavities

pushes dislocations and voids out to the grain boundaries, decreasing the number of pinning sites. In the tertiary stage the presence of microcracks will cause a magnetic flux change and a possible reduction in remanence. Results from hysteresis measurements suggest that while there is a general trend of reduction in remanence with creep damage, the product of the coercivity and remanence gives the most reliable indication of creep degradation. Lattice defects affect the magnetic spin rotation of ferromagnetic materials as well as the domain wall motion, so any measurement system that can infer the influence of the spin should have a better ability to monitor damage accumulation.

Despite some encouraging results using the theory of detecting creep damage with hysteresis analysis and some lab-based experimentation, the method of measurement has proved susceptible to interference from external noise [145].

7.5.2. Magnetic Barkhausen Noise

Magnetic Barkhausen noise (MBN) is explained in Chapter 8, Section 3. MBN has the potential to provide information relating to the presence of lattice defects, due to them pinning magnetic domain walls. In the presence of an applied magnetic field domain walls become unpinned and take a new form where the magnetic state changes locally and forms a Barkhausen event. The combined Barkhausen events from all the domain movements are referred to as the Magnetic Barkhausen Noise, which can be detected using induction coils. This is however, an irreversible micromagnetic technique as the domains will never return to exactly the same state they were previously in. The presence of lattice defects pinning the domain walls will suppress the movement of domain walls relative to areas where no lattice defects are present. As with hysteresis

analysis the MBN responses are not consistent throughout the damage accumulation process [150] so it is essential that it is constantly monitored throughout the material life-cycle.

Magnetic Barkhausen noise measures the rms values of the pulses received by the pick-up coil and is sensitive to the damage at or near the material surface. This may not be ideal for detecting creep damage if the greatest damage is located through-wall, however it is no worse than the current method of replication.

MBN peaks may also be caused by grain boundaries, precipitates and inclusions [145]; however, since the peak position changes for each of the pinning mechanisms, these can be distinguished from each other.

In summary, MBN has the potential to distinguish the presence of creep-related lattice dislocations, but the relationship varies between creep regimes. Inspection is limited to the accessible surfaces of the material and results are not repeatable.

7.5.3. Acoustic Barkhausen Noise

Magnetostriction is a property of ferromagnetic materials that is analogous to the piezo-electric effect in piezo-electric crystals. Whereas a piezo-electric crystal will change shape when an electric current is applied to it, a ferromagnetic material will change dimensions when a magnetic field is applied to it. When the reverse occurs and a magnetic material is placed under stress it will show spontaneous magnetisation. These magnetostrictive effects cause the emission of acoustic signals during Barkhausen events known as Acoustic Barkhausen Noise or Magneto-mechanical Acoustic Emission

(MAE), see full explanation in Chapter 8 Section 2.

Attempts to use micromagnetic measurements (specifically concerning magnetic and acoustic Barkhausen noise, incremental permeability and tangential field strength) to assess creep damage were made by Dobmann [151]. Unfortunately it was discovered that the micromagnetic measurements were too sensitive to surface condition and any attempts to improve this affected the Barkhausen noise parameters, and so consistent measurements could not be achieved. Measurements of the tangential field strength were however unaffected and have the added bonus of having a larger analysing depth than Barkhausen noise (which is a surface and near surface technique). These measurements give an indication of bulk properties and may provide some useful information about the creep degradation of a material.

Despite the slightly disappointing results of Dobmann's work, it does seem likely that magnetic methods are useful in the detection of creep damage because of their sensitivity to strain and to material inhomogenities such as cavities [140].

In addition to the work described above, attempts to evaluate the incipient stages of creep damage (i.e. prior to cavity nucleation) using magneto-acoustic emission have had some success [152]. This work attempts to quantify the damage in terms of the volume fraction of non-magnetic precipitates and the average distance between domain pinning locations. Results for magnetic Barkhausen noise showed a general trend but suffered from a lot of variability.

7.5.4. SQUID (Superconducting Quantum Interference Devices)

SQUIDs are ultra-sensitive magnetic sensors with a typical resolution of 10^{-14} Tesla. The SQUID sensor can be incorporated into an eddy-current-style detection system [153] and gives excellent sensitivity and spatial resolution (around 0.1mm). SQUID sensors are conventionally very large and have to be helium cooled making them unsuitable for site-based applications. A successful attempt to create a smaller SQUID (152mm diameter) was utilised to detect fatigue damage in stainless steel 316 associated with a martensitic transition. SQUIDs, by nature of their sensitivity are susceptible to interference from noise, though improvements through shielding have shown improvements in results. It is suggested that SQUID sensors could detect the lattice defects associated with material degradation through creep (Umakoshi 2004), though the practicalities of the system currently make it unsuitable for on-site inspection.

7.5.5. Ultrasonic Techniques

Ultrasonic techniques have the advantage of being able to evaluate the volume of a material rather than just the surface or near-surface area. Reflections from physical features make direct detection of some of the physical features of creep damage feasible, if unlikely. Ultrasound can also be used to make bulk measurements of material properties which may be varied by the effects of creep degradation, such as build up of discontinuities affecting sound velocity and acoustic attenuation. Phased array ultrasound gives an extra degree of control in generating and detecting ultrasonic information enabling greater depth of data analysis.

7.5.6. Laser Ultrasound

Laser-generated ultrasound can be used to generate surface acoustic waves with small

enough wavelengths to be able to detect and image defects in the region of 30μm [154], and possibly below in some metals. This makes it potentially applicable to direct detection of micro-cracking and clustered cavitation. Additionally, the technique can be used to image the grain structure of the material which could help to identify elongation in the grains which would be indicative of the latter stages of creep deformation. Finally, by using the Spatially Resolved Acoustic Spectroscopy (SRAS) [155] a velocity map of the material could identify localised variations in the acoustic impedance which may be indicative of localised creep degradation.

7.6. Conclusions

Although no single method has been able to reliably detect creep damage, or the lattice defects associated with it, a number of methods in the literature have shown some success.

The common themes regarding the failure to produce consistent results include: inconsistency in results in the different creep regimes; problems associated with the sensitivity of the sensors to other influences, especially noise, and the fact that domain wall motion never repeats identically, and this could influence the repeatability of results.

It appears that the magnetic effects in the creep process which can be detected by non-destructive means do not follow clear trends throughout the creep life and are easily affected by other influencing factors. Also, in the case of Barkhausen noise, the magnetic effects are irreversible and thus do not lend themselves to continuous component monitoring. Consequently it is likely that these particular approaches will be

insufficient on their own to reliably detect creep damage in main steam pipe-work. This theory is echoed in the work by Dobmann [151] who recommends a complementary inspection using both micromagnetic and ultrasonic inspection. Though this work comes some way short of proving a reliable combination, it does explore the use of ultrasonic velocity measurements as part of the solution. A combination of electromagnetic tests as employed in the MAPS stress detection system [156] may further enhance the reliability of the results.

In order to address the three areas of interest in creep damage assessment; detecting creep damage; quantifying creep damage and detecting micro-cracking, there are a number of methods that have shown promise. Not all are suitable for inclusion in this project due to the extensive work required to analyse their potential for creep assessment NDE. Some techniques are already under investigation by universities involved in RCNDE, including the use of Full-Matrix Capture (FMC) phased array at Bristol University and Shear Wave Birefringence at Imperial College.

There are a few methods for which some further exploration is appropriate and possible within the scope of this thesis. These fall into two broad categories:

- Direct detection methods, which would detect/quantify cavitation levels and/or material phases present.
    - Detection by Phased-array Ultrasound.
    - Detection by laser ultrasound and SRAS.
- Bulk measurement methods, which would imply the creep state of the material from measurement of other material properties.
    - Bulk Ultrasonic measurements.

- Barkhausen Noise Methods.

The direct detection methods will be investigated in Chapter 9, this will involve finding practical limits of minimum detectable defect sizes using current available [to RWE] ultrasonic technology and also looking at lab-based laser ultrasound as a means of characterising creep damage.

The bulk measurement methods will be investigated in Chapter 10 along with an extension of the work from Chapter 6, looking at detecting aberrant martensitic materials. The intention here is to see whether a combination of ultrasonic and electromagnetic measurements can detect areas of creep degraded material.

Chapter 8 Background Theory on NDE Methods

8.1. Introduction

This thesis is primarily focussed on electromagnetic methods, however, these are not always the most suitable methods for NDE solutions. In the following chapters, 9 & 10, there are a number of instances where ultrasound-based techniques are used. Due to the widespread awareness of the ultrasonic test method, a basic level of understanding of ultrasonic testing methods and terminology by the reader is assumed. Further information on the Ultrasonic NDE method can be found in the ASNT Handbook, Vol. 7, Ultrasonic Testing [157]. There are some techniques which span both fields of study (ultrasound and electromagnetism), which will be described in more detail with reference to the electromagnetism theory. The techniques which will be discussed in this section are EMATs (Electro-Magnetic Acoustic Transducers, Magnetic Barkhausen Noise (MBN), Acoustic Barkhausen Noise Emission (ABN) and Laser Ultrasound.

8.2. EMAT

EMATs (ElectroMagnetic Acoustic Transducers) are ultrasonic transducers which use electromagnetic coupling to generate acoustic waves in metals. An EMAT transducer consists of a coil for generating a varying magnetic field and a permanent magnet to provide a biasing magnetic field. There are three mechanisms which can contribute to electromagnetic coupling, these are: Lorentz force mechanism, magnetising force mechanism and the magnetostriction mechanism. The latter two mechanisms are only applicable to ferromagnetic materials, in which the magnetostrictive mechanism is the dominant effect [158].

The Lorentz force mechanism is applicable to all conducting media. When a current carrying medium is placed within a magnetic field it will be subject to a force that is at

right-angles to both the magnetising field and the current. In the case of an EMAT, the magnetic field is provided by the permanent magnet and the current is generated in the test material by induction from the coil. This force will create an ultrasonic wave within the material.

The magnetostrictive mechanism only works on ferromagnetic materials as the applied magnetic field from the coil will cause the magnetic domains to change their dimensions as the field fluctuates. The minute variations in the domain dimensions sum to form a larger overall vibration in the crystal structure of the material, creating an acoustic wave. The returned sound wave will vibrate the crystal structure mechanically and cause a change in the magnetic field which will create a differing signal in the transducer.

There are two elements contributing to the electromagnetic field generated by an EMAT transducer; the coil produces a dynamic magnetic field and the permanent magnet produces a static magnetic field. The transfer mechanism is relatively straight-forward for non-ferromagnetic metals as it is only dependent on the Lorentz-force mechanism, however it is far more complicated in the ferromagnetic case where the magnetostrictive mechanism dominates.

When an alternating current passes through the coil it generates a dynamic magnetic field which will penetrate any material in its vicinity as is the case with eddy current testing. This magnetic field interacts with the static magnetic field and causes body forces which will generate elastic waves. The generation of acoustic waves is dependent on three interactions; the generation and interaction of the magnetic field within the material, the interaction between these fields and the elastic field causing the generation

of body forces, and the generation of acoustic waves from the body forces.

The governing equations for EMATs include several of those governing eddy current, namely Ampère's law, Faraday's law for induction and Ohm's law. A mathematical description of the influence of the three coupling mechanisms and how they relate to the governing laws, can be found in Appendix E.

There are a number of advantages to the use of EMATs; unlike with contact UT where coupling can vary, particularly with geometric variations, EMAT coupling is largely consistent provided the whole aperture is in contact with the test material. Additionally, it is possible to generate many different wave modes with EMAT transducers. These features make EMATs ideal for measuring attenuation and also for measuring and comparing the velocity of different wave modes.

The majority of EMATs developed for industrial applications will generate shear waves, these are produced more efficiently and, due to their slower speed, offer greater resolution. A planar current carrying coil with a biasing magnet placed directly behind it as shown in Figure 8.1 will generate a dominant shear wave and a weak longitudinal wave from the Lorentz force and a shear wave from magnetostriction when used on a ferromagnetic material.

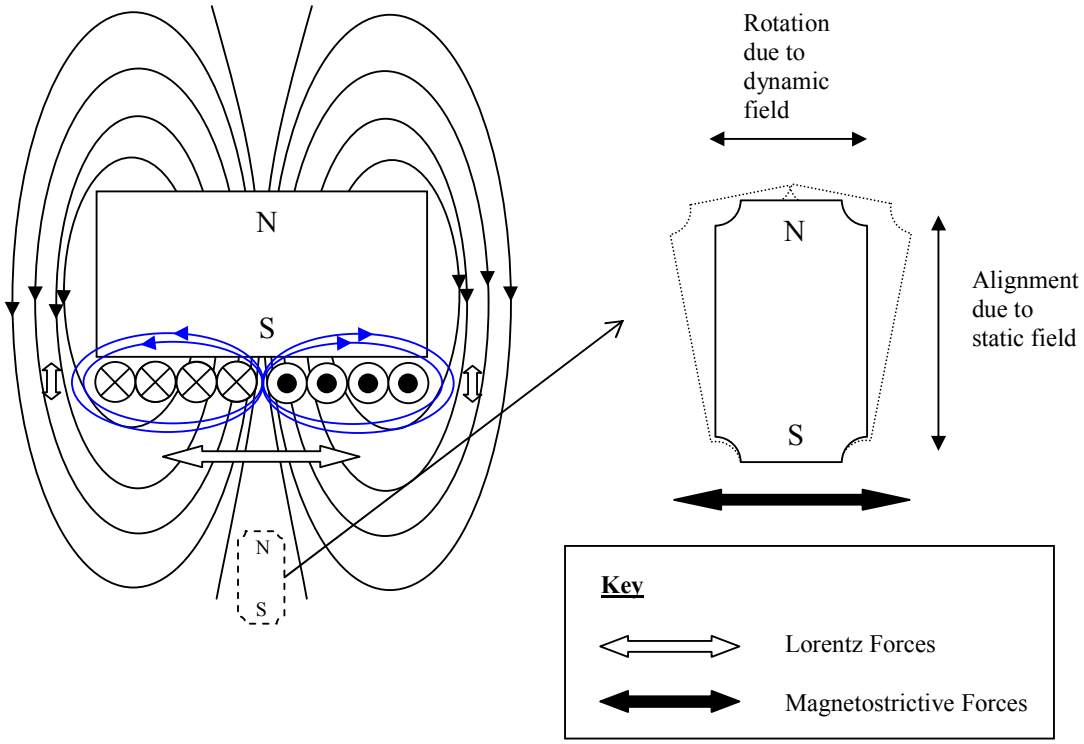

Figure 8.1 – EMAT generating dominant shear wave from Lorentz and magnetostrictive forces

To generate a dominant longitudinal wave a different arrangement is required. This is most easily achieved using a U-shaped magnet to re-orientate the static field in the same direction as the dynamic field. The resultant forces are shown below in Figure 8.2. The efficiency of Longitudinal-wave generation with EMAt is significantly lower than for Shear-wave generation.

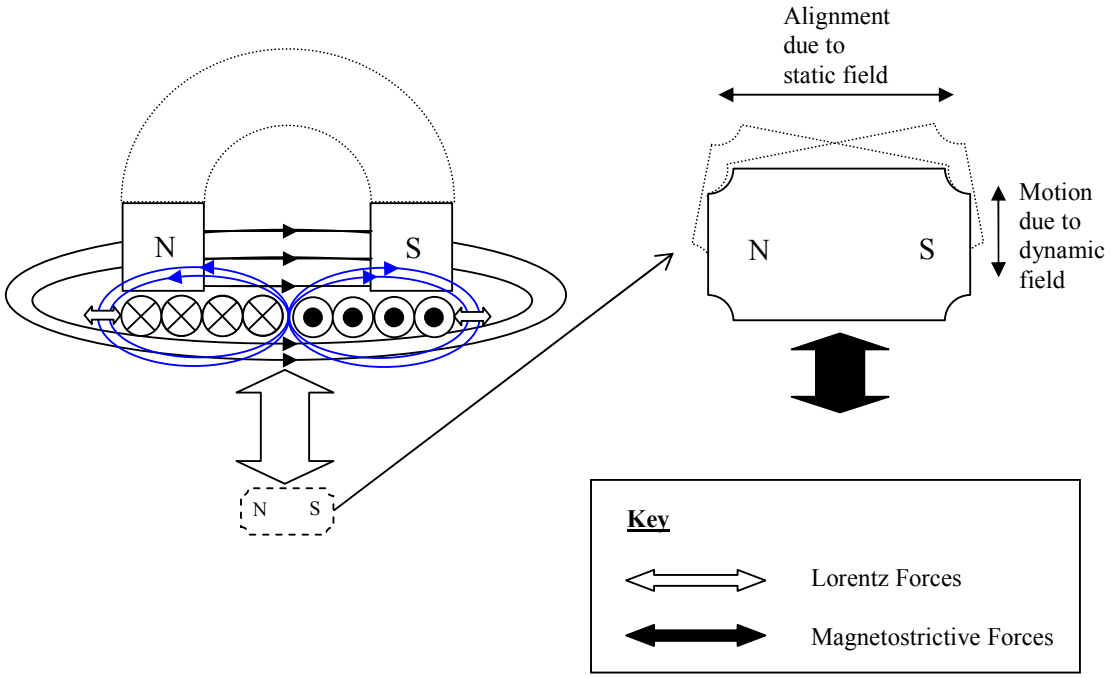

Figure 8.2 – EMAT generating dominant longitudinal wave from Lorentz and magnetostrictive forces

Shear wave EMATs may also be polarised using different coil shapes. As shown in Figure 8.3 a circular coil EMAT will generate through thickness shear waves at all radial orientations. If an elongated coil is used with a magnet covering the straight part of the coil then the shear waves will be polarised perpendicular to the coil winding – this approximates to the case shown in Figure 8.3 also.

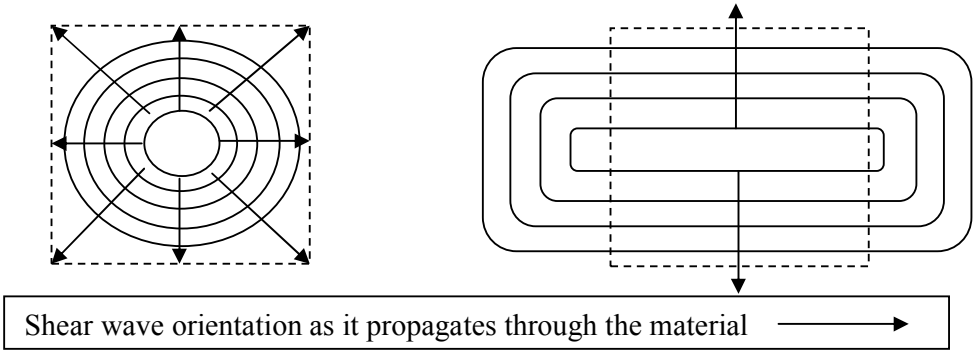

Figure 8.3 – Shear wave propagation with (right) and without (left) radial polarisation

8.3. Acoustic (ABN) and Magnetic (MBN) Barkhausen Noise

Acoustic Barkhausen noise (or Magneto-Acoustic Emission) is one of the two Barkhausen noise techniques and differs from Magnetic Barkhausen noise (MBN) in its method of measurement and in the magnetic characteristics that it is sensitive to. In a similar manner to MBN, ABN measures magnetic domain activity when a test object is subjected to a magnetic field, typically from a U-shaped electromagnet at a frequency < 100Hz, creating a magnetic field strength in the order of tens of kilo-Amperes per metre. This causes domain wall motion, which in turn produces acoustic emissions. These acoustic emissions can be detected by piezo-electric sensors, usually operating in the 50 – 250kHz range [159] and summed together to produce a profile of magneto-acoustic activity. The magnetic Barkhausen technique uses a sensing coil to record the steps in material magnetisation as domain realignment takes place. Neither technique is particularly repeatable because the test material will never return to exactly the same magnetic state, however the techniques can be used to highlight certain trends in the magnetic behaviour of components.

Where Magnetic Barkhausen Noise activity results from the displacement, both reversible and irreversible, of 180º and non-180º domain walls, ABN arises only by the discontinuous motion of non-180º domain walls [160]. ABN can also be caused by the irreversible rotation of magnetic domains through angles other than 180º. This difference in sensitivity to domain motion means that the two Barkhausen noise methods have sensitivity to different material characteristics. The movement of non-180º walls generates stresses, which produce the acoustic pulses detected in ABN. No stresses are generated from 180º domain wall rotations because the strain along a given axis is independent of the direction of the magnetic moments if they lie along the axis [161]. It

stands to reason from the points above that ABN will be more sensitive to the effects of stress than MBN, by virtue of the fact that there is no influence from 180º wall motions in the make-up of the signals. The exciting magnetic field will cause a number of non-180º domain wall movements, each of which will produce a stress wave in the material. These waves will vary greatly in magnitude and will impinge on the piezo-electric sensor producing a series of electrical spikes at different points in time depending on the distance from the source of emission to the sensor. This series of electrical spikes forms a waveform representative of the energy of each of the Barkhausen events. By rectifying the waveform and calculating the area under it, the absolute energy of the ABN activity can be determined, providing a useful indication of the level of domain movement.

There are many physical effects that can alter the Barkhausen activity of a material under test, but of most interest to this study is the presence and density of dislocations. Dislocations act as pinning sites for magnetic domains, restricting the movement and rotation of domains and thus reducing the Barkhausen activity. A significant increase in dislocation density from plastic deformation, such as in the latter stages of creep, will have a significant bearing on the magnetisation required to move the magnetic domains. The strength of the applied field is an important factor in any Barkhausen activity trend and there will only be a reliable decrease in Barkhausen activity with increasing dislocation density where the magnetising field is constant and above the saturating level for that material [161].

ABN and MBN are both influenced by the skin effect determined by the excitation frequency, however the differing methods of detection mean that ABN is sensitive to

information from far greater depths than MBN. The drop off in sensitivity with depth in the MBN system means the maximum measurement depth is somewhere in the region of 1mm, whereas for ABN where the activity is recorded from acoustic waves which travel relatively uninhibited through the material; the maximum measurement depth is only limited by the excitation which can produce Barkhausen events in the region of 10mm deep dependent on material properties. This means that ABN is far better for examining bulk characteristics of materials and, if used in conjunction with sensor arrays and signal processing, could provide activity location information as well [162]. It has also been proposed that by using pulsed excitation further depth dependent information can be established by examining the frequency content of the signals in a similar manner to pulsed eddy current [159].

8.4. Nottingham University Laser Ultrasound System

It is possible to generate very high frequency surface acoustic waves (SAWs) in the near-surface region of materials using pulsed lasers. The SAWs are guided waves which penetrate roughly one wavelength into the material [163]. This explanation of laser ultrasound systems relates specifically to the equipment used at Nottingham University for the purposes of this investigation. The optical energy of the laser is absorbed by the test material causing it to expand and relax with the same temporal characteristics as the laser, producing acoustic waves in the process. The characteristics of the generated waves can be controlled by use of a Spatial Light Modulator (SLM), which is a series of curved fringes which will determine the direction, focal length and spatial frequency of the SAWs [164]. Each wideband pulse from the laser will generate SAWs at a velocity determined by the material being tested, which will propagate radially from a circular spot. If the spot is linear, i.e. generated from a cylindrical lens, then the propagation will

occur in the two directions perpendicular to the line as shown in Figure 8.4.

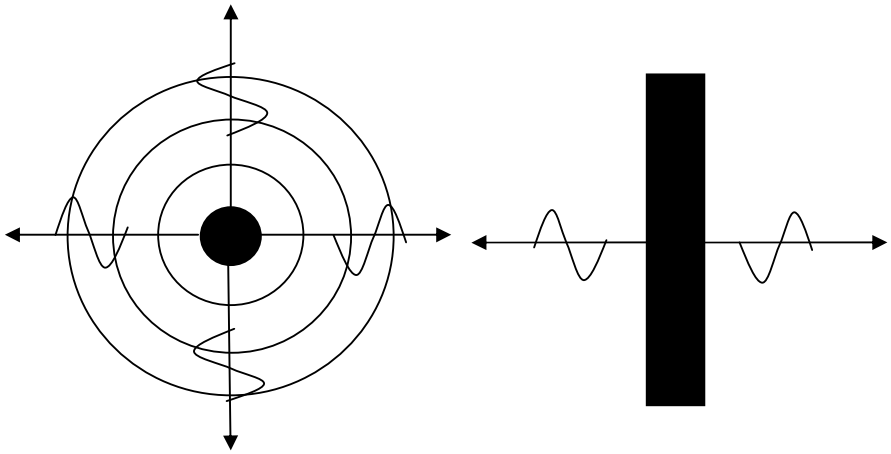

Figure 8.4 – SAWs propagating from circular source (left) and linear source (left)

If the generating laser pattern is a series of parallel lines with a spacing *d*, where

$$d = \frac{v_{SAW}}{f_{temporal}} \qquad (8.4.1)$$

then the SAWs generated by a pulse will pass under the neighbouring line as the next pulse occurs and by constructive interference a larger amplitude wave will be generated as shown in Figure 8.5 [165].

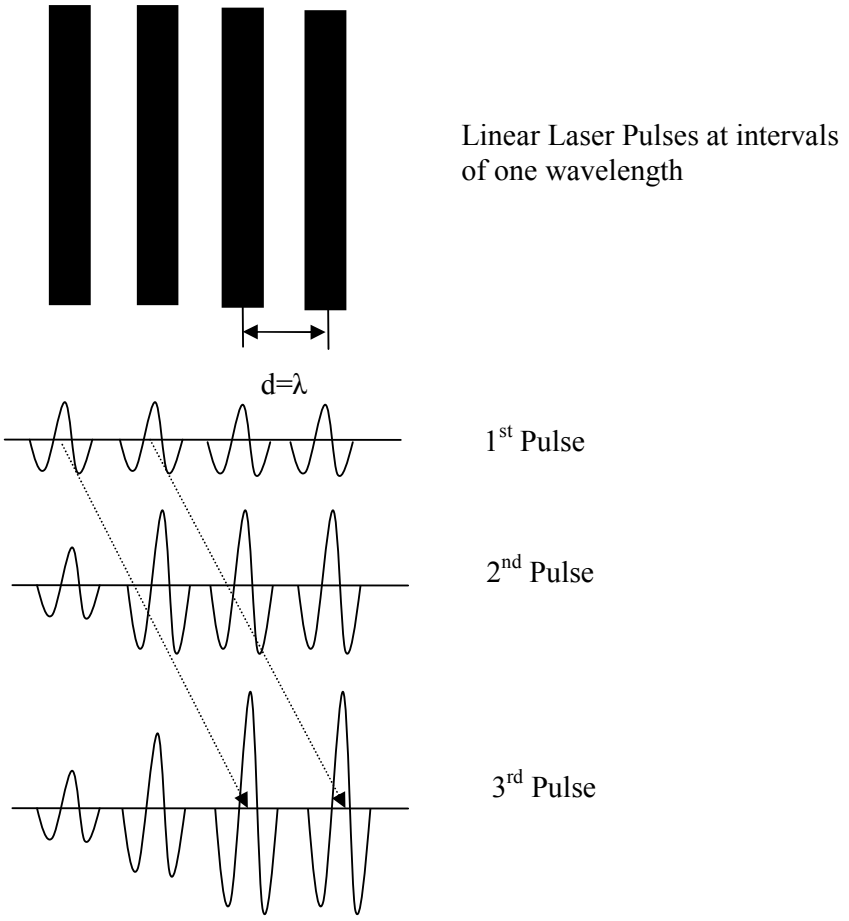

Figure 8.5 – SAWs propagating from multiple pulses causing constructive interference

By making the SLM pattern a series of concentric circles of radius

$$r = L + nd \qquad (8.4.2)$$

where L is the desired focal length and n is any positive integer, the SAWs will focus in the direction of interest and diverge in the opposite direction [166].

Typically laser ultrasound systems will use a Nd:YAG Q-switched laser [166]. A Q-switched laser allows the build up of energy in the laser prior to its pulse emission leading to higher peak power as a result of the shorter pulse duration. Often mode locked lasers are used which emit very short pulses as a result of fixing the phase of all

the exited modes. Repetition rates up to 10s of Kilohertz can be achieved and energy levels per pulse range from μJ to mJ. The pulse width of lasers for laser-UT are typically in the range 8-20ns [166]. Very high frequencies can be produced, but they must be a multiple of the mode-lock frequency.

The ability to generate and detect SAWs at very high frequency without contact with the test component opens up the possibility of imaging surface microstructure with high resolution acoustic imaging. SAWs generated at frequencies in the order of hundreds of MHz could conceivably image in the tens of microns range in steel. This would make the imaging of microcracks and aligned cavitation a real possibility.

As well as physically imaging the microstructural damage caused by creep degradation, a laser-UT technique known as SRAS (Spatially Resolved Acoustic Spectroscopy) could be used to indicate localised variations in material phase velocity [155]. The phase velocity on a localised scale could vary with dislocation accumulation, grain elongation and/or material phase. This could provide useful diagnostic information on the creep state of 0.5CrMoV and 9Cr1Mo steels. SAWs are generated at a fixed excitation frequency then the fringe spacing of the excitation is varied. The amplitude of the resulting SAWs are detected by a detection laser and the highest amplitude will occur when the fringe spacing matches the SAW wavelength, which will in turn provide an accurate measure of the localised material velocity [167].

8.5. Conclusions

The preceding theory provides background for the non-eddy current NDE which will be undertaken in the experimental work detailed in Chapters 9 and 10. With this information and that contained in the previous chapter a plan of experiments for assessing creep damage with NDE has been compiled. Full details are given in Chapters 9 & 10, but below is a summary of the work carried out.

8.5.1. Direct Detection Methods

Laser ultrasound tests on prepared creep-damaged samples were carried out in laboratory conditions at the University of Nottingham. The samples contained differing levels of creep cavitation damage characteristic of that found in 0.5CrMoV pipe-work. High frequency SAWs were generated in the samples to compare the effectiveness of microstructure imaging with an acoustic microscope compared to optical images of the same samples. Secondly, the SRAS method was used to assess the microstruture in terms of grain orientation and whether any correlation between this and the creep condition is possible. Particular attention was put on whether the resolution obtainable is sufficient to characterise the more advanced stages of cavity nucleation and coalescing. Additional discussion on the practical limitations of the test- whether site-based measurements would be possible and whether they would have any advantages over current metallurgical replication techniques is also included. Comparisons with the level of sensitivity and resolution of micro-defects with established focussed phased array ultrasonic technology will also be made.

8.5.2. Bulk Detection Methods

EMAT probes are used to make bulk ultrasonic measurements on 0.5CrMoV samples with low level cavitation to assess its effectiveness as a search tool for creep damage. Two measurements are made, attenuation and ultrasonic velocity. For the former a compression wave EMAT is used and for the latter both shear wave and compression wave generating EMATs are used as comparators.

Barkhausen Noise measurements are taken on a cracked section of Grade 91, to assess whether there is potential for the technique as a site-based method of checking Grade 91 welds for indication of creep degradation.

Chapter 9 Detection of Creep Damage Using Direct Methods

9.1. Introduction

This chapter is the first of two chapters looking at NDE methods that may provide a means to assess creep damage in power generation steam pipe-work. It will concentrate on the detection and quantification of localised creep damage, by direct detection of micro-defects. The next chapter will look at generalised creep damage and how its presence and severity might be implied by measurement of acoustic and/or electromagnetic properties. Because of the scale of the work involved in trying to find and thoroughly test a technique for its suitability in assessing creep damage, these chapters simply take the first steps in assessing the potential suitability of the techniques discussed in Chapter 8. This work does help to set out a series of plausible paths for future research work in this field, as well as assessing the current state and limitations of NDE for creep damage assessment.

This chapter exclusively uses ultrasonic techniques and it is written on the assumption that the reader has reasonable knowledge of basic ultrasonic terminology.

9.2. Pulse-echo ultrasonic detection

An NDE method that has been employed to detect creep damage employs highly focused ultrasonic beams, i.e. high-frequency annular phased arrays, which allow easy variation of focal depth [141]. These have the potential of picking up areas of aligned cavitation or micro-cracks, however the detection of individual cavities would be unfeasible. Structural Integrity Associates, Inc. (www.structint.com) have developed this technology extensively and report that "incipient creep damage is determined by the existence of low amplitude responses exhibiting a 'cloudy' or 'mottled' planar band appearance in the image. This band consists of pixels with reflected UT energy greater than the baseline noise value." [141]. Assessment is also made from the density and amplitude distribution of the responses and uses a metric to ascertain the level of damage in terms of the volume fraction it affects and the severity of the damage.

9.3. Phased array

It is interesting to quantify what can be achieved in ideal laboratory conditions with current equipment owned by RWE and how this compares to Structural Integrity Associates' method. The most tightly focussed ultrasonic beam that can be produced using RWE's current library of phased array probes uses a 15MHz, 16 element annular array. At a distance of 25-35mm, which is approximately the half-wall thickness of a main steam pipe-work section, the spot size is around 0.8mm diameter as shown in Figure 9.1 Annular arrays are axisymmetric so will produce a conical beam rather than the elongated oval beam produced by a linear array. The ultrasonic beam can be focussed at or before the end of the near field, so by using multiple delay laws the

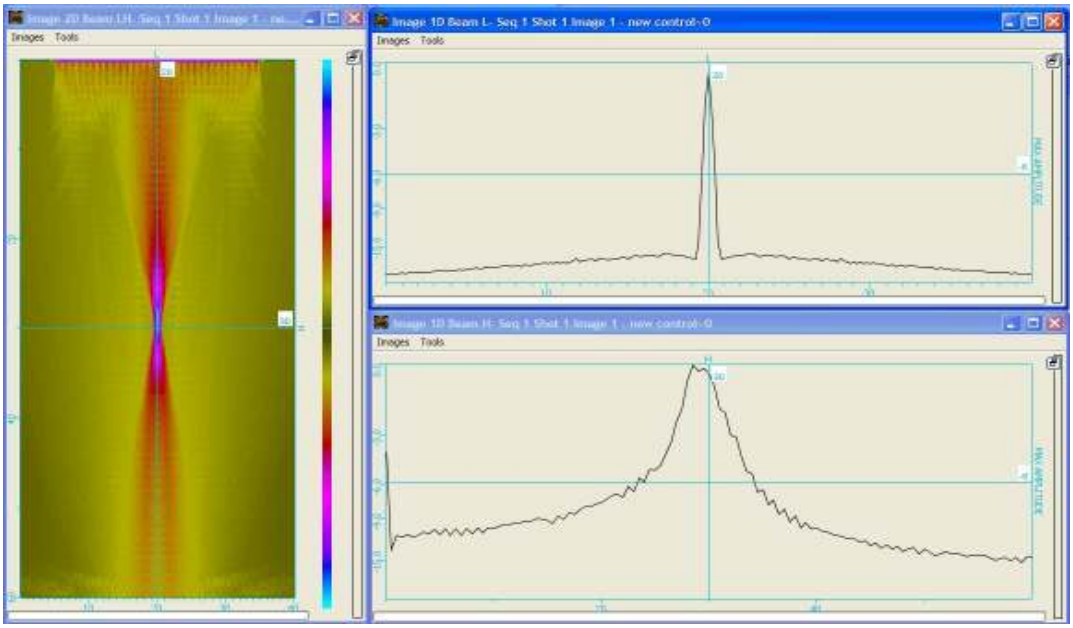

Figure 9.1 – (Left) CIVA simulated beam profile of 15MHz annular probe focussed at 30mm into test object,.(Top Right) Profile across the beam at focal point, (Bottom Right) Profile down the centre of the beam.

transducer can be made to inspect a test piece at a range of focal depths. For each specified focal depth; the depth of field is quite short – the sound amplitude drops by 50% (6dB) before 24mm and after 34mm. To overcome this to an extent a technique called Dynamic Depth Focussing (DDF) can be employed to improve the ultrasonic imaging. DDF does not alter the transmission delay laws, but adds focussing reception delays across a specified range to improve the image focus. The effect of this is shown in a CIVA simulation in Figure 9.2, using DDF on a block containing a series of 1mm diameter side drilled holes at varying depths and offset. I was unable to use a real experiment to illustrate this as the DDF function is not licensed on RWE's copy of the phased array software. Because of this no like-for-like comparison could be made for DDF between CIVA and the real data acquired with Zetec's Ultravision 1.2R4. Comparisons without DDF could be made between real and simulated results, which are of greater significance than those with DDF, since DDF is just a data processing option.

This was done by modelling steel test pieces containing side-drilled holes as reference reflectors. An image of a reference block containing a diagonal line of 1mm diameter side-drilled holes is shown in Figure 9.3. On this block, pulse-echo tests and simulations were performed for 10mm, 20mm, 30mm, 40mm and 50mm deep focus and the results compared. In each case CIVA underestimated the depth of field, so that the clarity/sensitivity reduced either side of the focal depth more than was experienced in reality. To illustrate the correlation between CIVA results and the actual data, a scan of a block containing side-drilled holes, using a 15MHz annular array focussed at 30mm, is displayed next to a CIVA simulation of the same setup in Figure 9.4.

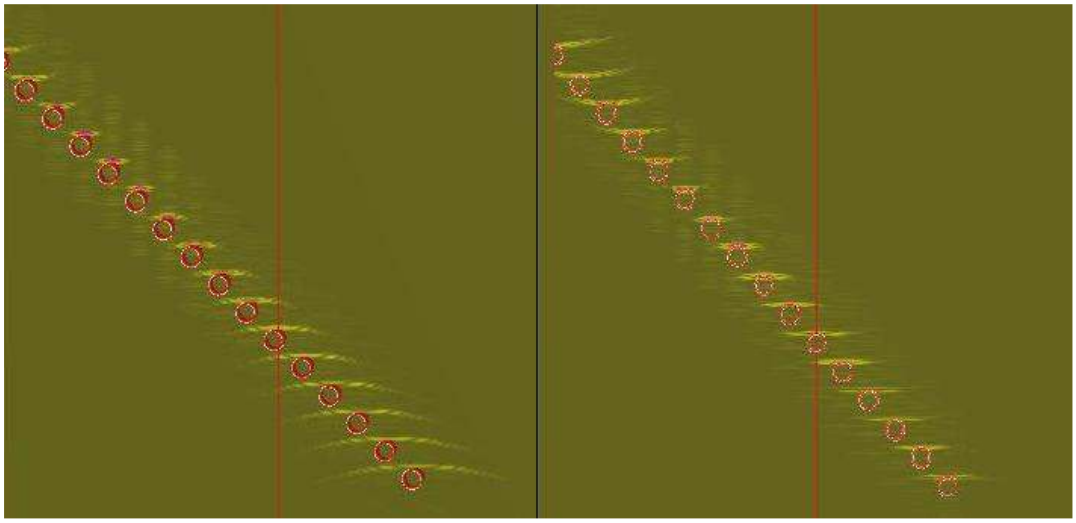

Figure 9.2 – CIVA simulation, 1mm side drilled holes at 30mm focal depth, (left) without DDF and (right) focused at 50mm with DDF. Imaging across the range of hole depths is more consistent with DDF but does not produce as good an image as where specific regions are targeted with focused beam.

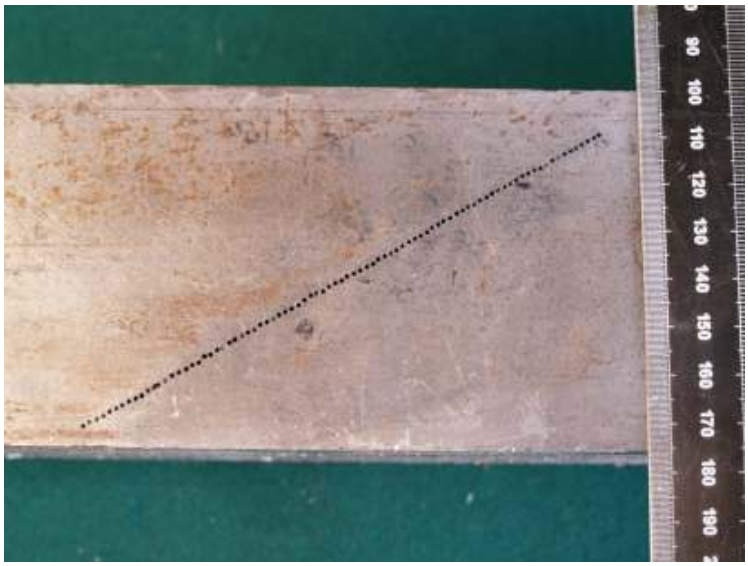

Figure 9.3 – Steel reference block containing 1mm side-drilled holes at various depths

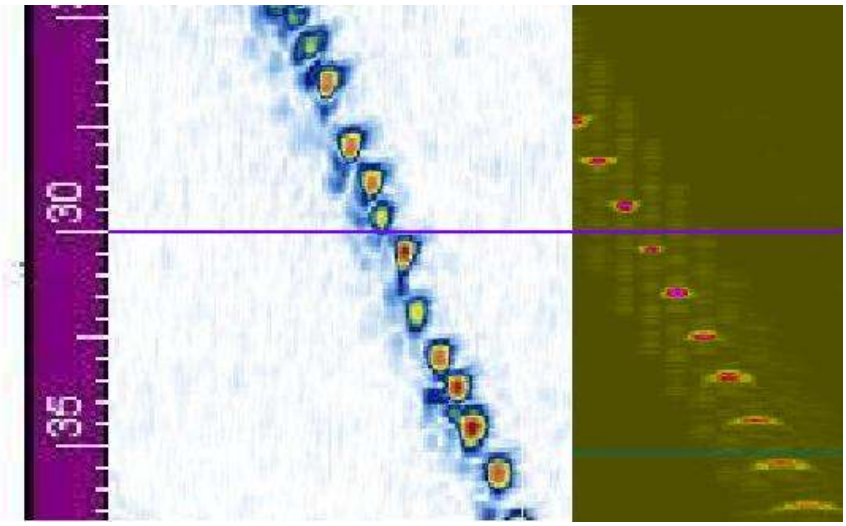

Figure 9.4 – Real data captured with Zetec Ultravision 1.2R (left) compared with CIVA simulation (right), 1mm side drilled holes at 30mm focal depth, scanned with a 15MHz annular phased array probe. Note how the sensitivity/clarity is better in reality than CIVA predicts.

Although it can be seen that DDF will improve the imaging slightly at all depths below the focal distance specified, the holes closest to the focal distance are just as clearly detected with DDF as without, as would be expected. The most important factor is that the correct transmission focal depth is selected and this is demonstrated in Figure 9.5

using a real test block with 1mm side drilled holes. Good sensitivity and resolution appear to be limited to a 10mm range centred around the transmission focal depth for this probe.

An enlarged view of the ultrasonic image, focussed at 25mm, shows that each individual hole can be detected and resolved, and this is true down to 40mm depth which represents the mid-wall depth of the thickest steam pipe-work. Although this has shown that in idealised conditions 1mm defects can be detected and resolved at the mid-wall distance, the micro-damage that is of interest is significantly smaller still.

It has already been shown in Figure 9.1 that the beam spot in the mid-wall region is around 0.8mm in diameter, consequently it is improbable that individual micro-cracks could be resolved using this technology. The ultrasonic wavelength, which for this case is 0.4mm, is generally considered to be equivalent to the minimum resolvable defect size. This is still a factor of 2-10 larger than typical individual micro-cracks. Micro-cracks ultimately form in bands as aligned cavities coalesce so there is the potential that the larger overall effective areas of groups of micro-cracks could be detected.

Having established that effective focussing can be achieved down to 40mm and that multiple transmission focal laws are required for effective imaging, the next stage is to scan some ex-service welded samples. A full description of the samples can be found in Appendix F.

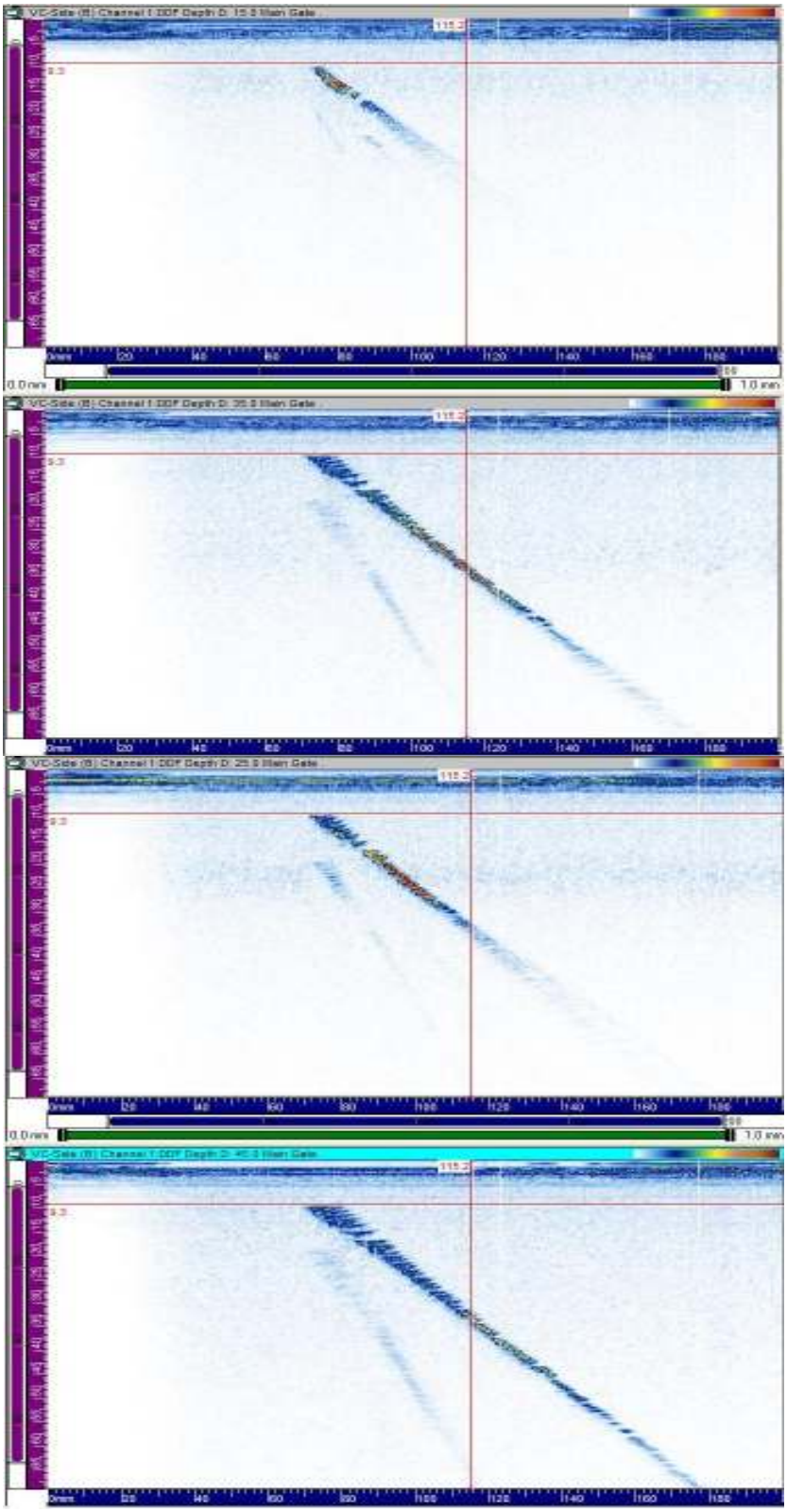

Figure 9.5 – 15MHz phased array B-scan images with DDF of series of 1mm side drilled holes; from top, at 15mm focal depth, at 25mm focal depth, at 35mm focal depth, at 45mm focal depth,.

9.3.1. Experiment PAUT 1

Equipment: *Zetec Omniscan MX with Imasonic 15MHz 16 Element Annular Array probe.*

Reference: *100% FSH reflection from a 1mm hole at 30mm depth. No DAC.*

Key parameters: *Focussed 20-50mm deep in 10mm steps.*

High-pass Filter 11 MHz:Low-pass Filter 22MHz

Digitizing Freq. 100MHz

Voltage 90V, Pulse Width 33ns.

Samples: 5, 7, 8, 9, 10, 12, 15.

In order to provide the best sensitivity through the thickness of the samples, multiple delay laws are required to accommodate focussing at a range of focal depths. For the purposes of consistency, all the delay laws are incorporated into one scan, which has an obvious detrimental effect on the scanning speed. Due to the relative small size of the samples, it was not possible to use a scanning rig, so they had to be scanned slowly by hand using a line encoder. Consequently a few lines of data are missing on the scans but this does not affect the overall image. If this technique were to prove a success, scanning acquisition speeds could be improved by reducing the number of delay laws and increasing the number of scanning passes.

Volume-corrected B-scan images of Samples 7, 10 and 12 are shown in Figures 9.6, 9.7 and 9.8 respectively. Sample 7 contains only low level fusion-face cavitation on the right-hand side of the weld. As would be expected, nothing is shown on the scans in Figure 9.6 in terms of damage. What is interesting however, is that there is a marked

increase in noise levels at the transmission focal depths, seemingly from grain-boundary interaction. This can be seen as a darker band centred at 20mm deep on the left image and just beyond 10mm on the right-hand image. This is a reassuring sign of increased sound intensity at the focal depths. Also of note is the fact that the weld location can be identified by a region of lower amplitude noise. This may be by virtue of the fact that the weld has finer grains, much smaller than the ultrasonic wavelength, causing less reflection.

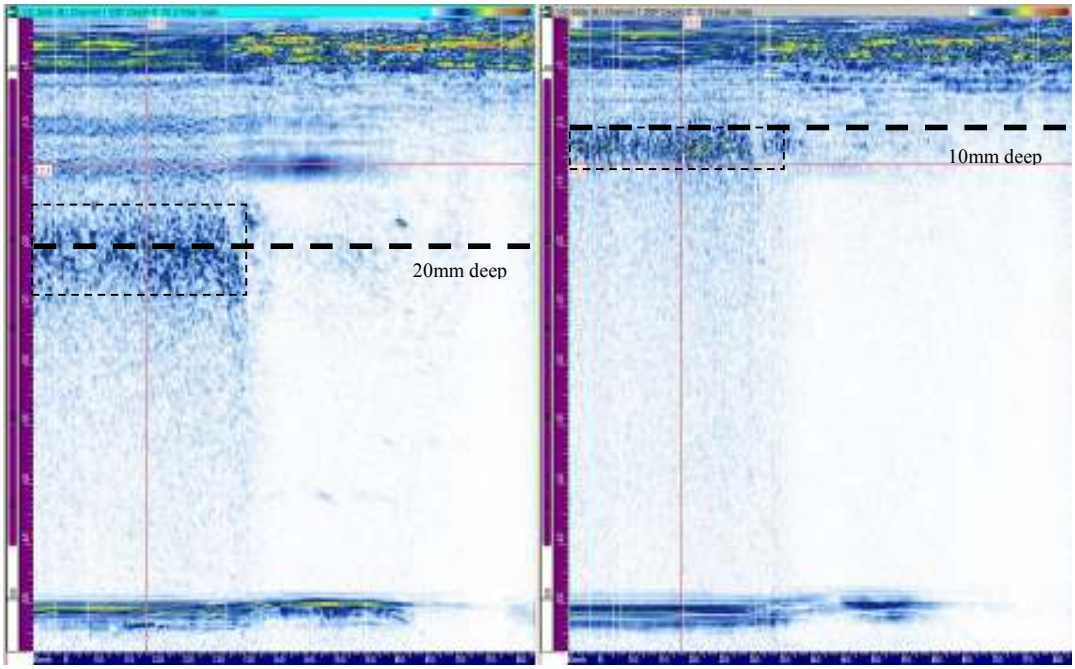

Figure 9.6 – 15MHz phased array B-scans of Sample 7 scanned with focal depth set to 20mm (left) and 10mm (right). Weld is visible to the right of both images due to the reduced ultrasonic interaction.

There are similar responses observed in Figure 9.7, but not entirely the same. In this case, the weld volume of Sample 10, which has very low cavitation levels on the fusion-faces, can again be seen. This time the outline is visible from the fine-grained region of the HAZ and the weld material itself has a similar noise level to that of the parent metal. On this sample the increased sensitivity at the focal depths shows up some features in

the weld itself. A number of different 80%FSH indications are observed at the two focal depths shown. These are most likely slag inclusions or individual gas pores, which potentially could be sub-millimetre. What is important here is that these are only detectable when they occur within about 5mm of the focal depth.

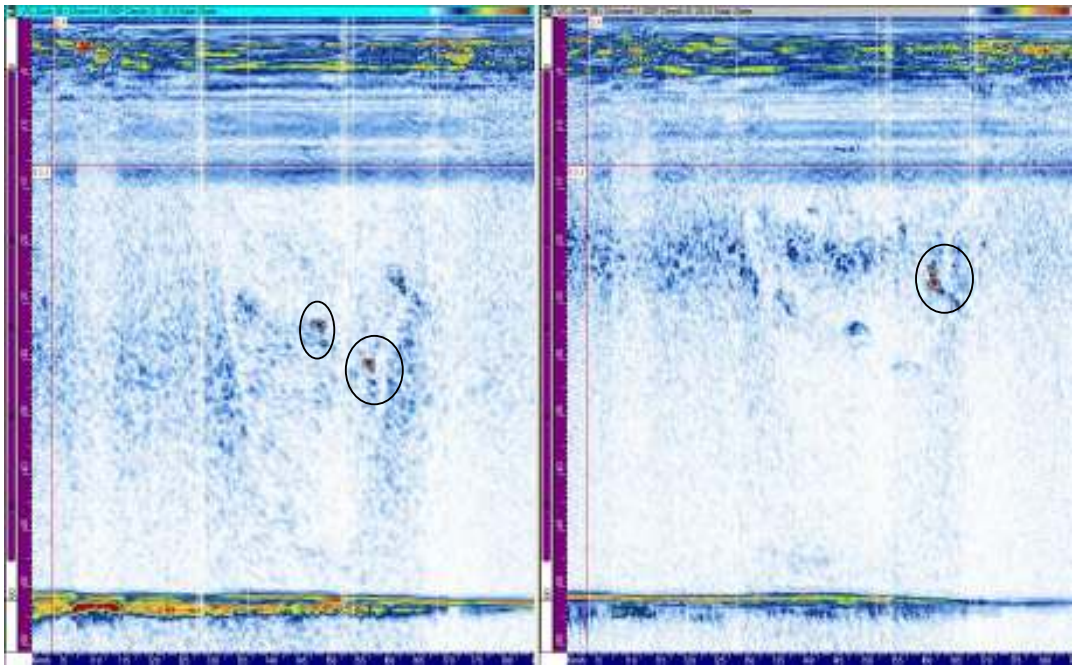

Figure 9.7 – 15MHz phased array B-scans of Sample 10 scanned with focal depth set to 30mm (left) and 20mm (right). Fine-grained HAZ is visible near centre of both images due to the reduced ultrasonic interaction. PossiblesSub-millimetre indications (circled, amplitude 80%FSH) observed in the weld near focal depths.

Sample 12 was the only sample available that has significant fusion-face damage (micro-cracking up to 300µm in length) and that could be accurately line-scanned across the HAZ and weld. The resultant images shown in Figure 9.8 appear to show "clouds" of ultrasonic reflections (15-30%FSH) right on the fusion face. Again this only appears in bands at the focal depths and, like Sample 7, the weld is visible due to the lack of ultrasonic reflection which helps to highlight the indications on the fusion face even more. It is not possible to conclude whether or not this technique can detect the micro-cracking without more samples with known volumetric defects, but it does provide

encouragement and similarities to the work reported by Bisbee [141]. Bisbee's work concludes that highly focused ultrasonic beams can detect grouped cavitation defects, as their amplitude is above the base-line noise of the weldment. When displayed on an B-scan side view, the defects appear as "mottled" patterns in the fusion region. Bisbee's work goes beyond detection of these defects and attempts to characterise damage by comparing the amplitude distribution of the reflections with a creep-damage metric. Assuming that the results shown here can be repeated on further samples, a similar approach could be adopted by RWE. The "mottled" patterns in the fusion region are higher in amplitude (around 30%FSH) than their immediate surroundings (>15%FSH), but not relative to the rest of the images, particularly at 10mm deep focus. This makes it more difficult to extract the data reliably by automated means, even though the human eye can pick out the pattern easily.

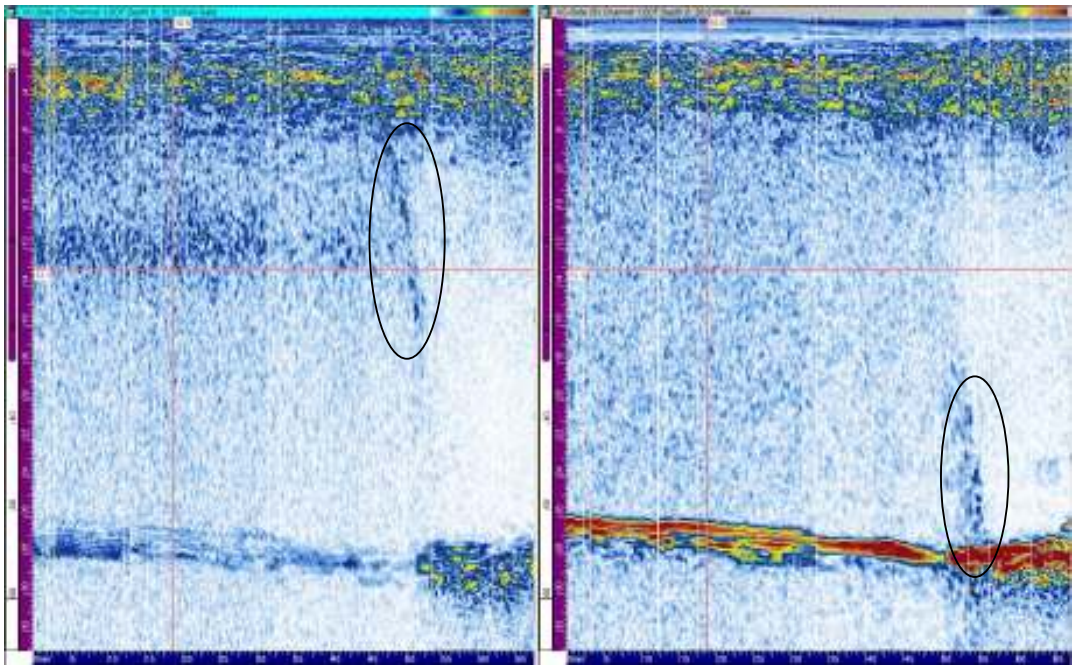

Figure 9.8 – 15MHz phased array B-scan of Sample 12 scanned with focal depth set to 10mm (left) and 20mm (right). Weld is visible to the right of both images due to the reduced ultrasonic interaction. Low amplitude reflection "clouds" can be seen on the fusion face (circled) near the focal depths, possibly as the result of high cavitation levels.

In the absence of more samples containing micro-defects, ultrasonic modelling was used to investigate the size of potentially detectable defects. CIVA 9.1 was used for the simulation, using side-drilled holes as reference indicators.

9.3.2. Experiment PAUT 2

Equipment: *CIVA 9.1 ultrasonic – Defect Response Mode.*

Key parameters: *Focussed 30mm deep.*

16 element Annular Array, 30mm diameter

Centre frequency 15MHz, 6dB bandwidth 90%,

Sampling frequency 100MHz, Phase 61°

Samples: *Isotropic Steel, 60mm thick.*

a) *1mm, 0.5mm, 0.3mm and 0.1mm diameter side-drilled holes at 30mm deep. All defects 5mm long.*
b) *1mm diameter (5mm long), 3 x 0.3mm diameter (0.3mm long), 2 x 0.3mm diameter (0.3mm long), 1 x 0.3mm diameter (0.3mm long) side-drilled holes. (Spaced 0.1mm horizontally, 0.5mm vertically).*
c) *1mm diameter (5mm long), 3 x 0.15mm diameter (0.3mm long), 2 x 0.15mm diameter (0.3mm long), 1 x 0.15mm diameter (0.3mm long) side-drilled holes (spaced 0.1mm horizontally and 0.5mm vertically).*

An ultrasonic simulation was set up to replicate the inspection of a 1mm diameter side-drilled hole in steel using a 15MHz annular array probe as this was used as the reference sensitivity in Experiment PAUT 1. Additional reflectors were placed adjacent to the 1mm hole representing smaller defects and the relative reflected sound intensities were

compared. A total of three simulations were performed using different small reflectors, these are designated a), b) and c) and are detailed above.

The first simulation, shown in Figure 9.9. uses decreasing sized side drilled holes. Given that the 1mm side drilled hole should produce a 100%FSH reflection, the simulation suggests that the 0.5mm, 0.3mm and 0.1mm holes would give reflection amplitudes of 74%FSH, 49%FSH and 34%FSH respectively.

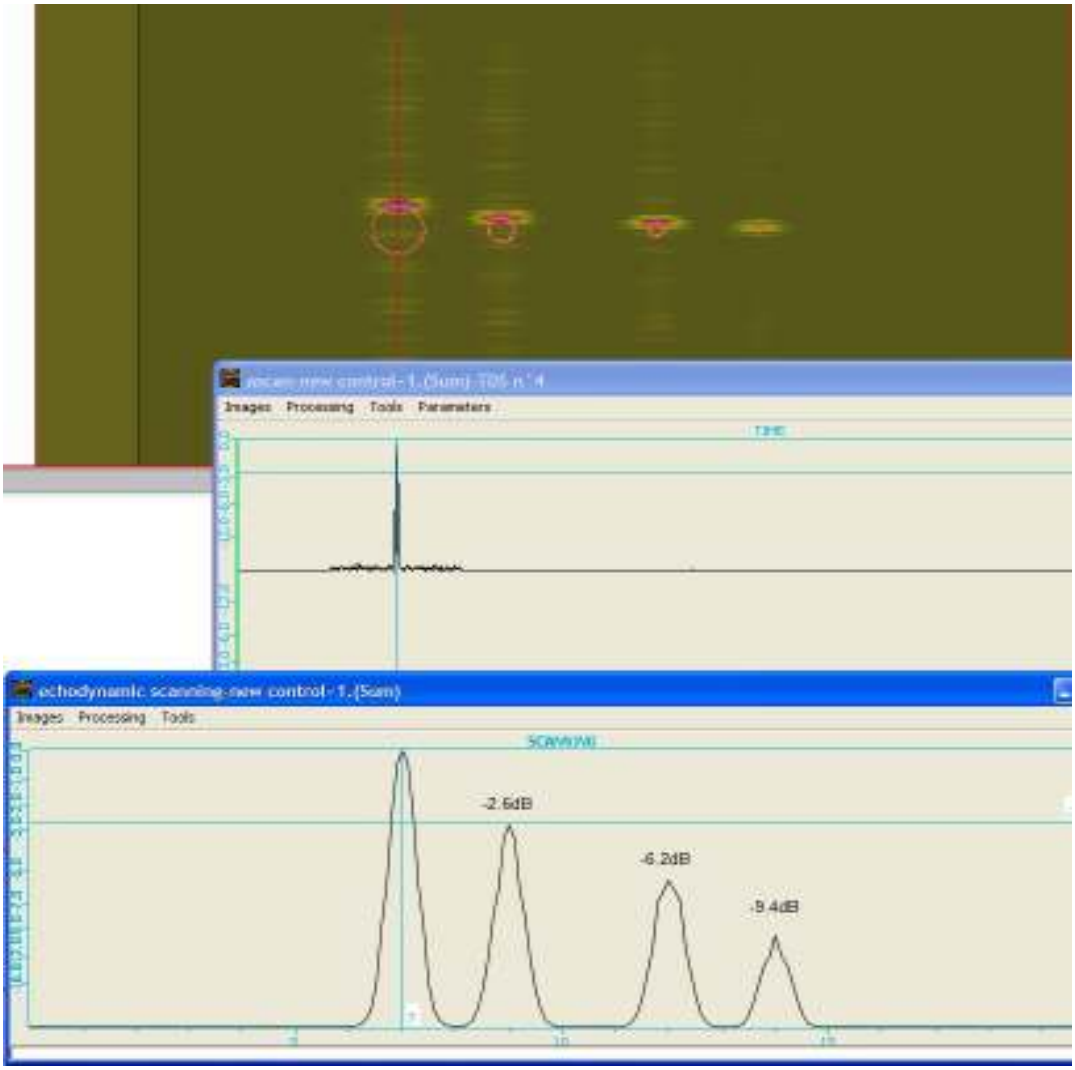

Figure 9.9 – CIVA simulated 15MHz phased array inspection defect response to side-drilled holes, (Top) B-scan with hole circumference overlaid, (Middle) profile along centre of beam through largest hole, (Bottom) echodynamic showing maximum reflected sound for all four side-drilled hole diameters

The reflection from the smallest (0.1mm diameter) hole is the closest in amplitude to the reflection seen on the fusion face of Sample 12, but is still considerably higher. However, the side drilled holes used are 5mm long, which is far greater than the length of a microcrack.

For the second simulation shorter defects are used, this time just 0.3mm in length, which is comparable to the length of some of the micro-cracks seen on the replica at the surface of Sample 12. 0.3mm diameter reflectors are compared this time individually and in clusters of two and three.

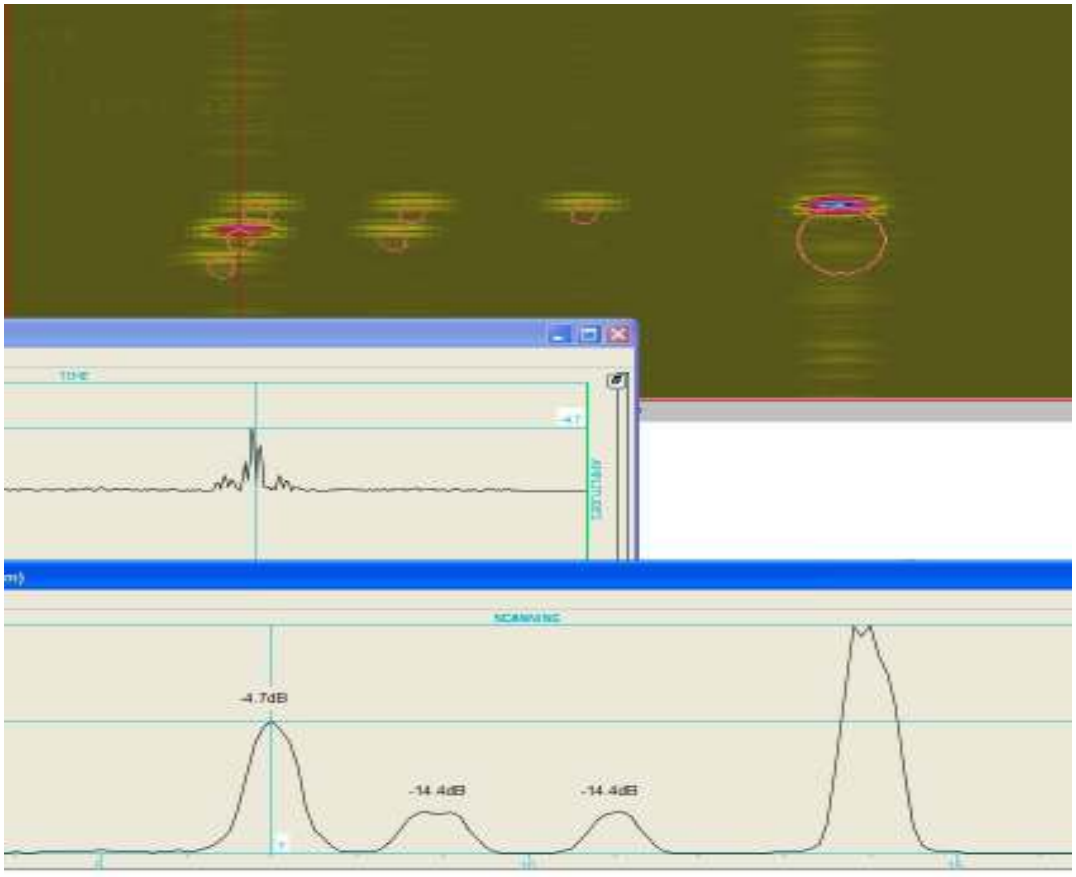

Figure 9.10 – CIVA simulated 15MHz phased array inspection defect response to clustered and individual micro-defects, (Top) B-scan with hole circumference overlaid, (Middle) profile along centre of beam through triple reflector, (Bottom) echodynamic showing maximum reflected sound for all clusters and individual micro-defects.

Looking at the echodynamic in Figure 9.10, there is little difference in the amplitude of response from the single reflector and the double reflector (both 19%FSH), but there is a far greater amplitude from the triple reflector (58%FSH); this is most likely due to the fact that the overall size of the triple reflector (0.75mm) is comparable in size to the beam width at this point (0.8mm). The amplitude from the single and double reflectors are similar to those witnessed on Sample 12, though the reflector sizes are still likely bigger than real micro-cracks. If the increased amplitude from a greater number of clustered defects is genuine, and not just a computational quirk of the simulation, then it is possible that the responses witnessed on Sample 12 are large clusters of smaller defects.

The third simulation is the same as the second, but halves the diameter of the reflectors to 0.15mm diameter. Again the cluster of three defects produces a much stronger response (36%FSH) than the single and double reflectors (13%FSH). What is noticeable this time is that the cluster of three defects covers the same area (0.5mm x 0.3mm) as the double reflector in the previous simulation, yet has a higher amplitude response.

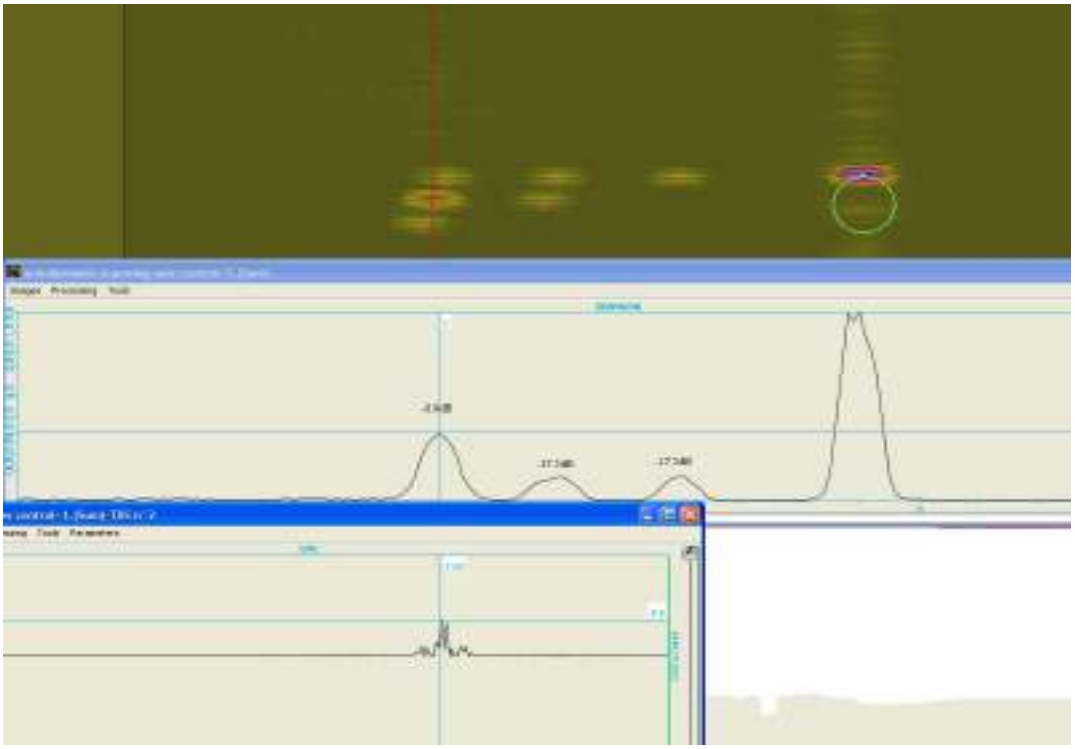

Figure 9.11 – CIVA simulated 15MHz phased array inspection defect response to clustered and individual micro-defects, (Top) B-scan with hole circumference overlaid, (Middle) profile along centre of beam through triple reflector, (Bottom) echodynamic showing maximum reflected sound for all clusters and individual micro-defects.

The outcome of this simulation (Figure 9.11) would suggest that the amplitude of the responses seen in Sample 12 is consistent with groups of micro-crack sized defects. However, there are limitations with any simulation and it is almost impossible to verify the accuracy of the software in simulating such small responses. In reality the micro-cracks will most likely behave very differently to the side drilled holes used and will not be preferentially orientated.

A common theme with trying to prove the sensitivity of an ultrasonic test to micro-defects is the lack of samples with clearly defined volumetric defects. Using real samples, this problem will never be overcome because the samples must be destructively

tested to examine the volume thoroughly. A possible alternative to real samples is testing a 3-D laser engraved image in a glass block. This technique has recently been employed to create simulated micro-cracks [168] for looking at creep damage with ultrasonic birefringence and velocity measurements. The glass used behaves very similarly to steel in terms of its acoustic velocity; 5590m/s for L-waves and 3360m/s for T-waves. The material is isotropic at ultrasonic frequencies, noise is considerably lower than in steel and attenuation is comparable. Using this technique, known volumetric micro-defects can be placed in a test sample to replicate creep damage. The defects are made up of a series of tightly-packed cracks created by the laser engraving technique, so are more elongated than a creep void, but comparable in size and shape to a line of coalesced creep voids. Although in the tests by Szelążek, reflection from the defects was insignificant, the work was carried out at just 2.25MHz, giving an acoustic wavelength of 2.5mm. This did demonstrate some velocity variation and birefringence with damage concentration, however, the effects are likely to be stronger at higher frequency, due to the smaller wavelength.

9.3.3. Experiment PAUT 3

Equipment: *Zetec Omniscan MX with Imasonic 15MHz 16 Element Annular Array probe.*

Reference: *100% FSH reflection from a 1mm hole at 30mm depth.*

Key parameters: *Focussed 20-50mm deep in 5mm steps.*

High-pass Filter 11 MHz:Low-pass Filter 22MHz

Digitizing Freq. 100MHz, Recurrence 2000,

Voltage 90V, Pulse Width 33ns.

Samples: *Glass block containing 3D laser-engraved image (Figure 9.11).*

Using the same setup as was used in Experiment PAUT 1, a single line scan of the 3D laser-engraved image shown in Figure 9.12 was taken. The image is formed from a series of spots which are approximately star-shaped and around 100μm in diameter and spaced up to 200μm apart.

Figure 9.13 shows the resultant B-scan image focussed at 25mm deep (left) and 35mm deep (right). The resultant image is an accurate representation of the 3D image with fairly strong reflections (up to 70%FSH) in places. This provides some more supporting evidence to suggest that clusters of small defects can prove to be reasonable reflectors when packed tightly even when they are not preferentially orientated.

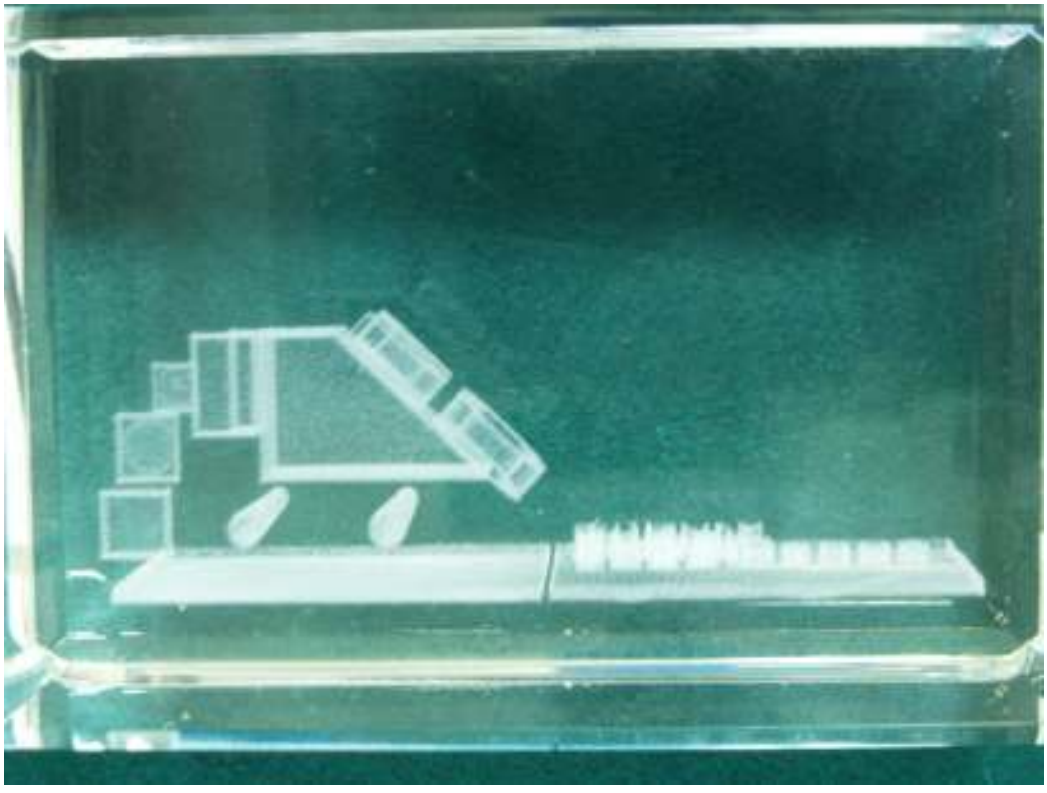

Figure 9.12 – Photograph of the 3D laser engraved glass block image made up of <100μm spots.

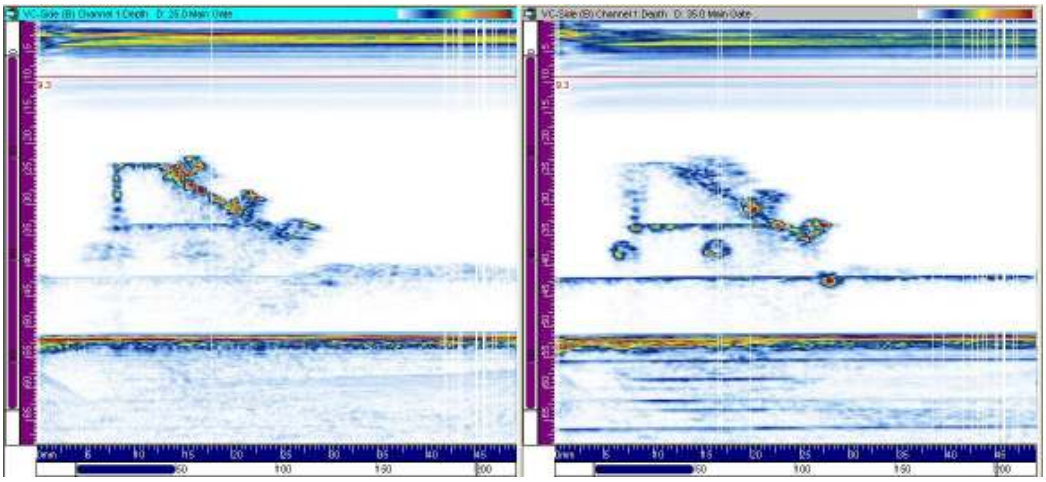

Figure 9.13 – B-scan image of laser-engraved glass block, using 15MHz annular array focused at 25mm (left and 35mm (right). This is a well-characterised sample, so the geometric position of each feature can be measured accurately and compared with ultrasonic results.

9.3.4. Conclusion on DDF Phased Array UT

The work presented here shows some consistency with the work of Bisbee [141], however the lack of samples and confidence in the accuracy of the simulation result in a shortage of evidence. There is scope to take this method forward using the laser-engraved glass block technology to make samples and investigate the effect of defects on ultrasonic birefringence and velocity as well as direct detection of clustered defects. It is worth noting however, that signal-noise ratios are far better in glass than steel. Testing of more samples showing signs of micro-cracking in the weld fusion region would also be required, if they become available. If good results can be obtained and verified then there is use for this technique in characterising sub-critical defects in welded components using a characterisation metric similar to that created by Structural Integrity Associates. A super-resolution approach may well help to enhance the B-scan images, allowing the indications (assuming they are a real feature) on the fusion face to remain but reducing the appearance of the non-relevant signals. A speckle quantification

metric, such as SDI [169] could then be use to evaluate the relevant features and compare them against a damage characterisation matrix if enough samples were made available.

In terms of overall component creep-life assessment however, the sensitivity of the system would need to be increased by at least an order of magnitude to compete with metallurgical replication, which is physically impossible at the ultrasonic path lengths required. Technology exists that has the potential to offer the increased sensitivity and resolution required, but only at the surface making it akin to metallurgical replication. This is the subject of the second half of this chapter – Laser generated ultrasound.

9.4. Laser Generated Ultrasound

In order to achieve the wavelengths necessary to resolve micro-defects an Optical Scanning Acoustic Microscope (OSAM) at Nottingham University was used to inspect samples containing creep cavitation and micro-cracking damage. A description of the principle of laser generated ultrasound can be found in Section 8.4.

This particular OSAM can be used to produce Surface Acoustic Waves (SAWs) in test material at frequencies up to 164MHz. In low carbon steels such as 0.5CrMoV where the SAW velocity is around 2900m/s; this produces a wave with a wavelength of 18μm. Taking an approximate rule of thumb that resolvable defect size is half the wavelength, so reflections from 9μm defects should be detectable.

In addition to potentially having the resolution to directly detect some micro-defects associated with creep deformation, the OSAM system can map the localised SAW velocity. Due to the highly-localised nature of creep in weldments, any influence of

creep damage on the bulk wave velocity in the material will likely be diluted and therefore undetectable. Using the OSAM to measure SAW velocity over short distances will provide more detailed information on sound wave velocity differences in the presence of creep damage. It has been reported that when assessing bulk creep damage of parent material there is a sharp decrease in the ultrasonic velocity at the onset of micro-cracking [170]. The study by Ohtani[170] also suggested however, that there is not a gradual reduction in velocity in the earlier stages of creep damage to reflect the damage progression but that there is only an observable change from the end of the secondary creep stage onwards. By analysing the velocity variations with local changes in creep damage, it should be possible to assess whether the findings of that study hold for localised creep damage in weldments.

Four samples, containing a total of six areas of interest, were used for this test. All the samples were flat, parallel-sided sections of ex-service 0.5CrMoV, which had been polished to a 1μm finish and triple-polished and etched in 2% Nital to reveal their microstructure. Two of the six areas contained no observable creep damage and the other four contained distinctly different damage levels as detailed in Table 9.1. One of the undamaged areas had a partially oxidised surface as a comparison to see how surface condition affected the consistency of results.

Sample	Region	Damage level	Notes
1	-	None	Oxidised surface. Parent material.
2	-	None	Parent material.
3	1	High	Aligned cavities in HAZ.
3	2	Medium	Some aligned cavities in HAZ.
4	1	Microcracking	Fine-grained HAZ
4	2	Med-High	Weld volume, aligned cavities

Table 9.1 – Creep damage level of samples for laser UT experiments.

All experiments were carried out by Dr. S. Sharples at the University of Nottingham using the department's laboratory OSAM. The OSAM uses a Q-switched mode-locked Nd-YAG laser with an 82MHz fundamental frequency. The SLM is 256 pixels x 256 pixels and an image of 1mm^2 of the surface was scanned at a resolution of 10μm.

9.4.1. Experiment LGUT 1

Equipment: *University of Nottingham OSAM.*

Reference: *Optical microscope images.*

Key parameters: *SAW velocity 164MHz.*

Resolution 10μm.

Samples: 6 creep damaged areas of 0.5CrMoV samples detailed in Table 9.1.

Using the OSAM an optical image of the sample can be produced from the DC component of the returned light on the detector. Compared to an optical microscope, this provides a low resolution image of the surface microstructure, which offers no advantages over metallurgical replication. The amplitude of the SAW can be used to create an acoustic image of the surface to a depth approximately one wavelength [166].

The resultant images for the six samples are shown in Figures 9.14 – 9.19 alongside comparative images from an optical microscope. In Figures 9.16 and 9.18 where the greatest damage occurs, features can be observed on the OSAM image but it lacks the detail and clarity of the optical image. Surface indications (Figure 9.14) and non-relevant indications (Figure. 9.15) are just visible on the images.

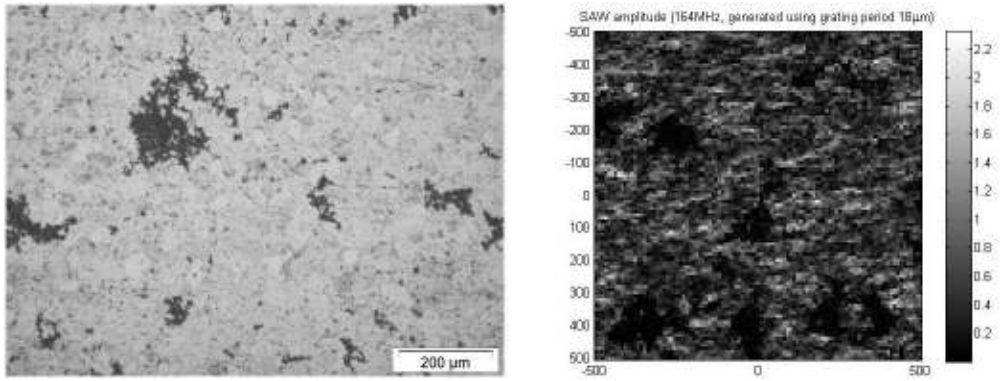

Figure 9.14 – Sample 1: No creep damage, oxidised surface. Comparison between typical surface images produced by optical microscope (left) and OSAM (right).

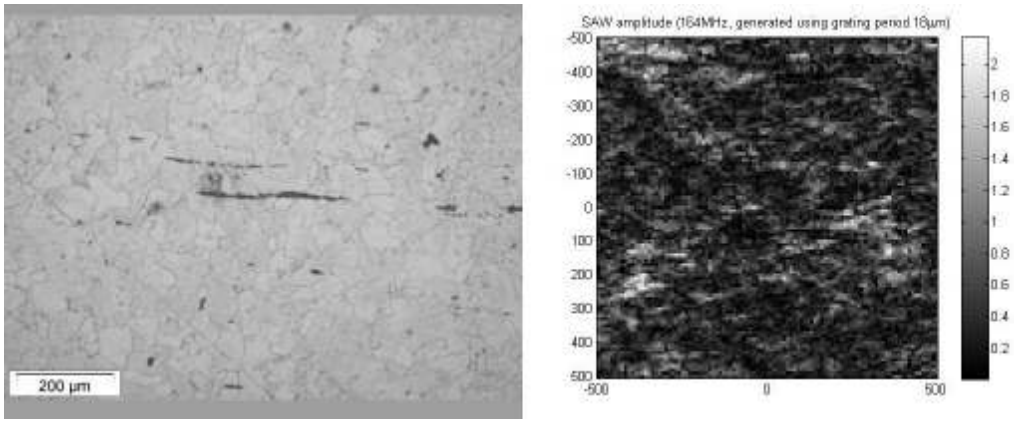

Figure 9.15 – Sample 2: No creep damage. Comparison between typical surface images produced by optical microscope (left) and OSAM (right).

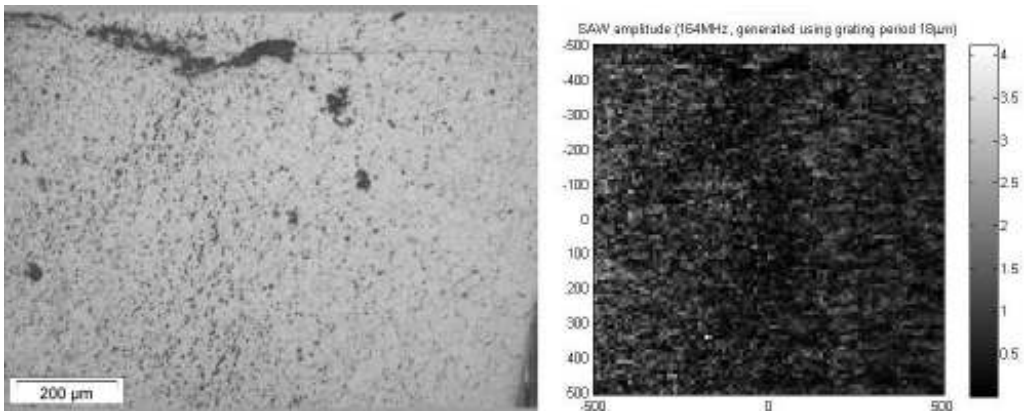

Figure 9.16 – Sample 3 Region 1: High creep damage. Comparison between typical surface images produced by optical microscope (left) and OSAM (right).

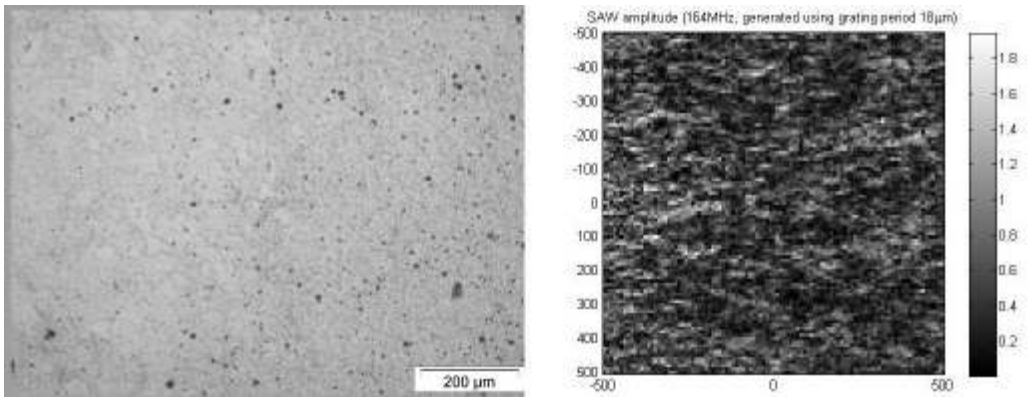

Figure 9.17 – Sample 3 Region 2: Medium creep damage. Comparison between typical surface images produced by optical microscope (left) and OSAM (right).

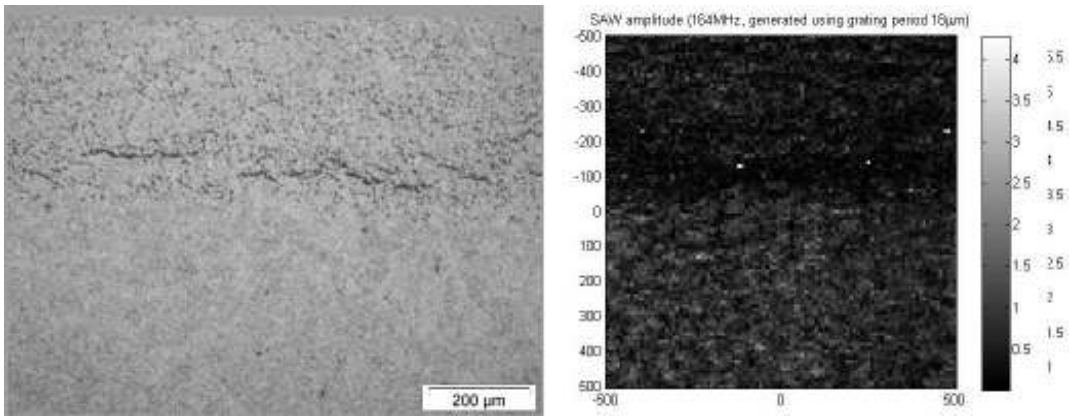

Figure 9.18 – Sample 4 Region 1: Micro-cracking. Comparison between typical surface images produced by optical microscope (left) and OSAM (right).

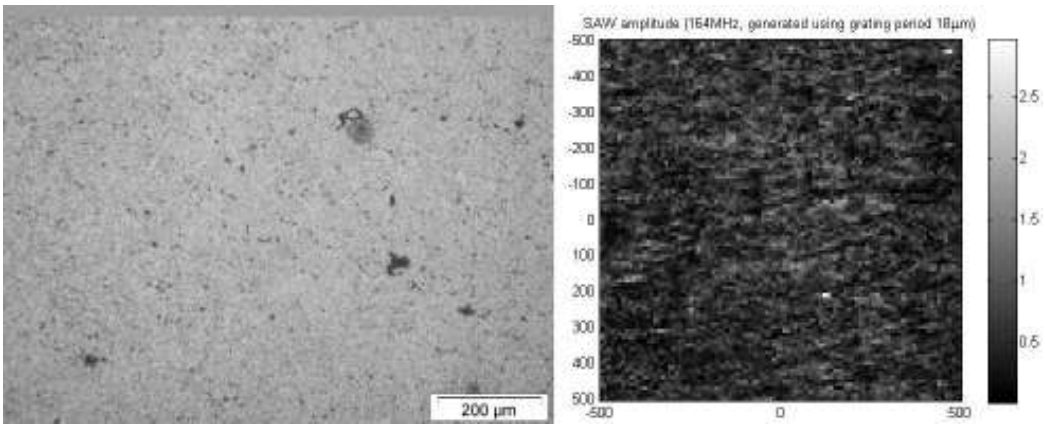

Figure 9.19 – Sample 4 Region 2: Med-High weld volume creep damage. Comparison between typical surface images produced by optical microscope (left) and OSAM (right).

In isolation, the above method offers no benefit over the current method of creep assessment through metallurgical replication; this is because the output lacks the clarity required to assess creep damage, the level of surface preparation is the same and the cost of the equipment is tens of thousands of pounds rather than hundreds. There are also notable drawbacks in terms of equipment size and resolution. Although micro-cracks and very high levels of aligned cavitation on the samples can be seen using the OSAM, at medium levels of cavitation the resolution of the system is insufficient to assess the creep degradation condition. However, it may be possible to extract more relevant data from these images through some novel image processing method. I have opted to follow a different approach, since there is more ultrasonic data acquired with this system which provides an alternative system of analysis for creep damage.

9.4.2. Experiment LGUT 2

Equipment: *University of Nottingham OSAM.*

Reference: *Optical microscope images.*

Key parameters: *SAW velocity 164MHz.*

Resolution 100µm.

Scanning orientation maintained

Samples: 6 creep damaged areas of 0.5CrMoV samples detailed in Table 9.1.

Using the same data from the OSAM as was collected for Experiment LGUT 1, the SAW velocity can be measured over 100µm increments. The SAWs propagate left to right from a generation region 192µm x 192µm. The six SAW velocity maps are shown in Figures 9.20 – 9.25.

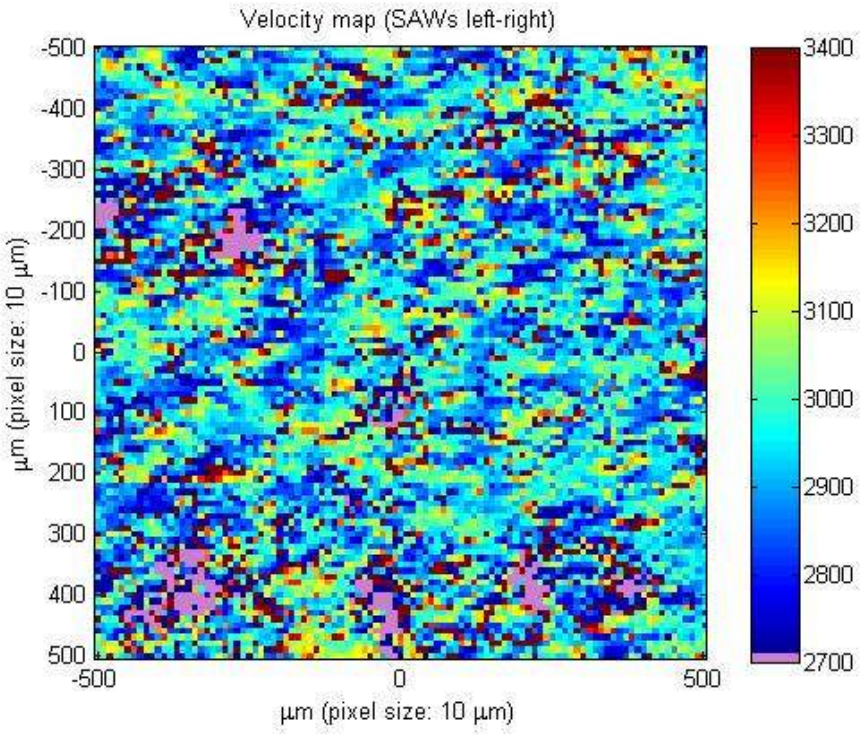

Figure 9.20 – Sample 1: No creep damage, oxidised surface. Mixture of SAW velocities observed.

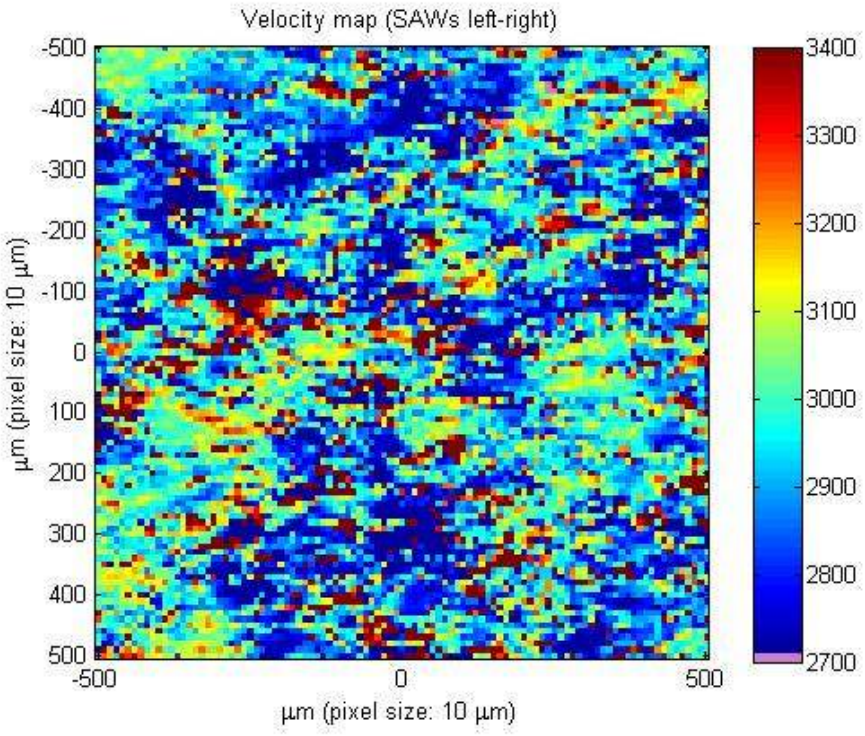

Figure 9.21 – Sample 2: No creep damage. Mixture of SAW velocities observed.

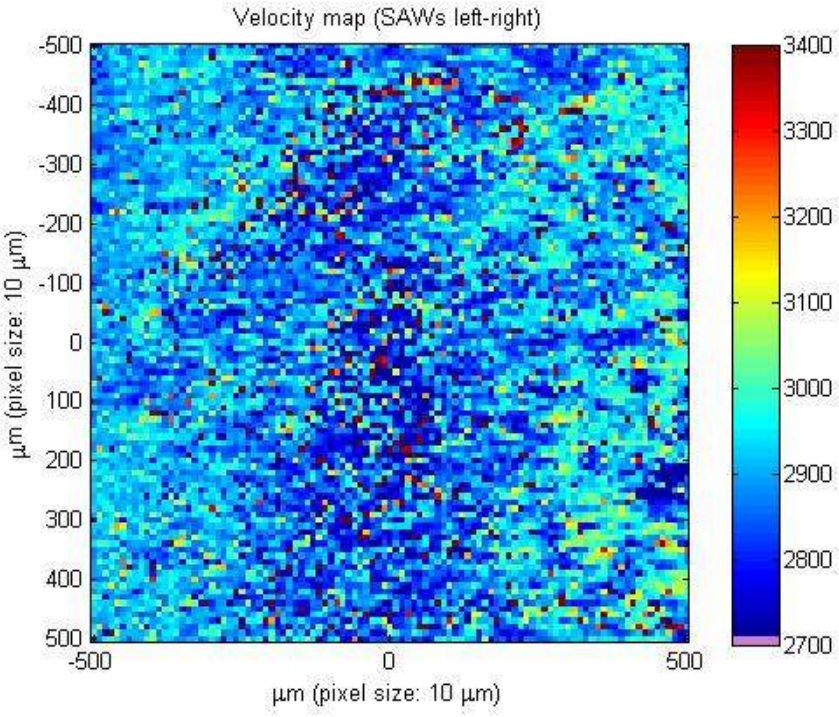

Figure 9.22 – Sample 3 Region 1: High levels of creep cavitation damage. Majority of SAW velocities at or below 2900m/s.

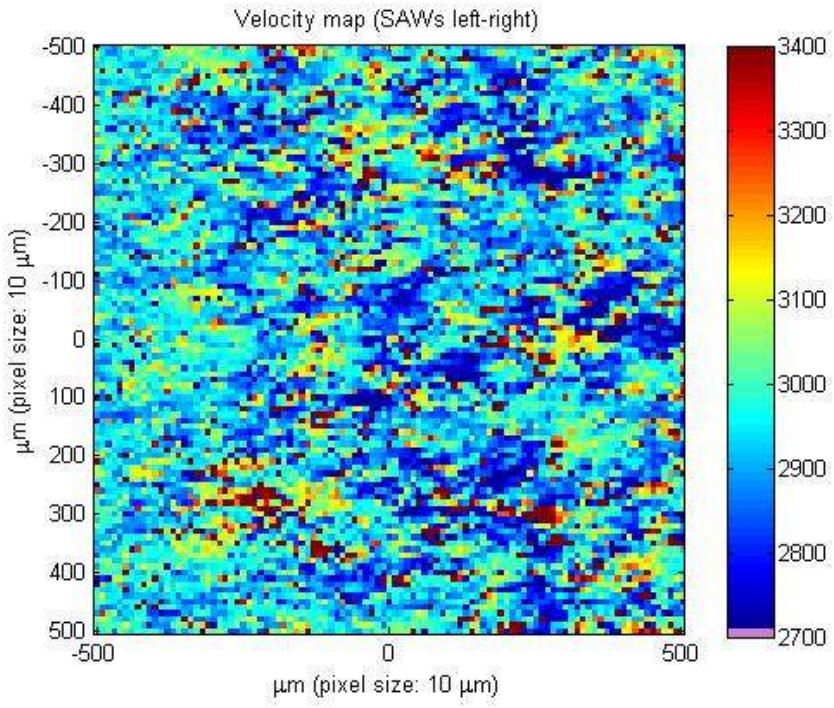

Figure 9.23 – Sample 3 Region 2: Medium levels of creep cavitation damage. Mixture of SAW velocities observed.

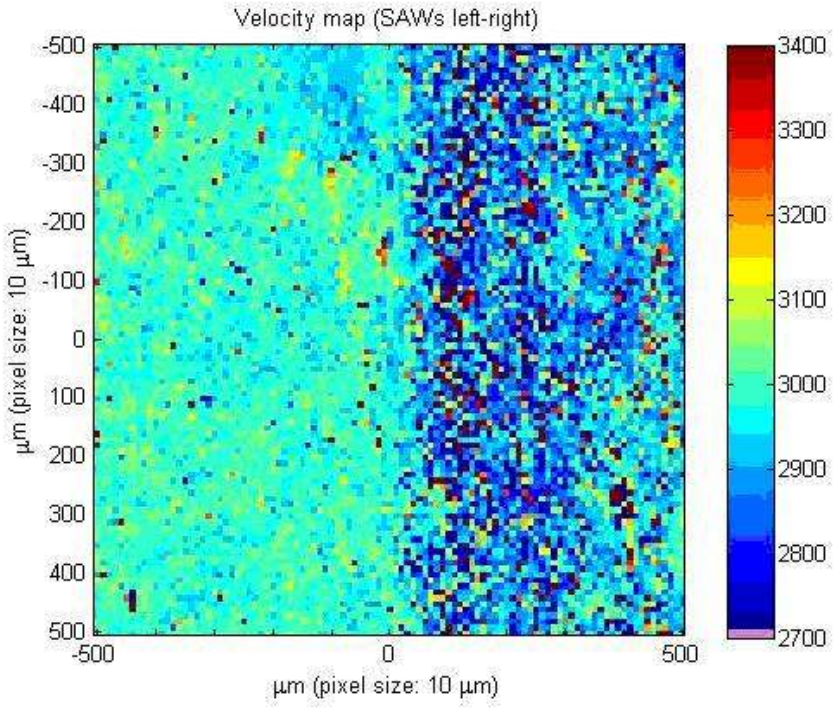

Figure 9.24 – Sample 4 Region 1: Micro-cracking near fusion face. Localised low SAW velocities observed.

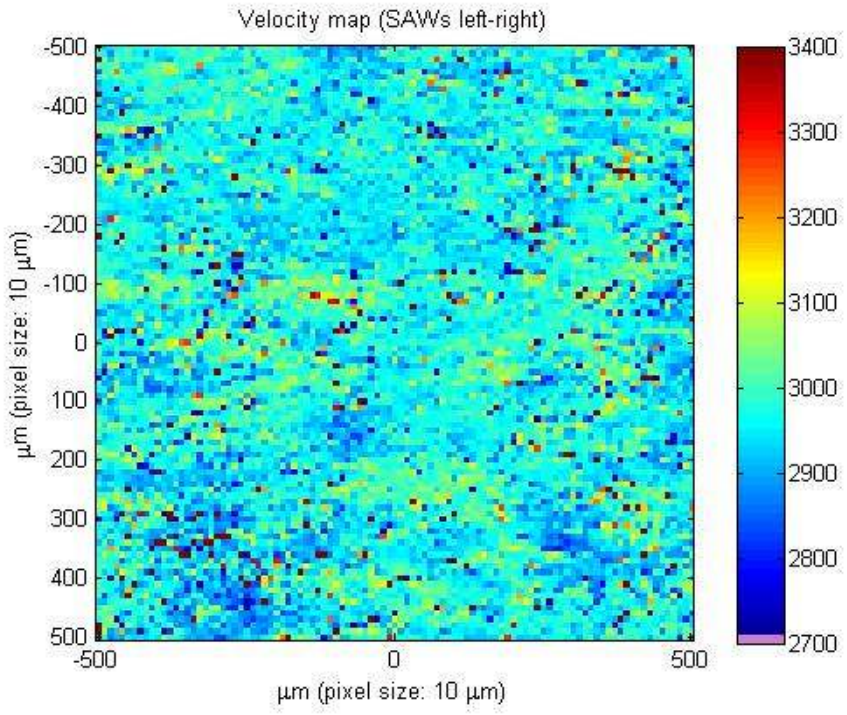

Figure 9.25 – Sample 4 Region 2: Med-High creep cavitation levels in the weld volume. Low deviation in SAW velocities observed.

Immediately there is a lot of visible variation in the velocity maps between the samples. There are also some similarities, particularly between Figures 9.20 and 9.21, which contain a large variety of SAW velocities mostly in the range 2700-3100m/s, which represents an even spread +/-200m/s from the typical SAW velocity of this material (2900m/s). These samples contain very similar damage levels, but have different surface conditions. The surface condition appears to have little or no influence on the results and the fact that the two "no-damage" samples have a similar SAW velocity make-up is encouraging. Figure 9.26 shows the percentage area of each image that contains SAW velocities below 2900m/s. This confirms that Samples 1 and 2 have similar amounts of low-velocity SAWs across the test area. The next most similar velocity map is that of the medium cavitation level damage in Figure 9.23. It appears very similar in make up to the two "no-damage" samples, with just a slight reduction in the concentration of

velocities around 3100m/s.

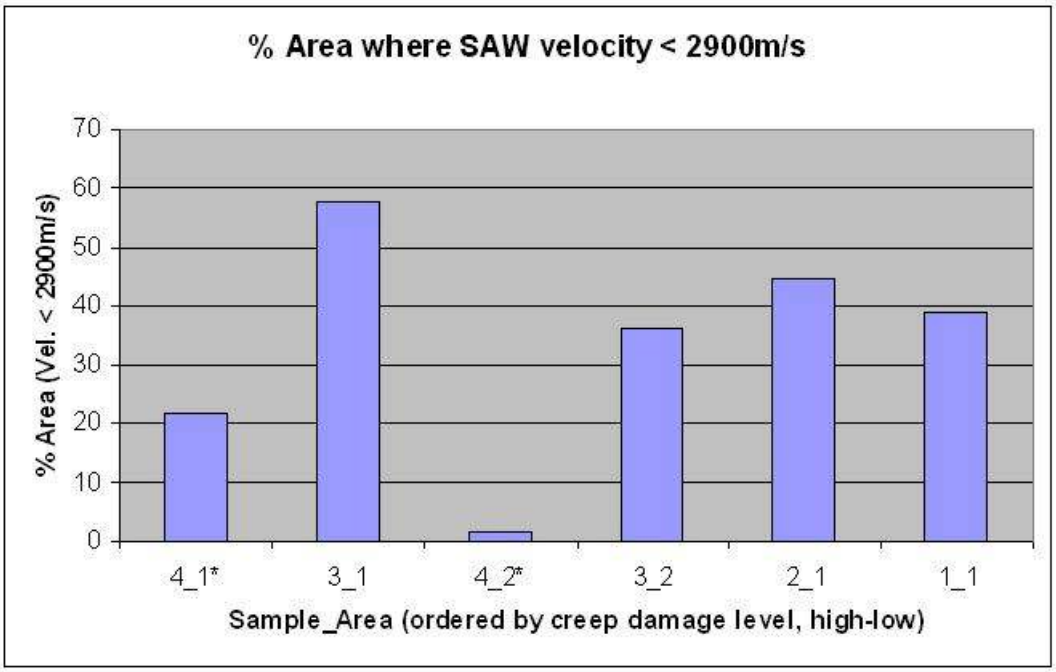

*Figure 9.26 – Plot showing % Area where SAW velocity is less than 2900m/s across all samples. Area is high for heavily damaged parent metal and low for weld material. *Denotes sample containing weld.*

Sample 3 area 1 has the lowest overall percentage of areas where the SAW velocity is below 2900m/s and this represents the area of parent material with the greatest creep damage. Sample 4 area 1 and Sample 4 area 2, both contain weld material which appears to have a much more consistent SAW velocity make up around 2900m/s, this is reflected in their higher mean SAW velocity of 3122m/s compared to 3036-3069m/s for the other samples. By removing the welded areas from the analysis and just concentrating on parent material, the data takes on a more encouraging trend as shown in Figure 9.27.

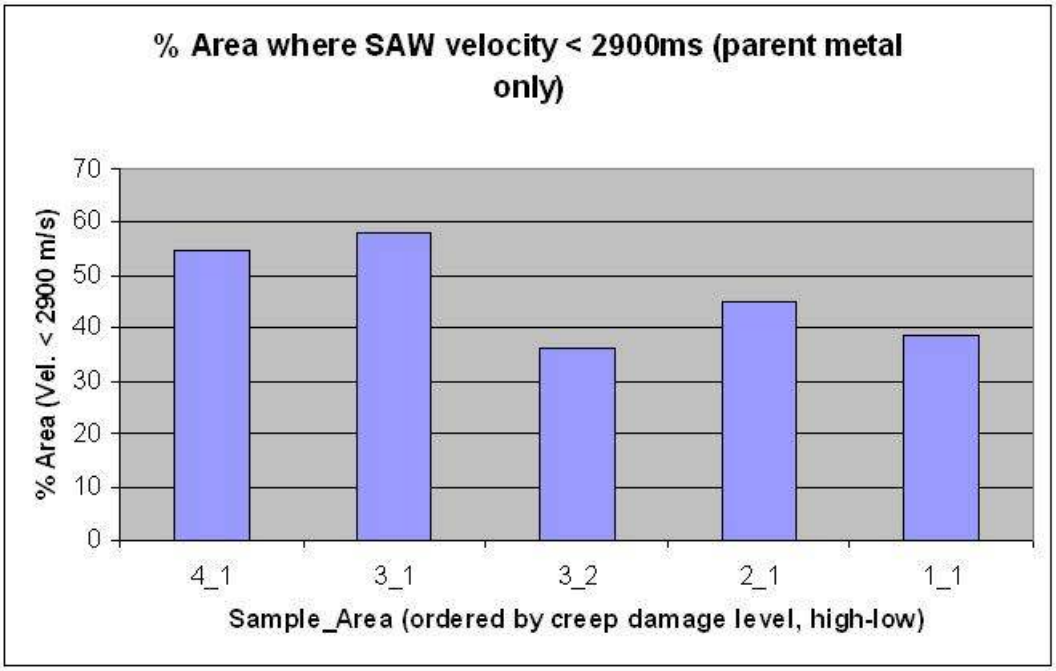

Figure 9.27 – Plot showing % Area where SAW velocity is less than 2900m/s across all parent metal area of samples. Area is high for heavily damaged parent material compared to less damaged areas.

Here, the two heavily damaged areas can be clearly distinguished from the other three areas of parent material.

Another point of interest is that the two visible areas of weld metal; bottom half of Figure 9.24 and the whole of Figure 9.25, have far less variation in their SAW velocity make up than areas of parent material. The undamaged area of weld in Figure 9.24 has very consistent velocity components around 3000m/s. The overall deviation of the SAW velocities across all sample areas is shown in Figure 9.28, indicating that there is a measurable decrease in standard deviation of velocities with increased damage and that there is very little deviation of velocity in the weld region.

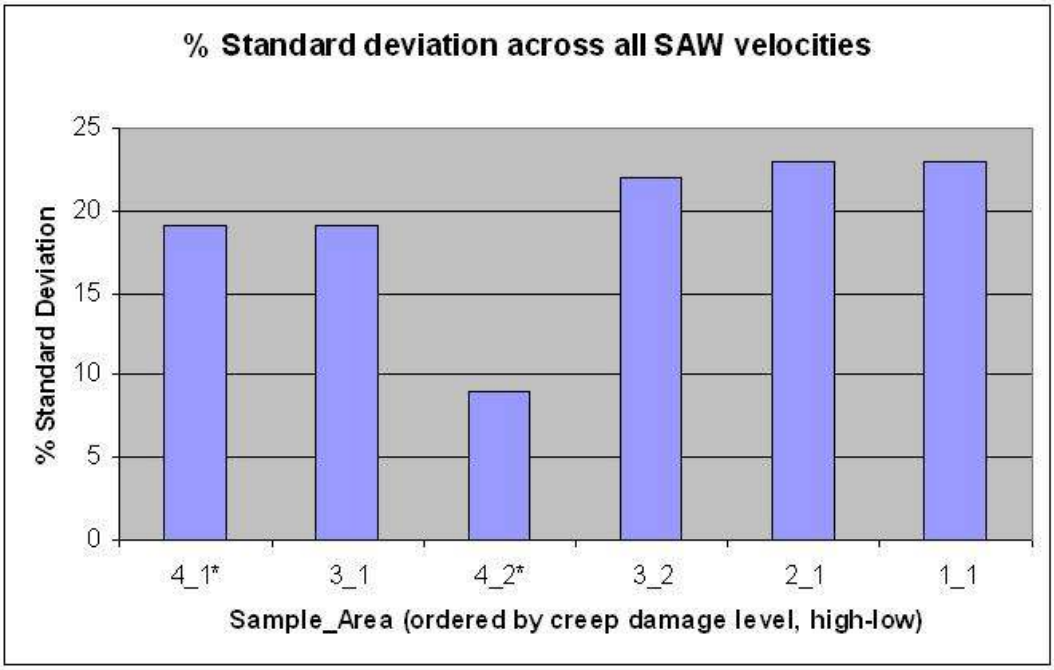

*Figure 9.28 – Plot showing standard deviation of SAW velocity across all samples. Deviation is higher for lower damage levels than it is for heavily damaged metal, but not as low as it is in weld metal. *Denotes sample containing weld.*

9.5. Discussion on Laser Generated UT

There are several points of interest observed in Experiment LGUT 2 with, potentially, some explainable trends emerging. In the most badly creep damaged areas of parent metal, Figure 9.22 (Sample 3_1) and the right-hand side of Figure 9.24 (Sample 4_1), there is a significant drop in the average SAW velocity to around 2800m/s and the greatest percentage area below 2900m/s (58% and 55% respectively). In addition to this there is a reduction in the variation in the velocity over the sampled area. Weld material appears to have considerably more consistent SAW velocities produced within it and, from these limited samples, it is unclear whether the SAW velocity within the weld decreases with creep damage.

From an ultrasonic perspective non-austenitic steels are generally considered to be isotropic. Sound will travel through isotropic materials with constant velocity, but in reality steels are not truly isotropic. The anisotropy of a metal is a result of its grain size, orientation and distribution. For steels such as 0.5CrMoV, the grains are generally of varying sizes of less than 100μm diameter. As all the size variation occurs within a range that is well below the wavelength of a normal ultrasonic operating range (i.e. 10MHz shear waves with a wavelength of 0.3mm) the ultrasonic wave is largely unaffected by grain size variation [171].

With laser generated ultrasound, the wavelength of the SAWs is around 18μm, well within the range of grain size variation. Looking at the microstructure of the samples inspected under a high magnification, the grain size characteristics of the test samples were recorded and are shown in Table 9.3,

Region	Mean Grain Diameter (μm)	Grain Diameter Range (μm)
Parent	30	10-70
HAZ	9	5-15
Weld	3	<5

Table 9.3 – Typical grain dimensions of samples by area.

Making the approximate assumption that objects equal to, or larger than, half a wavelength will influence the ultrasonic wave, then it stands to reason that the anisotropy observed in the parent will be the most pronounced, some anisotropy will be observed in the HAZ and the weld should still appear to be approximately isotropic. This theory is upheld by the results shown in Figure 9.28, which illustrates that the greatest velocity variation (and hence anisotropy) occurs in the parent metal, then there

is slightly more consistency in the HAZ whilst the greatest consistency occurs in the weld regions of Figure 9.24 (right-hand side of image) and Figure 9.25.

If an ultrasonic test is operating at wavelengths where the grain dimensions can influence the localised sound velocity, then the ability to detect creep deformation becomes more likely. At a granular level, if the ultrasonic wavelength is similar to the mean grain size, then deformation of grains could be detected. In the latter stages of creep deformation grains will become slightly elongated so that their primary axis aligns with the principal stress. In isotropic materials the sound velocity along the major axis of elongated grains is lower than normal [171]. Therefore, as the grains in a region elongate in the direction of the primary stress, their acoustic velocity in that direction will also diminish. This is evident in Figures 9.22 and 9.24, which have increased concentrations (58% and 55%) of low acoustic velocity regions compared to Figure 9.21 (45%) which covers a similar area of HAZ, but with less creep damage evident. Where larger grains elongate in the primary stress direction, their minor axis dimension will reduce. Where this dimension reduces below the ultrasonic wavelength, the grains may appear more isotropic to the ultrasonic waves. This could explain the reduction in acoustic velocity observed in the heavily creep damaged regions of HAZ.

This would suggest that there is a degree of directional sensitivity associated with the velocity measurements. Since all the data recorded here was taken in the direction of the primary stress, no comparison could be made. However, since completing this piece of work Dr Sharples has tested some further samples, in line, and at ninety degrees to the principle stress. The results [172] show localised variation in velocity with orientation as shown in Figure 9.29, but not much overall difference, suggesting more influence from

overall grain size than the effects of elongation. Again the left-hand side, which shows the small-grained HAZ has a more consistent velocity profile than the parent on the right-hand side.

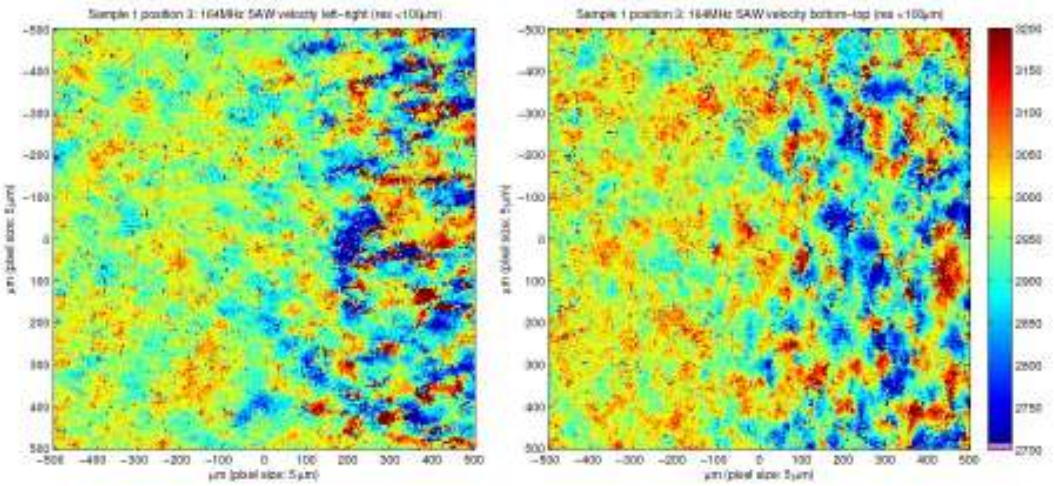

Figure 9.29 – Plot showing SAW velocity profile of a 0.5CrMoV sample containing parent and HAZ regions. SAW propagation direction is left-to-right (left) and bottom-to-top (right) producing localised SAW velocity variations.

The presence of cavities will also have a bearing on the localised acoustic velocity where their concentrations reach critical levels. The presence of voids will impede the efficient transmission of ultrasound and thus reduce the acoustic velocity. This will most likely contribute to the overall drop in acoustic velocity observed in Figures 9.22 and 9.24. It would also explain the localised acoustic velocity drops and increase in anisotropy observed in the weld in Figure 9.25. Although the grain sizes are too small to influence the acoustic velocity due to elongation, the concentrations of cavities in some regions creates anisotropy on a scale large enough to be comparable to the acoustic wavelength.

This method has shown some potential and with a much larger family of samples would provide a more definitive indication of the SAW characteristics under creep deforming

loads. There are many further areas to investigate with this technique, including:

- How do the results vary with orientation across a more broad range of samples?
- Is there a measurable reduction in SAW velocity between undamaged and damaged welds?
- Are similar results obtained on materials that display similar creep morphology?
- Do undamaged samples always contain the widest variation in SAW velocity and is the deviation consistent/repeatable?
- Are there any other microstructural differences that will affect the SAW velocity and thus impede the results?

9.6. Conclusions on Direct Detection Methods

The work on phased array ultrasound, falls some way short of being able to reliably detect defects comparable in size to creep damage. There is a suggestion from these results that clusters of micro-defects are detectable in the sub-millimetre range where signal-to-noise ratios are appropriate. Using laser-engraved samples should provide some more compelling evidence and this will form part of an RWE npower R&D project for 2010. If it can be proved that clusters of defects are detectable with focussed phased arrays then the Full Matrix Capture (FMC) approach proposed by Bristol University could provide useful results at the latter stages of creep damage and deformation. Using post-processing techniques on the reflections recorded on each element all possible beam laws can be recreated, optimised and displayed in a manner than may be representative of aligned cavitation and micro-cracks. The super-resolution post-processing technique developed at Imperial College, London, may also benefit the technique.

The work on laser generated ultrasound has shown some promising results, particularly

in relating the localised ultrasonic velocity to the level of creep damage in 0.5CrMoV. It seems logical that the presence of micro-cracks and cavities would reduce the acoustic velocity of a material as they will impede the propagation of sound waves. The key observation is that in the HAZ and parent regions as the creep damage increases it appears that the ultrasonic wave velocity reduces and becomes more consistent. This is most noticeable in the very last stages of creep from just prior to the onset of micro-cracking. This is in excellent agreement with the observations of Ohtani [170] on accelerated creep samples. There may be potential for creep damage assessment by this method prior to the onset of micro-cracking, but at present there are insufficient appropriate samples available. If the technique can be employed on a larger population of samples with a good selection of creep damage levels then it is possible that a reference matrix of average velocity and velocity deviation could be indicative of creep damage.

In terms of laser generated ultrasound ever providing a viable alternative to replication there are several key problems. Firstly, the equipment used to obtain these results is lab-based and too large to be portable. If the equipment could be miniaturised sufficiently to make a portable instrument, then the level of component preparation required to accurately locate and take the measurements would potentially be a little lower, and hence preparation time shorter, than for a metallurgical replica. Whilst the generation of SAWs with laser UT is possible with a rougher (>1μm) surface finish, as demonstrated with Sample 1, to ensure consistency within a group of results, the roughness should not exceed the depth of pentration of the waves, thus reducing the risk of wave reflection off the surface undulations. For the SAWs this is approximately one wavelength, 18μm, so realistically the polishing stages at 9μm, 3μm and 1μm could be removed from the

process, reducing preparation time by up to a quarter. In terms of taking the measurements and analysing the data, durations are comparable to replication also. The only perceivable advantage is the electronic record of data, which would never justify the equipment outlay should a portable system be feasible.

The use of laser generated SAWs is an interesting project in relation to observing the influence of grain properties and creep morphology on localised acoustic velocity; however, in its current guise it is unlikely to provide an economically viable tool for on-site creep damage detection. This is simply because, for this application, it requires the same amount of preparation as metallurgical replication, but significantly higher capital investment, whilst not reducing inspection/analysis time, operator training or improving plant-life data.

Chapter 10 Detection of Creep Damage Using Bulk Measurements

10.1. Introduction

This chapter is the second detailing experimental data, and looking at ways of classifying creep damage in power generation steam pipe-work using NDE methods. Following on from the work in Chapter 9 on detection of localised creep damage, this chapter will look at generalised creep damage and how its presence and severity might be implied by measurement of acoustic and/or electromagnetic properties. Because of the scale of the work involved in trying to find and thoroughly test a technique for its suitability in assessing creep damage, this chapter simply takes the first steps in assessing the potential suitability of the techniques discussed in Chapter 8. It does not cover in detail the fundamental scientific issues, rather it sets out a series of plausible paths for future research work in this field, as well as assessing the current state and limitations of NDE for creep damage assessment. This chapter explores NDE methods to detect a reduction in creep strength in Grade 91, general creep damage in 0.5CrMoV and general creep damage in Grade 91. Grade 91 and 0.5CrMoV are the most common steels used for main steam pipe-work in UK power generation.

This chapter focuses on ultrasonic techniques and it is written on the assumption that the reader has reasonable knowledge of basic ultrasonic terminology.

10.2. Aberrant Grade 91 Material

Like the 12Cr turbine blade steel tested in Chapter 6, Grade 91 pipe-work has a tempered martensite microstructure. Where incorrect heat treatment has been carried out on Grade 91, either in post-weld heat treatment or during fabrication, the material is considered to be aberrant. This may result in the material being too hard, and thus brittle, or it may be too soft. In the case of the latter there is a significant risk that the creep resistant properties of the component will be greatly reduced from the design specification. This could lead to catastrophic failure prior to the start of the component's inspection schedule if the material condition is not verified. This is consistent with the theory that hardness in Grade 91 reduces with creep life expiry [133] [134].

A logical progression from the work in Chapter 6 is to see if the eddy current method developed previously is capable of distinguishing the aberrant Grade 91 from good material. The test will focus on the difference between components, rather than localised variation so there is no value in producing a mapping technique. A single-channel eddy current test will be used to provide information from discreet points on the test component. Samples were available for testing containing six different material variations. They were:

1. Virgin Grade 91
2. Ex-service Grade 91
3. Grade 91 Weld
4. Aberrant Grade 91
5. Soft, but not aberrant, Grade 91
6. Grade 92 (similar composition to Grade 91).

All test samples were ground to a 240 grit finish at measurement locations to reduce variation due to surface condition. As with the work in Chapter 6 on the turbine blades, currently, the material condition is assessed with portable hardness testing.

10.2.1. Experiment HTAB 1

Equipment: *Proceq Equoptip 1 hardness tester.*

Reference: *P91 reference hardness block (496HL).*

Samples: *Virgin Grade 91, Ex-service Grade 91, Grade 91 Weld, Aberrant Grade 91, Soft Grade 91, Virgin Grade 92.*

Using a portable hardness tester to perform Leeb (rebounding ball) hardness test, the hardness of each test piece was measured, taking an average of 5 point-readings across the sample. The results are shown below in Table 10.1.

Virgin Grade 91	Soft Grade 91	Ex-service Grade 91	Aberrant Grade 91	Virgin Grade 92	Grade 91 Weld
502HL Std. Dev. 5	457HL Std. Dev. 8	500HL Std. Dev. 7	400HL Std. Dev. 11	486HL Std. Dev. 4	520HL Std. Dev. 5

Table 10.1 – Leeb hardness data from testing of Grade 91 and 92 samples.

There is a good correlation between material condition and hardness, with a significant drop in hardness observed for the aberrant material, but virtually no change for the ex-service material. Additionally, the soft material is clearly distinguishable from both the virgin and aberrant material. On the basis of the above information, hardness testing would appear to be a very suitable technique for detecting aberrant Grade 91; however it is still interesting to see how the eddy current response correlates with this data.

10.2.2. Experiment ECAB 1

Equipment: *Zetec MS5800 with ECP3 probe.*

Reference: *Nulled on Virgin P91 material at known reference.*

Key parameters: *175 kHz at 3V input with 38dB gain.*

Samples: *Virgin Grade 91, Ex-service Grade 91, Aberrant Grade 91, Soft Grade 91.*

Using a single channel from probe ECP3, comparative impedance data was collected from all the samples, using the Virgin P91 as a reference. The probe was placed on a defined position on each sample in turn and the resultant coil response recorded on X and Y-axis strip charts, shown in Figure 10.1.

On this initial test there is a measurable difference in the impedance response to the four different samples. This variation appears to be the most pronounced in the Y-direction. There is a marked difference between the response to the virgin material compared to the other materials, which have only minor variation between them. Looking at the X-axis, Y-axis and overall magnitude of the values (it is easier to identify the small changes on a strip chart rather than on a C-scan) there is little consistent trend with deteriorating material condition and thus hardness. Table 10.2 ranks the four material types by voltage displacement, 4 being the least displacement and 1 being the most. Obviously the Virgin Grade 91 is a 4 in each rank because it is the same piece as the reference, but the other materials vary with rank and none of the orders match that observed with the hardness in HTAB1

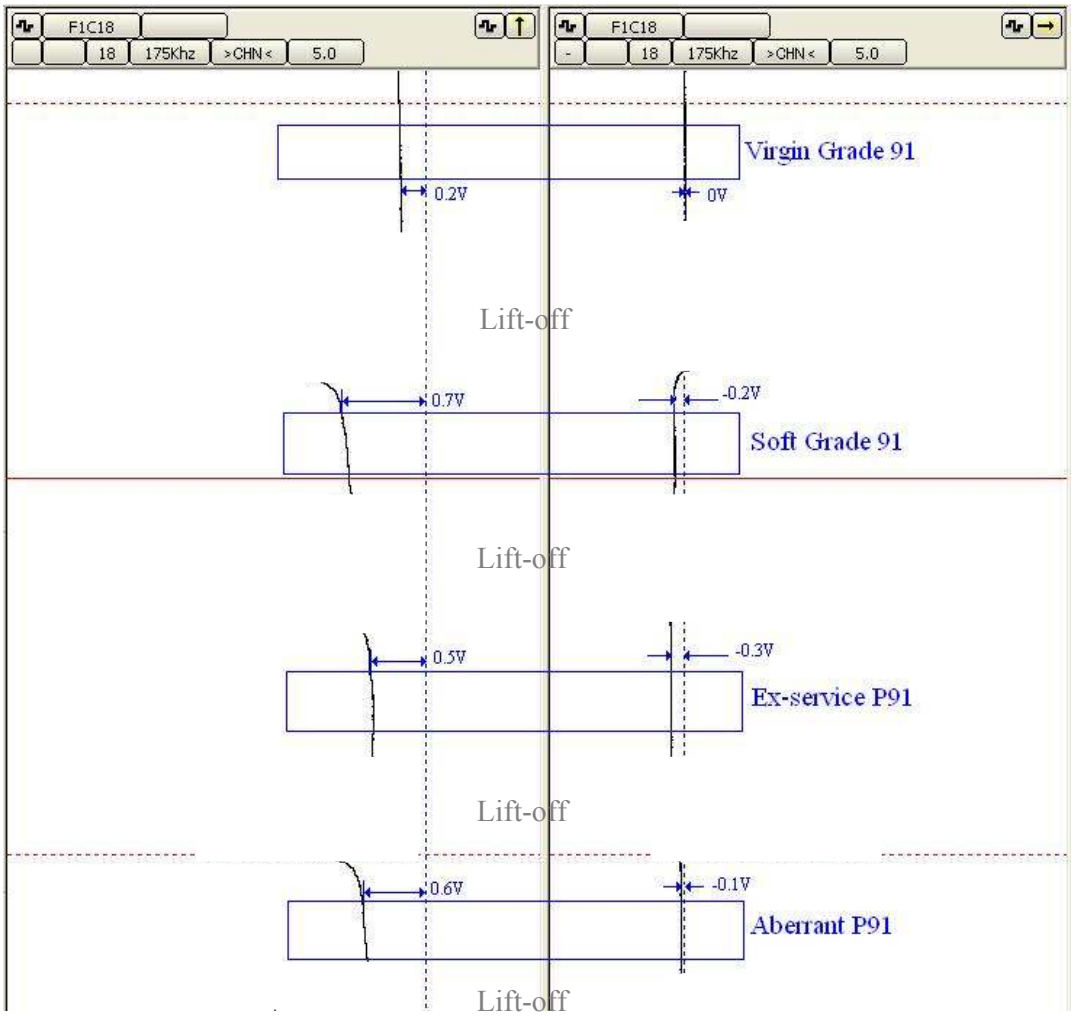

Figure 10.1 – Y=axis (left) and X-axis (right) normalised eddy current voltage displacement plots for four different Grade 91 samples, normalised to virgin Grade 91. This shows the difference in voltage/impedance between the four samples.

Sample	X-axis Displacement Rank	Y-axis Displacement Rank	Overall Magnitude Rank	Hardness Rank (High-Low)
Virgin Grade 91	4	4	4	4
Soft Grade 91	2	1	1	2
Ex-service Grade 91	1	3	3	3
Aberrant Grade 91	3	2	2	1

Table 10.2 – Voltage displacement rank (4-lowest to 1-highest) for four Grade 91 samples

10.2.3. Experiment ECAB 2

Equipment: *Zetec MS5800 with ECP3 probe.*

Reference: *Nulled on Virgin P91 material at known reference.*

Key parameters: *175 kHz at 3V input with 38dB gain.*

Samples: *Virgin Grade 91, Ex-service Grade 91, Grade 91 Weld, Aberrant Grade 91, Soft Grade 91, Virgin Grade 92.*

Using the same setup and but with different sample positions to ECAB1, the experiment was repeated and extended to include a Grade 91 weld (520HL) and some virgin Grade 92 (486HL). Again the results showed no real correlation with the results of HTAB1 and more significantly displayed a significant amount of deviation from ECAB1. The strip-chart data is shown in Figure 10.2 and shows the greatest deviation coming from the Aberrant Grade 91. In isolation, this would have been encouraging, but this shows no consistency with the results of ECAB1. Also, the material that produces the most similar response to the aberrant Grade 91 in ECAB2 is the Grade 91 weld which is at the opposite extreme of the hardness range.

The errors/variability of the measurements taken on each sample is too large compared to the signals caused by relevant material variation to make the technique feasible, even if there was an observable trend to the relative data. To illustrate just how pronounced the variation is, a series of measurements were made on the virgin Grade 91 sample, displayed in Figure 10.3. There was a 0-0.2V variation on the X-axis and 0.0.3V variation on the Y-axis, which is around 50% of the total variation observed across all samples. This is shown in Figure 10.4, where the component of the detected complex

voltage response is compared to material hardness.

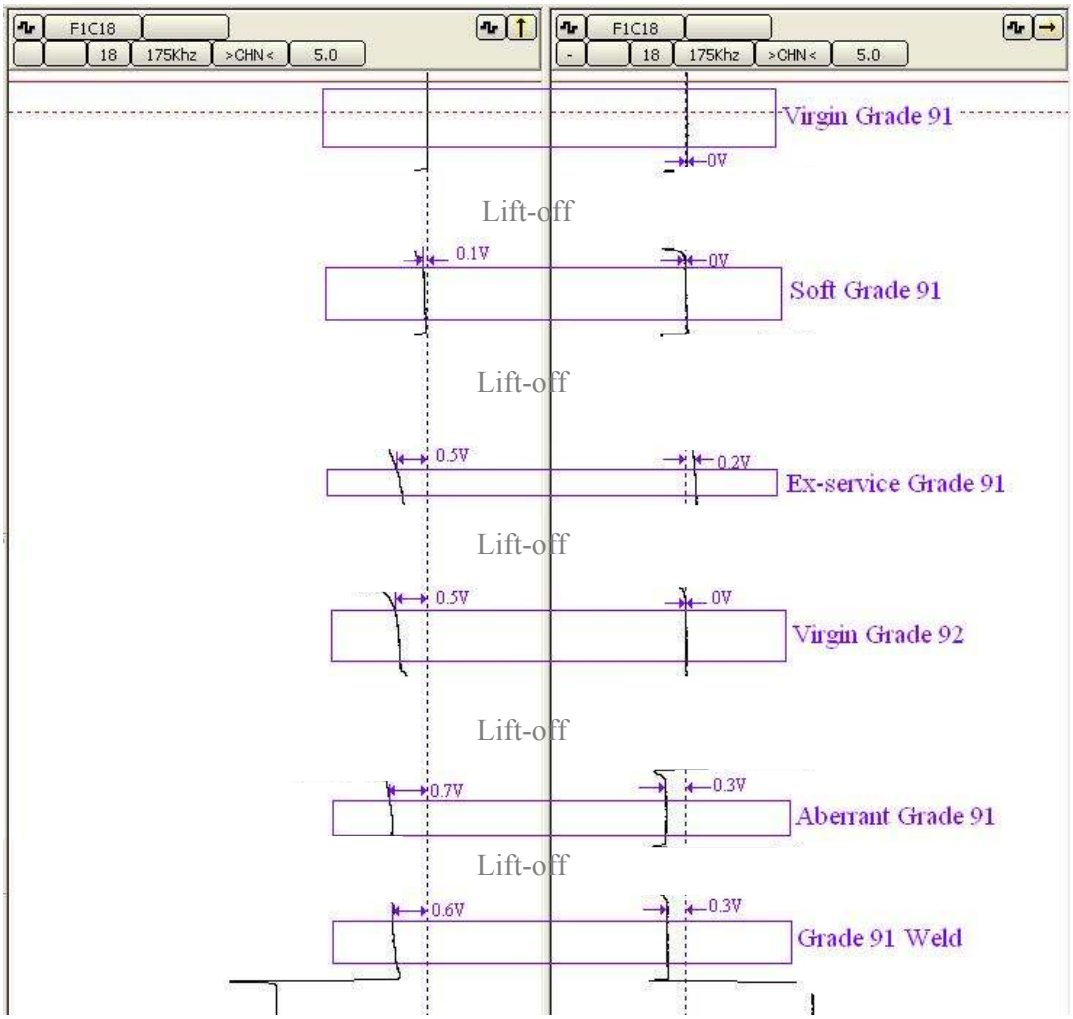

Figure 10.2 – Y and X-axis voltage displacement for Grade 91 samples, normalised to Virgin Grade 91

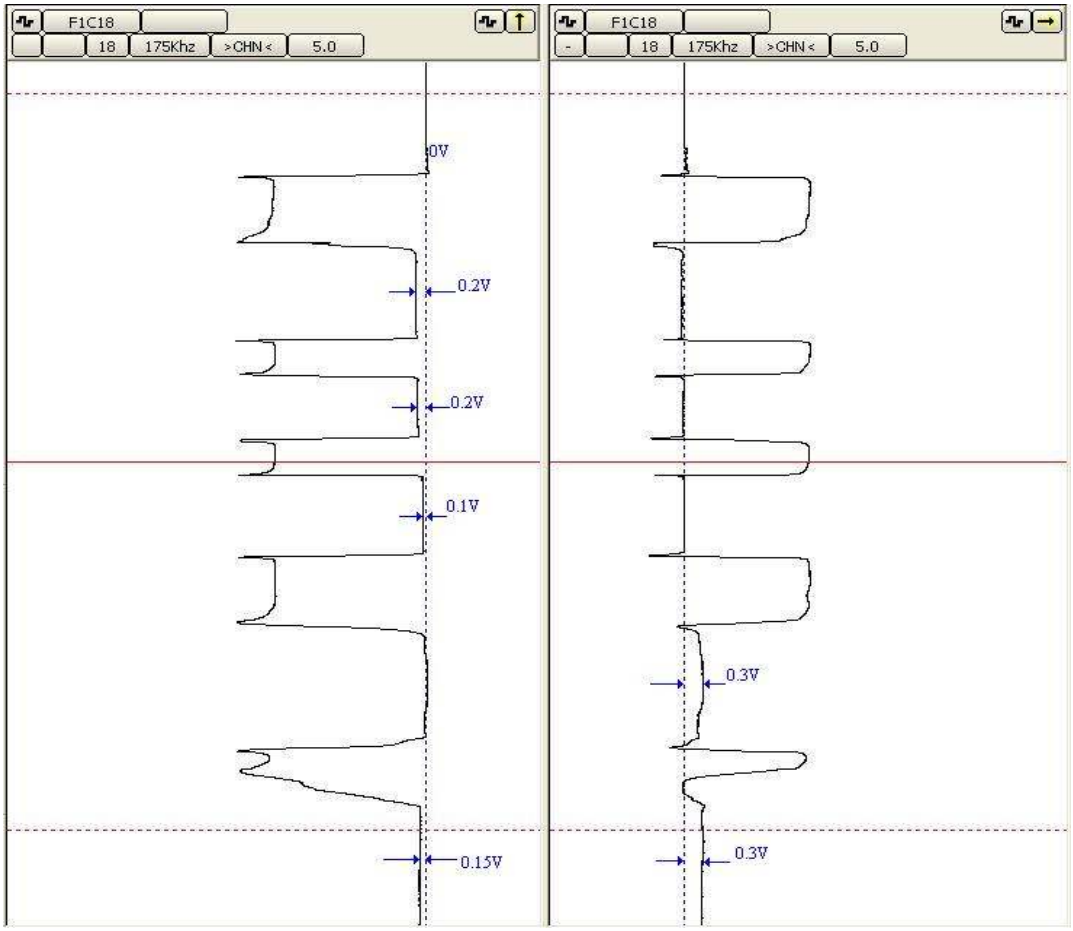

Figure 10.3 – Y and X-axis voltage displacement for various positions on virgin Grade 91 sample

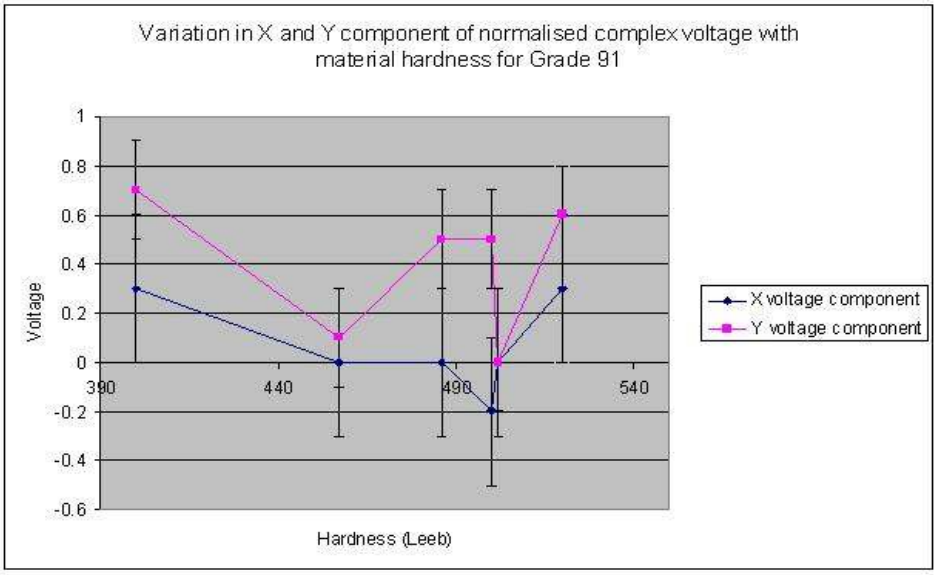

Figure 10.4 – Y and X-axis voltage component vs. material hardness with error bars based on variation across Virgin Grade 91 sample.

10.2.4. Conclusions on Aberrant Grade 91

The eddy current response to aberrant Grade 91 showed no consistency or correlation with the material condition. This was a little surprising given the good results achieved on martensitic steel in Chapter 6. The major issue was variation across the samples, which would potentially mask any variations associated with a change in material hardness. As a suitable technique, there is no doubt that portable hardness testing offers a far more reliable, cheap and easy to apply method. Despite this eddy current technique's inadequacy, NDE for material creep life assessment can still provide some useful indicators of material condition as will be demonstrated in the rest of this chapter.

10.3. Bulk Ultrasonic Methods

The chemical composition, micro-structure, crystal structure and dislocation density all affect the material properties and hence the material condition. Some of these material properties can be (and have been) correlated with ultrasonic testing parameters [173]; these include inclusion content, elastic modulus, fracture toughness and yield strength as well as degradation estimates of creep and fatigue. Suitable ultrasonic measurements for correlation with these properties include velocity measurements (shear, longitudinal, surface or ratio of longitudinal to shear) and attenuation, but they must be measured accurately to be of any relevance. Bulk measurements will only be suitable for the assessment of volumetric creep in the parent material rather than localised creep in the vicinity of the welds, which covers too small an area to reliably influence the measurements. These measurements will be restricted to 0.5CrMoV material as this exhibits a greater density of cavitation than Grade 91 and is more readily available for making samples.

10.3.1. Ultrasonic Velocity Measurements

The most simple bulk measurement is ultrasonic velocity. Using either bulk or surface waves over a known distance, the ultrasonic velocity can be calculated once the time-of-flight has been determined. Theoretically, the presence of creep damage should result in the reduction of ultrasonic velocity in that particular medium. According to Ohtani [170] there is a sharp decrease in the ultrasonic velocity at the onset of micro-cracking, however there is not a gradual reduction in velocity in the earlier stages of creep damage to reflect the damage progression. My work in Chapter 9 suggests that the localised sound velocity on a localised scale does decrease in the later stages of cavitation nucleation and decreases further at the onset of micro-cracking.

For in-service inspection it is unlikely that the thickness of the test component will be known to a suitable degree of accuracy. In such cases the ratio of longitudinal velocity to shear velocity may be a useful parameter as this is independent of the material thickness.

10.3.1.1. Experiment UTB 1

Equipment: *Tektronix TDS 2024B 4-channel oscilloscope*
PAR Industrial APS SPIKE 250 Pulser-Receiver
L-Wave & S-Wave EMAT made by Warwick University
Radially polarised broadband send-receive EMAT made by Warwick University (5MHz centre frequency, 10MHz upper frequency)

Key parameters: *Averaging – 16 samples*

Samples: 0.5*CrMoV creep-accelerated samples 1-10*

Ten 0.5CrMoV samples were made from an ex-service piece of pipe-work that had been

machined into a tapered bar of circular cross-section. The bar was subjected to an accelerated creep test until failure after 2040 hours. The creep test was conducted at 590ºC with a maximum stress of 90MPa at the thinnest section, where it failed. The tapered shape of the rod meant that the stresses were lower in the thicker sections and so creep damage levels were reduced. The ten samples cut from the rod were thick-disc shaped and contained varying levels of creep cavitation as shown in Table 10.3. The creep life expiry estimates in the right-hand column are made using Dobrzański's descriptions of creep life expiry [126].

Sample	Cavitation Count (per mm^2)		Thickness (mm)	Creep life expiry (%)
	Peak	Background		
1	150	45	16.8	70
2	90	30	16.2	64
3	90	45	14.1	63
4	75	30	14.1	62
5	60	15	13.9	60
6	30	15	16.8	57
8	30	0	14.6	55
7	15	15	15.3	52
9	15	0	13.7	50
10	0	0	15.3	40

Table 10.3 – Sample data from creep-accelerated CrMoV pieces

The velocity measurement tests required each of the EMATs in turn to be placed on one of the flat, parallel sides of the samples and an averaged trace of the first and second back-wall reflection was recorded on the oscilloscope. There was far less variation in the velocities recorded by the shear wave EMAT compared to the longitudinal wave EMAT. This is most likely due to the lack of efficiency of L-wave EMAT probes as explained in Section 8.2. This resulted in less well defined back-wall reflections as shown in Figure 10.5 compared with the shear wave response, making accurate measurement of the time of flight more difficult and prone to error.

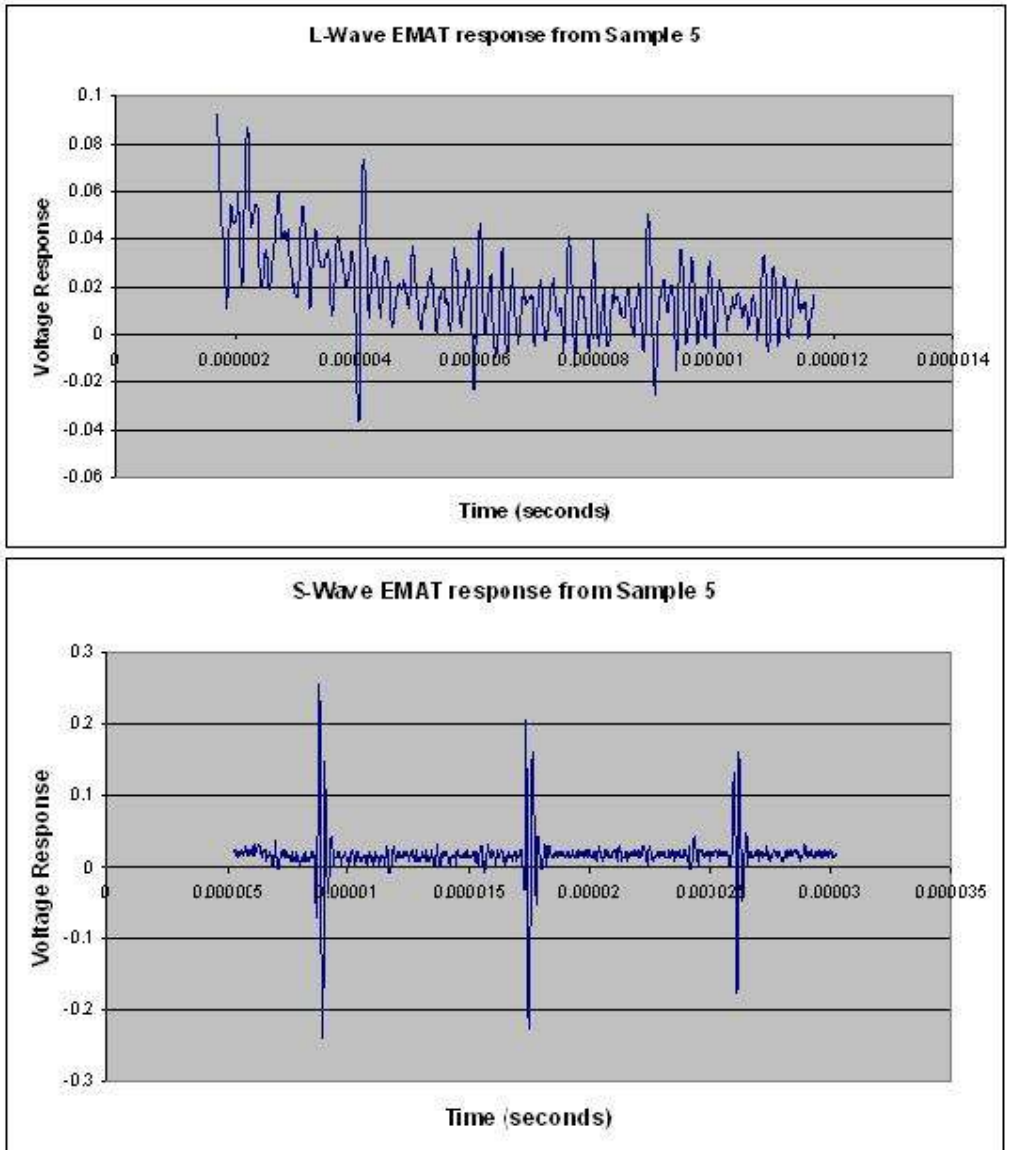

Figure 10.5 – Sample 5, L-Wave (top) and S-Wave (bottom) repeating back-wall reflections from EMAT-generated ultrasound, showing the difference in sound generation efficiency

The results from all ten samples are presented in Figure 10.6. The samples are ranked in terms of the severity of their creep cavitation damage from the lowest on the left to the highest at the right side of the x-axis. Data trends are shown for the ultrasonic velocities calculated for each EMAT type and the ratio of the L-Wave velocity to the two S-Wave velocities.

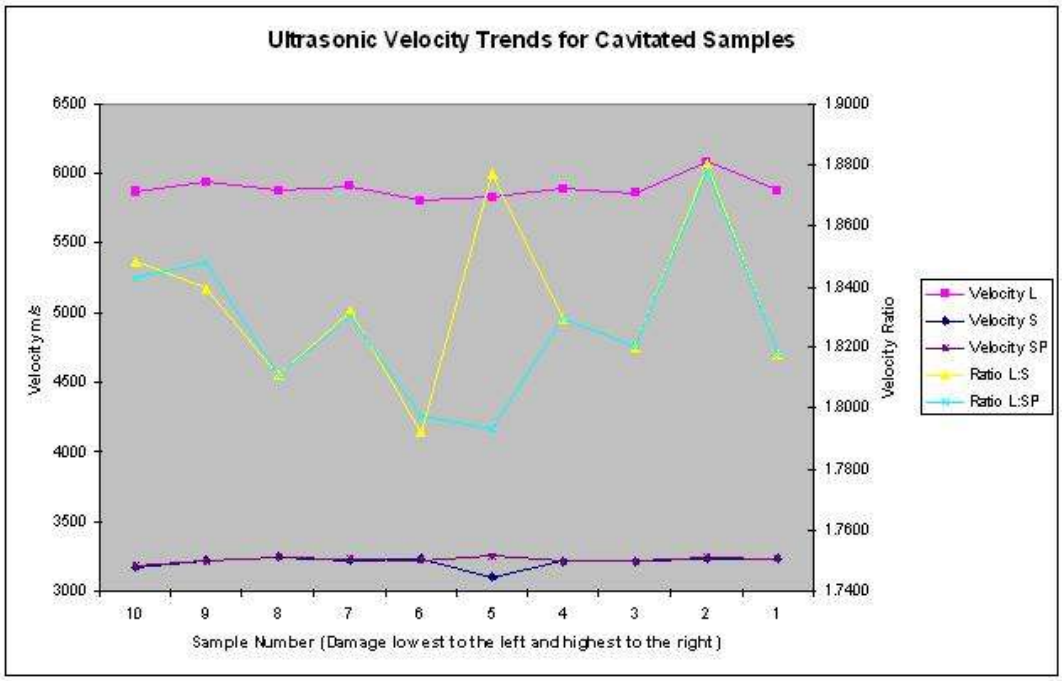

Figure 10.6 – Compiled ultrasonic velocity measurements for all ten samples ranked from lowest (left) to highest (right) levels of creep damage.

It is immediately evident from Figure 10.6 that there is no observable trend between the damage level and the ultrasonic velocity of the different wave modes. Also there is no trend between the damage and the velocity ratios. Figure 10.7 shows the more reliable shear wave velocity data plotted against the estimated creep life expiry. Aside from a slight increase in velocity from low level damage to high, there is no obvious trend between the velocity and creep life expiry: this is in agreement with the work of Ohtani [170] who only observed a significant velocity drop above 90% creep life expiry. This suggests that the levels of damage in the available samples are insufficient to have a bearing on the velocity and consequently there is no suggestion that this method is worth pursuing, since an assessment is required before higher levels of damage are accumulated.

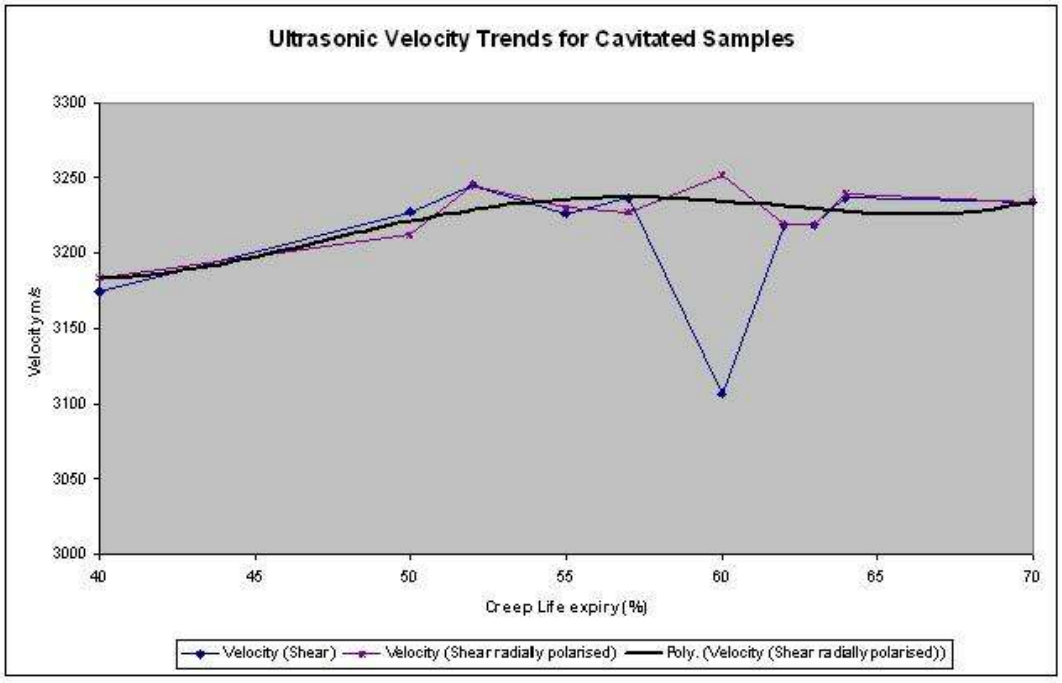

Figure 10.7 – Shear wave ultrasonic velocity measurements plotted against creep life expiry (estimated).

10.3.2. Ultrasonic Attenuation Measurements

Attenuation measurements made by measuring the difference in amplitude between two back-surface echoes will provide the attenuation coefficient. Losses due to the absorption component are a result of damping due to dislocations and thermoelastic effects and losses due to scattering are dependent on the ratio of grain size to wavelength [173]. Broadband EMAT probes are the most suitable ultrasonic transducers for these tests since the coupling between transducer and component is consistent. Reliably consistent coupling cannot be achieved with conventional ultrasonic probes without using immersion testing which is impractical for site use. Other practical difficulties with attenuation measurements arise from irregularities in the pipe's shape resulting in surfaces that are not entirely parallel. As the extent of this will differ with each location inspected the amount of sound reflected back will not be consistent and so any small

changes in attenuation may be masked by other sound energy losses due to contact inefficiency and incomplete detection of the reflected wave.

Using EMAT transducers can help overcome the problem of inconsistent coupling to a large extent since the coupling mechanism should be repeatable. EMATs couple with the test piece electromagnetically, forming a uniform active area across the test piece surface, whether it is flat or curved. A related method called electromagnetic acoustic resonance (EMAR) [158] uses a resonant technique to superimpose many signals to overcome the problem of low transduction efficiency.

Attempts to measure creep damage using EMAR have been made, and the most recent, and promising, is by Ohtani [170]. By monitoring the shear wave attenuation and velocity, and then comparing changes with the evolution of the microstructure, as seen under a TEM, the study revealed a novel phenomenon in creep development in 0.5CrMoV ferritic steel. An attenuation maximum which appeared to be independent of the applied stress was detected at approximately 30% creep life expiry. This was followed by an attenuation minimum at approximately 50% creep life expiry. Having concluded that grain scattering and scattering by precipitates cause negligible variations in the attenuation coefficient, dislocation damping remained the only viable mechanism to cause the observed acoustic response. It was also suggested that not all dislocations interact with the ultrasonic waves. Ohtani [170] breaks the creep process down into four stages: stage I relates to primary creep, stages IIa and IIb relate to secondary creep and stage III relates to tertiary creep.

In stage I where precipitation and softening occur, but there is no significant dislocation

movement, the attenuation coefficient and velocity do not change significantly.

In stage IIa the initiation of dislocation multiplication is observed, dislocation restructuring starts and coarsening and condensation of precipitates advance. The attenuation coefficient increases and the velocity decreases.

In stage IIb the dislocation density increases further, but only at grain boundaries where the dislocations are considered redundant in the creep process. Consequently the overall effective dislocation density will have reached a maximum so attenuation peaks and velocity drops to a minimum and begins to rise again.

In stage III the total dislocation density is further increased and internal energy is released resulting in the creation of sub grains and recovery of cell structures; recrystallisation can also occur. The result is an increase in attenuation and rapid decrease in velocity until rupture occurs.

It was observed that the increase in attenuation at about 10% strain corresponded to the onset of secondary creep and the attenuation minimum at 50% was in line with the tertiary creep regime.

10.3.2.1. Experiment UTB 1

Equipment: *Tektronix TDS 2024B 4-channel oscilloscope*

PAR Industrial APS SPIKE 250 Pulser-Receiver

Radially polarised broadband send-receive EMAT made by Warwick

University (5MHz centre frequency, 10MHz upper frequency)

Key parameters: *Averaging – 16 samples*

Samples: 0.5*CrMoV creep-accelerated samples 1-10*

The same data used for the measurement of ultrasonic velocity of the radially polarised shear waves was used to measure the bulk attenuation in the ten samples (refer to Table 10.3 for full details). To make accurate attenuation measurements two conditions are met, consistent ultrasonic coupling and parallel sided test pieces. Using the difference in the maximum peak-to-peak voltage range of the first two echoes, the attenuation coefficient can be found. Since attenuation causes an exponential decrease in sound pressure with propagation the measured attenuation coefficient (α_m) can be calculated, in the narrow bandwidth case, from

$$\alpha_m = \frac{-1}{2d}\ln\left(\frac{A_2}{A_1}\right) \quad (10.2.1)$$

This value differs from the actual material attenuation, since α_m also contains losses due to diffraction and eddy current losses thus:

$$\alpha_m = \alpha + \alpha_d + \alpha_e \quad (10.2.2)$$

The eddy current losses can be ignored, since they are negligible for materials of low conductivity [158]. Since the wavelength and effective transducer radius is constant for all tests, the diffraction losses are only proportional to the propagation distance, as is α_m [158]. Consequently, the relative material attenuation coefficient for all samples, can be compared using α_m.

The attenuation coefficient values are plotted against the estimated creep life expiry in Figure 10.8 along with a 4th order polynomial trend line. This shows the greatest

attenuation occurring at, or prior to 40% creep life expiry and then an attenuation minimum between 50% and 60% creep life expiry, followed by a slight increase at higher life expiry. This is very similar to the trend observed by Ohtani [170] using EMAR. Whilst it is encouraging that there is similarity between these results and those by Ohtani, this method is of little practical use if the pattern is not reproducible for real pipe work examples, where the pipe walls are not flat and parallel. Given that this physical restriction cannot be changed, the only way to measure attenuation without excess sound losses off non-flat and non-parallel surfaces would be a through-wall transmit-receive system; however this is impractical as the transducer on the inner surface would impede the steam flow through the component, overheat and erode away, which would be unacceptable.

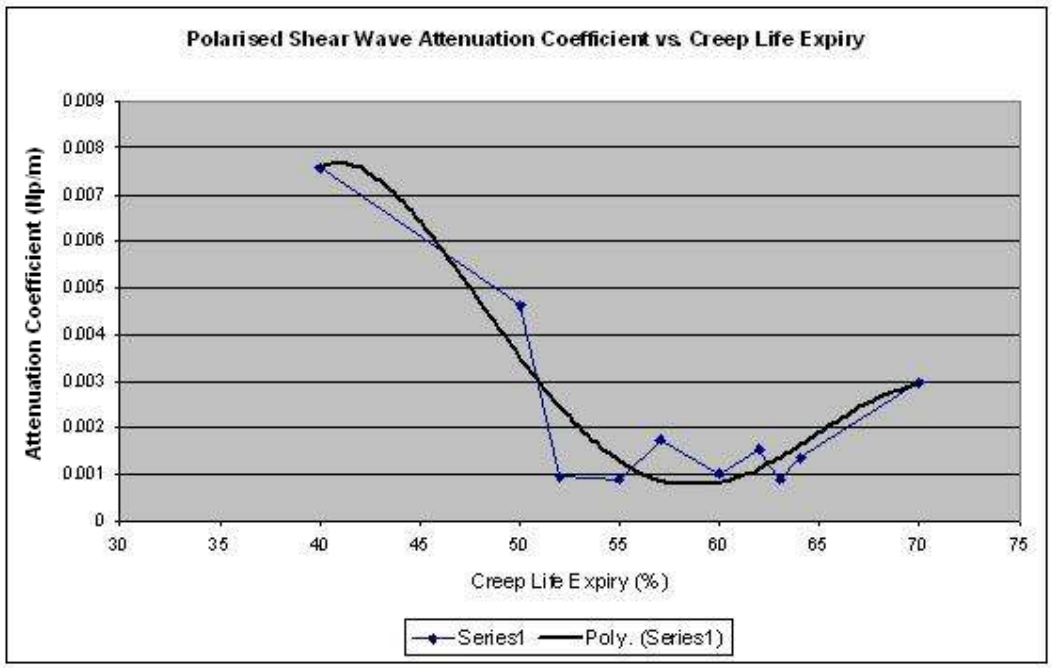

Figure 10.8 – Polarised shear wave attenuation coefficient vs. creep life expiry for flattened samples

10.3.2.2. Experiment UTB 2

Equipment: *Tektronix TDS 2024B 4-channel oscilloscope*

PAR Industrial APS SPIKE 250 Pulser-Receiver

Radially polarised broadband send-receive EMAT made by Warwick University (5MHz centre frequency, 10MHz upper frequency)

Key parameters: *Averaging – 16 samples*

Samples: *CrMoV ex-service samples 1, 3, 12 & 14*

The same set-up was used on four ex-service samples of varying thickness and damage levels. Unfortunately the population of samples was restricted due to a lack of differing cavitation levels between the available components. The key parameters of the four samples can be seen in Table 10.4 below.

Sample I.D.	Cavitation Count (per mm^2)	Creep life expiry (%)	Thickness (mm)	Attenuation Coefficient (Np m^{-1})
CMV – 1	30	55	34.1	0.011
CMV – 3	75	62	34.5	0.014
CMV – 12	150	70	26.6	0.027
CMV - 14	30	57	34.4	0.012

Table 10.4 – Polarised shear wave attenuation coefficients for non-flattened ex-service samples

What is immediately apparent is that the attenuation coefficients are a factor of 10 larger than in Experiment UTB2. This is most likely due to increased scattering at the front and back walls. This will almost certainly result in poor accuracy of results because this will dominate over the attenuation from the creep process. However, there is also good consistency shown between the three samples in the 55-62% creep life expiry range and plotting the attenuation values vs. the creep life expiry does show a possible trend as

depicted in Figure 10.9.

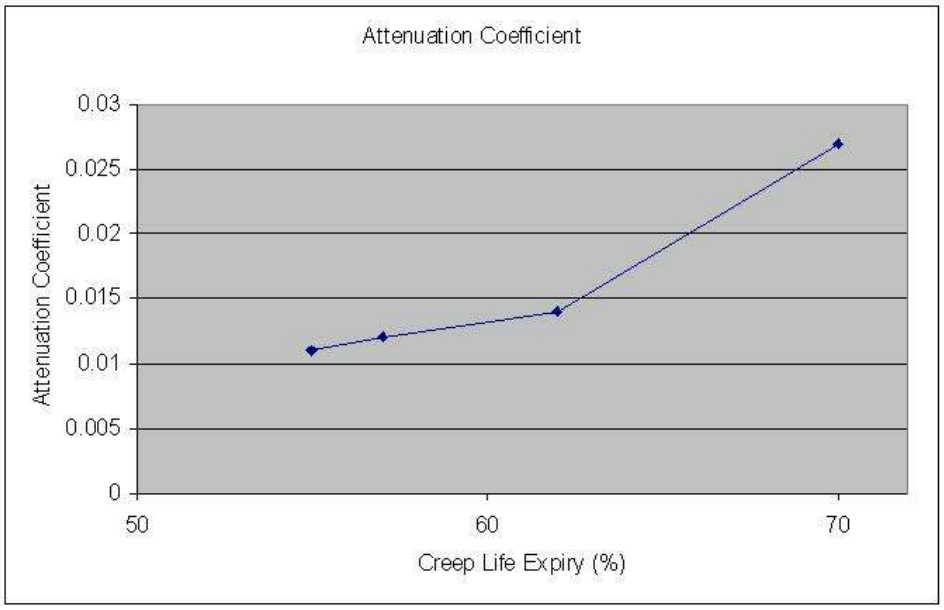

Figure 10.9 – Polarised shear wave attenuation coefficients vs. creep life expiry %

The 70% creep life expired sample exhibits higher attenuation as was the case in Experiment UTB2. While there is no definite disagreement between the trends shown in UTB2 and UTB3, there is insufficient data to conclude that there is a definite link. The small magnitude of the increase in attenuation with non-flat and parallel walls makes it highly unlikely that reliable trends could be observed even if more samples become available in the future.

10.3.2.3. Discussion on bulk ultrasonic methods

The bulk ultrasonic measurements taken in this study have shown good agreement with previous work in this area but still fall short of being viable assessment techniques. The ultrasonic velocity methods show little or no correlation with creep damage in the creep life range examined. This may improve if more efficient longitudinal wave EMATs can be produced, making the measurement of the longitudinal velocity more accurate and reliable. Good estimations of the shear and longitudinal sound velocities would permit

the approximation of material elastic properties [174]. Elastic modulus values in particular are a good indication of strength, since it is related to the inter-atomic forces and elastic properties have a significant effect on the propagation of sound waves through the media. The following elastic modulus parameters can be calculated from the ultrasonic velocities, provided the density of the material is known:

$$Young's - Modulus(E) = \rho.V_T^2.(3V_L^2 - 4V_T^2)/(V_L^2 - V_T^2) \qquad (10.2.3)$$

$$Shear - Modulus(G) = \rho.V_T^2 \qquad (10.2.4)$$

$$Bulk - Modulus(B) = \rho.(V_L^2 - 4.(V_T^2)/3) \qquad (10.2.5)$$

$$Poissons - Ratio(\upsilon) = (V_L^2 - 2.V_T^2)/2(V_L^2 - V_T^2) \qquad (10.2.6)$$

Shear modulus and Young's modulus are affected by the pore/cavitation density in a material and clearly the number of cavities will have an effect on the material density, thus information about the material creep condition can be gauged from the velocity measurements. The presence of cavities will also affect the attenuation in the material under test [175]. High attenuation is associated with high levels of creep damage and low attenuation with low levels of damage. Fatigue damage can cause a detectable variation in the ultrasonic attenuation where physical deformation and micro-cracks impede the propagation of sound waves.

The propensity of in-service pipe work to scatter the ultrasound on reflection means that ultrasonic attenuation measurements are never likely to be a reliable indication of volumetric creep damage even if a trend can be observed by extending this study to a greater range of flat, parallel-sided samples. Combining this test with other

measurements may reduce false calls, though using any other ultrasonic based techniques are likely to suffer the same pitfalls. Electromagnetic techniques may provide complementary information to increase confidence in results, but these are better suited to testing Grade 91 metal rather than CrMoV steel.

10.4. Creep detection in Grade 91 with MBN

A number of studies on detecting degradation in power generation steels with the Magnetic Barkhausen Noise technique have shown some potential [176][144]. However, these studies have taken place on creep-accelerated samples or materials that differ from those covered in this project, i.e. 11Cr1Mo and 2.25Cr Steels. RWE npower have acquired a section of Grade 91 header with in-service creep damage in the vicinity of a branch weld. The level of creep damage varies across the sample while the thermal aging of the sample does not. This consistency of thermal aging removes one of the sample characteristics that could potentially have a bearing on the MBN behaviour.

10.4.1. Experiments using MBN on Grade 91

The test sample is shown below in Figure 10.10, it consists of a half section of header (final superheater outlet header) body with a half section of the branch line attached. There are ten sites for measurements (marked) which have been metallurgically replicated and found to contain varying levels of creep damage, which was quantified by cavity counting in discrete areas of each site [Section 7.3.1]. The details of the creep damage are shown in Table 10.5. The sample has been polished to a 1μm finish at the test locations, which is not ideal for influencing MBN measurements but should provide consistency across all sites.

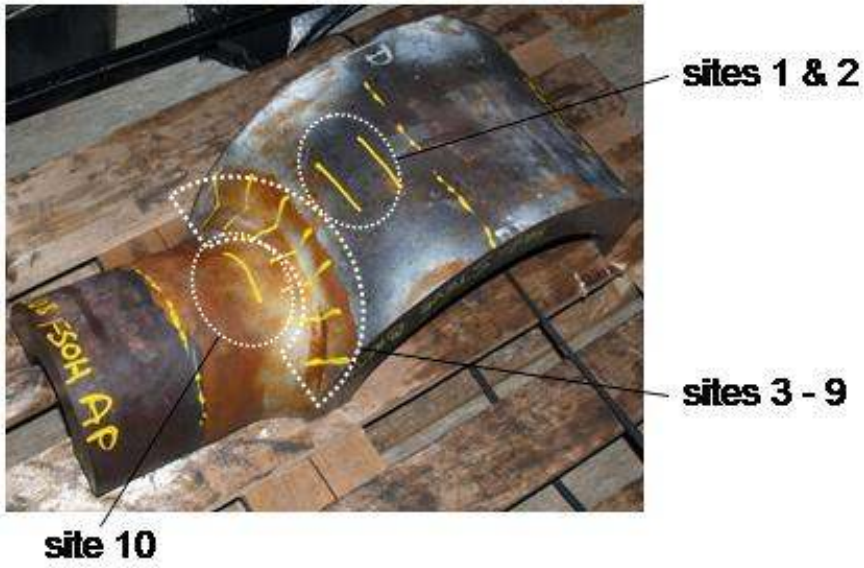

Figure 10.10 – Ex-service Grade 91 header (G91H) sample showing measurement locations.

Location	Peak Cavitation	Background Cavitation	Damage Rank (1: low – 10: high)
1	60	15	2
2	240	30	5
3	195	60	4
4	195	60	3
5	300	165	6
6	375	270	8
7	480	180	9
8	930	600	10
9	345	150	7
10	0	0	1

Table 10.5 – Creep damage levels at the 10 measurement locations on Grade 91 header sample.

Yardley's work[176] looks at non-creep-related degradation, but recommends future work on creep damage assessment. The experiments in that work were performed under the supervision of Dr V. Moorthy at Newcastle University and used a Stresstech 'µSCAN 500' commercial Barkhausen Noise testing machine. For my work, I approached Newcastle University to arrange testing of the test sample using Barkhausen noise methods using both the Stresstech commercial equipment and their own laboratory system.

10.4.1.1. Experiment MBN 1

Equipment: *Stresstech Rollscan with miniature spring-loaded probe.*

Key parameters: *Excitation frequency: 125Hz.*

MBE High-pass Filter 10 KHz:MBE Low-pass Filter 70KHz

Measurement: *RMS value.*

Samples: G91H, positions 1-10.

The sample available for this experiment was unfortunately an irregular shape and could not be altered. Fortunately the Rollscan system can maintain acceptably consistent contact with the sample, which results in consistent. There are a number of drawbacks to the commercial system, including its depth of penetration, which is just tens of microns and the lack of a raw data output.

The measurements were taken under the supervision of Dr V. Moorthy and the RMS values are recorded in Figure 10.11. Three measurements were taken in both the axial and circumferential directions (relative to the header body). The maximum, minimum and mean value for each location is plotted for both directions, as is a composite value. The high excitation frequency of the probe can cause large variance in the results due to its sensitivity to surface inhomogeneity and this is illustrated by the errors bars on the figure. This is countered by the fact that the probe is sensitive to only a small localised area. This is well suited to detection of localised creep damage in the weld fusion and HAZ region.

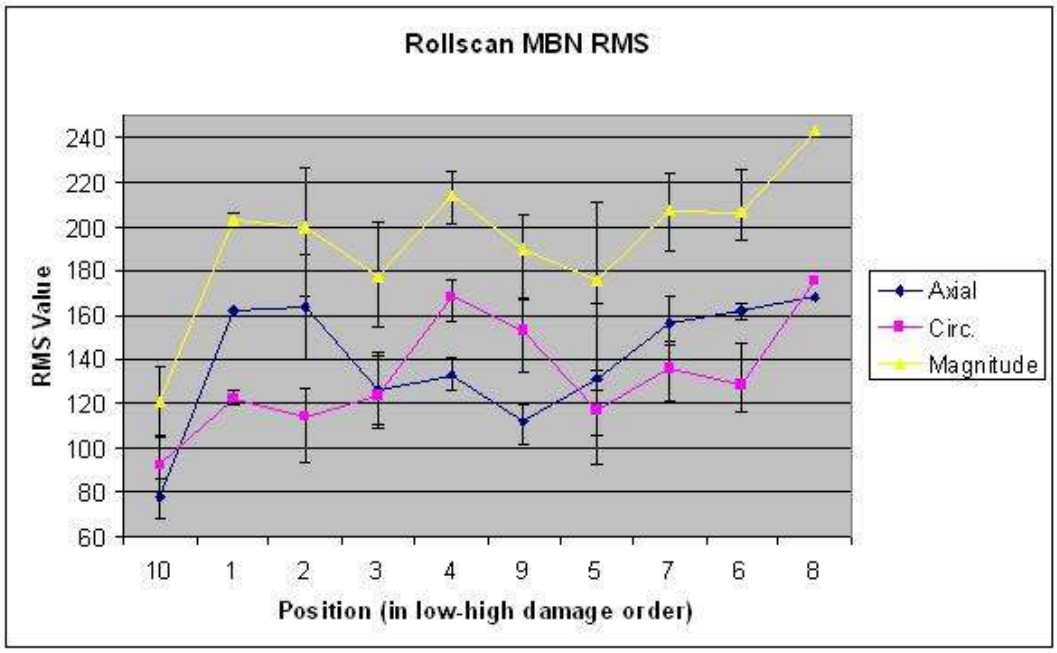

Figure 10.11 – RMS voltage output (measured axially, circumferentially and as the magnitude of the two components) from Rollscan system from measurements at the ten test locations, ranked in order of creep damage (low-high). Error bars show variation recorded over 5 measurements per location.

The trends shown in the figure show an approximate correlation with the creep damage levels recorded by replication. Position 10, which is an undamaged region exhibits consistently low Barkhausen activity and Position 8, which has the greatest damage level exhibits the highest overall Barkhausen activity. Taking the overall magnitude of Barkhausen RMS voltage as the most consistent trend, there appears to be an initial increase in RMS voltage with creep damage, then the RMS level hovers at around 200, then begins to increase for the most damaged areas. An increase in RMS voltage with creep damage, and hence dislocation density, would seem illogical, since an increase in domain pinning sites would reduce the overall Barkhausen activity. It should, however, be noted that the creep degradation of Grade 91 also results in the formation of carbides which will have their own effect on the magnetic behaviour and that the data shown here is subject to large errors.

The work of Mitra [144] on accelerated creep samples suggests that the trend is more complex with different behaviour in the three creep regions. Mitra reports that in the primary creep region, RMS voltages decrease slightly from the starting point, then increase in the secondary creep region before the rate of increase slows in the tertiary creep region. As a rough approximation the primary creep region relates to Position 1, 2, 3, 4 & 9 on the diagram, Positions 5, 6 & 7 relate to secondary creep and Position 8 relates to tertiary creep.

Overall, there is poor agreement between this work and that of Mitra and although there is a loose correlation with creep damage for the ten positions, the large deviations encountered in the measurements make the data very unreliable.

10.4.1.2. Experiment MBN 2

Equipment: *Agilent 33250A 80MHz Function/Arbitrary Waveform Generator*
N4L LPA05 Power Amplifier
Small, ferrite-cored MBN probe with fixed pick-up coil.

Key parameters: *Excitation frequency: 2Hz.*
MBE High-pass Filter 0.5 KHz:MBE Low-pass Filter 40KHz

Measurement: *MBN profile .*

Samples: G91H, positions 1-10.

The sensitivity of the Rollscan system to surface inhomogeneity made it unsuitable for providing reliable data for this investigation in spite of its consistent contact with the test piece. In order to use a more appropriate excitation frequency and be able to access the raw data the consistent contact had to be compromised when using a Newcastle

University laboratory MBN system.

This work was supervised by J. Wilson, with support from Prof. G-Y. Tian and Dr M. Morozov. The smallest probe available was used that could operate at 2Hz was used, giving it a depth of penetration of hundreds of microns, thus reducing its sensitivity to surface inhomogeneity. By capturing the raw data, the whole MBN profile can be reproduced and RMS voltage, peak position and pulse height distribution (PHD) measured. Using these additional characteristics can help to relate MBN activity to hysteresis and pinning site density. The downside of this probe is that there is poor consistency in surface contact as illustrated in Figure 10.12.

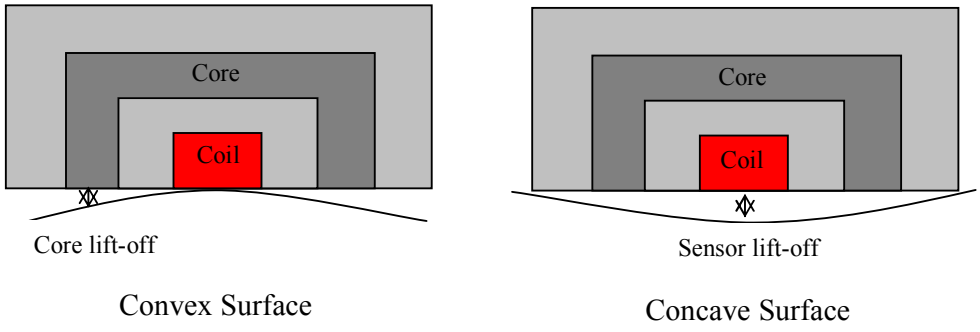

Figure 10.12 – Illustration of lift-off issues with small, fixed-coil MBN probe.

There are a number of problems arising from varying air gaps between the core and/or coil and the sample [177]:

- Gaps between the core and the sample can be affected by interference from stray fields from the core itself, increasing signal noise. This can be partially suppressed by an aluminium pot surrounding the sensor (not present on this probe).
- Gaps between the core and the sample will vary the induced field. A reduced

induced field will cause the profile peak to move to a higher voltage and the profile amplitude will be reduced.

- Variations in sensor lift-off will cause variations in signal amplitude and a change in the overall profile shape.

Acquisition of the raw MBN data allows more flexibility in terms of signal processing. The signals from ten excitation cycles are recorded from the pick-up coil, along with the excitation voltage which serves as a reference for the measurements and then filtered as shown in Figure 10.13 [177].

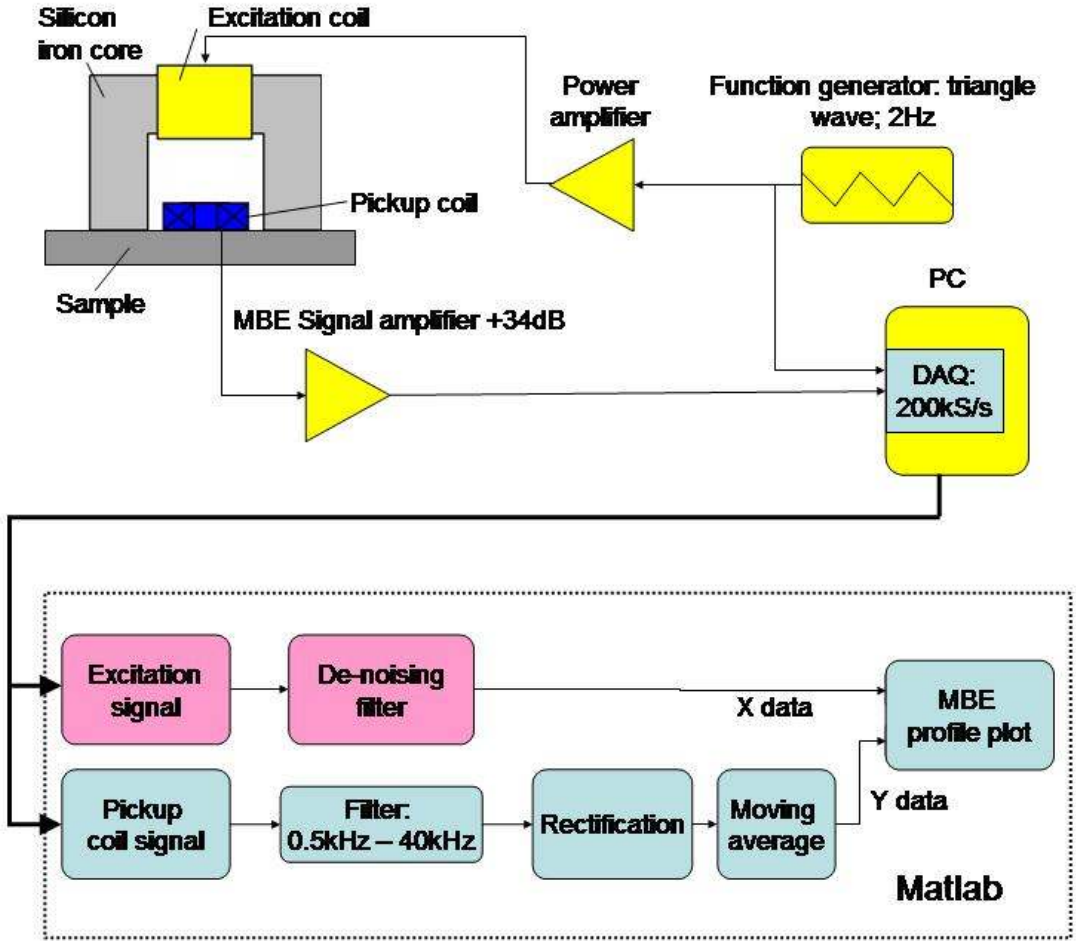

Figure 10.13 – MBN setup and signal processing sequence

The results of the measurements taken at each of the ten positions are shown in Figure 10.14. For the sake of clarity, only the profile from the rising part of the signal is shown

for each position and the sites have been split into two plots, one covering sites 1-5 and the other covering sites 6-10. Creep damage levels from replication are shown in the plot legends.

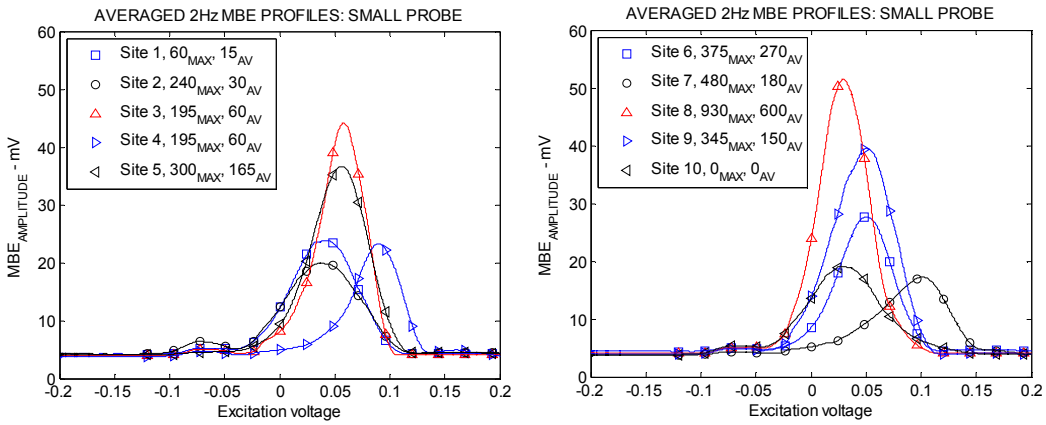

Figure 10.14 – MBN plots for all ten positions using small fixed-coil probe at 2Hz.

Correlation between the peak amplitude and creep damage level is poor; this is shown more clearly in Figure 10.15 below, with the only encouragement coming from the fact that the heavily damaged Site 8 again has the largest peak. There is also no correlation between the peak position and creep damage evident either. The clearest evidence that the strongest influence in this test is coming from something other than the creep damage is that Sites 3 & 4, which have very similar levels of degradation have two completely different MBN profiles.

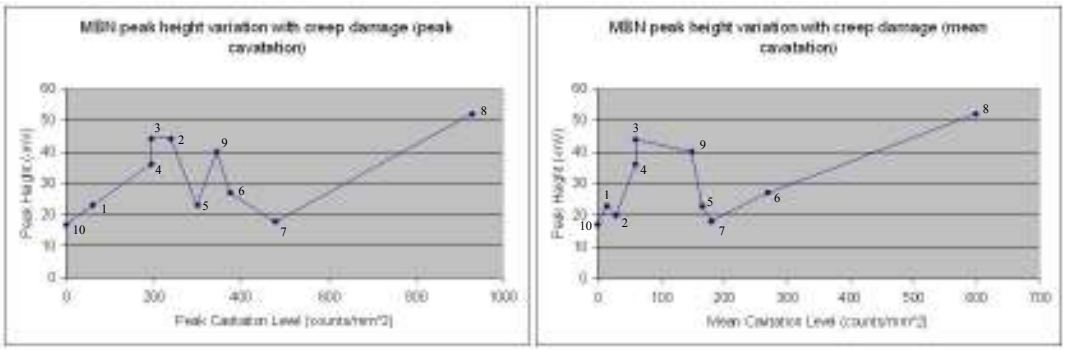

Figure 10.15 – MBN peak amplitude plotted against (left) peak cavitation level and (right) mean cavitation level (site numbers are shown next to each point).

Clearly in this guise, there is too much variation and uncertainty in the system to produce meaningful results, even if dropping the test frequency has reduced some of the variance associated with surface inhomogeneity. An alternative probe with an adjustable sensor was required to produce more meaningful results.

10.4.1.3. Experiment MBN 3

Equipment: *Agilent 33250A 80MHz Function/Arbitrary Waveform Generator*

N4L LPA05 Power Amplifier

Large, SiFe-cored MBN probe with adjustable pick-up coil.

Key parameters: *Excitation frequency: 2Hz.*

MBE High-pass Filter 0.5 KHz:MBE Low-pass Filter 40KHz

Measurement: *MBN profile* .

Samples: *G91H, positions 1-10.*

The problem of sensor lift-off can be overcome to some extent by using a probe with an adjustable coil. By protruding or retracting the coil from the probe, a better fit can be obtained with a concave or convex surface respectively, as illustrated in Figure 10.16.

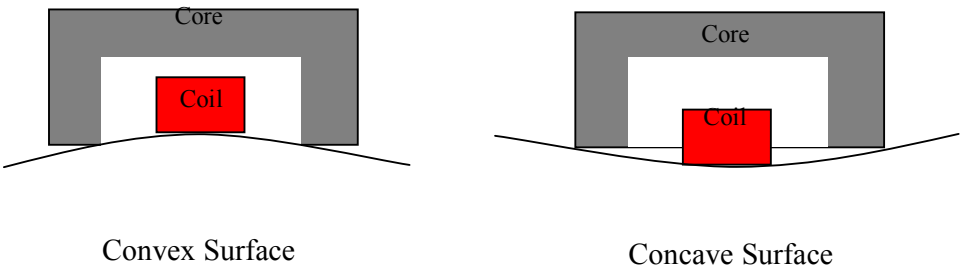

Figure 10.16 – Illustration of lift-off reduction with large, adjustable-coil MBN probe.

Aside from the ability to adjust the coil position, the only other difference between this experiment and MBN 2 is the larger probe size. Despite the increased size of the probe the improved coil-to-sample contact produces more consistent results than observed in the previous experiment. Figure 10.17 shows the profile from the rising part of the MBN signal, shown for each position. The sites have been split into two plots, one covering sites 1-5 and the other covering sites 6-10.

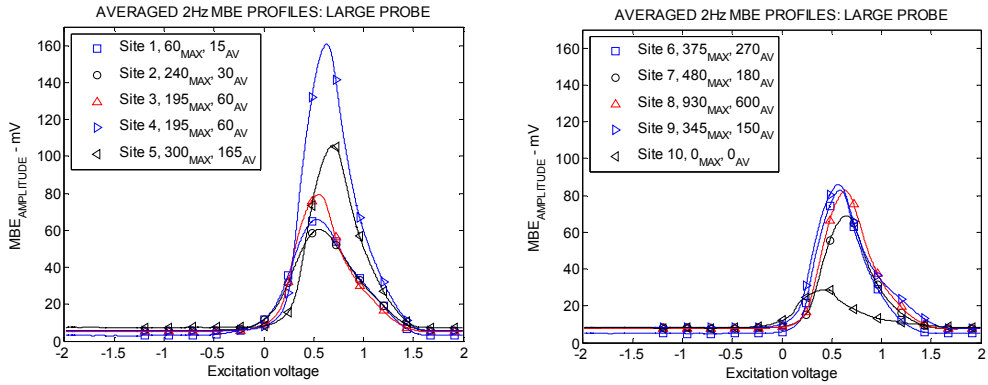

Figure 10.17 – MBN plots for all ten positions using large adjustable-coil probe at 2Hz

It would appear from the results that the lift-off of the core is still a large influence on the results. The two largest peaks occur at positions 4 and 5, to the side of top-dead-centre of the branch weld. This is one of the easiest places to put the sensor flat on the sample along with sites 1, 2 and 10, and thus get good contact. There is a large difference in peak amplitude between the undamaged site 10 and the creep degraded sites, but variations with increasing creep damage follow no coherent pattern.

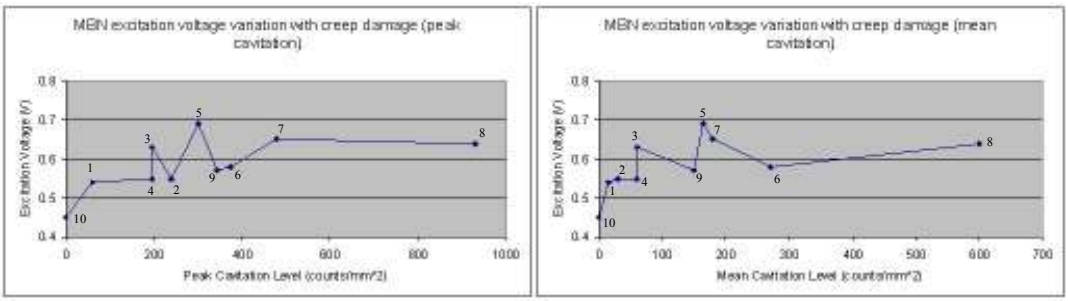

Figure 10.18 – MBN Excitation Voltage plotted against (left) peak cavitation level and (right) mean cavitation level.

Looking at the peak position (excitation voltage) of the ten sites, does provide more encouragement. The peak of the undamaged site occurs at a noticeably lower excitation voltage than the other sites and there is a general trend of increased excitation voltage with increased creep damage as observed in Figure 10.18. In Figure 10.19 the samples are ranked by overall creep damage and separated into primary, secondary and tertiary creep stages. Taking positions 10, 1, 2, 4 and 5 as having the most reliable measurements; based on geometric position and peak amplitude, there is an increase in peak position with creep damage accumulation.

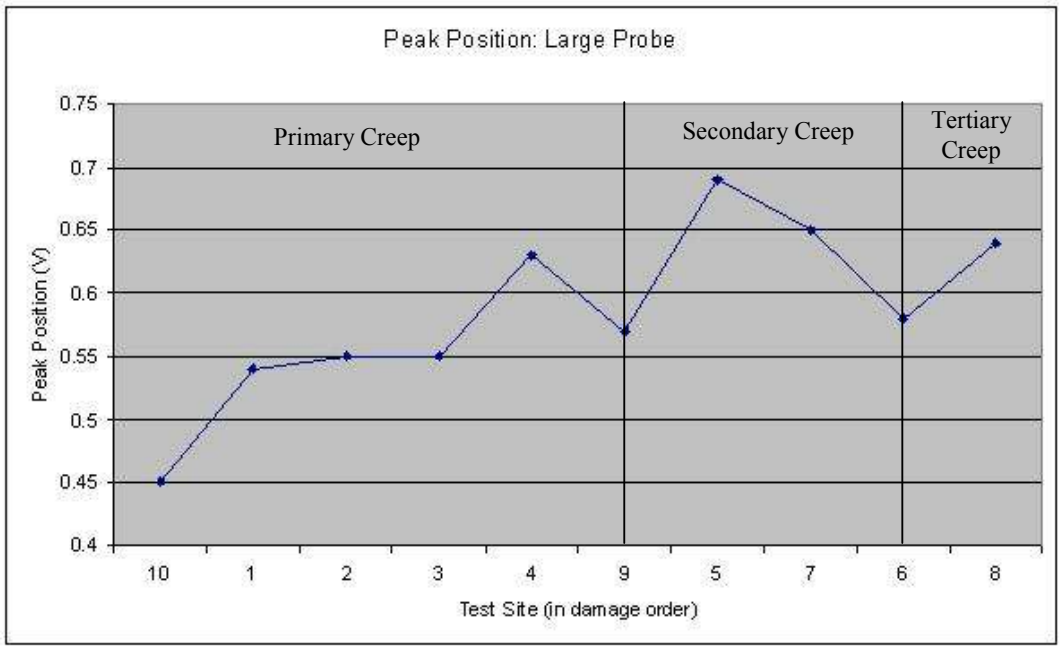

Figure 10.19 – MBN peak position for large probe at 2Hz through three creep regions.

The results take on more significance when compared to the work of Mitra [144]. The peak position is related to the coercivity of the material, which was measured by Mira during the creep life of his test materials. Mitra observed that the coercivity increased in the primary creep region, and decreased in the secondary creep region before increasing again in the tertiary region as is illustrated in Figure 10.20 below, taken from his work.

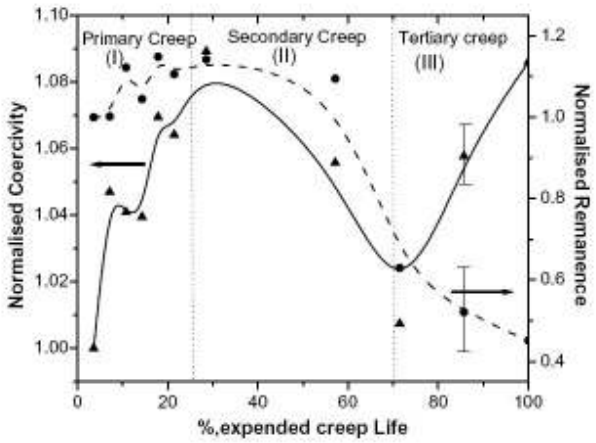

Figure 10.20 – Coercivity profile for creep life of Grade 91, taken from Mitra [144]

Given that my plot is made up of points at random in the material's creep life expiry, rather than continuous monitoring of a creep-accelerated sample, there is reasonably good agreement between the two data sets. Like Mitra's work, there is an increase in the primary creep region, a decrease in the secondary and then a further increase in the tertiary region.

10.4.2. Conclusions of Experiments using MBN on Grade 91

The three tests performed here produced mixed results, which can, for the most part, be put down to physical constraints such as sensor geometry and test surface curvature. The work with the Rollscan was too sensitive to surface inhomogeneity due to its excitation frequency and the small, low frequency probe was too rigid to permit consistent contact. Where this latter issue was partially addressed using the larger, adjustable-coil probe, the results showed some correlation with creep damage and also with Mitra's work on accelerated creep samples.

The most encouraging results came from the MBN peak position which is related to the coercivity. In the primary creep, fine carbides and nitrides are formed [144] which increase the number of pinning sites and increase the coercivity, making the material

magnetically harder. Then as the carbides coarsen in the secondary stage of creep, the density of pinning sites actually reduces as does the coercivity. Finally, in the tertiary creep region, although even larger carbides are formed, brittle phases such as the Laves phase reduce the creep strength [133] and as micro-cracks begin to form which have an increased pinning effect on the domains.

The results shown here give some encouragement to make a thorough investigation into testing Grade 91 for creep damage with MBN worthwhile. If it is deemed appropriate to investigate this problem further, then RWE npower will propose a university research project on this subject. The most important obstacle to overcome is the production of a MBN probe that can be positioned consistently and accurately on real samples. Additional use of acoustic Barkhausen noise could be used to provide additional volumetric information and hopefully reduce uncertainties due to surface inhomogeneity and machining. More samples will be required before the project can be planned properly.

10.5. Discussion on creep detection with bulk measurements

Although the use of eddy current systems to detect aberrant Grade 91 proved to be unsuccessful, two further methods of assessing creep damage with bulk NDE measurements were trialled. The ultrasonic measurement techniques are applicable to 0.5CrMoV parent material and the Barkhausen Noise method is applicable to localised fusion/HAZ creep damage, though its correlation with Mitra's work suggests that it could equally be applied to parent metal. A lack of available samples, prevented investigation of the latter.

Ultrasonic measurements showed some promise and consistency with previous work but will always suffer from practical complications. Velocity measurements were generally poor in the laboratory and there would be an additional large error caused by inaccurate thickness measurement of in-service pipe-work thickness. Attenuation measurements worked fine on flat, parallel-sided samples in the laboratory, but real components are neither flat, nor parallel-sided. Additional experiments involving taking attenuation measurements from these samples before they were milled flat showed no coherent trends at all and have not been included in this document.

Magnetic Barkhausen Noise measurements on Grade 91 showed some promise and have the potential for further investigation with a more specialised experimental setup. Experiments not included in this document, showed that testing of 0.5CrMoV steels with this method did not produce observable trends, most likely due to the lack of carbide formation altering the metal's coercivity.

Overall, the problem of detecting creep damage with NDE remains a significant problem. Ultrasonic techniques are gradually reducing the minimum detectable defect sizes but there are physical limits that will prevent the detection of early creep damage even with the most up to date equipment.

- For 0.5CrMoV steels, metallurgical replication remains the best method of assessing creep damage. This material is coming to the end of its useful life and is being replaced gradually by newer materials, so to some extent the problem of detecting creep damage in it will pass. For the remainder of its service life the current creep management strategy will suffice.

- Grade 91 will be around for a lot longer and occurrences of creep damage will increase over the next ten years. Fortunately the possibility of detecting creep degradation with NDE on this material looks far more promising, due to the effect of the material's phase transition on its magnetic characteristics.

10.6. Conclusions from work on creep testing

The work presented here gives a clearer idea of the best ways to approach the problem of creep damage assessment in power generation pipe-work. The problem is material composition and location dependent, so requires a range of solutions. I have separated the work into two categories, local and general creep damage since the manifestation of serious damage is considerably different for both.

The localised creep manifests itself as much more dense concentrations of micro-damage and thus leads to it being easier to detect. However, it is also confined to very localised regions, no more than a few millimetres wide, which must first be accurately located, before they can be characterised. The use of focussed Phased Array Ultrasonic Testing, has demonstrated some level of success in detecting the latter stages of creep damage, where cavities align and micro-cracks form. In order to maximise the resolution of ultrasound over the required sound paths, it is necessary to consider techniques to enhance imaging rather than looking at the ultrasonic hardware. Logically, the best starting place would be to use Full Matrix Capture to acquire the data, then apply the Total Focussing Method (TFM) to maximise the response from the full material volume. Super-resolution techniques may be applicable to enhance the results further and it will be interesting to see what level of detail can be achieved. It may be appropriate to quantify the resolvable limit using Sub-Surface Laser Engraving, so as to

accurately control flaw size and concentration. Shear wave birefringence measurements may also provide useful information on the acoustic anisotropy of a sample, which may be indicative of creep damage.

The work using laser generated SAWs, demonstrated a degree of acoustic velocity variation where localised creep damage occurred. Where the acoustic wavelength was similar in magnitude to the grain diameter, the effects appeared to be quite pronounced. Although, the practical limitations of this test, (i.e. cost, portability) make it impractical for replacing metallurgical replication, it is worth pursuing this work to better understand the effect of creep damage on acoustic velocity and the range of frequencies/wavelengths over which it is effective. A larger population of samples will be made available to thoroughly quantify if the trends observed in this short study are consistent and repeatable.

Looking back at the work on generalised creep damage, it was a little surprising that the eddy current technique was not appropriate for detecting aberrant Grade 91 material, given the positive results on a similar material in Chapter 6. Despite the fact that the range of hardness variation observed on the reference samples was comparable to that observed in Chapter 6, the level of impedance variation across a sample was too great and too random to extract the relevant signals effectively.

There was a small degree of correlation between bulk ultrasonic measurements and creep damage, but these results were obtained from idealised conditions and, in practice, measurements would be prone to unacceptable errors. This is entirely down to geometric influences on the results; primarily, the curvature on the pipe scattering the

sound. If the pipes were of uniform geometry, it is likely that a compensation algorithm could be written to account for the scattering, even accounting for where the pipe is of an unknown thickness. Sadly, due to regular surface preparation, sampling, grinding etc. during the service life of the component, the pipe-work shape is completely non-uniform, thus eliminating such an approach.

Finally, the work on Barkhausen Noise testing of creep damage Grade 91, could conceivably be applied to either localised or generalised creep damage. Initial trends appear to have some consistency with previous work and associated theory, but deeper investigation is required. The major problem here is the availability of suitable samples not only to validate the technique's ability to detect and quantify creep damage, but also to quantify the errors associated with the Barkhausen Noise technique due to geometry, surface preparation and service history.

Chapter 11 Conclusions

The work presented in this thesis has covered two distinctly different topics and a wide range of NDE methods. As a consequence of this, I will be covering the conclusions of the two topics separately in this chapter. There are a number of conclusions, however, which are relevant to the whole Engineering Doctorate program.

In the introductory chapter, I explained the aims and objectives of the Engineering Doctorate scheme, these included:

- Bridging the divide between academic research and industrial applications in the field of NDE.
- Providing an scientifically rigorous approach to genuine industrial NDE solutions.
- Provide the Research Engineer with extensive knowledge of multiple NDE techniques, including their core theory, applications and the current state of the associated technology. This should then provide the industrial partner with an employee who can not only add value through his own personal increase in NDE knowledge and skill, but also drive future NDE research in conjunction with academic institutions.
- Provide the academic partner with knowledge of specific industrial challenges and restrictions, in order to generate and direct future research.

I would conclude that all of these objectives have been met by the work contained within this thesis. In both projects, but more so in the second on creep damage detection, there has been a two-way flow of knowledge between industrial and academic partners, which has brought us closer to devising a solution to a long-standing problem. Academic partners have gained a greater understanding of the practical constraints encountered in

creep testing, as well as the specific material microstructural evolution, whilst industrial partners have gained an awareness of techniques which further enhance their understanding of the material and its properties that can be evaluated by non-destructive methods.

In the first project on microstructure mapping of steam turbine blades, a working industrial NDE solution has been created, through an scientifically rigorous development process. Whilst it is possible that a practical solution may have been achievable with a less scientific approach, the solution that has resulted is considerably more robust, reliable and based on sound physical principles. In addition, the solution provided much deeper insight into the specific material/electromagnetic interactions, which not only aid the assessment of components by this technique but also significantly increase my own ability to design electromagnetic inspections in the future, so the benefit is two-fold.

The improvement in my ability to design eddy current inspections, and increase the use of such techniques in the power generation industry, is an obvious benefit to the Inspection Management team, where expertise in this field was previously sparse. Through the taught element of the Engineering Doctorate scheme and to a greater extent, through the work in the project on creep damage detection, I have gained extensive knowledge of many established and emerging NDE techniques.

I believe that involvement in the two projects has been enlightening to the academic collaborators as well. The creep project, in particular, has opened up a number of research areas. Some of these research areas can now focus on modification of promising techniques, such as Barkhausen Noise assessment, for industrial

implementation; this will bring a new set of technical challenges which will ultimately move the technology forward and further improve understanding.

Most importantly, this thesis has demonstrated areas of novelty and furthered NDE research. In the microstructure mapping project, although the technology and the design process are both well established, the novelty comes from the application. To the best of my knowledge, no one has ever used the eddy current inspection technique to create a two-dimensional map of material microstructural phases. There are features specific to the material examined that made the technique feasible; however there are almost certainly other materials/situations that this could be applied to.

In the creep project, the aims, in terms of scientific advancement were modest, due to the large scope of the work that was to be undertaken. Despite this, a previously untried use of laser-generated ultrasonic wave velocity measurement for assessment of localised creep damage has been proposed. This has increased our understanding of the interaction of high-frequency acoustic waves with creep degraded materials; this is expected to generate exciting new challenges for further research work. Other work on this project has provided additional evidence to support the findings of previous research and explored the practical complications that need to be addressed by further research, or new applications. Although, not expanding significantly on in-depth science associated with this inspection problem, the work contained here has helped to clarify the state of the art of NDE for creep damage assessment in power generation steels; it sets out a clearer path for future research which, it is hoped will result in a workable solution.

11.1. Conclusions from Microstructure Mapping Project

The main aim of this project was to produce a working inspection method for identifying embrittled areas of steam turbine blades. To that end, the project was successful. The new inspection technique meets the main objective of reducing the inspection time. The inspection time required for the existing technique was approximately five man-days; this has been reduced to one and a half man-days, including analysis of results and validation on a 10% sample of the total number of turbine blades. The sample of 10% was deemed by the RWE npower engineers to be a sufficient representation of the larger population of the rotor blades to give some confidence in the technique. The second benefit of the new technique is that it produces a novel 2-D map of the microstructure, in terms of what is tempered compare to non-tempered. This aids identification of the causes of embrittlement so that operational procedures can be adjusted to reduce future instances of accidental material transformation. The third benefit is that the technique reduces the number of hardness indents made on the blade surface by 90%. Whilst these indents have never proved problematic in the experience of RWE npower, some external companies who are interested in the technique have expressed a desire to reduce the amount of indents made, as they fear they will become stress-raisers.

An scientifically rigorous approach to designing the inspection has been taken and thoroughly documented. Subsequent trials of the technique, though limited in their scope, have shown good accuracy; it yielded no missed defective areas and a 10% spurious indication rate. However, due to a temporary down-turn in work of this type, caused by cyclic inspection periods and improvements in overhaul procedures, I have been unable to validate the technique further. Should this situation change in the future, everything is in place to carry out the inspection and re-start the validation process,

including a formal technique procedure, reference samples and the prototype array probe.

There are some disadvantages to this inspection method as well - the equipment required is far less portable and there is a lot more of it. This is not a major handicap as work will exclusively be carried out in a workshop environment with easy access to the turbine. Secondly, because there are now two techniques involved, the operator requires twice the amount of training before being able to carry out the inspection. All inspection staff at RWE npower receive training in hardness testing, so all eddy current trained personnel will be fully trained to carry out the inspection task. Although there are only a limited number of staff trained in the eddy current technique, there are adequate numbers to cover the work should it increase to previous levels. Finally, the cost of the equipment is considerably higher, given that array eddy current probes and equipment will be required at a combined cost of £40,000. This cost is offset by the fact that some of the equipment is multi-purpose and has already been purchased for other work. Overall, the time-saving advantages of this technique far outweigh the disadvantages and cost.

A number of technical conclusions were drawn in Chapter 6. The key to the technique is that there is a material phase transformation associated with the embrittlement of Grade 91 steel and that there is an electrical conductivity change associated with this material phase transformation of approximately 0.5 MS/m in the range 0.75-2.75 MS/m. This conductivity change is detectable by the eddy current method and it is accompanied by a change in magnetic permeability; however this change is variable in its magnitude and direction. Using magnetically-backed coils the effects of magnetic permeability can be

minimised, leaving conductivity as the dominant effect; this results in a response to a non-tempered martensite region that is in excess of 0.3 V in the negative direction over a dynamic range of 4V.

The technique has a minimum reliable detectable defect size is 5 mm x 5 mm. This compares to 10 mm x 20 mm for the existing hardness testing matrix technique. However, whilst the eddy current technique will almost certainly not pick up anything much smaller than 5 mm x 5mm, the hardness testing technique can detect smaller areas due to its sub-millimetre indent size, although due to the sparsity of the indents, it is entirely down to chance whether or not the indent hits a small defective area.

Since 12Cr Martensitic steel is a common engineering material in both the electricity and aviation industries, there is a possibility that there could be additional application for this technique, or a derivative of it. The material is used for the construction of aero-engine disks, which could potentially benefit from using the technique to check the uniformity of the tempering process, thus identifying any areas with a susceptibility to cracking. Additionally, many valves and pumps in the nuclear industry use 12Cr Martensitic steel; the fatigue failure resistance of these components would be significantly reduced if any brittle areas were present.

As alluded to earlier in this chapter, the microstructure mapping project also satisfied many of the other objectives of the Engineering Doctorate scheme. The project has vastly expanded my knowledge of how to create eddy current based inspection schemes, particularly how different factors affect the impedance plane and how this can be best exploited to give the most repeatable and clear results. It has also increased the

understanding of 12Cr steel, how the material phases develop, and their effect on the electromagnetic properties. In the case of the increase in conductivity as the material transforms to the stressed state, this is the opposition to what occurs in most other metals. Although content relating to other NDE techniques was limited in this project, Magnetic Barkhausen Noise, Pulsed-Eddy current, Thermography and Magnetic Winding Magnetometer techniques were all touched on, thus broadening the knowledge base of less-common NDE techniques at RWE npower.

There was an element of novelty is this project, which derived from the use of eddy current arrays to map material microstructure. Whilst it is highly likely that this technique will only work on a limited number of materials, should a situation arise where a similar test is required on an alternative material, the process can be evaluated using the method laid out in this thesis. Consequently, future research work in this area will likely focus on specific applications, as is the case with most recent eddy current research. At present there are no other requirements for a similar technique at RWE npower; however, the next generation of power stations which will be commissioned within the next deacde, will use modern metals which are unlikely to be amenable to ultrasonic inspection due to anisotropy and structural form (e.g. rifling of tube bores). There will be an increased demand for electromagnetic based material evaluation techniques for these components.

11.2. Conclusions from Creep Damage Detection Project

The main aim of this project was to assess the current state of potential NDE techniques for the evaluation of creep damage in power generation steam pipe-work and to try to focus future research in this field. Whilst no major leaps forward were made with

finding a solution, I do believe that this work has helped to move us closer to finding solutions and has clarified some of the areas that require focus from both an scientific and industrial perspective.

The work on detecting micro-defects ultrasonically showed promising results, within the ranges specified. There was reasonable agreement with previous research work using focused ultrasonic techniques. It was concluded that detection was possible for larger micro-defects or groups of small defects. The physical constraints of ultrasound, such as attenuation at higher frequencies, restrict the ability to get more sound intensity into the target area. This can be improved by focusingr, although in order to extract greater defect detail from the inspection data, post-processing techniques are required to improve signal-to-noise ratios. This could be achieved through Full Matrix Capture phased array ultrasound, which permits focusing at all positions throughout the scanned volume. This is a very computationally intensive way of inspecting but would give the most complete and sensitive set of data, from which any appropriate post-processing operation can be performed. A potentially useful method to employ would be the super-resolution technique [178] to enhance features. I would recommend the integration of these two techniques with a view to assessing the maximum achievable resolution with current technology. In order to quantify this, some use of sub-surface laser engraving on glass, as a transparent mimic for steel, would provide micro-defects of known dimensions; however, any conclusions should take into account the fact that the background noise for glass will be considerably lower than for steel structures. I believe that future research work in this area should be carried out by collaborations between industry and academia, focussing on what can be practically achieved on in-service components.

Laser generated ultrasound produced some of the most interesting results in this project and further research is planned to verify the validity of the theories proposed in this thesis regarding the distribution of SAW velocities in the presence of creep damage. There appeared to be an increase in the density of areas of low SAW velocity in the latter stages of creep, particularly in the parent material. This results in a decrease in the overall variation of SAW velocity across the sample and a reduction in the bulk acoustic velocity. Future work on a larger sample population is planned in order to validate the theory and further investigate the effects of orientation, grain-size, surface condition and wavelength. Although the cost of laser-generated ultrasound relative to metallurgical replication makes it unfeasible for in-service inspection at the present time, there is a lot of scope to further understand the interaction of SAWs with microstructural features.

Using eddy current inspection to test for aberrant Grade 91 material was a logical progression from the work in the previous project on microstructure mapping. The steels involved were similar in composition and structure, and the associated phase changes were both manifested by hardness variations of >50Hv. It was therefore disappointing that the technique proved unsuccessful. This was attributed to the increase in noise, or more accurately, local material variation in electromagnetic characteristics. This caused a much greater impedance change than any caused by the presence of aberrant material, rendering the test invalid. The increase in local material variation is most likely due to the composition and also variations in temperature during component operation. Unlike the final stage low-pressure steam turbine blades which are only subjected to temperatures <100° C, the Grade 91 pipe-work will be subjected to varying temperatures up to 600° C. At these higher temperatures, the stress state and thus the electromagnetic properties of the metal can vary, causing a varying magnetic history and

significant magnetic permeability changes. This work was a logical extension of the microstructure mapping project and highlights the pitfalls when trying to transfer this method to other materials.

Bulk ultrasonic measurements for the assessment of creep damage remain hampered by practical constraints. Using ultrasonic velocity measurements proved unsuccessful in this instance and physical, precise measurement of through wall thickness is impossible due to access limitations. Triangulation techniques and/or the use of multiple wave modes could potentially overcome the problem of needing a physical wall thickness measurement and other studies have shown a trend between bulk acoustic velocity and creep damage. Unfortunately, at practical frequencies, this trend is only observable at the very end of the secondary creep phase and in the tertiary region. Given that current metallurgical replication techniques provide much more detailed information all through the secondary region, these provide better confidence in the ability to assess creep life expiry. Attenuation measurements proved to be impractical in this study. The non-flat, non-parallel pipe-work that requires inspection, scatters the ultrasound to a greater degree than any structural change due to creep damage. If the scattering due to the geometry was constant, then it could be accounted for, but unfortunately that will never be the case due to surface grinding throughout the component's service life. It seems logical that only ultrasonic measurements independent of the geometry are likely to provide a solution, so wave-birefringence may provide some useful indicators.

The work on Magnetic Barkhausen Noise concluded that results achieved previously on artificial creep samples, are likely to be reproducable on an ex-service component with real creep damage. This will need to be investigated further; consequently, when more

appropriate samples become available, a larger research project is proposed to test the reliability of the inspection and subsequent re-inspections. Due to the sensitivity of MBN to factors which affect the magnetic history of the sample, results can never be 100% repeatable. Therefore, a future study needs to examine how the magnitude of the variation caused by surface preparation, re-testing, operational temperature etc. compares to the magnitude of the variation caused by creep damage. Once this has been established, and if the results are favourable, then a system robust enough to take reliable readings on site could be developed. It is also worth pursuing the use of Acoustic Barkhausen Noise to assess creep damage. The primary benefit of ABN is that it has sensitivity to magnetic activity within the volume of the material, rather than just being sensitive to the surface. As a consequence of this, ABN is less sensitive to surface influences, which again is beneficial. Whether ABN's sensitivity to material stresses is beneficial or not would require extensive research, however it seems logical that a combination of Acoustic and Magnetic Barkhausen noise would provide the most robust set of data. Consequently there is a lot of potential for research in this area and I believe, as a result of this work, the academic community now has a far greater appreciation of the practical constraints that must be overcome to develop a workable system.

This project has helped to direct both industry and academia towards techniques that are most likely to provide practical solutions to the creep damage problem; it has also expanded the knowledge base from which RWE npower can draw future work. This was my main objective from the Engineering Doctorate and I feel it has put me in position to rapidly raise the quality of NDE research and development at RWE npower and forge stronger links with academic institutions. To that end, I conclude that both these projects have been successful.

Appendix A. References

[1] Slack K.J. , 2009, 'Inspection and summary report for Didcot 'A' Unit 2 – 2009 Major Outage', *RWE npower report TECH/PLI/09/DCA/100/000.*

[2] Dickinson D. , 2008, 'Drax Power Station Unit No. 1 Major Outage 2008 NDT Inspection Summary Report', *RWE npower report TECH/PLI/08/DRO/192/000.*

[3] Hi-Energy.org.uk, 2008, 'How Electricity is Generated in the UK', Available at http://www.hi-energy.org.uk/Why/howelectricityisgenerated.html. ***[Accessed Feb 2010].***

[4] RWE npower plc, 2010, 'Power Generation', Available at www.rwenpower.com ***[Accessed Feb 2010].***

[5] Jones D., 2009, 'Inspection Management Policy', *RWE npower policy document ENG/TECH/300/PLI/003.*

[6] Department of Trade and Industry, 2002, 'Residue Utilisation at Didcot Coal-Fired Power Station'. Available online at
http://webarchive.nationalarchives.gov.uk/+/http://www.berr.gov.uk/files/file17971.pdf
[Accessed Feb 2010].

[7] Sposito, G., Ward, C., Cawley, P.B., Nagy, P., Scruby, C., 2010, 'A review of non-destructive techniques for the detection of creep damage in power plant steels', *NDE&E International, Vol. 43, 555-567.*

[8] Hulance, J., 2009, 'Tilbury Unit 9 2010 Creep Life Review', *RWE npower report TECH/JJE/1184/09.*

[9] Brear, J.M., 'Prediction of P91 life under operating conditions', Available online at http://www.seseurope.com/htm/SESpapers_pdf/ ***[Accessed Feb 2010].***

[10] Rao N. N., 2004, Elements of Engineering Electromagnetics, 6th Edition, Pearson Prentice Hall.

[11] Dobbs, E.R., 1993, 'Basic Electromagnetism', 1st Edition, Chapman & Hall.

[12] NDT Resource Centre. Self-Inductance and Inductive Reactance [online],
Available at
http://www.ndt-ed.org/EducationResources/CommunityCollege/EddyCurrents/Physics
[Accessed Jan 2006].

[13] McMaster, R.C., 1986, Nondestructive Testing Handbook: Electromagnetic Testing, *Second Edition, ASNT Press.*

[14] Dodd C.V., Deeds W.E, 1968, Analytical Solutions to eddy-current probe-coil problems, *Journal of Applied Physics, Vol. 39, No. 6, 2829-2838.*

[15] Theodoulidis T., 2000, Eddy current Testing Simulation on a Personal Computer, *15th WCNDT 2000, Rome 15th-21st October 2000*, Available at
http://www.ndt.net/article/wcndt00/papers/idn228/idn228.htm.

[16] Theodoulidis T., Kriezis E., 2005, Series expansions in eddy current non-destructive evaluation models*, Journal of Materials Processing Technology, Vol. 161, 343-347.*

[17] Theodoulidis T., 2008, *Teddy V1.2*, [Email] Personal Communication 14th October 2008.

[18] Ditchburn R. J., Burke S. K., 2005, Planar rectangular spiral coils in eddy-current non-destructive inspection, *NDE&E International, Vol. 38*, *690-700.*

[19] Fava J., Obrutsky A., Ruch E. M., 2004, Design and construction of eddy current sensors with rectangular planar coils*, 16th WCNDE 2004 Montreal, ,* CNEA; San Martin; Buenos Aires; Argentina.

[20] Fava J., Ruch M., 2006, Calculation and simulation of impedance diagrams of planar rectangular spiral coils for eddy current testing*, NDE&E International, Vol.39, 414-424.*

[21] Helifa B, Oulhadj A., Benbelghit A., Lefkaier I.K., Boubenider F., Boutassouna D., 2006, Detection and measurement of surface cracks in ferromagnetic materials using eddy current testing*, NDE&E International, Vol.39, 384-390*

[22] Zergoug M., Boucherrou N., Hammouda A. and Kamel G., 2005*,* Characterization of multilayer corrosion by pulsed eddy current*,*
3rd Middle East NDT Conference and Exhibition, Bahrain, Manama 27-30th Nov 2005, Available at http://www.ndt.net/article/mendt2005/pdf/05.pdf.

[23] Hinken J. H., Barenthin B., Halfpaap J., Moebes C., Wrobel H., Ziep C., Hekli M., 2005, NDT.net "Thickness measurement of chromium layers on stainless steel using the thermoelectric method with magnetic readout (TEM)" [online], Available at http://www.ndt.net/article/v10n05/hinken1/hinken1.htm.

[24] Huang P., Zhou Z., Wu Z.., 2005, Quantifying Hidden Defect in Multi-layered Structures by Using Eddy Current System Combined with Scanner*, Journal of Physics: Conference Series 13*, *385-388.*

[25] Huang P., Zhang G., Zhou Z., Wu Z., **2006,** Inspection of defects in conductive multi-layered structures by an eddy current scanning technique: Simulation and experiments*, NDE&E International, Vol.39, 578-584.*

[26] Franklin B., Cohen I.B., **1941,** Benjamin Franklin's Experiments; A new edition of Franklin's Experiments and observations on electricity*, Harvard University Press.*

[27[Faraday M., **1832,** Experimental Researches in Electricity, *The Society (London)*.

[28] Maxwell J. C., 1873, A Treatise on Electricity and Magnetism, *Clarendon Press (Oxford).*

[29] Hughes D. E., **1875,** On the Physical Action of the Microphone, *Proceedings of the Physical Society, London, Vol. 2, 255-261*.

[30] Gunn R., **1941,** An eddy-current method of flaw detection in non-magnetic metals, *Journal of Applied Mechanics*, *Vol. 8, A22-A26.*

[31] Vigness I., Dinger J. E. and Gunn R., **1942,** Eddy current type flaw detectors for non-magnetic metals, *Journal of Applied Physics, Vol. 13, 377-383.*

[32] Trost A., **1942,** Testing non-ferrous pipes, bars and shapes with eddy currents, *Metallwirtschaft, Vol. 20, 697-699.*

[33] Armour A. M., 1947, Eddy current and electrical methods of crack detection, *Journal of Scientific Instrumentation, Vol. 25, 209-210.*

[34] Hastings C. H., **1947,** Recording magnetic detector locates flaws in ferrous metals*, Product Engineering, Vol. 18, 110-112.*

[35] Hochschild R., 1954, Eddy current analysis by impedance analysis, *NDE, Vol. 12*.

[36] Knopp W.A., Jnr, **1943,** Rapid nondestructive testing with a cathode ray oscilloscope*, Instruments, Vol. 16, 14-15.*

[37] Cavenagh P.E., **1947**, The progress of failure in metals as traced by changes in magnetic and electrical properties, *Proceedings, ASNT, Vol. 47, 110-112.*

[38] Bowman G.B., **1947,** Measurement of thickness of copper and nickel plate, *Monthly review, Vol. 34, 1149-1151.*

[39] Brenner A., Kellogg E., **1948,** Magnetic measurement of the thickness of composite copper and nickel coatings on steel, *Journal of Research, Vol. 40, 295-299.*

[40] Dodd C. V., 1965, A Solution to Electromagnetic Induction Problems, *Thesis: University of Tenessee.*

[41] Kahn A. H., Spal R., Feldman A., 1977, Eddy-current losses due to a surface crack in conducting material, *Journal of Applied Physics, Vol. 48, No.11, 4454-4459.*

[42] Yi J.-Y., Lee S., 1986, Magnetic effects in eddy current nondestructive method*, Journal of Applied Physics, Vol. 59, 671*.

[43] Bowler J. R., **1986,** Eddy current calculations using half-space Green's functions, *Journal of Applied Physics, Vol. 61, No. 3, 833-839*.

[44] Bowler J. R., Norton S.J., Harrison D.J., 1994, Eddy-Current Interaction with an Ideal Crack, Part II: The Inverse Problem, *Journal of Applied Physics, Vol. 75, No. 13, 8138-8144.*

[45] Bowler J. R., **1994,** Eddy-Current Interaction with an Ideal Crack, Part I: The Forward Problem, *Journal of Applied Physics, Vol. 75, No. 12, 8128-8137.*

[46] Norton S. J., Bowler J. R., **1992,** Theory of Eddy-Current Inversion, *Journal of Applied Physics, Vol. 73, No. 2, 501-512.*

[47] Bowler J. R., Sabbagh L. D., Sabbagh H. A., 1990, Eddy Current Probe Impedance Due to a Surface Slot in a Conductor*, IEEE Transactions on Magnetics, Vol. 26, No. 2, 889-892.*

[48] Bowler J., Harfield N., **1998,** Evaluation of probe impedance due to thin-skin eddy-current interaction with surface cracks*, IEEE Transactions on Magnetics, Vol. 34, No 2, 515-523.*

[49] Bowler J., Harfield N., **2000,** Thin-skin Eddy current interaction with semi-elliptical and epi-cyclic cracks*, IEEE Transactions on Magnetics, Vol. 36, No 1, 281-291.*

[50] Kolyshkin A. A.,Vaillancourt R., 1994, Method of solution of forward problems in eddy-current testing*, Journal of Applied Physics, Vol. 77, No. 10, 4903-4913.*

[51] Satveli R., Moulder J. C., Wang B., Rose J. H., **1995,** Impedance of a coil near an imperfectly layered metal structure: The layer approximation, *Journal of Applied Physics, Vol. 79, No. 6, 2811-2821.*

[52] Bowler J. R., Jenkins S. A., Sabbagh L. D., Sabbagh H. A., 1991, Eddy-current probe impedance due to a volumetric flaw, *Journal of Applied Physics, Vol. 70, No. 3, 1107-1114.*

[53] Uzal E., Moulder J. C., Mitra S., Rose J. H., 1993, Impedance of coils over layered metals with continuously variable conductivity and permeability: Theory and experiment**,** *Journal of Applied Physics, Vol. 74, No. 3, 2076-2089.*

[54] Harfield N., Bowler J. R., 1997, Theory of thin-skin eddy-current interaction with surface cracks**,** *Journal of Applied Physics, Vol. 82, No. 9, 4590-4603.*

[55] Burke S.K., 1987, Eddy-current NDI of cracks in thin plates, *Journal of physics D, Vol. 20, 797-800*

[56] Harfield N., Bowler J. R., 1995, Solution of the two-dimensional problem of a crack in a uniform field in eddy current non-destructive evaluation, *Journal of Physics D. Vol. 28, 2197-2205.*

[57] Harfield N., Bowler J. R., **1994,** Analysis of Eddy-Current Interaction with a Surface-Breaking Crack, *Journal of Applied Physics, Vol. 76, No.8, 4853-4856.*

[58] Harfield N., Bowler J. R., **1997,** A geometrical theory for eddy-current non-destructive evaluation*, Proceedings of the Royal Society of London A. Vol. 453, 1121-1152.*

[59] Bowler J., Yoshida Y., Harfield N., 1997, Vector-Potential Boundary-Integral Evaluation of Eddy-Current Interaction with a Crack, *IEEE Transactions on Magnetics, Vol 33, No 5, 4287-4294.*

[60] Liaw J.W., Chu S. L., Yeh C. S., Kuo M. K., 1998, Analysis of Eddy Currents in a Bar obtaining an Embedded Defect*, NDE&E International, Vol. 32, 293-303.*

[61] Theodoulidis T., Bowler J., **2005,** Eddy current coil interaction with a right-angled conductive wedge*, Proceedings of the Royal Society of London A. Vol. 461,3123-3139.*

[62] Bowler J., 1999, Eddy Current Inversion for the Determination of Crack Geometry*, IEE, 8/1-8/4.*

[63] Bowler J. R., 1999, Time domain half-space dyadic Green's functions for eddy-current calculations, *Journal of Applied Physics, Vol. 86, No. 11, 6494-6500.*

[64] Theodoulidis T., Bowler J., 2005, Eddy-current Interaction of a Long Coil with a Slot in a Conductive Plate*, IEEE Transactions on Magnetics, Vol. 41, No 4, 1238-1247.*

[65] Yoshida Y., Bowler J., 2000, A Vector potential integral formulation for eddy-current probe response to cracks*, IEEE Transactions on Magnetics, Vol. 36, No 2, 461-469.*

[66] Theodoulidis T. P., **2003,** Model of ferrite-cored probes for eddy current nondestructive evaluation*, Journal of Applied Physics, Vol. 93, No. 5, 3071-3078*.

[67] Huang H., Takagi T., Uchimoto T., 2003, Fast numerical calculation for crack modelling in eddy current testing of ferromagnetic materials*, Journal of Applied Physics, 5866-5872*.

[68] Rodríguez A. A., Hiptmair R., Valli A., 2004, Mixed finite element approximation of eddy current problems*, IMA Journal of Numerical Analysis, Vol. 24, 255-271*.

[69] Sikora R., Chady T., Gratkowski S., Komorowski M., 1998, Identification of Flaws Using Eddy Current Testing, *Compel, Vol. 17, No. 4, 516-527.*

[70] Koyama K., Hoshikawa H., Kubota S., 2004, Fundamental study of flaw estimation in eddy current testing using genetic algorithm, *16th WCNDE 2004 Montreal,*
Available at http://www.ndt.net/article/wcndt2004/pdf/eddy_current/317_koya.pdf.

[71] Berthiau G., de Barmon B., **2000,** MESSINE: Eddy current modelling in CIVA*, 15th WCNDT 2000, Rome 15th-21st October 2000*, Available at
http://www.ndt.net/article/wcndt00/papers/idn638/idn638.htm.

[72] Pichenot G., Sollier T., 2002, NDE.net "Eddy current modelling for nondestructive testing**"***, Vol. 8, No. 6***,** Available at
http://www.ndt.net/article/ecndt02/322/322.htm.

[73] Sollier T., Buvat F., Pichenot G., Prémel D., 2004, Eddy current modelling of ferrite-core probes, application to the simulation of eddy current signals from surface breaking flaws in austenitic steels*, 16th WCNDE 2004 Montreal,*
Available at http://www.ndt.net/article/wcndt2004/pdf/eddy_current.

[74] Waidelich D.L., 1956, Measurement of coating thickness by use of pulsed eddy currents*, Materials Evaluation, Vol. 14, 14-16.*

[75] Busse T.H., Beyer N.S., **1970,** Pulsed eddy current inspection of thin-walled reactor fuel tubing*, Materials Evaluation, Vol. 28, 228-236*.

[76] Allen B., Ida N., Lord W., **1985,** Finite element modelling of pulsed eddy current NDE phenomena*, IEEE Transactions on Magnetics, Vol. Mag-21.*

[77] Davey K., Turner L., 1988, The use of time space Green's function in the computation of transient eddy current fields*, Journal of Applied Physics, Vol. 6, 6132-6137.*

[78] Lepine B.A., Wallace B.P., Forsyth D.S., Wyglinski A., 1999, Pulsed eddy current method development for hidden corrosion detection in aircraft structures*, 1st PACNDT '98 Proceedings, Toronto 14th-18th September 1998.* Available online at
http://www.ndt.net/article/pacndt98/17/17.htm.

[79] Smith R.A., 2001, Detection of deep corrosion and cracks in aging aircraft using transient eddy-current NDE*, Proceedings of 40th annual BINDT conference.*

[80] Yang H.-C., Tai C.-C, 2002, Pulsed eddy-current measurement of a conducting coating on a magnetic metal plate*, Measurement Science Technology, Vol. 13, 1259-1265.*

[81] Sophian A., Tian G.-Y. 2005, NDE of coated steel structures using Pulsed Eddy Current techniques, *Draft copy, Personal Communication.*

[82] Panaitov G., Krause H.-J., Zhang Y., 2002, Pulsed eddy current transient technique with HTS SQUID magnetometer for non-destructive evaluation, *Physica C, 278-281.*

[83] Tian G.-Y., Sophian A., 2005, Defect classification using a new feature for pulsed eddy current sensors, *NDT&E International, Vol. 38, 77-82* .

[84] Edwards R.S., Sophian A., Dixon S., Tian G.-Y., Jian X., 2006, Dual EMAT and PEC non-contact probe: applications to defect testing, *NDT&E International, Vol. 39, 45-52*

[85] Sheiretov, Y., 2001, Deep Penetration Magnetoquasistatic Sensors, *PhD Thesis, Massachussetts Institute of Technology.*

[86] Goldfine N.J., 1993, Magnetometers for improved materials characterization in aerospace applications, *Materials Evaluation, Vol. 51, 396-405.*

[87] Goldfine N., Sheiretov Y., Washabaugh A., Zilberstein V., 1999, Materials characterization and flaw detection for thermal barrier coating repairs, *Private Correspondence [Email] to P. Crowther, National Power PLC.*

[88] Washabaugh A., Zilberstein V., Schlicker D., Goldfine N., 2000, Absolute electrical property measurements using conformable MWM eddy-current sensors for quantitative materials characterization, *15th WCNDT 2000, Rome 15th-21st October 2000*, Available at http://www.ndt.net/article/wcndt00/papers/idn360/idn360.htm.

[89] Goldfine N., Schlicker D., Sheiretov Y., Washabaugh A., Zilberstein V., Grundy D., 2002, Surface mounted and scanning periodic field eddy-current sensors for structural health monitoring, *IEEE Aerospace Conference 2002: Track 11. Diagnostics, prognostics and health management.*

[90] Zilberstein V., Walrath K., Grundy D., Schlicker D., Goldfine N., Abramovici E., Yentzet T., 2003, MWM eddy-current arrays for crack initiation and growth monitoring, *International Journal of Fatigue 25, 1147-1155.*

[91] Michael D.H., Waechter R.T., Collins R., 1982, The measurements of surface cracks in metals by using A.C. electric fields, *Royal Society of Proceedings of the London A 381,139–57.*

[92] McIntyre P., Priest A.H., 1971, Measurement of sub-critical flaw growth in stress corrosion. Cyclic loading and high temperature creep by the DC electrical resistance technique, *BISRA report MG/54/71.*

[93] Venkatasubramanian T.V., Unvala B.A., 1984, An AC potential drop system for monitoring crack length, *Journal of Physics E: Sci. Instrum., Vol. 17, 765-771.*

[94] Mayes I.C., 1980, Inclusion induced anisotropy in the fatigue crack growth behaviour of steels, *PhD Thesis, Imperial College, London.*

[95] Bowler N., 2006, Theory of a four-point alternating current potential drop measurements on a metal half-space, *Journal of Physics D: Applied Physics, Vol. 39, 584-589.*

[96] Raine A., 2000, The Development of Alternating Current Field Measurement (ACFM) Technology as a Technique for the Detection of Surface Breaking Defects in Conducting Materials and its Use in Commercial and Industrial Applications, *15th WCNDT 2000, Rome 15th-21st October 2000*, Available at
http://www.ndt.net/article/wcndt00/papers/idn644/idn644.htm.

[97] Topp D., Lugg M., 2005, Advances in thread inspection using ACFM, *3rd Middle East NDT Conference and Exhibition, Bahrain, Manama 27-30th Nov 2005.*

[98] Ward, C., 2008, MWM Inspection for embrittled area detection on steam turbine blades, *RWE npower Internal.*

[99] Sposito G., Cawley P., Nagy P. B., 2009, Potential Drop Mapping for Corrosion Monitoring, *Review of Progress in Quantitative Nondestructive Evaluation, Vol. 28*, *(in press).*

[100] Cox, J., 2000, Programmed Instruction Handbook, Eddy Current Volume 1 – Basic Principles, *PH Diversified, Inc.*

[101] NDT Resource Centre, Self-Inductance and Inductive Reactance [online],
Available at
http://www.ndt-ed.org/EducationResources/CommunityCollege/EddyCurrents/Instrumentation
[Accessed Jan 2006].

[102] Buckey, J., An introduction to Eddy Current Testing theory and technology [online],
Available at http://www.joe.buckley.net/papers/eddyc.pdf
[Accessed Jan 2006].

[103] Manz Electronic Systeme, 2008, Nanocrystalline soft magnetic material [online], *http://www.manz-electronic.de/index/download/FINEMETmaterials.pdf.*

[104] Spink G., 2004, 'Evaluation of the susceptibility of laser hardened steam turbine last stage blade material to fatigue and environmentally assisted cracking', *RWE npower report TECH/JJE/257/04.*

[105] Spink G., 2003, 'Preliminary Metallurgical Examination of Failed Final Stage Blade, Didcot A Unit 3 LP2' *RWE Innogy Internal.*

[106] Shaw N., 2006, Personal communication [Email], *received 15th June 2006.*

[107] Ward, C., 2008, 'Hardness testing of LP turbine blade aerofoil', *RWE npower work instruction TS601/007.*

[108] Reigl M., Goch G., 1998, Thermal wave analysis of hardened samples: evaluation with the finite difference method, *Measurement 23, 215-220.*

[109] Zergoug M., Lebaili S., Boudjellal H., Benchaala A. , **2004**, Relation between mechanical microhardness and impedance variations in eddy current testing, *NDT&E International, Vol. 37, 65-72.*

[110] Mercier D., Kesage J., Decoopman X., Chicot D. , **2006**, Eddy currents and hardness testing for evaluation of steel decarburizing, *NDT&E International 39, 652-660.*

[111] Allen T.R., Tan L., Gan J., Gupta G., Was G.S., Kenik E.A., Shutthanandan S., Thevuthasan S. , **2006**, Microstructural development in advanced ferritic-martensitic steel HCM12A, *Journal of Nuclear Materials 351, 174-186.*

[112] Lee M.K., Kim G.H., Kim K.H., Kim W.W. , **2004**, Control of surface hardnesses, hardening depths, and residual stresses of low carbon 12Cr steel by flame hardening, *Surface and coatings technology 184, 239-246.*

[113] Schleithoff K., Schmitz F., **1981**, Corrosion fatigue of steam turbine blade materials in: R.I. Jaffee (Eds.) Workshop Proceedings, Palo Alto, CA, EPRI, *Pergamon Press.*

[114] Heitkemper M., Bohne C., Pyzalla A., Fischer A. , **2003**, Fatigue and fracture behaviour of a laser surface heat treated martensitic high-nitrogen tool steel, *International journal of Fatigue 25, 101-106.*

[115] Callister W. Jr, **1997,** Materials Science and Engineering, An Introduction, *Wiley*.

[116] Beardmore, R., Plain Iron Carbon Steels [online],
Available at http://www.roymech.co.uk/Useful_Tables/matter/phase_diagram.html
[Accessed May 2006].

[117] Lee M.K., Kim G.H., Kim K.H., Kim W.W. , **2006**, Effects of the surface temperature and cooling rate on the residual stresses in the flame hardening of 12Cr steel, *Journal of Materials Processing Technology 176, 140-145.*

[118] Dybiec C., Koslowska A. , **1998**, Determining residual austenite with the eddy current method, *7th European Conference on Non-destructive Testing, Copenhagen 26-29 May 1998*. Available online at http://www.ndt.net/abstract/ecndt98/ecndt98.htm.

[119] Uzal E., Moulder J.C., Rose J.H. , **1994**, Experimental determination of the near-surface conductivity profiles of metals from electromagnetic induction (eddy current) measurements, *Inverse Problems 10, 753-764.*

[120] Ma X., Peyton A.J., Zhao Y.Y., **2006**, Eddy current measurements of electrical conductivity and magnetic permeability of porous metals, *NDT&E International, Vol. 39, 562-568.*

[121] Yin W., Hao X., Peyton A., Strangwood M., Davis C., 2009, Measurement of permeability and ferrite/austenite phase fraction using a multi-frequency electromagnetic sensor, *NDT&E International, Vol. 42, 64-68.*

[122] Konoplyuk S., Abe T., Uchimoto T., Takagi T., Kurosawa M., **2005**, Characterization of ductile cast iron by eddy current method, *NDT&E International, Vol. 38, 623-626.*

[123] Uchimoto T., Takagi T., Konoplyuk S., Abe T., Huang H., Kurosawa M. , **2003**, Eddy current evaluation of cast irons for material characterization, *Journal of Magnetism and Magnetic Materials 258-259, 493-496.*

[124] O'Sullivan D., Cotterell M., Meszaros I. , **2004**, The characterisation of work-hardened austenitic stainless steel by micro-magnetic techniques, *NDT&E International, Vol. 37, 265-269.*

[125] Ward, C., 2009, Eddy current hardness testing of LP last stage blades, *RWE npower work instruction TS402/009.*

[126] Dobrzański, J., 2004, Internal damage processes in low-alloy chromium-molybdenum steels during high-temperature creep service, *Journal of Materials Processing Technology, Vol. 157-158, 297-303.*

[127] Parker, J.D., Stratford, G.C., **1996**, Strain localization in creep testing of samples with heterogeneous microstructures, *International Journal of Pressure Vessels and Piping, Vol. 68, 135-143.*

[128] Haarmann, K., Vaillant, J.C., Vandenberghe, B., Bendick, W., Arbab, A., 2002, The T91/P91 Book, *2nd Edition*, *V&M.*

[129] Sanchez-Hanton, J., 2009, Failure of Modified 9Cr, *Personal Communication [email]*, *Received 22nd January 2009.*

[130] Furtado, H.C., de Almeida, L.H., Le May, I., **2007**, Precipitation in 9Cr-1Mo steel after creep deformation, *Materials Characterisation 58, 72-77.*

[131] Abe, F., Horiuchi, T., Taneike, M., Sawada, K., **2004**, Stabilization of martensitic microstructure in advanced 9Cr steel during creep at high temperature, *Material Science and Engineering A, Vol. 378, 299-303.*

[132] Spigarelli, S., Quadrini, E., **2002**, Analysis of the creep behaviour of modified P91 (9Cr-1Mo-NbV) welds, *Materials and Design, Vol. 23, 547-552*

[133] Okamura, H., Ohtani, R., Saito, K., Kimura, K., Ishii, R., Fujiyama, K., Hongo, S., Iseki, T., Uchida, H., **1999**, Basic investigation for life assessment technology of modified 9Cr-1Mo steel, *Nuclear Engineering And Design, Vol. 193, 243-254* .

[134] Masuyama, F., **2006**, Creep degradation in welds of mod. 9Cr-1Mo steel, *International journal of Pressure Vessels and Piping, Vol. 83, 819-825.*

[135] Gooch, D.J., Kimmins, S.T., 1987, Proceedings of international conference on creep and fracture of engineering materials and structures*. London, The Institute of Metals*.

[136] Singh, R., Singh, S.R. , **1997**, Remaining creep life study of Cr-Mo-V main steam pipe lines, *International Journal of Pressure Vessels and Piping, Vol. 73, 89-95.*

[137] Fujibayashi, S., **2007**, Creep behaviour leading to type IV cracking for service-exposed 1.25Cr-0.5Mo steel welds, *Engineering Fracture Mechanics, Vol. 74, 932-946.*

[138] Uesaka, M., Sukegawa, T., Miya, K., Takahshi, S., Echigoya, J., Yamada, K., Kasai, N., Morishita K., Ara, K., Ebine, N., Isobe, Y., **2000**, Round-robin test work for the magnetic nondestructive evaluation of structural materials in nuclear power plant, *Proc. Of Relationship between Magnetic and Structural Properties.*

[139] Willems, H., **Dobmann, G., 1991**, Early detection of creep damage by ultrasonic and electromagnetic techniques, *Nuclear Engineering and Design, Vol. 128, 139-149.*

[140] Govindaraju, M.R., Kaminski, D.A., Devine, M.K., Biner, S.B., Jiles, D.C., **1997**, Nondestructive evaluation of creep damage in power-plant steam generators and piping by magnetic measurements,, *NDT&E International, Vol. 30, 11-17.*

[141] Bisbee, L., Queen, H.E., Bezzant, R.K., **2006**, Structural Integrity *'Ultrasonic testing metric for creep damage assessment*', Available online at www.structint.com.

[142] Raj, B., Choudhary, B.K., Singh Raman, R.K., **2004**, Mechanical properties and non-destructive evaluation of chromium-molybdenum ferritic steels for steam generator application, *International Journal of Pressure Vessels and Piping, Vol. 81, 521-534.*

[143] Kim, D.-W., Kwon, D., **2003**, Quantification of the Barkhausen noise method for the evaluation of time-dependent degradation, *Journal of Magnetism and Magnetic Materials Vol. 257, 175-183.*

[144] Mitra, A., Mohapatra, J.N., Swaminathan, J., Ghosh, M., Panda, A.K., Ghosh, R.N., 2007, Magnetic evaluation of creep in modified 9Cr-1Mo steel, *Scripta Materialia, Vol. 57, 813-816.*

[145] Kneller, E., **1966**, Ferromagnetismus, *Springer-Verlag.*

[146] Umakoshi, Y., Yasuda, H.Y., 2008, Nondestructive lifetime prediction by magnetic measurements, *Encyclopaedia of Materials: Science and Technology, 1-9.*

[147] Kronmüller, H., 1972, Magnetic Techniques for the study of dislocations in ferromagnetic materials, *International Journal of Nondestructive Testing 3.*

[148] Chen, Z.J., Jiles, D.C., Kameda, J., 1994, Estimation of fatigue exposure from magnetic coercivity, *Journal of Applied Physics 75, 6975.*

[149] Hilzinger, H.R., Kronmuller, H., **1975**, Statistical theory of the pinning of Bloch walls by randomly distributed defects, *Journal of Magnetism and Magnetic Materials, Vol. 2, 11-17.*

[150] Moorthy, V., Vaidyanathan, S., Jayakumar, T., Raj, B., Kashyap, B.P., 1999, Effect of tensile deformation on micromagnetic parameters in 0.2% carbon steel and 2.25Cr-1Mo steel, *Acta Materialia, Vol. 47, 1869-1878.*

[151] Dobmann, G., Kröning, M., Theiner, W., Willems, H., Fiedler, U., **1992**, Nondestructive characterization of materials (ultrasonic and micromagnetic techniques) for strength and toughness prediction and the detection of early creep damage, *Nuclear Engineering and Design, Vol. 157, 137-158.*

[152] Sablik, M.J., Augustyniak, B., Piotrowski, L., **2004**, Modelling incipient creep damage effects on Barkhausen noise and magnetoacoustic emission, *Journal of Magnetism and Magnetic Materials, Vols. 272-276, Supplement 1, E523-E525.*

[153] Krause, H.J., Kreutzbruck, M.V., 2002, Recent developments in SQUID NDE, *Physica C, Vol. 368, 70-79.*

[154] Somekh, M.G., Liu, M, Ho, H.P., See, C.W., **1995,** An accurate non-contacting laser based system for surface wave velocity measurement, *Measurement Science Technology 6, 1329-1337.*

[155] Sharples, S.D., Clark, M, Li, W, Somekh, M.G., 2008, Rapid Imaging of Microstructure using Spatially Resolved Acoustic Spectroscopy, *1st International Symposium on Laser Ultrasonics: Montreal, Canada.*

[156] Russell, D., Buttle, D., **2006**, On-line monitoring of absolute stress values in pipelines, *Pigging Products and Services Association.*

[157] Birks, A.S., Green, R. E., **1991**., Nondestructive Testing Handbook 2nd Edition: Volume Seven Ultrasonic Testing, *ASNT.*

[158] Hirao, M., Ogi, H., **2003,** EMATS for Science and Industry, *Kluwer Academic Publishers.*

[159] Wilson, J., Tian, G-Y., **2007,** Pulsed Electromagnetic Methods for Defect Detection and Characterisation, *NDT&E International, Vol. 40, 275-283.*

[160] Buttle, D.J., Scruby, C.B, Jakubovics, J.P., Briggs, G.A.D., **1987**, Magneto-Acoustic and Barkhausen Emission: Their Dependence on Dislocations in Iron, *Philosophical Magazine A, Vol. 55, 717-734* .

[161] O'Sullivan, D., Cotterell, M., Tanner, D.A., Mészáros, I., **2004,** Characterisation of Ferritic Stainless Steel by Barkhausen Techniques, *NDT&E International, Vol. 37, 489-496.*

[162] Wilson, J., Tian, G-Y., **2007,** Comparative quantification of acoustic and magnetic Barkhausen noise data with respect to various excitation waveforms, *46th BINDT Conference, 18th-20th September 2007, Glasgow, UK.*

[163] Hess, P., Lomonosov, A.M., **2009,** Solitary surface acoustic waves and bulk solutions in nanosecond and picosecond laser ultrasonics, *Ultrasonics (Accepted Manuscript).*

[164] Sharples, S.D., **2003,** All-Optical Scanning Acoustic Microscope, *PhD Thesis: University of Nottingham.*

[165] Collison, I.J., Stratoudaki, T., Clark, M., Somekh, M.G., **2008,** Measurement of elastic nonlinearity using remote laser ultrasonics and Cheap Optical Transducers and dual frequency surface acoustic waves, *Ultrasonics 48* .

[166] Sharples, S.D., 2009, Optical and Thermographic NDE: *Personal* Communication [*RCNDE Course notes]*, Received 2nd September 2009.

[167] Hong, Y., Sharples, S.D., Clark, M., Somekh, G., **2004,** Rapid and accurate analysis of surface and pseudo-surface waves using adaptive laser ultrasound techniques, *Ultrasonics 42, 515-518.*

[168] Szelążek, J., Mackiewicz, S., Kawalewski, Z.L.., **2009,** New samples with artificial voids for ultrasonic investigation of material damage due to creep, *NDT&E International, Vol. 42, 150-516.*

[169] Joshi, K.R., Kamathe, R.S., 2008, SDI: New metric for quantification of speckle noise in ultrasound imaging, *Proc. Of the 2008 IEEE 10th Workshop on Multimedia Signal Processing, 122-126.*

[170] Ohtani, T., Ogi, H., Hirao, M., **2006**, Evolution of microstructure and acoustic damping during creep of a Cr-Mo-V ferritic steel, *Acta Materialia 54, 2705-2713.*

[171] Taylor, J.L., 1996, Basic Metallurgy for Non-Destructive Testing: Revised 1996, *Stantons Press*.

[172] Sharples, S.D., Personal communication [Email], *received 4th August 2010.*

[173] Nanekar, P.P., Shah, B.K., **2003**, *Characterization of material properties by ultrasonics*, *BARC Newsletter 249, 25-38.*

[174] Lofaj, F., Smith, D.T., Blessing, G.V., Luecke, W.E., Wiederhorn, S.M., **2003**, Instrumented indentation and ultrasonic velocity techniques for the evaluation of creep cavitation in silicon nitride, *Journal of Materials Science, Vol. 38, 1403-1412.*

[175] Martinez-Oña, R., Pérez, Ma.C., **2000**, Research on Creep damage Detection in reformer tubes by Ultrasonic testing, *15th WCNDT 2000, Rome 15th-21st October 2000*, Available at http://www.ndt.net/article/wcndt00/papers/idn238/idn238.htm.

[176] Yardley, V., 2003, Magnetic Detection of Microstructural Change in Power Plant Steels, *PhD Thesis, Emmanuel College, Cambridge University.*

[177] Wilson, J., 2008, Evaluation of creep degradation in Grade 91 steel using magnetic Barkhausen emission, *Personal Communication [Email],* Received 19th December 2008.

[178] Fleming, M., Lowe, M.J.S., Simonetti, F., Cawley, P., **2006,** Super resolution imaging: performance studies, *Review of Progress in Quantitative NDE, eds. D.O. Thompson and D.E. Chimenti, American Institute of Physics, New York, vol. 25, pp. 736-743.*

[179] Moon, F.C., 1984, Magneto-Solid Mechanics, *Wiley-Interscience.*

[180] Vincent, A., Pasco, L., Morin, M., Kleber, X., Delnondedieu, M., 2005, Magnetic Barkhausen noise from strain-induced martensite during low cycle fatigue of 304L austenitic stainless steel, *Acta Materialia, Volume 53, Issue 17, Pages 4579-4591.*

Appendix B. Deriving Maxwell's Equations

Consider a flux passing through an element of area $d\underline{S}$ due to a field, such that

$$d\phi = \underline{A} \cdot d\underline{S} \qquad \text{(B1.1)}$$

If the field is an electric field then, by Coulomb's law

$$\underline{E} = \frac{q}{4\pi\varepsilon_0 r^2} \qquad \text{(B1.2)}$$

the flux becomes

$$d\phi = \frac{q}{4\pi\varepsilon_0 r^2} \cdot dS = \frac{q d\Omega}{4\pi\varepsilon_0} \text{ (B1.3) where } d\Omega = \frac{\Delta S}{r^2} \text{ is a solid angle element.}$$

The total flux out of the surface for a given number of charges (i) is therefore

$$\phi = \frac{\sum_i q_i}{\varepsilon_0} \text{ (B1.4)}$$

Using the divergence theorem

$$\int_S \underline{E} \cdot d\underline{S} = \int_v \nabla \cdot \underline{E} dv = \frac{q}{\varepsilon_0} \qquad \text{(B1.5)}$$

So for an infinitesimal volume of charge density ρ

$$div\underline{E} = \nabla \cdot \underline{E} = \frac{\rho}{\varepsilon_0} \qquad \text{(B1.6 - Gauss' Law)}$$

Eq. B1.6 also yields

$$div\underline{D} = \nabla \cdot \underline{D} = \rho \qquad \text{(B1.7) since the electrical displacement } \underline{D} = \underline{E}\varepsilon_0 \quad \text{(B1.8)}$$

The current I passing through any surface is given by

$I = \underline{J} \cdot d\underline{S}$ (B2.1) where J is the current density.

Within a given volume any rate of increase in charge must be equal to the net flow of charge into the volume. Put mathematically

$$\frac{\partial}{\partial t}\left(\int \rho dr\right) = \int \frac{\partial \rho}{\partial t} dr = -\int \underline{J} \cdot d\underline{S} \qquad \text{(B2.1)}$$

Again using the divergence theorem

$$-\int \underline{J} \cdot d\underline{S} = -\int div\underline{J} dr \quad \text{(B2.2)}$$

So $div\underline{J} = -\dfrac{\partial \rho}{\partial t}$ (B2.3)

If ρ is constant (i.e. the steady-state) then

$$div\underline{J} = 0$$

The magnetic field for a path encircling a current I is given by

$$\oint \underline{B} \cdot d\underline{S} = \mu_0 I \quad \text{(B2.4)}$$

combining with Eq. B2.1 and by Stokes' theorem

$$\oint \underline{B} \cdot d\underline{S} = \int curl\underline{B} \cdot d\underline{S} = \mu_0 \int \underline{J} \cdot d\underline{S} \quad \text{(B2.5)}$$

and so

$$curl\underline{B} = \mu_0 \underline{J} \quad \text{(B2.6)}$$

and since $div\underline{J} = 0$, $div\underline{B} = 0$ (B2.7 – Gauss' Law for magnetism)

From Faraday's law we know that the induced EMF is dependent on the rate of change of magnetic flux and from Lenz's law we know that this EMF acts in opposition to the field that created it, thus

$$EMF = -\frac{d\Phi}{dt} \quad \text{(B3.1)}$$

Where Φ, the total inducing magnetic flux is $\Phi = \int \underline{B} \cdot d\underline{S}$ (B3.2)

And $EMF = \int \underline{E} \cdot d\underline{S}$ (B3.3)

Thus $\int \underline{E} \cdot d\underline{S} = -\dfrac{d}{dt} \int \underline{B} \cdot d\underline{S}$ (B3.4)

Using Stokes' theorem

$curl\underline{E} = \nabla \times \underline{E} = -\frac{d\underline{B}}{dt}$ (B3.5 – Maxwell-Faraday equation)

From Eq. B2.6 we can deduce that since $\underline{B} = \mu_0 \underline{H}$ in a vacuum

$curl\ \underline{H} = \underline{J}$ (B4.1 - Ampères law – Uncorrected)

However, for Eq. B4.1 to be true then $divcurl\underline{H} = \underline{divJ} = 0$ (B4.2)

But we know from Eq. B2.3 that $div\underline{J} = -\frac{\partial \rho}{\partial t}$

So we use $\underline{J}'$ in place of $\underline{J}$ in Eqs. B4.1 and B4.2, where $\underline{J}' \neq \underline{J}$

From Eq. B1.7 $\frac{\partial \rho}{\partial t} = \frac{\partial}{\partial t} div\underline{D} = div\frac{\partial \underline{D}}{\partial t}$ (B4.3)

$curl\underline{H} = \underline{J} + \frac{\partial \underline{D}}{\partial t}$ (Ampères law – corrected)

So $div\underline{J} = -div\frac{\partial \underline{D}}{\partial t}$ (B4.4)

Rearranging gives $div\left(\underline{J} + \frac{\partial \underline{D}}{\partial t}\right) = 0$ (B4.5)

Thus we can deduce from the revised version of Eq. B4.2 that $\underline{J}' = \underline{J} + \frac{\partial \underline{D}}{\partial t}$ (B4.6)

Thus the corrected version of Eq. B4.1 becomes

$curl\underline{H} = J + \frac{\partial \underline{D}}{\partial t}$ (B4.7)

J is the conductor current and

$\frac{\partial \underline{D}}{\partial t}$ is known as the displacement current.

Appendix C. Variation Inherent in Hardness Testing

Hardness testing has always had a degree of ambiguity associated with its results, largely due to it being a relative rather than absolute measurement. Hardness is a measurement of material flow, which is dictated by material microstructure; particularly grain size and orientation. Since grain size and orientation are not constant in practice there will always be localised variation in the hardness of a material. Most hardness testers make a small, sub-millimetre, indentation which is hardly representative of the whole component test area because of these local variations.

The most reliable way to hardness test a material is to use a calibrated bench indenter with a high load on a polished, flat surface that is perpendicular to the indenter. Unfortunately, this is not practical for testing in the field and portable hardness testers have to be used, which use lower loads and can rarely be applied at 90° to a smooth flat surface. In the past I have done several studies on the use of portable hardness testers and levels of confidence in their results. Although these results are for a low-alloy steel with a hardness of typically 130-160Hv compared with 300-500Hv on 12Cr blades, the levels of confidence will be similar or worse for the 12Cr case we are interested in; this is because of the inconsistent curvature of the turbine blades which inhibits the ability to reliable indent at 90° to the blade surface.

Table C1.1 shows variations experienced when three different operators used the same piece of portable hardness testing equipment (G.E. TIV) on the same reference pieces, one flat and one curved.

Operator	Mean Value (of 9 readings)		Standard Deviation of Readings	
	Flat Sample	Curved Sample	Flat Sample	Curved Sample
1	141	137	5.5	3.3
2	137	128	4.1	5.7
3	137	127	5.1	9.6
4	136	138	5.6	9.7
5	138	140	4.5	4.4

Table C1.1 – Hardness testing variation with operator (lab conditions)

Although there is an acceptable level of variation on the flat surface, it should be noted that this test was made in idealised conditions and thus these should be representative of the best achievable results with this equipment. The results on a curved surface; which would be the similar when testing 12Cr blades, show a far more extensive variation in the results obtained as well as (generally) much higher standard deviations of the data acquired. The total range of measurements across the different operators is 14Hv, which for these reference pieces is almost 11% of the mean value.

There is also a variation within results obtained with two supposedly identical machines, operated by the same operator. Table C1.2 shows data obtained by individual operators testing the same flat and curved samples using two G.E. TIV portable hardness testers. The results given are the average variations of five operators taking the same test.

	G.E. TIV 1		G.E. TIV	
	Flat Sample	Curved Sample	Flat Sample	Curved Sample
Mean Value	138	133	137	141
St. Deviation	5	7	5	6

Table C.1.2 – Hardness testing variation between TIV units (lab conditions)

It must be stressed that the variations inherent in the materials own hardness will affect all the results from Tables C1.1 and C1.2, so the total scatter due to operator/kit variation is not as great as it may appear. Shown in Table C1.3 is what the report concluded the likely confidence levels were in the technique, assuming best practice is followed and

adequate support is provided to produce a good indentation.

	Average variation from true mean	Average standard deviation of results	Confidence range
G.E TIV	6	6.09 (4.3%)	+/-12 Hv

Table C1.3 – Overall confidence levels in G.E. TIV portable hardness testers

As mentioned previously these results provide an indication of the level of variation in the hardness test results we can expect on 12Cr blades but the deviations and range cannot be directly translated. This is because any measurement errors in the system will be amplified when looking at the higher hardness values associated with 12Cr blades and also because of the additional errors associated with the varying curvature of turbine blades. To get an idea of the local hardness variations on 12Cr blade material an area the size of an MWM probe (16mm x 16mm) was prepared to a suitable standard on an area of low hardness and on a hardened area. Test C1 used a G.E. TIV hardness tester to indent the area 49 times (7 rows of 7 measurements at 2mm spacing). The summarised results are shown in Table C1.4.

	Non-hard area	Hard area
Mean	331	456
Max	362	486
Min	304	416
Range	58	70
Standard Deviation	17 (5%)	18 (4%)

Table C1.4 – Variation in mechanical hardness testing results

Although the range of readings is very high, the standard deviation of the results expressed as a percentage is in line with the previous studies on the accuracy and consistency of the G.E. TIV portable hardness tester. The results for the hardened area have a lower standard deviation, relative to the range, than the non-hard area but a higher range, suggesting that there is little difference in the spread of hardness value in a hard area compared to a non-hard area.

Appendix D. Alternative Electromagnetic Techniques

D.1. Flux Leakage

Magnetic flux leakage is the basis of magnetic particle inspection as well as being a magnetic method of nondestructive testing in its own right. It can be used to detect corrosion/pitting in ferromagnetic components such as pipes or tanks. Where there is a discontinuity due to missing metal (i.e. in the presence of cracks/corrosion) the magnetic field leaks. Where a discontinuity or inclusion exists the magnetic field lines crowd together, thus the flux density rises. At high levels of induction the material becomes magnetically saturated and thus less permeable at a local level; though it remains much greater than for air, and a detectable magnetic flux leaks from the surface. A powerful A.C. magnet is used to magnetize the steel and a magnetic detector is placed on the test object between the magnet's poles to detect the leakage field. Analysis of the leakage field in damaged areas has the potential to estimate the extent of metal loss. Hall-effect sensors are commonly used as detectors and it is normal to use three sensors orthogonal to each other as each Hall-effect sensor can only detect the magnetic field in one direction.

D.2. Remote Field Sensing

Remote field testing is a useful technique in pipe inspection for external defects where only internal access is available. It has been employed as a method of corrosion detection since the 1960s. Using conventional eddy current techniques with a standard bobbin probe a very low frequency (i.e. 30 Hz) would be necessary to through-penetration test a pipe wall of 10mm thickness. This has an obvious drawback of very

poor sensitivity to flaws. The application of a saturated magnetic field to aid the penetration at lower frequencies is often impractical due to the amount of metal to be inspected.

A remote field probe consists of an exciter coil driven with a low frequency sinusoidal current and one or more detectors (often Hall-effect sensors) fixed apart at a distance of two tube diameters or more (this puts the detectors in the remote field zone).

The changing magnetic field caused by the sinusoidal current induces eddy currents which are strongest directly underneath the probe but which extend radially through the tube wall and along the tube wall in an axial direction. A magnetic field from these eddy currents, which opposes the magnetic field of the exciter coil is produced, but it does not entirely counterbalance the exciting field. The magnetic field due to the eddy currents is more spread out than the magnetic field from the exciter coil and thus the magnetic field from the eddy currents extends further along the tube axis. Consequently there comes a point where the magnetic field due to the induced eddy currents becomes dominant, this is the remote field. In this region the magnetic field is relatively weak, but is sensitive enough to be able to detect changes in wall thickness from the inside or outside of the tube; though the technique cannot differentiate which side the change is coming from.

D.3. ACPD

Alternating current potential drop (ACPD) is a simple NDE technique whose strength lies in the sizing of defects. It compares the drop in voltage over a crack in a sample

against the voltage drop across an un-cracked sample. The current and frequency of the test must be maintained to a very high degree to obtain accurate results. This is made difficult because of the temperature dependent nature of the test material's resistivity, so a comparison system is used in the assumption that the temperature of the reference sample and test sample are as similar as possible. A similar, even simpler NDE system exists, known as direct current potential drop (DCPD): this suffers from errors due to drift voltages and returns much smaller voltages than ACPD (thus it is less sensitive). DCPD is however, useful for measuring electrical conductivity. Unlike DCPD there is a skin-effect similar to that encountered in eddy current testing in materials of high conductivity or permeability. This makes the problem almost two-dimensional for these materials and results in accurate crack length measurement; since this is the only geometrical feature that can affect the potential drop in such a case. The relationship between the ratio of reference voltage to test sample voltage and the crack length is approximately linear for ferromagnetic materials.

The ACPD probe usually consists of two points (though some systems use four) between which the potential drop is measured. These two points should be equi-spaced either side of the flaw and the points on the reference sample set to the same separation. Since the flaw creates either a complete discontinuity or a localised change in resistivity the impedance of the path between the two points is different for the test piece than for the reference sample. Thus a flaw gives us a potential drop. Provided the point separation is maintained, ACDP can be used as a crack detection tool, but is not as reliable as other methods.

ACPD is significantly affected by increases in tensile strength and plasticity of the

material; both characteristics associated with crack propagation. Because of this and its accuracy in crack lengthing, it has applications in crack growth monitoring.

For materials that don't exhibit a strong skin effect, where eddy current formation is not limited to the near surface, there is scope for obtaining depth data about a defect. The depth of penetration is frequency dependent, so by observing voltage drop variations at known depths, further information about the crack geometry can be obtained. Much of the research in this area has focussed on the more complex situation where multiple cracks are encountered in close proximity.

D.4. ACFM

Alternating current field measurement (ACFM) is a technique that has similarities to both ACPD and conventional eddy current testing. Like eddy current, it is a non-contact method making it suitable for flaw detection through coatings and it works as well on ferritic metals or welds as it does on non-ferritic metals. It can locate flaws and accurately length them up to 25mm as well as providing some depth information.

The system measures two orthogonal components of the magnetic field; the x-component (in the direction of the crack length) and the z-component (in the direction of the crack depth). The test arrangement is similar to that of ACPD, the essential difference being the fact that the uni-directional current (in the y-direction: across the crack) is induced in the material rather than conducted and that it is the magnetic field that is measured not the potential drop. There is also no need for a reference signal.

Since the magnetic field is orthogonal to the current, where no defect is present the x-component is constant and the y and z components of the magnetic field are zero. Where a crack is present, this diverts current away to near the tips of the crack, causing an increased field density and significant variation in the z-component of the field over the crack ends; the signal resembles one cycle of a sine wave. The x-component will see a reduction in the magnetic field along the length of the crack.

Since the strength of the input current and the magnetic field disruption decay slowly with height above the specimen, lift-off is less of a consideration than with conventional eddy current. Consequently, ACFM can be used on materials with thicker (approx. 5-6mm) non-conductive coatings than conventional eddy current.

Scanning is performed parallel to the expected defect orientations, with the characteristic sine wave signals denoting the two ends of the cracks. ACFM's strength lies in the inspection of welds where conventional eddy currents struggle with the change in material properties and the geometry variations.

D.5. MWM

Meandering Winding Magnetometers (MWMs) are similar in many respects to eddy current tests though as the name suggests, they assess magnetic fields rather than coil impedance. This is however done by analysing the impedance derived from the complex voltage induced periodically in the sensing windings. MWMs are imposed ω-k magnetometers: that is to say that their characteristics are determined by the angular frequency (ω) of the input current and the spatial wavenumber (k). This permits accurate measurement of layer thickness, electrical conductivity and magnetic

permeability which can be correlated to infer material stress and microstructural changes and also to detect defects.

The primary and secondary windings of the magnetometer are arranged in a meandering pattern on a non-conducting substrate of negligible thickness to form a transformer that is effectively two-dimensional (see Figure D.5.1). When a current (I_P) is applied to the primary winding a time-varying magnetic field is imposed on the test object by the ω-k magnetometer. This magnetic field is at a prescribed frequency, determined by the input current as with conventional eddy current testing. The MWM also imposes a magnetic field with a prescribed spatial wavelength independent of the input current frequency. This spatial wavelength is determined by the spacing of the windings (λ) shown in Figure D.5.1. This arrangement produces a spatially periodic magnetic vector potential. In the absence of a conducting material the vector potential and the intensity of the magnetic field satisfy Laplace's equation and will decay away from the sensor surface at a distance proportional to the spatial wavelength. In the presence of a conducting media however the decay will be governed by the skin-depth if this is shorter than the decay distance dictated by the spatial wavelength. It is this independence of the control of frequency and wavenumber that gives this type of sensor an additional degree of freedom over conventional eddy current. Consequently more information about the material under test can be obtained.

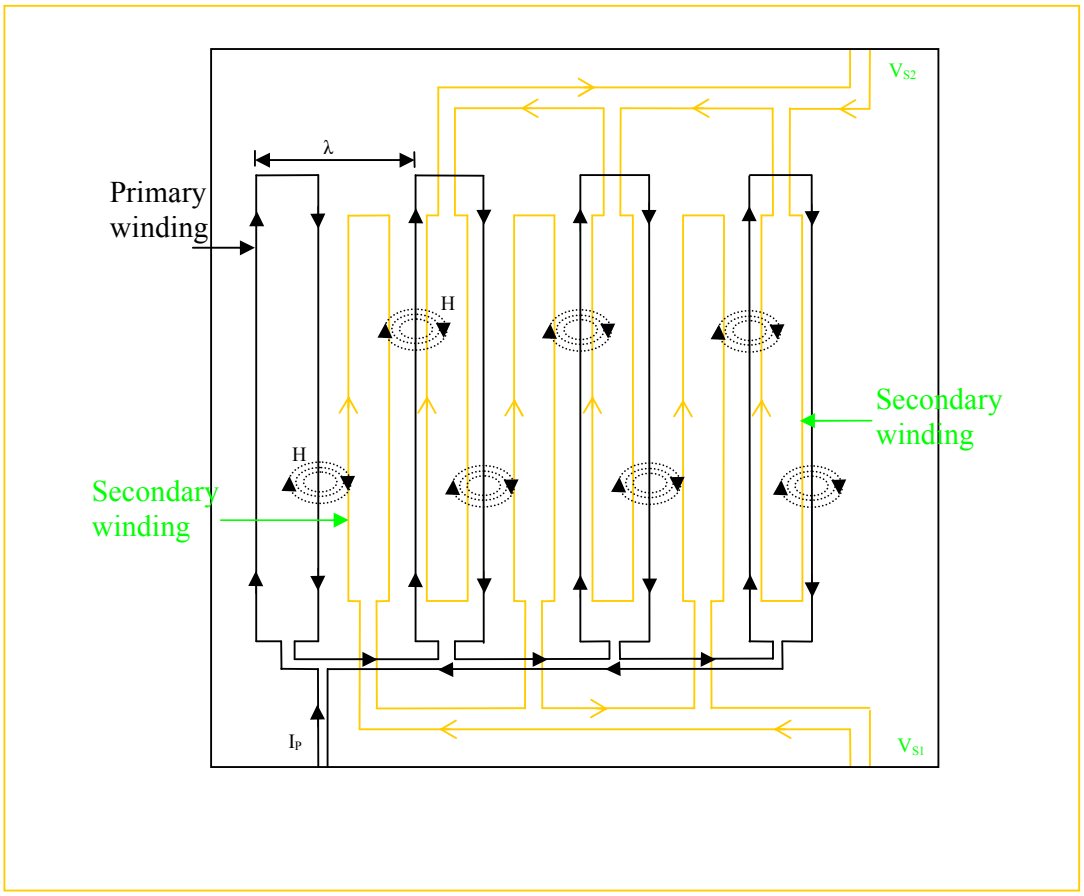

Figure D.5.1. Illustration of an MWM sensor

The spatially periodic magnetic field H is produced by driving the primary winding with current I_P. This links with the two secondary windings and induces a voltage in each one (V_{S1} and V_{S2} respectively). To produce an output voltage from the secondary coil (V_S) these two windings can be connected in series ($V_S = V_{S1}+V_{S2}$) or in parallel ($V_S = V_{S1}=V_{S2}$). Dividing this output voltage by the input current gives the complex impedance of the secondary winding.

The primary winding of the MWM excites a surface current density that can be modelled as an infinite number of Fourier modes. The length of the windings (l) is relatively long compared with λ and the secondary winding meanders either side of the primary

winding. A dominant Fourier mode of the surface current density with wavenumber k can be imposed along the y-axis. An inverse method is used, modelling the dominant mode plus other higher-order spatial-mode excitations. As a result the system can estimate one-dimensional distributions of properties under test; conductivity, complex permeability etc. without need for calibration.

The analysis of MWM data is complex, the system consists of the magnetometer whose response is analysed by an impedance analyser which then feeds the data into a property estimator. The property estimator consists of a continuum model, a measurement grid and a property analyser specific to the property the system is to measure.

The grid measurement system maps the magnitude and phase of the secondary winding impedance response into measurable properties. These grids are similar to look-up tables using a two-dimensional inverse interpolation method to obtain material properties. The specific nature of the measurement system requires various grids for various property/material combinations.

Multi-frequency and multi-spatial-wavelengths can be used to create multiple spatial Fourier models for more complex processing, such as measurement and analysis of multiple conducting layers in a structure. However, for the measurement of a single property such as the conductivity of a non-ferritic metal, a single dominant mode is sufficient.

The depth of penetration also varies from conventional eddy current, since it can be changed by varying either ω or k. It is given by

$$\delta = \frac{1}{\mathrm{Re}(\gamma)} \quad \text{(D.5.1)}$$

where γ (the complex wavenumber) is given by

$$\gamma = \sqrt{k^2 + j\omega\mu\sigma} \qquad \text{(D.5.2).}$$

Drawbacks of the MWM method include the cost and complexity of the equipment. The amount of information and time required to create an accurate property estimator and the physical size of the sensor footprint.

Appendix E. EMAT Theory

E.1. Introduction

Taking the case of a pancake coil, which is uni-directional and located at a height *h* above a conducting material in the *z*-direction. With a biasing magnetic field applied along the z-axis, the magnetisation and the magnetic field are related by

$$\underline{M} = [\chi]\underline{H} = \begin{bmatrix} \chi_{xx} & 0 & 0 \\ 0 & \chi_{xx} & 0 \\ 0 & 0 & \chi_{zz} \end{bmatrix} \underline{H} \qquad \text{(E.1.1)}$$

$$\underline{M} = \frac{\chi_m}{1+\chi_m}\frac{\underline{B}}{\mu_0} \qquad \text{(E.1.2)}$$

Thus

$$\underline{B} = \begin{bmatrix} \bar{\mu}_{xx} & 0 & 0 \\ 0 & \bar{\mu}_{xx} & 0 \\ 0 & 0 & \bar{\mu}_{zz} \end{bmatrix} \underline{H} \qquad \text{(E.1.3)}$$

Eqs. E.1.1 – E.1.3 then simplify to

$$\frac{\partial H_x}{\partial z} - \frac{\partial H_z}{\partial x} = J_y \qquad \text{(E.1.4)}$$

(Note: The displacement current can be neglected according to Hirao [158] because frequencies used by EMAT are typically <100MHz).

$$\frac{\partial E_y}{\partial z} = \mu_0 \bar{\mu}_{xx} \frac{\partial H_x}{\partial t} \qquad \text{(E.1.5a)}$$

$$\frac{\partial E_y}{\partial x} = -\mu_0 \bar{\mu}_{zz} \frac{\partial H_z}{\partial t} \qquad \text{(E.1.5b)}$$

$$J_y = \sigma E_y \qquad \text{(E.1.6)}$$

Differentiating Eq. E.1.5a with respect to *x* and Eq. E.1.5b with respect to z yields

$$\bar{\mu}_{xx}\frac{\partial H_x}{\partial x} = -\bar{\mu}_{zz}\frac{\partial H_z}{\partial z} \qquad \text{(E.1.7)}$$

Differentiating Eq. E.1.4 with respect to z, and inserting Eqs. E.1.5a, E.1.6 and E.1.7, we obtain

$$\left(\frac{\bar{\mu}_{xx}}{\bar{\mu}_{zz}}\frac{\partial^2}{\partial x^2} + \frac{\partial^2}{\partial z^2}\right)H_x - j\omega\sigma\mu_0\bar{\mu}_{xx}H_x = 0 \qquad \text{(E.1.8)} \quad [158]$$

From Eq. 2.1.2.4 the magnetic flux density due to a current element is given by

$$\underline{B} = \frac{\mu_0}{4\pi}\frac{I\ d\underline{l}\times\underline{a}_R}{R^2} \qquad \text{(E.1.9)}$$

Thus

$$\underline{H} = \frac{1}{4\pi}\frac{I\ d\underline{l}\times\underline{a}_R}{R^2} \qquad \text{(E.1.10)}$$

Taking a current element $nIdx$ at x, the tangential magnetic field at the origin in a vacuum is expressed by

$$dH_x^V = \frac{nIdx}{2\pi\sqrt{x^2+h^2}}\cdot\frac{h}{\sqrt{x^2+h^2}} \qquad \text{(E.1.11)} \quad [158]$$

And so the total tangential field at z=0 caused by the current in the coil is

$$H_x^V = 2\int_0^\infty dH_x^V = 2\frac{nI}{2\pi}\int_0^\infty \frac{h}{x^2+h^2}dx = \frac{nI}{2} \qquad \text{(E.1.12)}$$

Where

$$\int_0^\infty \frac{h}{x^2+h^2}dx = \frac{\pi}{2} \qquad \text{(E.1.13)}$$

At the interface of the material the magnetic field at the extreme of the material must equal that at the extreme of the vacuum. From Eq. E.1.13, the following must then be true

$$H_x^V(x,0) = H_x^M(x,0) = \frac{nI}{2} \qquad \text{(E.1.14)}$$

Because there is no variation with respect to x for all quantities, and introducing a term q which is equivalent to

$$q \equiv -\frac{1}{\delta}(1+j) \qquad \text{(E.1.15)}$$

where δ is the standard depth of penetration as defined in Eq. 3.1.1.25,

Eq. E.1.11 can be written as

$$\frac{\partial^2 H_x^M}{\partial z^2} - q^2 H_x^M = 0 \qquad \text{(E.1.16)}$$

To satisfy the boundary conditions laid out in Eq. E.1.14, Eq. E.1.16 becomes

$$H_x^M = \frac{nI}{2} e^{qz} = \frac{nl}{2} e^{-\frac{z}{\delta}} e^{-j\frac{z}{\delta}} \qquad \text{(E.1.17)}$$

So the magnetic field decays exponentially along the z-axis and is dependent on the electromagnetic depth of penetration. The depth of penetration for steels is typically 10μm, so it is a reasonable approximation to suggest that the electromagnetic field is only present at the material surface, since the ultrasonic wavelength is much larger than the depth of penetration [158].

E.2. Lorentz force

From Chapter 2 we know that when an electric field is applied to a conductor the Coulomb force $-e\underline{E}$ occurs on the individual electrons. The biasing magnetic field produces a Lorentz force $e\underline{v}_e \times \underline{B}$ where $\underline{v}_e$ is the mean electron velocity. The force of the electron-ion collision is denoted by $\frac{m\underline{v}_e}{\tau}$ where m is the electron's mass and τ is the collision time, typically of the order of 10^{-14} s for common metals. These elements combine to give the equation for motion of an electron is

$$m\frac{d\underline{v}_e}{dt} = -e\left(\underline{E} + \underline{v}_e \times \underline{B}_0\right) - \frac{m\underline{v}_e}{\tau} \qquad \text{(E.2.1)}$$

Multiplying by the electron density n_e, Eq. E.2.1 can be used to produce the force per unit volume of ions

$$\underline{f} = -n_e e\underline{v}_e \times \underline{B}_0 = \underline{J}_e \times \underline{B}_0 \equiv \underline{f}^{(Lorentz)} \qquad \text{(E.2.2)}$$

Returning to Eq. E.1.4, we can derive that

$$\frac{\partial H_x^M}{\partial z} - \frac{\partial H_z^M}{\partial x} = J_e \qquad \text{(E.2.3)}$$

Because the changes along the *z*-axis are much more significant than changes along the *x*-axis, the second term of the left-hand-side is insignificant compared to the first. Introducing the effects of the dynamic field from the EMAT coil, yields the Lorentz forces in the *x* and *z* direction.

$$f_x^{(Lorentz)} = \left(B_{0z} + \mu_0 \bar{\mu}_{zz} H_z^M\right)\frac{\partial H_x^M}{\partial z} \qquad \text{(E.2.4a)}$$

$$f_z^{(Lorentz)} = \left(\underbrace{B_{0z}}_{Static\_field} + \underbrace{\mu_0 \bar{\mu}_{xx} H_x^M}_{dynamic\_field}\right)\frac{\partial H_x^M}{\partial z} \qquad \text{(E.2.4b)} \quad [158]$$

Ordinarily the static field dominates and causes vibration at the same frequency as the driving current. Where a large driving current is used the dynamic field will begin to dominate and a second frequency will be produced at twice the driving current frequency.

E.3. Magnetising Force

The following formula can be derived for the force acting on the surface of, and in the volume of the material in the presence of a magnetising field [179]

$$\underline{F} = \int_V \nabla * (\underline{M} \cdot \underline{H}) dv + \frac{1}{2}\mu_0 \int_S \underline{n} M_n^2 dS \qquad \text{(E.3.1)}$$

The * denotes *nabla* only operating on $\underline{H}$, M_n is the normal component of the magnetisation. The first term integral, relating to the volumetric forces, is the magnetisation force or body force per unit volume.

$$\underline{f}^{M} = \nabla * (\underline{M} \cdot \underline{H}) \qquad \text{(E.3.2)}$$

The second term in Eq. E.3.1 is the surface force which disappears inside the material. When a biasing magnetic field is present, as is often the case with EMAT, Eq. E.3.2 becomes

$$f_x^{(Mag)} = M_{0x} \frac{\partial H_x^M}{\partial x} + M_{0z} \frac{\partial H_z^M}{\partial x} \qquad \text{(E.3.3a)}$$

$$f_z^{(Mag)} = M_{0x} \frac{\partial H_x^M}{\partial z} + M_{0z} \frac{\partial H_z^M}{\partial z} \qquad \text{(E.3.3b)} \quad [158]$$

The right-hand terms of each equation can be neglected as they are insignificant compared with those on the left-hand side. Combining the remainder of the equation with the Lorentz forces from Eq. E.2.4 yields

$$f_x^{(Mag)} + f_x^{(Lorentz)} = B_{0z} \frac{\partial H_x^M}{\partial z} + M_{0x} \frac{\partial H_x^M}{\partial x} \qquad \text{(E.3.4a)}$$

$$f_z^{(Mag)} + f_z^{(Lorentz)} = \left(M_{0x} - B_{0z}\right) \frac{\partial H_x^M}{\partial z} = -\mu_0 H_{0x} \frac{\partial H_x^M}{\partial z} \qquad \text{(E.3.4b)}$$

E.4. Magnetostrictive Force

When a ferromagnetic material is subjected to an external magnetic field, an isovolumetric dimension change occurs called magnetostriction. In polycrystalline materials the magnetostriction occurs in two stages; firstly the magnetic domains orientated approximately parallel to, and in the same direction of, the applied field will expand in volume, causing an elongation along the field. Following the rearrangement of the expanding domain the magnetization rotates about the easy-axis within the

domain, which reduces the dimension perpendicular to the external field due to the rotation of spins. The magnetostriction in the direction of the applied field is a function of the magnitude of the applied field and the magnetostriction curve of the polycrystalline material. For steels the magnitude of magnetostriction is of the order of 10^{-6} [158]. In an alternating field the magnetostrictive effect will cause piezomagnetic strains in the material, resulting in the formation of elastic waves. At high frequencies the piezomagnetic strains will fail to respond simultaneously with the external field, causing magnetostrictive stress inside the material.

The constitutive equation among the stress strain and field is given by [158]

$$\sigma_I = -e_{Ij}^{(MS)} H_j + c_{IJ}^H S_J \qquad \text{(E.4.1)}$$

Where $e_{Ij}^{(MS)}$ is the piezomagnetic stress coefficient,

H_j is the applied field,

c_{IJ}^H is the elastic-stiffness coefficient at a constant field and

S_J is the strain.

Using the body forces from Eq. E.4.1 in conjunction with the equation of motion

$$\rho \frac{\partial^2 u_i}{\partial t^2} = \frac{\partial \sigma_{ij}}{\partial x_j} + f_i \qquad \text{(E.4.2)}$$

permits the calculation of the acoustic fields generated by magnetostriction when the piezomagnetic coefficients are known.

Appendix F. 0.5CrMoV Samples for Creep Tests

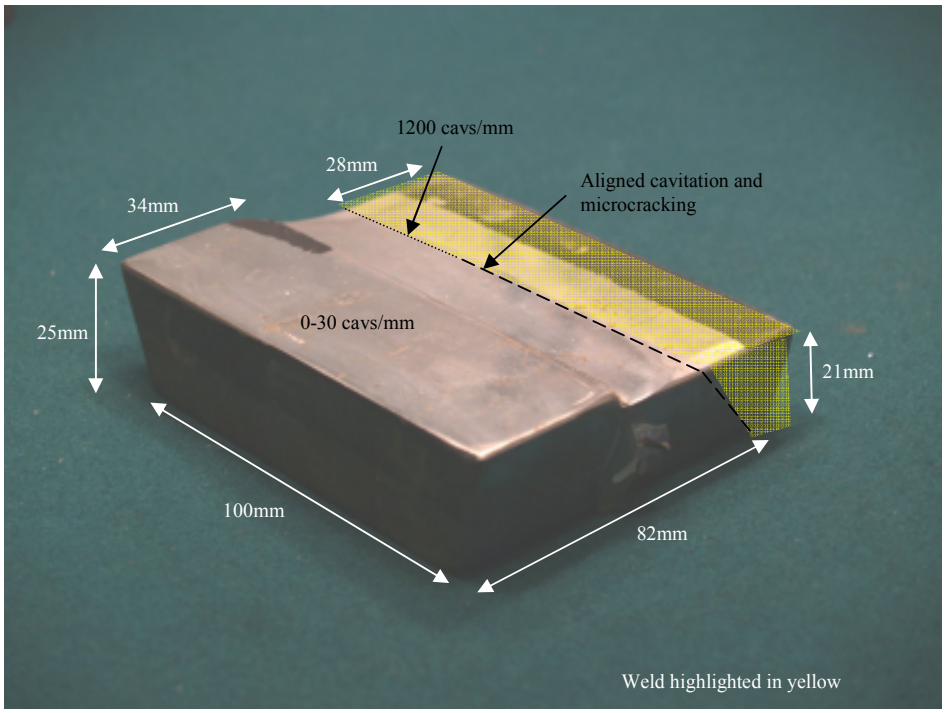

Figure F1.1 – Dimensional and positional information for 0.5CrMoV Sample1/2

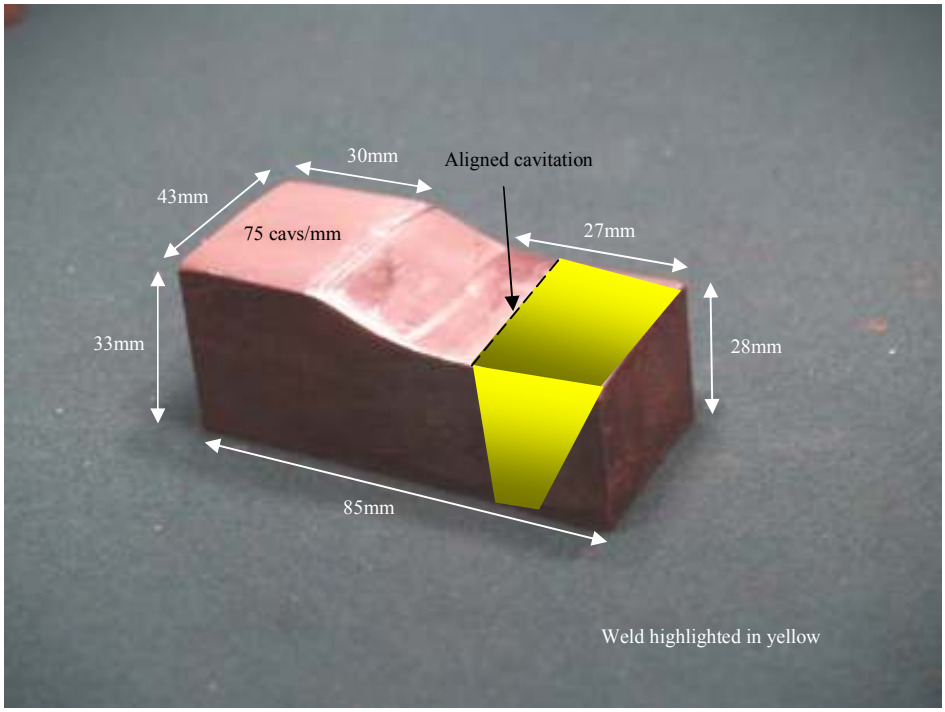

Figure F1.2 – Dimensional and positional information for 0.5CrMoV Sample3

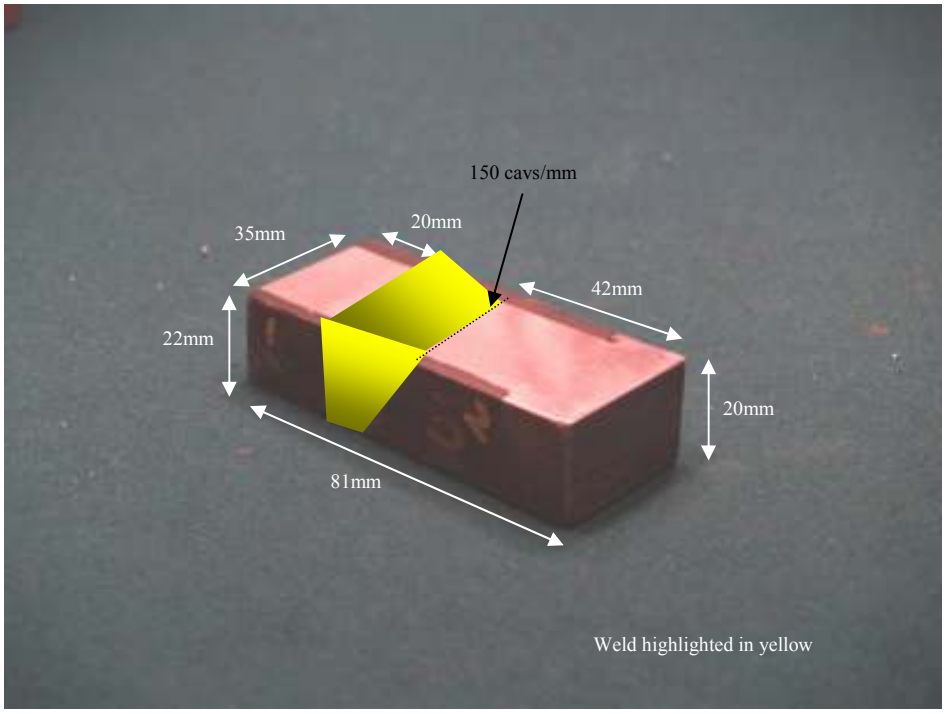

Figure F1.3 –Dimensional and positional information for 0.5CrMoV Sample5

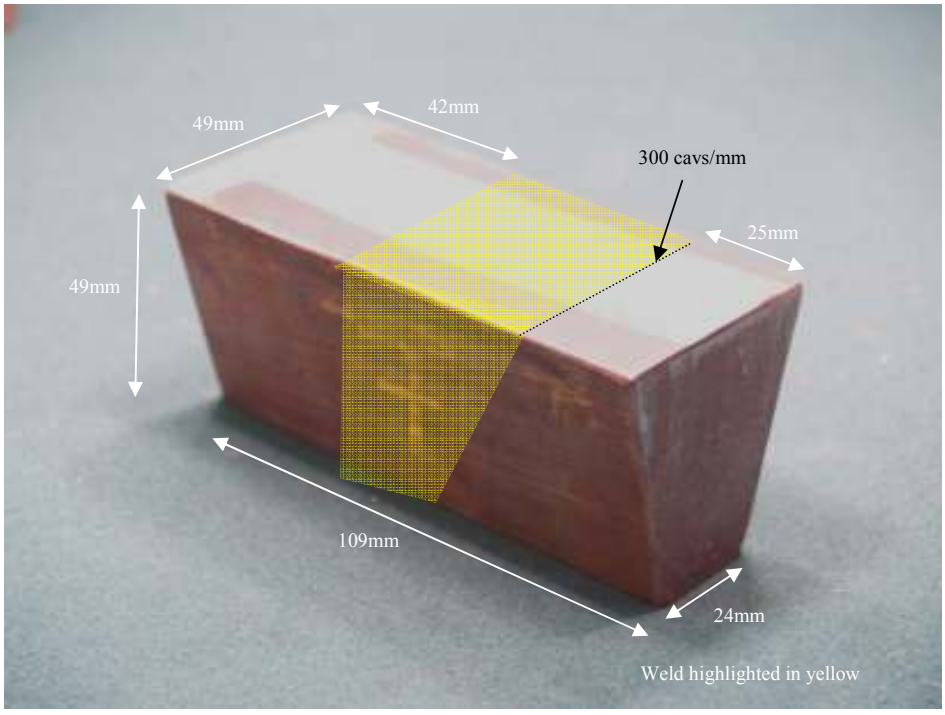

Figure F1.4 – Dimensional and positional information for 0.5CrMoV Sample7

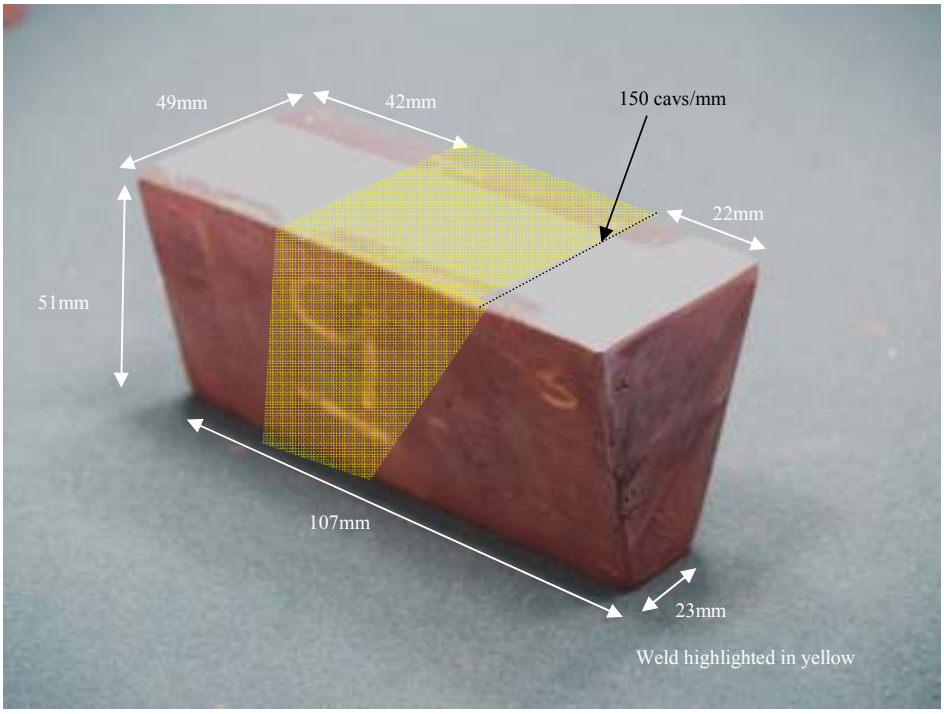

Figure F1.5 – Dimensional and positional information for 0.5CrMoV sample 9

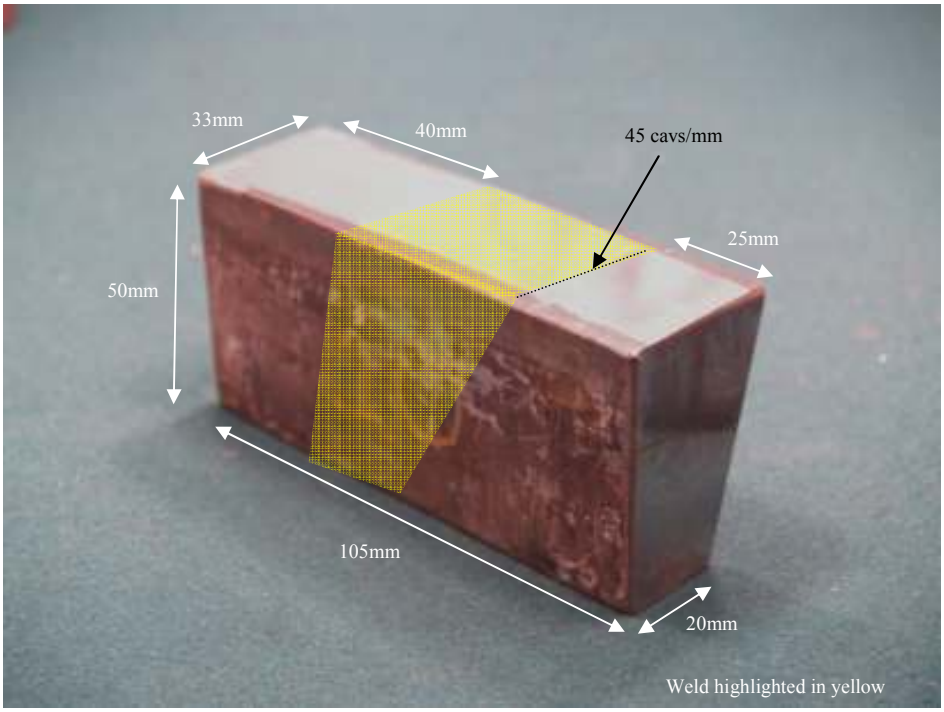

Figure F1.6 – Dimensional and positional information for 0.5CrMoV Sample10

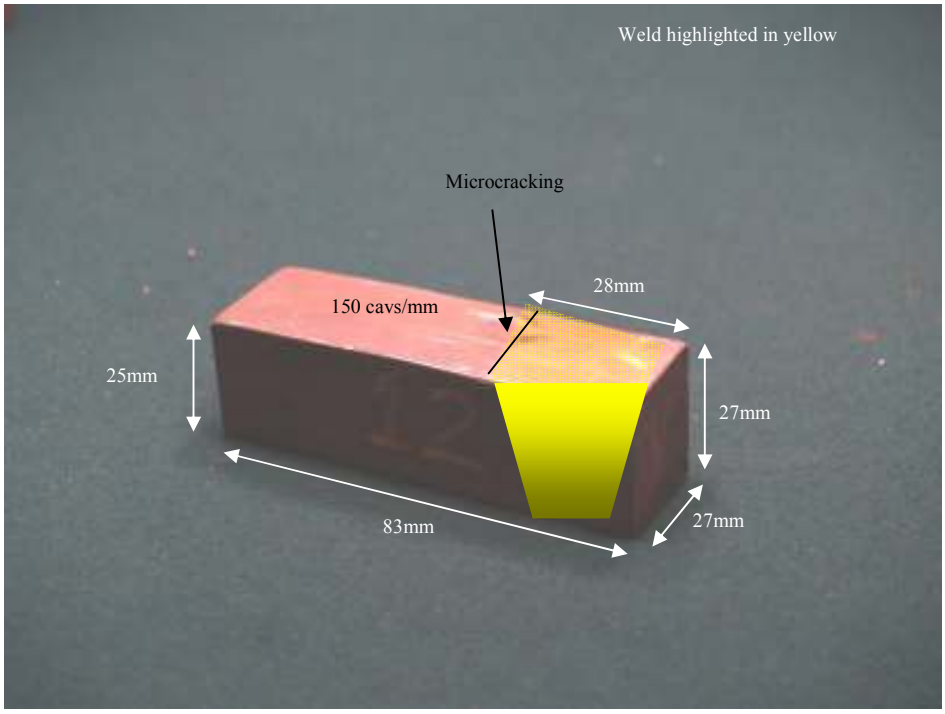

Figure F1.7 – Dimensional and positional information for 0.5CrMoV Sample12

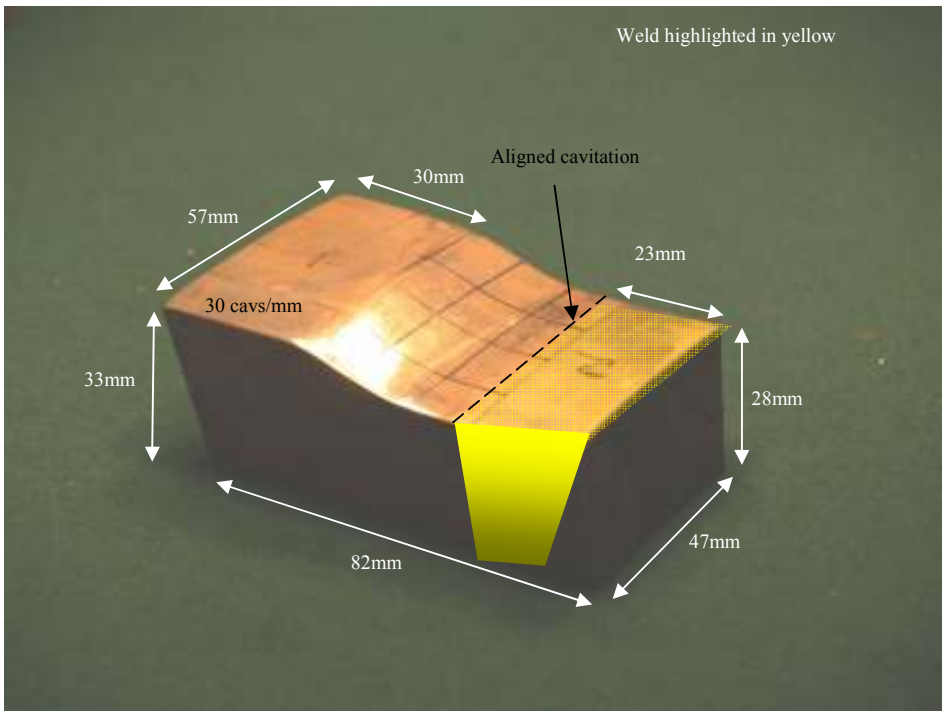

Figure F1.8 – Dimensional and positional information for 0.5CrMoV Sample14

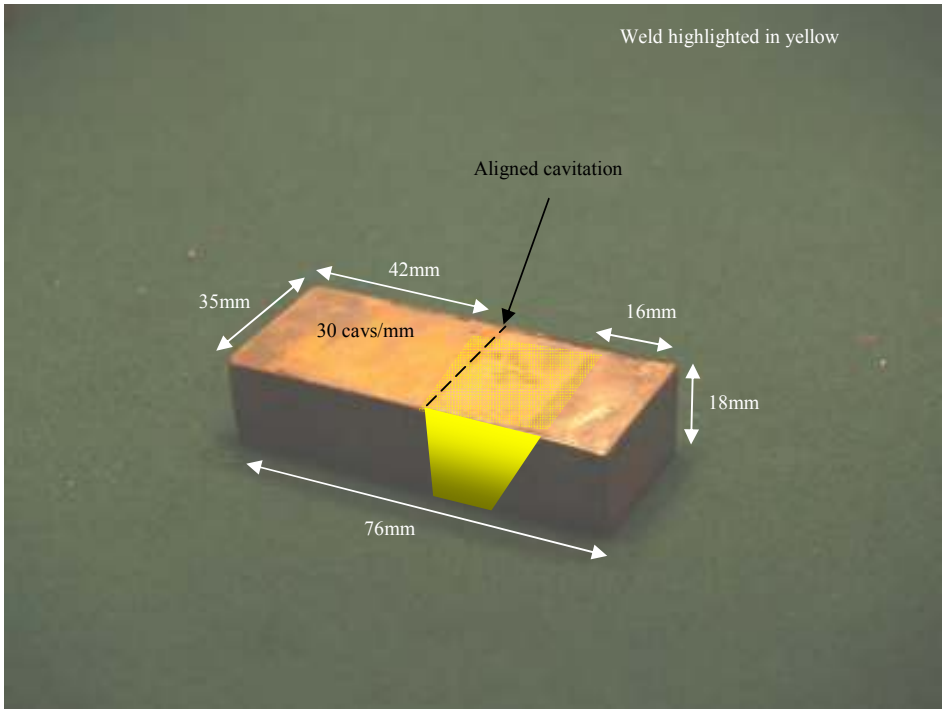

Figure F1.9 – Dimensional and positional information for 0.5CrMoV Sample15

Appendix G. Barkhausen Noise and PEC measurements on Blades

G.1. Magnetic Barkhausen Noise tests performed on 12Cr turbine blades for C. Ward by Newcastle University

Test report on RWE NPower turbine blades

John Wilson Maxim Morozov Gui Yun Tian

School of Electrical, Electronic and Computer Engineering, Newcastle University

G.1.1. Sample summary

Three ferromagnetic turbine blade sections were used in the tests, with two test regions defined for each blade. The three blades are shown in Figure G1.1; blade 1 has two test regions on the sharp (trailing) edge of the blade and the two remaining blades have two test regions on the opposite edge and towards the middle of the blades.

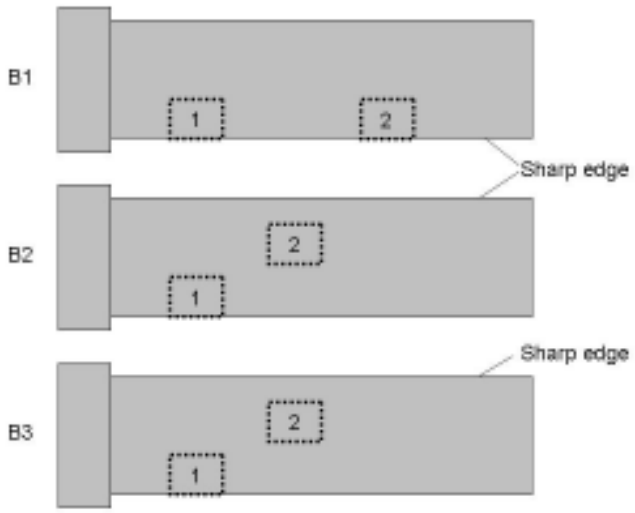

Figure G1.1 - Test regions for all three blades

G.1.2. Experimental systems

Three separate experimental systems were used in the tests:

Lab-based PEC inspection system featuring the following characteristics:

Probe: Circular coil;

Excitation repetition frequency: 500 Hz;

Response:

Difference signal $\Delta B_Z = B_Z - B_{AIR}$ dependent on magnetic permeability and conductivity;

Normalised difference signal $\Delta B_Z^{NORM} = B_Z/\max(B_Z) - B_{AIR}/\max(B_{AIR})$ mainly proportional to the electric conductivity of the material, where B_{AIR} is the reference signal obtained in air;

Features:

Max value of ΔB_Z reflecting magnetic permeability and conductivity

Peak value of ΔB_Z^{NORM} mainly proportional to the electric conductivity of the material

Lab-based MBE inspection system; 2Hz excitation frequency, 2kHz – 100kHz analysis frequency range.

Rollscan from Stresstech; commercial MBE inspection system, 125Hz excitation frequency, 70kHz – 200kHz analysis frequency range.

One of the major differences between the two MBE systems is the effective measurement depth. As eddy current shielding is governed by the skin depth formula, maximum measurement depth (δ) for a high-pass filter frequency (f) is given by:

$$\delta = \frac{1}{\sqrt{f\pi\mu\sigma}} \qquad \text{(G1.2.1)}$$

Where, μ is magnetic permeability and σ is conductivity, substituting values for a generic ferromagnetic steel, gives a maximum measurement depth of around 76μm for the Rollscan system and 634μm for the lab-based system. Although the lab based system offers a greatly increased measurement depth, both systems will be heavily influenced

by any treatment which alters that surface microstructure or stress state. Consequently, grinding, heat treatments and processes such as indentation hardness testing (Vickers/Brinell) will have a substantial effect on test results.

G.1.3. Experimental results

Figures G1.2a – G1.2d show the amplitude response for the three test systems. It can be seen from the plots that the amplitude results for all three test system exhibit the same general trends with a similar level for blade 1, region 1 (B1R1) and blade 1 region 2 (B1R2) for both of the lab-based systems. This is not the case for the Rollscan system, but this may be due to the increased sensitivity of this system to surface conditions. Different orientation measurement using the Rollscan system are illustrated in the Figure G1.2b; it is understandable that the vertical measurement has high errors due to edge effects from the probe. All the systems exhibit a similar trend for blades 2 and three, with an increase in amplitude for region 2, further towards the centre of the sample. Plot of the maximum value of difference signal, which is dependent on magnetic permeability and conductivity, appears to be uncorrelated to other results, as shown in Figure G1.2d. As illustrated in Figure G1.2d, the permeability influences are grouped by the samples. Accurate measurement of magnetic permeability on an open sample (open from the point of view of magnetic circuit) is required further processes, which didn't provide in the report.

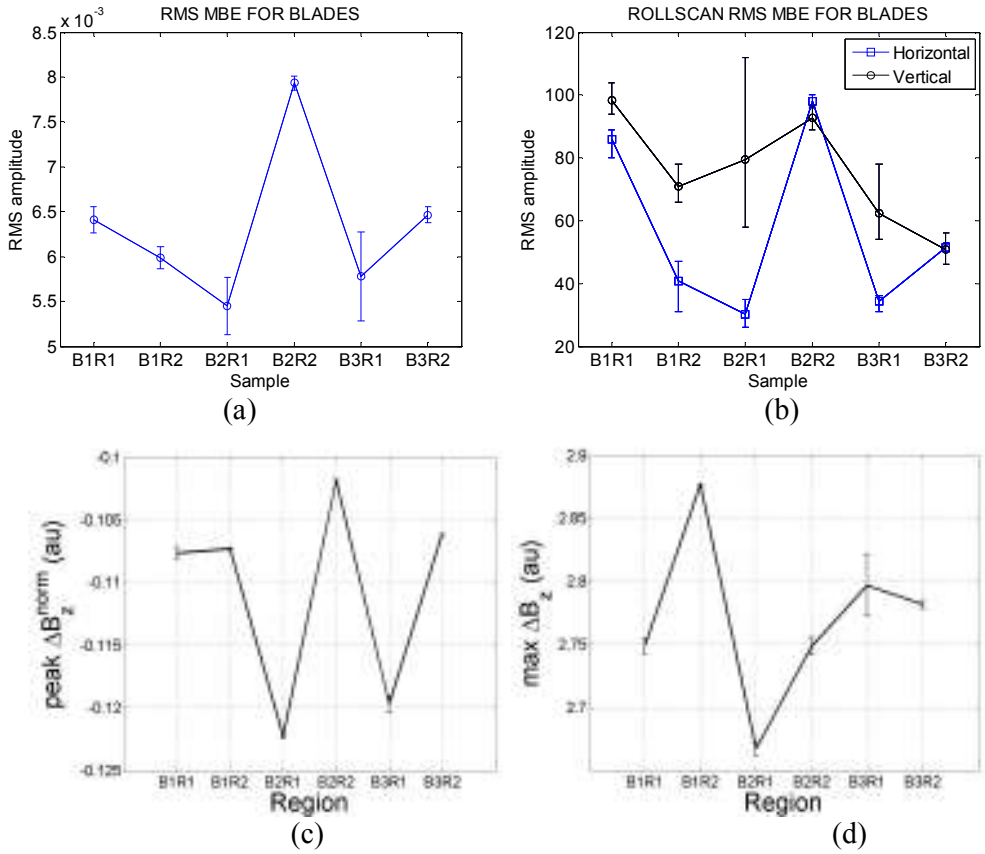

Figure G1.2 - a) RMS MBE for lab-based system, b) RMS MBE for Rollscan system, c) PEC Peak value of normalised difference signal ΔB_Z^{NORM}, d) Max value of absolute difference signal ΔB_Z

Although the amplitude plots are informative, the mechanisms which give rise to the change in amplitude cannot be deduced from this simplistic representation of the data. However, analysis of the MBE profiles, shown in Figure G1.3, provides an opportunity for further qualitative interpretation of the data. Through examination of the MBE profiles, the inspection sites can be broadly grouped into three categories:

B2R2 and B3R2; single high amplitude peak (peak 1) at around 0.05v – 0.1v.

B1R1 and B1R2; two peaks, peak 1 and peak 2 at around 0.2v.

B2R1 and B3R1; very low amplitude signal.

The major difference in the profiles is between the single peak (B2R2 and B3R2) and dual peak (B1R1 and B1R2) activity. There are several possible explanations for this, including:

The test regions on B1 are magnetically harder than the rest of the test regions, thus they magnetise at a higher applied field. This could be because they are physically harder also from work hardening or surface treatments.

The two peaks in the profiles correspond to different microstructural phases in the material [180]; peak 1 corresponds to the large peaks exhibited by B2R2 and B3R2 and peak 2 corresponds to a microstructural phase which is present in addition to this.
The lift off was greatest for these test regions, thus a higher excitation amplitude was needed for the same field to be applied to the sample.

As the microstructure of a material is intrinsically linked to hardness (magnetic and physical), points 1 and 2 are linked and the most likely explanation would involve a combination of both these factors.

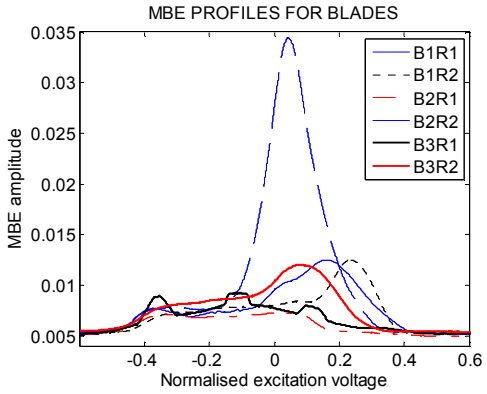

Figure G1.3 - MBE profiles for lab-based system

G.1.4. Discussion and conclusions

For the pure amplitude analysis shown in Figure 2, the test results from the three systems broadly agree, but further qualitative analysis of the MBE profiles from the low frequency, lab based system is needed to gain understanding of the amplitude changes. From a combination of MBE amplitude and profile results, the test regions can be grouped into three categories; low amplitude (B2R1 and B3R1), higher amplitude + single peak (B2R2 and B3R2) and higher amplitude + dual peak (B1 – both regions). Without further information on the history and original microstructure of the samples, it is not possible to provide a definitive explanation of this behaviour, but there is clearly variation in the microstructure / stress state between these regions. Particularly, MBE profiles in figure 3 group the three different material properties. The major conclusion from the bind test can be derived as follows:

- Different EM NDT&E methods and systems (PEC, lab-made MBE and commercial MBE systems) can provide similar results

- The lab-made MBE system can provide MBE profiles for further interpretation linking to sample material properties in Figure G1.3.

- Similarly, PEC system can provide conductivity and permeability response linking to sample material properties in Figure G1.2d.

- Further discussion in association with manufacturing process of the samples would be interesting and useful.

G.2. Pulsed Eddy Current tests performed on 12Cr turbine blades for C. Ward by Maxim Morozov of Newcastle University

Test report: NPower turbine blades
Time-harmonic eddy currents

The blades have been tested with Time-harmonic eddy currents with excitation frequencies being 100 Hz, 500 Hz and 1 kHz (the upper limit of our system). Figure G2.1 shows respective responses: (a) real part, (b) imaginary part, (c) absolute value, (d) complex plane. Since we measure difference of magnetic field ΔB with respect to air, the responses are shifted in phase by $\pi/2$ with respect to impedance measured by conventional eddy currents. Fig.1a agrees qualitatively with the max. value of the non-normalised difference signal. Fig.1b agrees qualitatively with the peak value of the normalised difference signal with opposite sign. Since there is $\pi/2$ phase shift, Figure G2.1a corresponds to the inductivity change (mostly due to magnetic permeability) and Figure G2.1b corresponds to the electrical conductivity change.

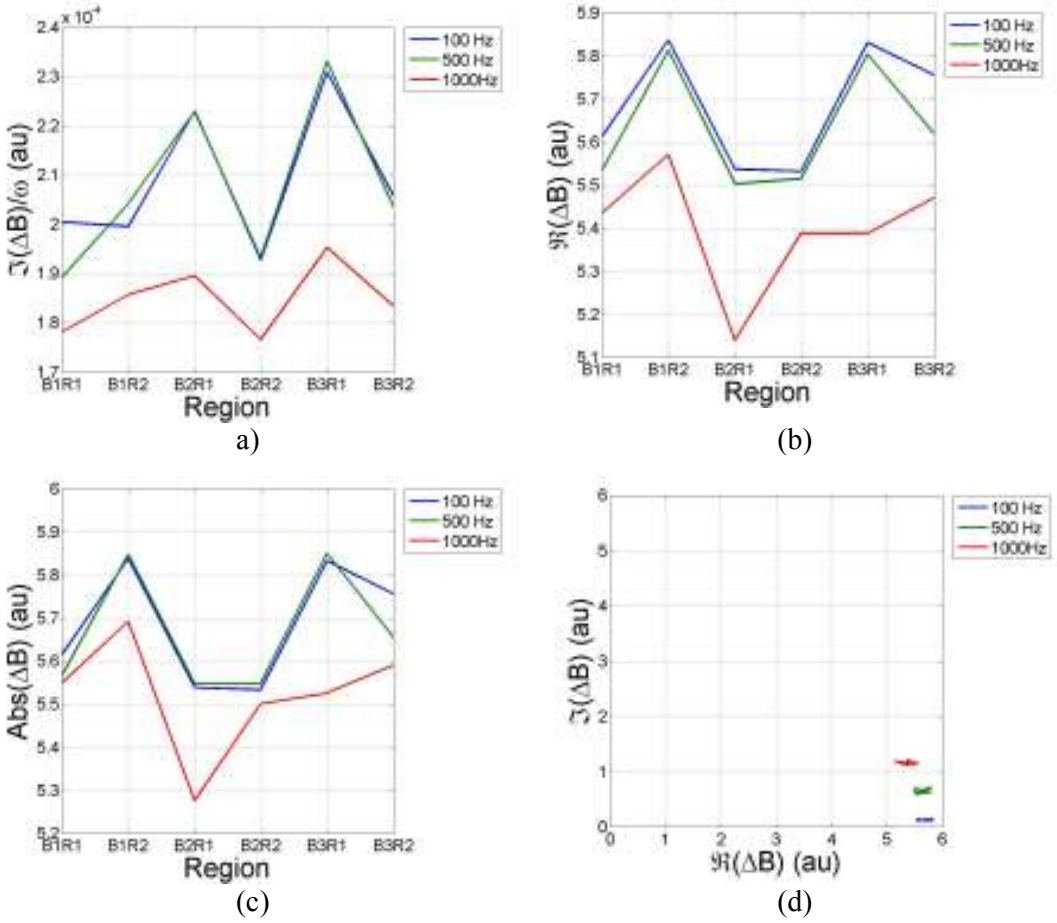

Figure G2.1 - Time-harmonic eddy current responses to blades: (a) real part, (b) imaginary part normalised to the excitation frequency, (c) absolute value, (d) complex plane.